



UNIVERSITAT DE
BARCELONA

Development of novel electroactive nanofluids for flow cells

Daniel Rueda García

ADVERTIMENT. La consulta d'aquesta tesi queda condicionada a l'acceptació de les següents condicions d'ús: La difusió d'aquesta tesi per mitjà del servei TDX (www.tdx.cat) i a través del Dipòsit Digital de la UB (diposit.ub.edu) ha estat autoritzada pels titulars dels drets de propietat intel·lectual únicament per a usos privats emmarcats en activitats d'investigació i docència. No s'autoritza la seva reproducció amb finalitats de lucre ni la seva difusió i posada a disposició des d'un lloc aliè al servei TDX ni al Dipòsit Digital de la UB. No s'autoritza la presentació del seu contingut en una finestra o marc aliè a TDX o al Dipòsit Digital de la UB (framing). Aquesta reserva de drets afecta tant al resum de presentació de la tesi com als seus continguts. En la utilització o cita de parts de la tesi és obligat indicar el nom de la persona autora.

ADVERTENCIA. La consulta de esta tesis queda condicionada a la aceptación de las siguientes condiciones de uso: La difusión de esta tesis por medio del servicio TDR (www.tdx.cat) y a través del Repositorio Digital de la UB (diposit.ub.edu) ha sido autorizada por los titulares de los derechos de propiedad intelectual únicamente para usos privados enmarcados en actividades de investigación y docencia. No se autoriza su reproducción con finalidades de lucro ni su difusión y puesta a disposición desde un sitio ajeno al servicio TDR o al Repositorio Digital de la UB. No se autoriza la presentación de su contenido en una ventana o marco ajeno a TDR o al Repositorio Digital de la UB (framing). Esta reserva de derechos afecta tanto al resumen de presentación de la tesis como a sus contenidos. En la utilización o cita de partes de la tesis es obligado indicar el nombre de la persona autora.

WARNING. On having consulted this thesis you're accepting the following use conditions: Spreading this thesis by the TDX (www.tdx.cat) service and by the UB Digital Repository (diposit.ub.edu) has been authorized by the titular of the intellectual property rights only for private uses placed in investigation and teaching activities. Reproduction with lucrative aims is not authorized nor its spreading and availability from a site foreign to the TDX service or to the UB Digital Repository. Introducing its content in a window or frame foreign to the TDX service or to the UB Digital Repository is not authorized (framing). Those rights affect to the presentation summary of the thesis as well as to its contents. In the using or citation of parts of the thesis it's obliged to indicate the name of the author.

Development of novel electroactive nanofluids for flow cells

Doctoral Thesis by Daniel Rueda García



UNIVERSITAT DE
BARCELONA

Development of novel electroactive nanofluids for flow cells

Memòria presentada per optar al grau de doctor per la
Universitat de Barcelona

Programa de doctorat en nanociències



Autor: Daniel Rueda García

Directors: Prof. Dr. Pedro Gómez Romero and Dr. Deepak Dubal

Tutor: Prof. Dr. Pere Lluís Cabot Julià

*Tesi realitzada a l'Institut Català de Nanociència i
Nanotecnologia, al grup de Novel Energy-Oriented Materials*



UNIVERSITAT_{DE}
BARCELONA

A scientist in his laboratory is not a mere technician: he is also a child confronting natural phenomena that impress him as though they were fairy tales. – Marie Curie

The force of the temptation which urges us to seek for such evidence and appearances as are in favour of our desires, and to disregard those which oppose them, is wonderfully great. In this respect we are all, more or less, active promoters of error. In place of practising wholesome self-abnegation, we ever make the wish the father to the thought: we receive as friendly that which agrees with, we resist with dislike that which opposes us; whereas the very reverse is required by every dictate of common sense. – Michael Faraday

Acknowledgements

I want to thank in first place all the people at the ICN2 who I have worked, talked and laughed with over these years, but in special to Marcos for our gaming sessions.

Second, to all my group mates in the novel energy-oriented materials group who have helped and guided me in my first days to the current people with whom I have a tremendous, but also exciting, project to face. I must highlight Zahilia, who has been there since my first day to almost the end of my PhD, helping me in everything I could need and shearing really good and nerdy moments.

Third, to Dr. Deepak P. Dubal, an old postdoc in our group and one of my thesis directors who not only helped and showed me a lot of things, but also became a reference for me. Also, to Prof. Fritz Huguenin, who gave me invaluable technical lessons and at the same time treated me as a friend.

Fourth, to my family, and especially to my parents who have given me the opportunity to keep studding all these years and made me the person who I am today.

Fifth, to my partner: Marta, your support has encouraged me every day to always do my best and overcome myself.

And finally, to the person who believed in me, who bet on me not one or two, but three times! (Bachelor's degree, Master, and PhD). Pedro, thanks to you, I could start my career as a scientist. But more important, you have showed me what a scientist should be: a researcher, a teacher and a popular communicator. Not only explaining to me the importance of each of them, but also by your example.

Abstract

Development of novel electroactive nanofluids for flow cells

Flow cells are on their way to become a key player for electrical energy storage (EES) thanks to their suitability as load-levelling devices thus contributing to the development of smart grid and to offset the intermittency of renewable energy sources. Until recently flow cells have been limited to Redox Flow Batteries (RFB), where energy storage is given by the redox reactions of dissolved ions. Very recently, new types of “flowable” electrodes have been proposed making use of capacitive storage mechanism (Electrochemical Flow Capacitors or EFCs). Our group has been one of the pioneering labs in this type of novel flow cells based on electroactive nanofluids. The present thesis aimed at harnessing the activity of well-known electroactive species (quinones, graphene, polyoxometalates, LiFePO_4) in novel electroactive nanofluids. An important part of our strategy has been the design of hybrid formulations and systems which could combine faradaic (redox) and capacitive (double-layer) storage mechanisms in order to improve the performance of the resulting flow cells.

We make an extended review and perspective of the electrochemical flow cell technology and their possible lines of evolution in the introduction of this thesis. With this we introduce the state of the art, the issues to solve and the different solutions proposed. Moreover, we also show our point of view and prospective for this technology and electrical energy storage in general.

In the chapter 4, the electrochemical fundamentals of quinones in lithium-organic electrolytes are studied. Quinones electrochemical mechanisms have been widely studied in aqueous media. In this work we study them in an organic electrolyte in an attempt to take advantage of the greater solubility and wider potential windows available in this media. We found and describe in detail several issues preventing the reversible functioning of quinones in Li^+ organic electrolytes which in turn preclude their use in flow cells under those conditions.

Chapter 5 describes the synthesis, characterization and electrochemical performance of hybrid materials based on reduced graphene oxide (rGO) and polyoxometalates dispersed in an aqueous H_2SO_4 electrolyte in order to produce a nanofluid. These nanofluids feature low viscosity and show an ultrafast electrochemical

response. We demonstrated their functioning as energy storage fluids with full charge and discharge of all solid material dispersed.

In chapter 6 a new kind of rGO nanofluid is presented. Instead of using conventional surfactants, we dissolved an aromatic molecule able to stabilize rGO in an aqueous electrolyte. With this approach we achieved a great increase in the stability of the nanofluid. Furthermore, this new nanofluid also showed a great charge transfer capability, as demonstrated by its enabling of the redox activity of LiFePO_4 nanoparticles. Thus, thanks to the presence of rGO in the nanofluid, electrons could reach the dispersed nanoparticles and thus be effectively and fully charged and discharged, something not possible in nanofluids containing only LiFePO_4 nanoparticles.

Graphene synthesis has been also deeply studied as part of this thesis as is shown in the chapter 7. As a result, a new method for the production of graphene by electrochemical exfoliation of graphite has been developed and patented. The patent, a summary of the results obtained and the state of the art of the electrochemical exfoliation method of graphene are presented in this thesis as the last chapter describing research work carried out within the framework of this thesis.

Table of Contents

Acknowledgements	i
Abstract	iii
Table of Contents	v
List of Publications	1
List of Acronyms	3
Chapter 1. Introduction	7
1.1 General introduction	9
1.2 To flow or not flow. A perspective on the evolution of flowable electroactive materials and devices for large-scale energy storage.....	17
Chapter 2. Motivation and Objectives	45
2.1 Motivation	47
2.2 Objectives	49
Chapter 3. Experimental Methods	51
3.1 Electrochemical techniques	53
3.1.1 General fundamentals	53
3.1.2 Cyclic Voltammetry	59
3.1.3 Chronoamperometry	66
3.1.4 Galvanostatic Cyclic with Potential Limitation	67
3.1.5 Potentiostatic Electrochemical Impedance Spectroscopy	68
3.2 Spectroscopic Techniques	75
3.2.1 Energy Dispersive X-ray Spectroscopy	75
3.2.2 X-ray Photoelectron Spectroscopy	76
3.2.3 Raman Spectroscopy	77
3.2.4 Ultraviolet-Visible Absorption Spectroscopy	78
3.3 Transmission Electron Microscopy	79
3.3.1 Selected Area Electron Diffraction	80
3.4 Scanning Electron Microscopy	82
3.5 X-ray Diffraction	82

3.6 Specific Surface Area	83
3.7 Rheology	85
3.8 Materials Preparation	85
3.8.1 Reduced Graphene Oxide	85
3.8.2 Reduced Graphene Oxide-Polyoxometalate	85
3.8.3 Lithium Iron Phosphate	86
3.8.4 Electrochemical Exfoliated Few Layers Graphene	86
3.8.5 Graphene Film Preparation	87
Chapter 4. Molecular Flowing Systems. Quinones in Organic Electrolytes	91
4.1 Context	93
4.2 Introduction	94
4.3 Experimental Section	96
4.4 Results and Discussion.....	97
4.5 Conclusions	114
Chapter 5. Hybrid Nanofluids Made of Reduced Graphene Oxide and Polyoxometalates	119
5.1 Context.....	121
5.2 Introduction	122
5.3 Experimental Section	123
5.4 Results and Discussion.....	124
5.5 Conclusions	136
Chapter 6. From hybrid Nanofluid to hybrid cells. The rGO/DABA-LiFePO₄ system	141
6.1 Context.....	143
6.2 Introduction	144
6.3 Experimental Section	148
6.4 Results and Discussion.....	151
6.5 Conclusions	161
Chapter 7. New and improved cell and method for the production of graphene by electrochemical exfoliation of graphites	165

7.1 Context.....	167
7.2 State of the art	167
7.3 Patent	170
7.4 Results.....	178
Chapter 8. Conclusions	191
Appendix. Resumen en Castellano	199

List of Publications

The following publications have been published or submitted directly related to the research carried out during this thesis:

- **Article: Rueda-García, D.**, Benages-Vilau, R., Gómez-Romero, P*. *To Flow or not to Flow. A perspective on the evolution of flowable electroactive materials and devices for large-scale energy storage*. Submitted Journal of Power Sources.
- **Article: Rueda-García, D.**, Dubal, D. P., Hugenin, F. & Gómez-Romero, P*. *Hurdles to organic quinone flow cells. Electrode passivation by quinone reduction in acetonitrile Li electrolytes*. J. Power Sources 350, 9–17 (2017). Doi: 10.1016/j.jpowsour.2017.03.048
- **Article: Dubal, D. P., Rueda-García, D.**, Marchante, C., Benages, R. & Gomez-Romero*, P. *Hybrid Graphene-Polyoxometalates Nanofluids as Liquid Electrodes for Dual Energy Storage in Novel Flow Cells*. Chem. Rec. 1–10 (2018). Doi:10.1002/tcr.201700116
- **Article: Rueda-García, D.** et al. *Battery and supercapacitor materials in flow cells. Electrochemical energy storage in a LiFePO₄ / reduced graphene oxide aqueous nanofluid*. Electrochim. Acta 281, 594–600 (2018). Doi: 10.1016/j.electacta.2018.05.151
- **Article: Rueda-García D.** et al. *From thermal to electroactive graphene nanofluids*. Energies 12(23), 4545 (2019). Doi: 10.3390/en12234545
- **European Patent application: Rueda-García D.** and Gomez-Romero P. *Electrolytic cell and procedure for the preparation of graphene by means of electrochemical exfoliation*. Application No./Patent No. 18382798.9 – 1108 (date of filing 12-11-18). Presently in PCT.

In addition to these articles, the author of this thesis is a co-author in the following articles as a result of various collaborative works/projects:

1. Lima, G., Dubal, D. P., Rueda-garcía, D., Gomez-Romero, P. and Huguenin, F. *Energy harvesting from neutralization reactions with saline feedback*. Electrochim. Acta 275, 145–154 (2018). Doi: 10.1016/j.electacta.2018.04.075
2. Ivana, Š. et al. *Comparison of insulin determination on NiNPs/chitosan-MWCNTs and NiONPs/chitosan-MWCNTs modified pencil graphite electrode*. Electroanalysis 1–11 (2018). doi:10.1002/elan.201800483
3. Šišoláková, I. et al. *Influence of a polymer membrane on the electrochemical determination of insulin in nanomodified screen printed carbon electrodes*. Bioelectrochemistry 130, (2019). Doi: 10.1016/j.bioelechem.2019.06.011

List of Acronyms

AC – Alternate current
AQ – Anthraquinone
BQ – Benzoquinone
CE – Counter electrode
CP – Cyclic Polarization
CV – Cyclic Voltammetry
DABA - 3,4-diaminobenzoic acid
DC – Direct current
EDL – Electrical double layer
EDX – Energy Dispersive X-ray Spectroscopy
EFC – Electrochemical flow capacitors
GCPL – Galvanostatic Cyclic with Potential Limitation
HENFs – Hybrid Electroactive Nanofluids
IHL – Inner Helmholtz layer
IL – ionic liquid
LFP – LiFePO₄
MBQ – Methyl-p-benzoquinone
NPs – nanoparticles
NQ – 1,4-naphthoquinone
OHL – Outer Helmholtz layer
PEIS – Potentiostatic Electrochemical Impedance Spectroscopy
POMs – Polyoxometalates
RE – Reference electrode
RFB - Redox flow battery
RGO – reduced graphene oxide
SAED – Selected Area Electron Diffraction
SCs – Supercapacitors

SEM – Scanning Electron Microscopy
SSA – Specific Surface Area
SSFC – Semi-solid flow cells
TEATFB - tetraethylammonium tetrafluoroborate
TEM – Transmission Electron Microscopy
WE – Working electrode
XPS – X-ray Photoelectron Spectroscopy
XRD – X-ray diffraction
Z – Impedance
 Z_j – Imaginary component of Impedance
 Z_r – Real component of Impedance

From the perspective “To Flow or not flow”

TEMPO - 2,2,6,6-tetramethylpiperidine 1-oxyl
2,7-AQDS - anthraquinone-2,7-disulfonic acid
BQDSH₂ - 1,2-dihydrobenzoquinone-3,5-disulphonic acid
AQDS - 9,10-anthraquinone-2,7-disulfonic acid (AQDS)/BQDS
BP – Benzophenone
DBB - 1,4-di-tert-butyl-2,5-dimethoxybenzene
TEATFSI - tetraethylammonium bis(trifluoromethylsulfonyl)imide
TEAPF₆ - tetraethylammonium hexafluorophosphate
EC - ethylene carbonate
PC - propylene carbonate
EMC - Ethyl methyl carbonate
2,6-DHAQ - 2,6-dihydroxyanthraquinone
2,6-DBEAQ - 4,4-((9,10-anthraquinone-2,6-diyl)dioxy)dibutyrate
Viologen - 1,1'-Dimethyl-4,4'-bipyridinium dichloride
LiTFSI - Lithium bis(trifluoromethanesulfonyl)imide
KB – Ketjen black
CB – Carbon black

MCM - Mesoporous carbon microspheres

RVC – Reticulated vitreous carbon

DMC - Dimethyl carbonate

DOL - 1,3-dioxolane

DME - 1,2-dimethoxyethane

DMTS - dimethyl trisulfide

SWNTs - single wall nanotubes

BMPL NTf2 - N-butyl-N-methyl pyrrolidiniumbis- (trifluoromethylsulfonyl) amide

CHAPTER 1
INTRODUCTION

1.1 General Introduction

The world's energy model is changing. The growing energy demand, a global awareness of climatic change and the search for more efficient energy models (combustion models show mean values of 20-25% of energy efficiency) are boosting this inescapable change. Almost 27% of the worldwide electrical energy generated in 2017 was from renewable energy sources¹. And by 2040, worldwide energy demand is expected to increase by 40%²; due mainly to the economic growth of countries like India, China and Africa. In contrast, the demand for energy in developed countries is expected to fall: the EU (-15%), USA (-3%) and Japan (-12%) due to the implantation of more efficient energy models³.

Efficiency is probably the most significant challenge, and thus a strong increase in electric systems/devices at the expense of fuel engine systems/devices is expected, leading to a 90% rise in electric power demand from today to 2040² and the emergence of smart grids as the key solution to face this challenge⁴. A smart grid allows several energy sources to be managed efficiently, saving energy when it is not needed and providing energy when it is necessary. Neither the demand for energy nor the production of energy from renewable sources is constant so devices able to store and provide large amounts of energy intermittently are necessary. Presently, flow cells constitute the energy storage technology that would contribute the most to make this possible and with efficiency⁵. Unlike conventional batteries, energy density is effectively detached from power density in flow cells: energy is proportional to the size of the external reservoir, so they allow a modular design, good scalability and flexible operation. Furthermore, as the electroactive materials are solutions, flow cells don't suffer the memory effects and phase changes of conventional batteries caused by their use of solid active materials. Such materials suffer a loss of capacity in each process of charge/discharge, which makes conventional batteries bad candidates for the long-term intermittent storage and provision of energy.

Flow cells can be the load-levelling devices to enable a smart grid to manage a more efficient use of the energy produced, but currently we need more than energy: we also need power. Time in $P=E/t$ becomes a critical point, energy must be provided in short periods of time and that's a problem for batteries because of the sluggish diffusion of ions in comparison with electron transport. A battery is an electro-ionic device in which each electron that moves from one electrode to the other must be compensated by an ion in order to keep the charge neutrality in the electrodes. Thus, ion mobility, which determines the current of the device, is the limiting step in batteries. In conventional solid

batteries the slower process is the ion diffusion though the solid active materials which depends on the crystal structure and morphology of the materials. Ion diffusion trough the solid material frequently implies phase changes that can lead to volume variations in the material that create defects in the crystal structure of the active material. These defects block the channels of ion diffusion preventing the ions from reaching part of the active site and therefore the capacity of the battery is reduced. In a battery a redox reaction takes place: in one electrode there is oxidation and in the other reduction. As a redox process takes place at a specific potential, the potential of a battery is constant (fixed by the redox process taking place). Although the slower step is the ion diffusion though the solid active materials, the diffusion of ions and the associated resistance through the whole cell can also have a huge impact on the battery's performance if it is not optimized particularly in respect of distance between the electrodes, pressure applied to them, electrolyte chosen and the separator used.

On the other hand, we have supercapacitors (SCs) devices that can be charged and discharged very quickly and cycled hundreds of thousands of times but that cannot store large amounts of charge. SCs store charge by a pure electrostatic mechanism. When the electrodes are polarized, the ions of the electrolyte balance the electrodes' charge, but only at the surface. Thus, energy storage in SCs is only at the surface and therefore the capacity of SCs is notability smaller than batteries, which store energy though all the bulk material. But, thanks to the fact that charge is only stored on the electrode surface, with SCs there's no ion diffusion though the material and as a result, SCs deliver notably higher power in comparison with batteries because the slower step of ion diffusion though the solid active materials is avoided. Furthermore, cyclability is also improved in SCs because defects generated in the active material are minimised due to the activity of ions at the electrode surface.

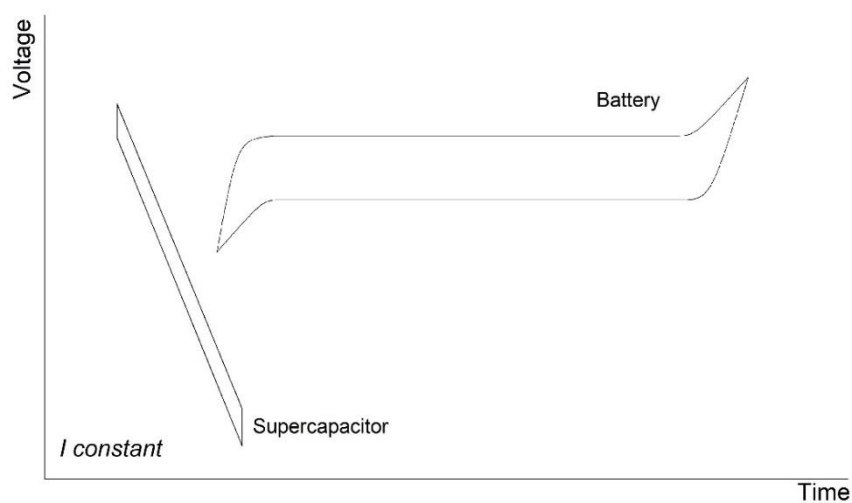


Fig.1 Potential evolution in a battery and in a SC.

Thus, it is highly desirable to combine a supercapacitor and a battery in the same device in order to get the large capacity of the batteries and the large power of the capacitors simultaneously⁶ with the grand challenge to reach values similar to those of the fuels shown in the Ragone plot, Figure 2, but in this case with better energy efficiency and without toxic emissions.

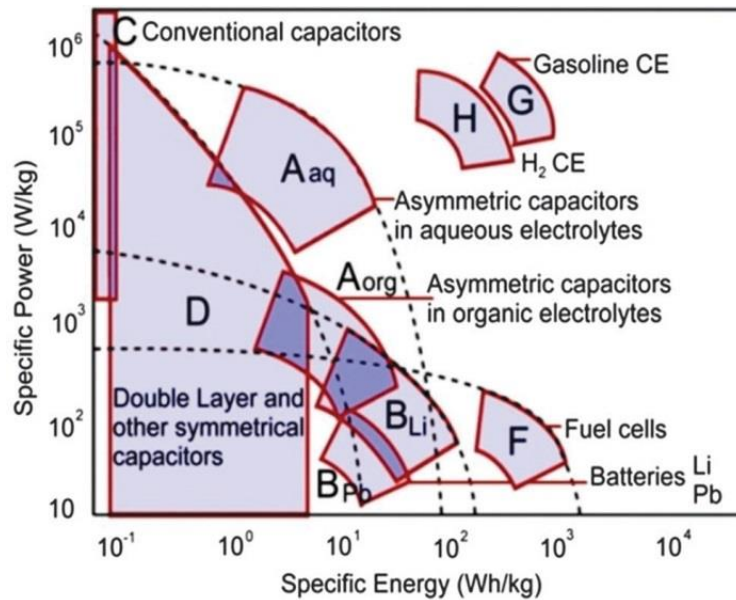


Fig.2 Ragone plot with Specific Energy and Power for different energy storage devices. . Reprinted from ref⁶ with permission of the corresponding author Pedro Gómez-Romero.

A hybrid system would allow faster charges and discharges given a device with large energy and power density. However, to achieve this synergy, it is necessary not only to create hybrid materials/solutions, but also to optimize the design of the electrochemical cells. Indeed, a hybrid device can be achieved without hybrid materials, simply by combining different kinds of non-hybrid materials in each electrode (e.g. battery material in one electrode and a capacitor material in the other). Therefore, cell design appears again as fundamentally important in the design of the device⁶.

Flow cell design (Fig. 3) usually consists of an electrochemical cell where the electroactive solutions flow through a pump system to the electrochemical cell and are oxidized/reduced, if it works as battery or charged/discharged if it works as a capacitor. The solutions and electrodes/current collector are separated by a selective ion membrane if the system works as battery and just by a physical separator if it works as a capacitor.

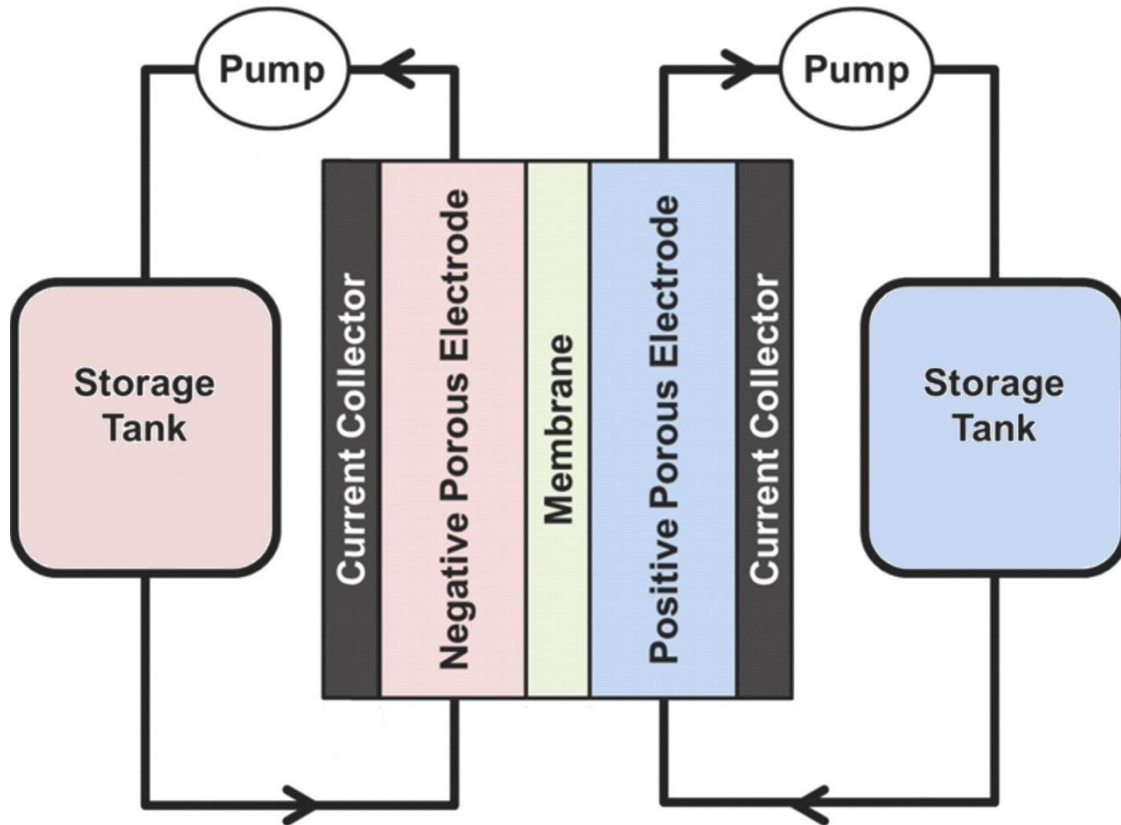


Fig.3 General flow cell scheme

The electroactive solutions are stored in external reservoirs, making flow cell capacity proportional to the size of the reservoirs (and of course to the concentration of the electroactive solutions). Power ($P = I \cdot V$) depends on the number of cells (in series, which improves V , in parallel, which improves I) and the area of the electrodes (larger area, larger I), so power and capacity are effectively decoupled, since increasing the reservoir size without increasing the area of the current collectors only increases the capacity but not the power. It is also critical to find a flow rate and channel design for the electrochemical cell that allow ions to pass through the membrane efficiently and also maintain efficient contact between the active species and the current collectors⁷⁻¹².

These features make flow cells ideal systems for coupling to energy production from intermittent renewable sources. Furthermore, thanks to the module design of the flow cells, they can be perfectly adjusted to any kind of intermittency, storage and power need, and are able to store the surplus energy produced during high activity production and return it when renewable sources stop producing energy. This would be very expensive with conventional batteries because repeated cycling decreases their capacity.

Flow cells based on the redox process have been widely studied since their invention by Thaller in 1974¹³ and were originally called redox flow batteries (RFBs).

However, flow cells based on capacitive energy storage mechanisms are relatively recent and are nowadays referred to as electrochemical flow capacitors (EFCs).

RFBs are usually classified according to the electroactive species (metal ions, molecules, complexes...) and its physical state inside the flow cell (liquid, solid, gas, slurry...). However, the channel structure/design, material, position and shape of the electrodes, kind of membrane and type of flow of the electrochemical cell are not normally considered. Consequently, flow cell design or configuration is not reflected in general classifications, cells used to be optimized for each case studied.

The main types of RFBs are: all-liquid, metal anode, hydrogen anode, oxygen cathode and semi-solid. As the name implies, in the all-liquid RFB, the electroactive species are completely dissolved in the electroactive fluid that flows in the cell and store the charge outside it. This kind of RFB works with ions, molecules and complexes, and can also work with water or polar organic solvents, which require a significant electrolyte concentration due to the large ionic resistance of the organic polar solvents, however, larger potential windows can be used in comparison with water. This helps to increase the energy of the battery, $E=Q \cdot V$ (energy E, charge Q and V potential). Semi-solid flow cells (SSFC) are based on carbon slurries combined with redox active materials. This approach allows a notable increase of energy density, but negatively affects the final efficiency of the devices due to the high energy needed to flow the high viscous slurries used. High viscosity is associated to the high concentration of solid needed in principle to get good electrical percolation, with carbon particles transferring electrons from the current collector to the redox active particles. Slurries can also be formulated without the addition of a redox active species, in which case they are used as electrodes for electrochemical flow capacitors (EFC).

Power and energy are completely decoupled in the all-liquid, semisolid RFB, hydrogen anode and oxygen cathode, but not in the metal anode because in this RFB an increase of the current collector (power) implies an increase in the amount of active solid metal material (capacity).

Finally, there are the nanofluids, a new topic that has appeared very recently in the field of flow cells. These fluids are based on stable dispersions of nanoparticles into an electrolyte with the aim of improving the energy density due to the large energy density of a solid active material in comparison with a solution, but without the large viscosity derived from the addition of large solid particles into an electrolyte.

However, large viscosity would only be a drawback in cases when flowing is unavoidable. Systems with large viscosity can be very interesting thanks to their potential for large energy density. Thus, we could pose the question: To flow or not to flow?

We tried to explore and answer this question in this thesis, but specially in the following perspective, which completes this introduction with an extended analysis of the state of the art of the flow cell technology.

References

1. Janet L., S., Jay, R. & Freyr, S. *Renewables 2018-Global status report. A comprehensive annual overview of the state of renewable energy. Advancing the global renewable energy transition-Highlights of the REN21 Renewables 2018 Global Status Report in perspective.* (2018). doi:978-3-9818911-3-3
2. OECD/IEA. 2018 World Energy Outlook: Executive Summary. 11 (2018).
3. International Energy Agency. World Energy Outlook. *Electron. Power* **23**, 329 (2014).
4. Amin, M. Energy: The smart-grid solution. *Nature* **499**, 145–147 (2013).
5. Zaghib, K., Mauger, A. & Julien, C. M. *Rechargeable lithium batteries for energy storage in smart grids. Rechargeable Lithium Batteries* (Elsevier Ltd., 2015). doi:10.1016/B978-1-78242-090-3.00012-2
6. Dubal, D. P., Ayyad, O., Ruiz, V. & Gómez-Romero, P. Hybrid energy storage: the merging of battery and supercapacitor chemistries. *Chem. Soc. Rev.* **44**, 1777–1790 (2015).
7. Dennison, C. R. *et al.* Effects of flow cell design on charge percolation and storage in the carbon slurry electrodes of electrochemical flow capacitors. *J. Power Sources* **247**, 489–496 (2014).
8. Aaron, D. S. *et al.* Dramatic performance gains in vanadium redox flow batteries through modified cell architecture. *J. Power Sources* **206**, 450–453 (2012).
9. Li, X. Modeling and simulation study of a metal free organic-inorganic aqueous flow battery with flow through electrode. *Electrochim. Acta* **170**, 98–109 (2015).

10. Watt-Smith, M. J., Ridley, P., Wills, R. G. A., Shah, A. A. & Walsh, F. C. The importance of key operational variables and electrolyte monitoring to the performance of an all vanadium redox flow battery. *J. Chem. Technol. Biotechnol.* **88**, 126–138 (2013).
11. Nikiforidis, G., Cartwright, R., Hodgson, D., Hall, D. & Berlouis, L. Factors affecting the performance of the Zn-Ce redox flow battery. *Electrochim. Acta* **140**, 139–144 (2014).
12. Leung, P. K., Ponce De Leon, C. & Walsh, F. C. The influence of operational parameters on the performance of an undivided zinc-cerium flow battery. *Electrochim. Acta* **80**, 7–14 (2012).
13. Thaller, L. H. Electrically rechargeable redox flow cells. (1974).
Report/Patent Number: NASA-TM-X-71540, E-7922

1.2 To flow or not to flow. A perspective on the evolution of flowable electroactive materials and devices for large-scale energy storage

Abstract

Massive energy storage is needed in order to match the steadily increasing share of intermittent renewable generation. Yet, no present technology is truly up to that task. Redox Flow Batteries were first postulated for high-capacity stationary storage but their limited energy density represents a serious drawback. In addition to new chemistries, new cell designs and new concepts are necessary and some have been proposed in recent years revolving around the idea of effective large-scale storage. From semi-solid to semi-liquid, to liquid metals or to nanofluids electrodes labels and concepts abound and are beginning to conform a constellation of competing technologies, each with their pros and cons. This perspective overview intends to relate and compare these concepts and technologies and to ponder the remaining gaps that still need to be addressed and filled in order to develop massive and cost-effective electrochemical energy storage.

Broader context

Energy storage has never been a key piece of our global energy cycle. Until now. The 20th Century witnessed the use of Li-ion batteries (LIBs) as the ultimate technology to just feed consumer electronics. But now we are witnessing a Cambrian explosion of energy storage variety, with demands that range from tiny, set-and-forget supercapacitors, to wearables, to EV batteries to high power storage. This is resulting in a feverish search for better LIBs, for beyond LIBs, for hybrid supercapacitors or for novel flow cells. The latter are the ones better suited for stationary applications to begin bridging the gap between our hastily growing needs of storage and our meagre overall present capacity. Indeed, global energy demand is expected to increase over this century¹. And by all accounts an increasing contribution to this energy will be generated by sustainable technologies¹. Redox Flow Batteries (RFBs) were the first to be

Desing of novel electroactive nanofluids for flow cell

postulated as the fittest for high-power stationary applications but their drawbacks are multiple and new concepts are popping up: semi-solid, semi-liquid and fully liquid electrodes are being proposed and the question arises as to whether alternative concepts and designs, in addition to battery chemistries, could be instrumental in finally finding the silver bullet (or the many lead pellets) needed for massive energy storage. Maybe to answer this grand challenge we should not go with the flow.

General overview

Renewable energy generation is advancing at a steady pace worldwide. Energy storage must catch up quickly in all its forms through a variety of biological, chemical or electrochemical vectors. Figure 1 shows some of these technologies on a plot that underscores the nominal power and discharge time for each of them. Pumped hydroelectric power used to be the only one with practical implementation in the GW scale, and although many pilot plants and demonstrators have been built for other technologies their consolidation is being excruciatingly slow.

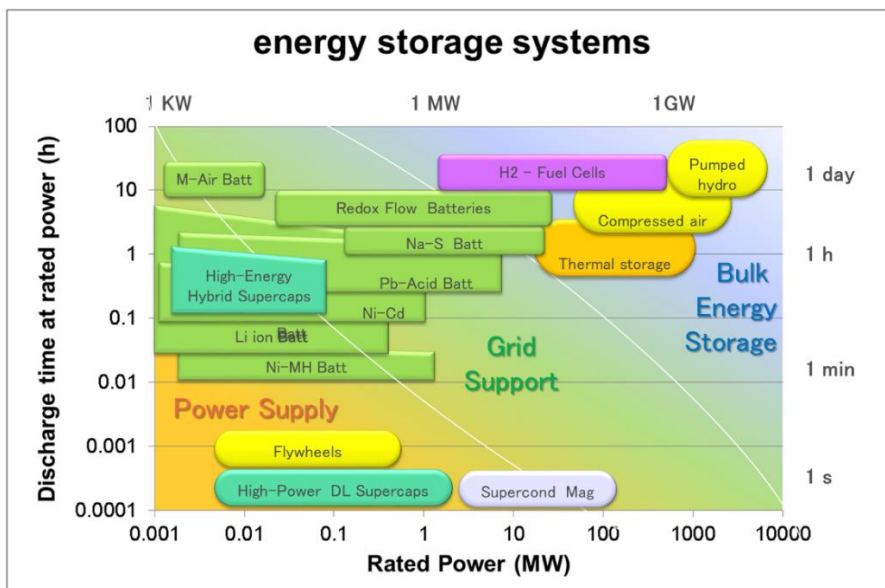


Fig.1 Various energy storage technologies depicted as a function of their nominal power and discharge time. Mechanical (yellow), magnetic (light grey) thermal (orange) chemical (purple), electrochemical (green) and electrophysical (blue-green) technologies are included.

Among batteries, Redox Flow Batteries (RFBs) have been postulated as the ones better suited for high capacity stationary applications. Yet, their drawbacks are multiple and new concepts are popping up: semi-solid, semi-liquid and fully liquid electrodes are being proposed

That is why there is still plenty of room for new concepts, new materials and new devices in the field of energy storage. New materials but also new types of materials have been reported to go beyond well-established state of the art Redox Flow Batteries like the “All-Vanadium” system. From nanofluids to pastes, from flowable to stationary dispersions the field is blooming with new concepts and ideas. This introduction is an attempt to relate these apparently dispersed approaches and analyze possible or desirable evolution of the materials and devices developed

Desing of novel electroactive nanofluids for flow cell

Actually, many of the newcomers to the take-off runway of storage technologies are essentially old concepts that were never fully developed due to a lack of technical means to address their drawbacks combined with a lack of specific niche applications. Lithium-Sulfur batteries or Flow Cells are two major examples.

Redox flow batteries (RFBs) were the first example of flow cells and were introduced by Thaller in 1974² with Fe(III)/Fe(II) and Cr(II)/Cr(III) solutions as cathode and anode fluids respectively. More recently, flow cells based on capacitive energy storage mechanisms have been proposed and are nowadays referred to as electrochemical flow capacitors (EFCs). Finally, there are the electroactive nanofluids, a new topic that has appeared very recently. These liquid materials are based on stable dispersions of nanoparticles into a liquid electrolyte with the aim of improving the energy density in comparison with electroactive solutions.

Generally speaking, we could highlight two main characteristics that will determine the overall performance of a flow cell, namely, the nature of the electrolyte and the physical state of the electroactive materials, Figure 2 summarizes the main advantages and drawbacks of each.

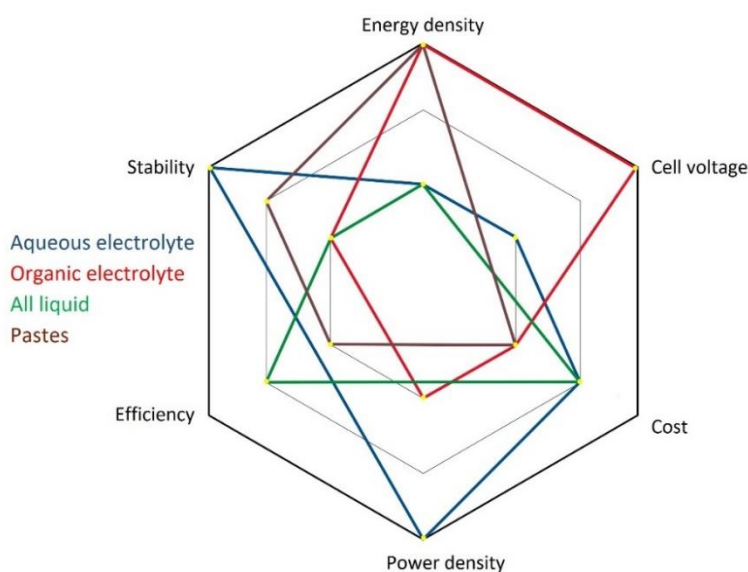


Fig. 2 Schematic diagram summarizing the performance of flowable electroactive systems

Aqueous electrolytes would provide large power density due to their greater ion mobility. And when metal ions are used as electroactive redox materials almost infinite cyclability could be reached but a thermodynamically limited voltage and low energy density related to low solubility limits would be expected. On the other hand, organic electrolytes would allow work with high voltages and large concentrations of organic redox active molecules thus would provide large energy density, but because this large

concentration would promote spurious reactions that would limit the cyclability and efficiency of the cell, finally because the reduced mobility of the ions into organic electrolytes would also limit the power density of a flow cell with an organic electrolyte. Solved active species into the electrolyte have an energy density limitation imposed by the solubility, the cyclability would depend on the stability of the solved active species which used to be more reactive when are solved, but the low viscosity and the continuous flux of current would provide good efficiency to the flow cell. Moreover, thick pastes or slurries would penalize the flow cell efficiency due to i) the extra high energy needed for pumping the heavily viscous pastes and ii) the variable current derived from an intermittent flow needed for the effective utilization of the electroactive particles in the paste.

Power and energy are completely decoupled in the all-liquid and semisolid RFB, which allows for a modular design that could be perfectly adapted to any kind of harvesting and power supply demand, thus are a perfect technology to be coupled to renewable energy sources.

All liquid RFB

There is one clear predominant chemistry related to RFB technology in research and applications, Vanadium RFBs are the most prominent example of that technology and have been deeply studied over the years to the point that, in recent years, research has been focused more on cell optimization than in the chemistry. Indeed, Vanadium RFB is the predominant RFB used in engineering studied about flow cells research. As a proof of it the present year papers published are mainly focus on two topics, first development^{3,4} and performance⁵ of the membrane, and second cell improvement: corrosion⁶, temperature^{7,8} and plane cell voltage^{9,10} effects on the performance of RFB. Vanadium RFB has an energy density of $40\text{Wh}\cdot\text{L}^{-1}$ and a specific energy of $25\text{Wh}\cdot\text{Kg}^{-1}$, operate between 1.6 and 1.3V¹¹, but corrosion issues, solubility limited up to 1.5-1.8M⁷ and the high price of vanadium, has promoted research on alternative RFBs. *Unfortunately, up today no better chemistry for RFBs than the Vanadium have been found when is considered the overall performance of the flow cell (capacity, efficiency, cyclability and stability).*

Inorganic solved active materials were the first chemistries studied in RFB, starting with the first RFB based on Fe/Cr chemistry published by Thaller, L.H in 1974². Cell voltage is 1.18V with a specific energy of $15\text{Wh}\cdot\text{Kg}^{-1}$ ¹², Fe³⁺/Fe²⁺ redox couple shows good reversibility and fast kinetics working in acid electrolyte. However, the slow

kinetics of $\text{Cr}^{3+}/\text{Cr}^{2+}$ usually requires an elevated operation temperature ($\sim 65^\circ\text{C}$)¹³ or catalysts like Bi or Bi/Pb on carbon¹¹, which significantly increases the cost. Meanwhile, the low redox potential of $\text{Cr}^{3+}/\text{Cr}^{2+}$ may cause H_2 evolution, which limits the coulombic efficiency and cycle life^{11,13,14}. Most recent publications have been about cross contamination through the membrane and system optimization¹⁵.

After Fe/Cr came the halogen RFB, based on a soluble metal ion in the anodic side and in general Br_2 in the cathodic side, with Zn/Br and V/Br being the most relevant examples but with the drawback of the generation of Br_2 possibly leading to corrosion problems. Many other redox couples have been tried over time standing out: polysulfide/Br, Zn/Cr, Zn/Mn, or Zn/halogen, but none of them could improve the performance of the vanadium RFB^{11-14,16}. Only the ZnI_2 couple has shown a clear improvement with an energy density of $166 \text{ Wh}\cdot\text{L}^{-1}$ brought about by utilizing an ambipolar electrolyte, where both cationic and anionic ions from a single soluble compound are both energy-bearing redox active species, the electrolyte eliminated the need for non-active counter ions and a high concentration ZnI_2 of 5.0 M was demonstrated¹⁷. Nevertheless, I_2 precipitation and high viscosity are important issues to be solved for a practical application of the system.

Redox active ambipolar electrolytes are one of the most prominent solutions for RFB technology as recently shown by Xiaohong Zhang and col. who used a synthetic ambipolar electrolyte a highly water-soluble (up to 1.2 M) artificial bipolar molecule containing cathode-active ferrocene moiety and anode-active bipyridinium moiety¹⁸. They achieved 4000 cycles of this ambipolar electrolyte with a 75% capacity retention and an efficiency of $> 99.8\%$, breaking the traditional cyclability limit of 100 cycles of the redox organic active species. Although their ambipolar electrolyte could reach 1.2 M, the study was done at a concentration of 0.5M of the ambipolar electrolyte supported by 1M of NaCl. Thus, the amazing stability demonstrated would need to be verified under high concentration conditions in order to apply this solution in real devices.

Desing of novel electroactive nanofluids for flow cell

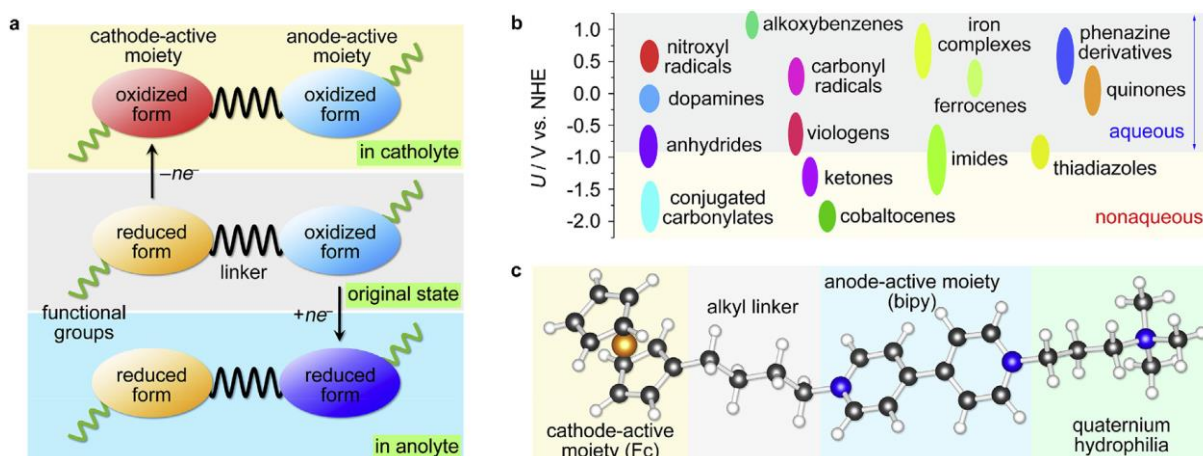


Fig. 3 “Artificial bipolar” molecules for SORFB application. (a) Schematic demonstration of the existence form of a general “artificial bipolar” molecule in a charged SORFB. (b) Representative redox-active molecules for the design of the “artificial bipolar” molecule. (c) A proposed bipolar Fc-bipy³⁺ for SORFB¹⁸. Reprinted from *Journal of Power Sources*, 417, Zhu, Y. et al, Enhanced cyclability of organic redox flow batteries enabled by an artificial bipolar molecule in neutral aqueous electrolyte, 83-89, Copyright (2019), with permission from Elsevier.

While ambipolar electrolytes are the most recent advance in the redox organic active species for RFB, a large variety of organic molecules have been studied as active redox species: single organic molecules, organic polymers, organic radicals and organic frameworks. The use of organic redox couples in aqueous or non-aqueous electrolytes is a promising approach for reducing the overall cost in the long-term, since these materials can be low-cost and abundant in comparison with large part of metals. The performance of such redox couples can be tuned by modifying their chemical structure. In recent years, significant developments in organic redox flow batteries has taken place with the introduction of new groups of highly soluble organic molecules, capable of providing a cell voltage and charge capacity comparable to conventional metal-based systems or even better^{19,20}.

Organometallic compounds and hybrid inorganic/organic systems have also been proposed and studied. Recently Aurore Lê et al. assembled a full and high soluble Fe complexes RFB²¹ stable hundreds of cycles with a volumetric capacity superior to 10 Ah·L⁻¹. In addition to improved solubility, metal complexes haven also been used to shift the potential of the active redox specie^{22,23} or increase the potential window of the RFB²⁴. The most common inorganic-organic approach is the combination of one of each species in each side of the redox battery, like the recent anthraquinone-2,7-disulfonic acid /KI RFB showed by Wonmi Lee et al. in which they proved that the addition of ethylene glycol increases the solubility of 2,7-AQDS and the redox activity of KI²⁵ but only 10 cycles were done in this study. Another recent work based on the combination of inorganic-organic RFB was the optimization cell performed by Amirreza Khataee and col. of a quinone/Br RFB²⁶, which studied the effect of electrode thickness, flow rate, membrane

thickness and concentration of redox active species. An increase of 12% in power density was achieved by cell optimization, however the performance of the cell was not better than the common Vanadium RFB.

Despite the fact that organic compounds have been relatively recent topics of RFB research they have assumed enormous importance and relevance because of their low equivalent weights, fast kinetics, wide window of electrochemical stability, flexibility and tuneability, and as just mentioned above, their complexes also allow their tuneability to be extended to metal ions. Consequently, current research in flow cells is now more focused on organic compounds than on inorganic metal ions^{19,20}.

In spite of poor solubility of organic compounds in water, a large amount of research has been done on water soluble organic compounds due to the fact that water is cheap, abundant, eco-friendly, safe and has a great ionic conductivity leading to great power density in comparison with polar organic solvents, which excel in cell voltage and energy density but are weaker in terms of cost, safety and power density²⁷. An example of the large complex organic compounds developed to work in aqueous electrolytes is the work done by Tino Hagemann et al. In their study they presented a RFB that employs a TEMPO containing copolymer as catholyte and the viologen derivative N,N-dimethyl-4,4'-bipyridinium dichloride as anolyte in an aqueous sodium chloride solution, which delivered a cell voltage of 1.3V and after cell optimization work in which the proper membrane, electrolyte concentration and flow rate were determined, after 100 cycles they achieved coulombic efficiencies of up to 95%, an energy efficiency of 85% and an energy density of 3.8Wh·L⁻¹. However, from 100 to 400 cycles the capacity of the system decreased from 44 mAh to 2.8 mAh²⁸. More simple molecules have been also studied with quinones probably the most studied organic molecules for RFB because of its good kinetics in water, low molecular weight, low cost and high energy density (2 moles of electrons per mole of quinone). However, as a variable, cell optimization has been shown to be as important as the redox active materials or the electrolyte. An example of quinones aqueous RFB cell optimization is the work done by Cao and col. in which they used nitrogen-doped porous graphene (NPG) as a highly efficient cathodic electrocatalyst for the redox reaction of 1,2-dihydrobenzoquinone-3,5-disulphonic acid (BQDSH₂), showing 6.7 times higher rate constant and much lower peak potential separation values compared to those of a glassy carbon electrode. Furthermore, a 9,10-anthraquinone-2,7-disulfonic acid (AQDS)/BQDS RFB with NPGs as the cathodic BQDS/BQDSH₂ catalyst exhibited a maximum power density of ca. 62.4 mW cm⁻², about 3.3 times higher than that of the pristine RFB without NPGs, and a minimal discharge capacity fade during the cycling test upon 100 cycles²⁹.

Low energy density is one of the most important issues concerning RFBs. Increasing the working voltage and specific capacity are the two possible lines of action for improvement. Higher voltages can be achieved by electrode engineering through molecular design whereas higher concentrations of active species would lead to greater capacities

A recent review³⁰ has summarized the many efforts along this line in recent years. Design new molecules with large potentials (electron-withdrawing groups tend to increase redox potentials and electron-donating groups tend to reduce redox potential) high solubility (alkane groups are usually the worst option and the amide groups are usually the best option); and high electrochemical activity and low chemical reactivity (promote steric repulsions).

For example, Wang et al substituted BP for electron-donating groups (4,4-dimethylbenzophenone) and obtained a cell open-circuit voltage of 2.97 V with DBB as cathode and working with 5mM concentration of actives species and 0.5M of TEAPF₆, they obtained an average discharge capacity of 52.1 mAh·L⁻¹, and an average coulombic efficiency of 72% over 95 cycles³¹.

And what about organic electrolytes for these electroactive organic molecules? The higher concentrations allowed by organic solvents could seem an obvious solution to the low energy density affecting liquid flow cells. Yet, most frequently, these systems have shown low stability and poor cyclability³². For example, Huang et al.'s studied a 3V RFB based on 2e⁻ redox process by phenothiazine catholyte and anthraquinone (AQ) anolyte in acetonitrile tetraethylammonium tetrafluoroborate (TEABF) 1M, but only 20 cycles where possible despite working with 0.05M active materials³³. In another report, X. Wei et al. reported record energy densities of 188Wh·L⁻¹, using half-cell based on Li metal anode and a 2M TEMPO solution in 2.3 M LiPF₆ /EC-PC-EMC cathode. However their system presented serious stability problems and was only subject to 20 cycles³⁴.

Rueda-Garcia et al have shown the occurrence of irreversible reactions (dimerization, polymerization and other intermolecular reactions) in specific quinones with organic electrolytes due to the formation of radicals and the influence of steric hindrance on the kinetics of those reactions³⁵. Paradoxically, the high concentrations which could allow for increased specific capacity and energy density also lead to the detrimental spurious reactions which dramatically reduce the energy density upon cycling²⁰. Thus, unwanted. irreversible and spurious reactions are probably the reason why most studies on organic solvents are performed with small concentrations and just a few cycles.

Steric hindrance has great potential for solving the problem of stability as Rueda-Garcia et al. proved by studding the electrochemical reversibility of different size

quinones in a Li-CH₃CN electrolyte³⁵ or as shown by David G. Kwabi who functionalized the 2,6-dihydroxyanthraquinone (2,6-DHAQ) with highly alkali-soluble carboxylate terminal groups. The resulting negative electrolyte material 4,4'-((9,10-anthraquinone-2,6-diyl)dioxy)dibutyrate (2,6-DBEAQ) was six times more soluble than 2,6-DHAQ at pH 12. Additionally, symmetric cell under Ar atmosphere with 0.1M cycling 2,6-DBEAQ on both sides of the cell demonstrated a remarkable capacity fade rate of <0.01%/day and <0.001%/cycle³⁶.

On the other hand, radicals can be stabilized and harnessed for energy storage (for example, by electron-withdrawing groups, donating groups or conjugation near the radical locus). And again, steric hindrance can significantly increase shelf-life by physically blocking bond formation³⁷.

Indeed, radicals have also been used as organic active redox materials, with TEMPO being the most studied, radical compounds have a great potential as shown by Bo Hu et al. In this study, TEMPO and 1,1'-Dimethyl-4,4'-bipyridinium dichloride (viologen) radicals were functionalized with 3-(trimethylammonium) and 3-(trimethylammonium)propyl respectively to provide steric and charge repulsion between them and used as 0.5M catholyte and anolyte respectively in 0.5M aqueous NaCl. The cell showed 1.38V and a remarkable 97.48% capacity retention after 500 cycles under Ar atmosphere³⁸. In addition, Xinyu Li reported another work based on a TEMPO/viologen RFB under Ar atmosphere in which they showed an improvement of cell performance by a capacity increase of 16.7%, and an energy efficiency improvement of nearly 20%. These were achieved by using nitrogen-doped three-dimensional reduced graphene oxide current collectors instead of carbon paper³⁹ showing again the great importance of cell optimization as a critical variable.

The electrolyte also plays a very important role in the chemical stability of the organic redox active species as shown by X. Wang and col. who tested the cyclability of a RFB based on benzophenone (BP) and 1,4-di-tert-butyl-2,5-dimethoxybenzene (DBB) with 4 different acetonitrile electrolytes. They found clear differences with tetraethylammonium bis(trifluoromethylsulfonyl)imide (TEATFSI) being the best option, although coulombic, voltage and energy efficiencies of the battery were 97%, 46% and 44%, respectively after 50 cycles⁴⁰. Wang et al. published a work in which they also studied the effects of the electrolyte in a RFB based on BP and DBB as the anode and cathode active species respectively. They used as base electrolyte acetonitrile 1M hexafluorophosphate (TEAPF₆) and mixed it with other more viscous polar organic solvents finding that the best ionic conductivity and also solubility of the BP and DBB was with the base electrolyte because it was the less viscous⁴¹.

Thus, low viscosity is not only important for optimal flowing but also for improved ionic conductivity and in some cases even for increased solubility of active species.

But there is one viscosity value even more important than that of the solvent, the viscosity of the whole fluid itself. Because, in addition to metal ions or molecular species, researchers are beginning to put lots of other materials, such as carbons or solid phase nanoparticles or clusters into base electrolytes, leading to new intriguing materials which bring about the question of whether to flow or not to flow.

Semi-solid flow battery (SSFB) and electrochemical flow capacitors (EFC)

As discussed above, solubility limits and chemical reactions between the active species have a negative effect on the energy density and stability of RFBs. A possible solution is the use of solid redox-active particles dispersed in the electrolyte instead of molecules⁴². The high density of these particles means larger energy density and solid particles are almost chemically inert in comparison with free dissolved molecules. However, due to the large size of those particles their diffusion to the current collectors is sluggish so an electrically conductive medium is needed to effectively charge and discharge them fully. Carbon slurries, which are pastes made of carbon particles usually with surfactants and a high viscosity, have been used as such effective electrical conductive media. Solid particles of a variety of active redox phases can be mixed into the carbon slurry to get anolyte and catholyte of the SSFB. Yet-Ming Chiang and col. developed a first so-called semi-solid battery in 2011⁴³, they tested 3 different configurations based on Ketjen black (KB) in 1M LiPF₆ slurry: LiCoO₂ and Li₄Ti₅O₁₂ (2.35 V average discharge voltage) delivered 397 Wh·L⁻¹ (168 Wh·kg⁻¹); LiNi_{0.5}Mn_{1.5}O₄ and Li₄Ti₅O₁₂ (3.2 V average discharge voltage) delivered 353 Wh·L⁻¹ (150 Wh·kg⁻¹); and LiCoO₂–graphite (3.8 V average discharge voltage) delivered 615 Wh·L⁻¹ (309 Wh·kg⁻¹).

Desing of novel electroactive nanofluids for flow cell

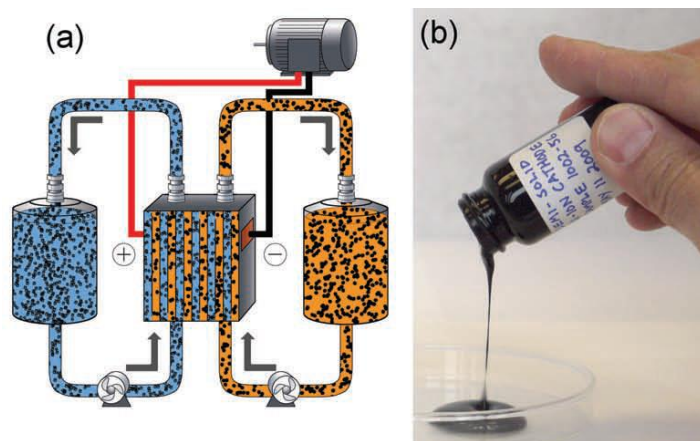


Fig. 4 Schematic diagram of a SSFB (a) and picture of typical electroactive paste(b)⁴³. Reprinted from Duduta, M. et al. *Adv. Energy Mater.* 1, 511–516 (2011) with permission from John Wiley & Sons, Inc.

It is also possible to use just the carbon slurries on their own to store energy by a purely capacitive mechanism, as it was introduced by Gogotsi and col. with their so-called Electrochemical Flow Capacitor (EFC)⁴⁴.

Carbon slurry is the key ingredient in both approaches as it enables good electrical and ionic conductivity, which are mandatory in both SSFBs and EFCs. The coexistence of different physical phenomena in suspension is not trivial and leads to complex behavior. The primary source of complexity of the SSFB and EFC is the competition between multiple phenomena (electrochemistry plus particle dynamics plus suspension dynamics) and quantifying the dynamics between parameters is as important as measuring a specific parameter (like active material content, carbon content, salt concentration, C-rate, channel depth, and so on). Monte Carlo simulations have been carried out in order to quantify the dynamics between parameters and detect generalizations regardless of type of cell setup⁴⁵.

The electrochemical characterization of various carbon slurries by Campos et al., showed that those slurries containing intermediate-sized spherical particles exhibited the highest capacitances and rate capabilities, and the longest self-discharge time for EFC operations. This can be attributed to improved percolation through the particle network, increased surface area and more favourable diffusion of ions through the pore-structure of the particles. Rheological measurements showed that slurries with spherical particles had, in general, lower viscosities than suspensions with anisometric particles.⁴⁶

In addition to shape, carbon activation can also have a great influence on performance. For example, Boota et al. found that a flowable electrode composed of carbon spheres previously activated at 1000°C for one hour yielded the highest capacitance (in comparison with 800, 900 and 950°C), rate performance, and lowest

equivalent series resistance values. These suspension electrodes showed a specific capacitance of $139 \text{ F}\cdot\text{g}^{-1}$ when tested in a static configuration⁴⁷.

Surfactants can also play an important role in the properties of slurries. Madec et al. demonstrated that the rheological and electrical properties of $\text{Li}_4\text{Ti}_5\text{O}_{12}$ /Ketjen Black/PC-LiTFSI suspensions can be improved with respect to SSFB systems if a non-ionic surfactant, i.e., the iso-octylphenylether of polyoxyethylene or Triton X-100 (TX), is added to the formulation. By decreasing the attractive interactions between the carbon black primary aggregates, TX allowed the formation of suspensions with higher electronic conductivity, unchanged stiffness at low shear rates, lower viscosity at high shear rates, improved stability over time at rest, and their suspensions showed energy densities of $63 \text{ Wh}\cdot\text{kg}^{-1}$ ($87 \text{ Wh}\cdot\text{L}^{-1}$)⁴⁸. Lee et al found that the use of surfactants for EFC systems effectively enhanced the volumetric energy density of the system; however, as the viscosity reduction is closely related to the decreased power performance, a careful balance between the viscosity and system resistance is required as a function of carbon concentration. However, a high concentration of surfactant was found to cause visible micelles formation. Moreover, they also found that flow operation showed a notably higher resistance in comparison with continuous non-flow operation. The different results for non-flow and flow operation related to particle sedimentation and the charge gradient in space as a function of time⁴⁹.

Nevertheless, non-spherical particles, like (KB) show different behavior compared with spherical particles as shown by Narayanan et al. in shear step experiments. Their study revealed a two timescale response. The immediate effect of decreasing the shear rate was an increase in both viscosity and electronic conductivity. In a much slower secondary response, both quantities changed in the opposite direction, leading to a reversal of the initial change in the conductivity. Stepwise increases in the shear rate led to similar responses in the opposite direction. This remarkable behavior is consistent with a picture in which agglomerating KB particles can stick directly on contact, forming open structures, and then slowly interpenetrate and densify. The fact that spherical CB particles show the opposite slow response suggests that the fractal structure of the KB primary units plays an important role. The fast and slow transient responses to a change in shear rate clearly indicate that KB agglomerates exhibit two build up (breakup) mechanisms after decreasing (increasing) the shear rate. The fast response was attributed to open agglomeration, and the slower response was ascribed to an interpenetration of the fractal-like KB units. The combination of these processes leads to a shear- and time-dependent agglomerate structure that gets frozen in on cessation of flow, with a higher pre-shear leading to a stronger gel with a lower electronic resistance, both critical to SSFB performance. An implication of these findings is that for

SSFBS operated in the absence of flow, a high pre-shear (through fast pumping or stirring) would be the best for minimizing the electronic resistance and maximizing the yield stress. For SSFBs operated in continuous flow, a high flow rate would minimize the electronic resistance⁵⁰.

New materials specifically designed for electrical percolative slurries have been proposed, for example, by Tian et al. who developed a simple spray-drying technique to produce mesoporous carbon microspheres with average particle sizes of 5 μm , high BET surface areas of 1150-1267 $\text{m}^2\cdot\text{g}^{-1}$, large pore volumes of 2-4 $\text{cm}^3\cdot\text{g}^{-1}$ and controllable mesopore sizes of 7-30 nm. The resulting MCM suspension electrode showed excellent stability and a considerably high capacitance of 100 $\text{F}\cdot\text{g}^{-1}$ and good cycling (86% of initial capacitance after 10000 cycles) under static conditions⁵¹. Again, as with RFBs, cell optimization is very important in order to take full advantage of the active materials. Akuzum et al. showed that a large improvement in cell performance could be obtained with 3D porous current collectors. With a reticulated vitreous carbon foam current collector with 45 pore per inch (ppi) (0.55 mm of pore size) they obtained the highest areal (290 $\text{W}\cdot\text{m}^{-2}$) and gravimetric (580 $\text{W}\cdot\text{kg}^{-1}$) power density values among all studied configurations, including the highest amount of Carbon Black addition (6 wt%) for the study. The addition of 45 ppi (0.55 mm) RVC into the EFC cell resulted in an almost 10 fold increase in power density and a 2 fold increase in gravimetric capacity, with just 5% of loss in coulombic efficiency under flow vs static and no significant difference in specific capacity between flow or static conditions⁵².

Electroactive slurries do not live by carbon alone. Several types of battery materials have been tested in combination with carbon slurries. Lithium intercalation compounds such as LiCoO_2 , $\text{LiNi}_{0.5}\text{Mn}_{1.5}\text{O}_4$, $\text{Li}_4\text{Ti}_5\text{O}_{12}$, LiMn_2O_4 , LiFePO_4 ; but also precipitation–dissolution chemistries (Li–sulfur, Mn–sulfur; as well as hybrid electroplating-polymer systems like Zn/polyaniline or MnO_2 /Polypyrrole⁵³. In many cases, the studies have sought to extrapolate the well-known lithium ion battery chemistry onto the SSFBs. An example is the work done by Liu et al. in which they used LiMn_2O_4 and activated carbon slurry electrodes, with 1M Li_2SO_4 , under static conditions achieving 23.4 $\text{Wh}\cdot\text{kg}^{-1}$, 50 $\text{W}\cdot\text{kg}^{-1}$ and an excellent coulombic efficiency after 1000 cycles⁵⁴. A large number of these types of studies use Li anodes which allow a notable increase of capacity at the expense of energy and power coupling in the cell. An example of the large capacities obtained is provided by the work by Hamelet et al. with a $\text{LiFePO}_4/\text{LiPF}_6$ EC-DMC/Li redox flow system that showed power density performances higher than 328 $\text{mW}\cdot\text{cm}^{-2}$ at 104 $\text{mA}\cdot\text{cm}^{-2}$ and an energy density of 50 $\text{Wh}\cdot\text{kg}^{-1}$ under static conditions⁵⁵. Li- O_2 battery research has also studied this kind of system, which has been shown as a promising solution for solving the high instability of Li- O_2 technology⁵⁶. Additionally,

systems based on Li ion technology but without metallic Li have been proposed. Chen et al. published a remarkable work based on monodispersed Si-C nanocomposite with ultrathin graphitic carbon coating catholyte coupled with highly concentrated LiI (5.0 M) in 0.2 M LiClO₄ 1,3-dioxolane (DOL)/ 1,2-dimethoxyethane (DME) (volume ratio 1:1). The system showed a stable cycle life of 60 cycles with a high Coulombic efficiency, above 90%, and more than 1200mAh·g⁻¹ of reversible capacity under static conditions⁵⁷.

A new approach to Li SSFB was recently reported by Li et al. they developed a *semiliquid* Li metal anode (SLMA) based on homogenous colloidal dispersion of Li microparticles (up to 40% vol) in a polymer/carbon composite matrix that provides for both ionic and electronic conductivity. By using Li_{6.4}La₃Zr_{1.4}Ta_{0.6}O₁₂ (LLZTO) solid electrolyte they studied the stripping/plating of the paste Li metal anode in comparison with planar Li foil⁵⁸. They found a big improvement in the performance of the semiliquid Li metal anode which showed, at 65°C, a stable Li deposition, with a resistance of ca. 100 Ω·cm⁻² for an SLMA/LLZTO/SLMA cell at 1mA·cm⁻². According to these researchers, the corresponding cell based on Li foil (Li foil/LLZTO/Li foil) showed a resistance between 4000-5000 Ω·cm² at just 0.1mA·cm⁻².

Although Li has been the main character in SSFBs (as in conventional solid batteries) it is important to look for alternatives since lithium can be considered an energy critical element. In this respect, sodium is the logical alternative but only a proof of concept regarding its use in SSFBs has been carried out. Ventosa et al. created a full SSFB based on a Na_xNi_{0.22}Co_{0.11}Mn_{0.66}O₂ cathode, a NaTi₂(PO₄)₃ anode and 1.3 wt% conductive additive dispersed in 0.5M NaPF₆ in ethyl carbonate/dimethyl carbonate (EC:DMC) as electrolyte. This system provided 2 V and only 9 Wh·L⁻¹ and 6Wh·Kg⁻¹ because experiments were done with dilute suspensions. However authors claimed that a 30 vol% of active material in the suspensions would deliver 150 Wh·L⁻¹⁵⁹.

Despite its name, SSFBs usually work in static conditions; once the material in the electrochemical cell is charged, it is replaced by fresh uncharged material. This is because, as it was shown above, the electrical connectivity between the particles is notably reduced under flow conditions. However, working in static conditions with the slurry resting on the current collectors could be considered alike a solid battery electrode. For high energy density slurries, a high load of active material is needed and thus, high viscosity is obtained which penalizes the efficiency of the process because high energy is needed in order to flow the viscous slurry. A possible solution to this problem, which keeps high energy density without increasing the viscosity, is to use shuttle molecules that deliver the charge from electrochemical cells to the active materials, which are stored in external reservoirs. This approach was used by Qizhao Huang et al. Who charged and discharged LiFePO₄ with 1,10-dibromofluorene and fluorene as shuttle

molecules⁶⁰. Recent works have focused on the complementation of the shuttle molecules solution with the Li-S chemistry, G. Li et al. evaluated dimethyl trisulfide (DMTS) as a multi-electron redox mediator for discharging and charging a solid sulfur cathode without any conductive additives. Using a Li metal anode, they got 3.83 Ah·L⁻¹ on the initial cycles and 3.23Ah·L⁻¹ after 40 cycles⁶¹. Full SSFB was developed by Juezhi Yu and col. using LiFePO₄ as cathode material and LiTi₂(PO₄)₃ as anode material with [Fe(CN)₆]⁴⁻/[Fe(CN)₆]³⁻ and S²⁻/S₂²⁻ as the redox mediators in the catholyte and anolyte respectively. The cell revealed an anodic and cathodic volumetric capacity up to 305 and 207 Ah·L⁻¹ for LiFePO₄ and LiTi₂(PO₄)₃ respectively and an excellent Coulombic efficiency after 55 cycles⁶².

Finally, we should also mention the development of slurry batteries without carbon. As an example, the recent work published by Z. Jin et al⁶³ made use of conductive polymers. They synthesized polymer microparticles based on polyhydroquinone (PHQ) for the cathode and naphthalene-1,4,5,8-tetracarboxylic acid dianhydride-ethylene diamine (PI1) copolymer for the anode. They prepared an all-polymer flow cell based on 1M micropolymer concentration and 2M sulfuric acid (7.8 mPa·s for PHQ and 3.1mPa·s for PI1). The cell delivered 0.8V and an initial discharge capacity of 8.95 Ah·L⁻¹ at 5 mA·cm⁻², (4.95 Ah·L⁻¹ at 20mA·cm⁻²), a loss in capacity of 0.36% per cycle (0.1% at 20mA·cm⁻²) and Coulombic efficiency of 87% (ca. 100% at 20mA·cm⁻²).

From 2D-confined liquids to Nanofluids

The presence of solvent molecules in solids is not a new discovery. But with few exceptions those solvent molecules, with water as the most paradigmatic example, do not constitute a separate phase from the solid. In 2D-Materials with nanoconfined liquids, could constitute a first stage into developing materials with an “internal electrolyte” as recently discussed by Augustin and Gogotsi⁶⁴. It should be noted though that even if an improved ion diffusion is provided within a single 2D particle, the inter-particle and particle to bulk conduction properties would also remain a challenge.

Alike liquid crystals, 2D- Materials with nanoconfined fluids could be considered as a first stage in a conceptual line that goes from dense crystalline solids to electroactive solutions (figure 5). Or conversely, they could be described as the final stage in the extensively studied sol-gel process (indeed, many of the examples of these type of materials are well-known gels such as V₂O₅· nH₂O). On the other extreme of this

conceptual line we could find electroactive solutions, like the ones used in RFBs, and sols, i.e. solid nanoparticles dispersed in a liquid.

Nanofluids are, by definition, *stable* dispersions of nanoparticles (NPs) in a base liquid medium (i.e. sols) which constitute materials with flowing as a primary characteristic. As such, nanofluids feature much lower viscosities than SSFBs, albeit also lower loadings of the solid phase. Electroactive Nanofluids (ENFs) constitute a novel type of materials which could be considered to lie halfway between pure solutions used in RFBs and the pastes conforming SSFBs. They represent an opportunity to increase the energy density with respect to the former by increasing substantially the nuclearity of the electroactive species, while maintaining a lower viscosity for effective flowing with respect to the latter. The primary challenge in working with nanofluids is to push forward the “solubility limit” of dispersed nanoparticles, which was initially precluding the formulation of practical and stable dispersions with superior energy density per liter of fluid. This apparent drawback is not an unsurmountable intrinsic barrier and, in this respect, nanofluids with 70 wt% (30 vol%) of solids in alkaline aqueous electrolytes and with a viscosity below 26 cP at room temperature have been recently reported⁶⁵.

Another challenge for nanofluids is to assure the total utilization of all the electroactive particles dispersed, whether through flowing or by enhanced electron-transfer. The percolation necessary for this was demonstrated by Yet-Ming Chiang and col by aggregation of conducting nanoparticles at ~1 vol % concentration in a lithium polysulfide half-flow cell⁶⁶. Similarly, stabilized graphene nanofluids have also been shown to be instrumental in providing the mechanisms to allow for this enhanced electron transfer in charge-discharge experiments^{67,68}.

Nanofluids are a very recent topic and currently there are few publications about them. Most are focused on thermal properties⁶⁹ and only a handful of them are related to electroactive nanofluids. As with RFB and SSFB, nanofluids can work though a capacitive or faradic mechanism.

Some of the early works on electroactive nanofluids were merely centered on the reduction of the electrolyte resistance in solid supercapacitors. For example, Kong et al. reported an increased ionic conductivity upon addition of single wall nanotubes (SWCNTs) in ILs of N-butyl-N-methyl pyrrolidiniumbis- (trifluoromethylsulfonyl) amide (BMPL NTf2) which formed a stable nanofluid electrolyte and, consequently, decreased the internal resistance of a conventional 5V supercapacitor, leading to higher capacitance, higher energy and power densities, compared to the pure IL system⁷⁰. Similarly, Vardhan et al. improved the capacitance of MnCO₃ by the addition of a small amount of SiO_x NPs (15nm) into the electrolyte, in 0.1 M Mg(ClO₄)₂. An enhancement of 60% in the capacitance was observed using the electrolyte with the SiO_x NPs in

comparison with the same electrolyte without NPs⁷¹. On the other hand, and along the line of the EFC discussed in the previous section, capacitive nanofluids can also be designed as active materials themselves, providing much lower viscosities than slurries while keeping the ability to charge dispersed solid nanoparticles. Thus, nanofluids made of rGO dispersed in aqueous H₂SO₄ have been shown to act as capacitive flowing electrodes themselves, with full utilization of the active material and showing fast charge transfer and low viscosity⁷².

Concerning electroactive nanofluids with faradaic activity, recent work has shown how to take advantage of a combination of the capacitive graphene species mentioned above with redox-active clusters or NPs. Thus, it has been shown how to harness the redox activity of polyoxometalates (POMs) in nanofluids made of hybrid rGO-POM nanoparticles dispersed in aqueous H₂SO₄⁶⁸. Furthermore, rGO has also been shown to enable the reversible and full cycling of conventional battery materials such as LiFePO₄ dispersed as nanoparticles in the fluid⁶⁷. Along this line of hybrid faradaic-capacitive nanofluids, a recent report by Lobato and col. has studied the effect of adding graphene derivatives to a conventional Vanadium RFB fluid⁷³.

On the other hand, faradaic nanofluids can also be formulated with just redox-active nanoparticles or clusters. Thus, Timofeeva and col. published a remarkable paper in which they functionalized iron oxide NPs (30-50 nm) with 3-(trihydroxysilyl)-1-propane sulfonic acid obtaining stable electrochemically active colloids (~125 nm) with up to 70 wt% solids in 5.5 M LiOH, with high specific capacity (176 mAh·g⁻¹) and low viscosity (<30 cP) with minimal shear dependence (±2 cP). Additionally, excellent colloidal stability (>2 weeks at rest) was demonstrated⁶⁵. In another pioneering previous work, Timofeeva and col. prepared stable nanofluids with TiO₂ loadings up to 50 wt % and low viscosity (4.33 cP) by grafting surfactant molecules. Thus, 3-(trihydroxysilyl)-1-propanesulfonic acid (SIT) forming (Ti-O)₃-Si-(CH₂)₃-SO₃⁻ bonds were used to modify the surface of titania nanoparticles with negatively charged sulfonate groups⁷⁴. However, this approach partially suppressed the electrochemical activity of the Ti (III)/Ti (IV) pair (22% less than in pristine TiO₂), which could be due to the blockage of active sites by the graft or due to a competing H₂ evolution reaction, which was observed at an early onset, most likely due to the acidic nature of the surface graft, resulting in the localized accumulation of [H⁺].

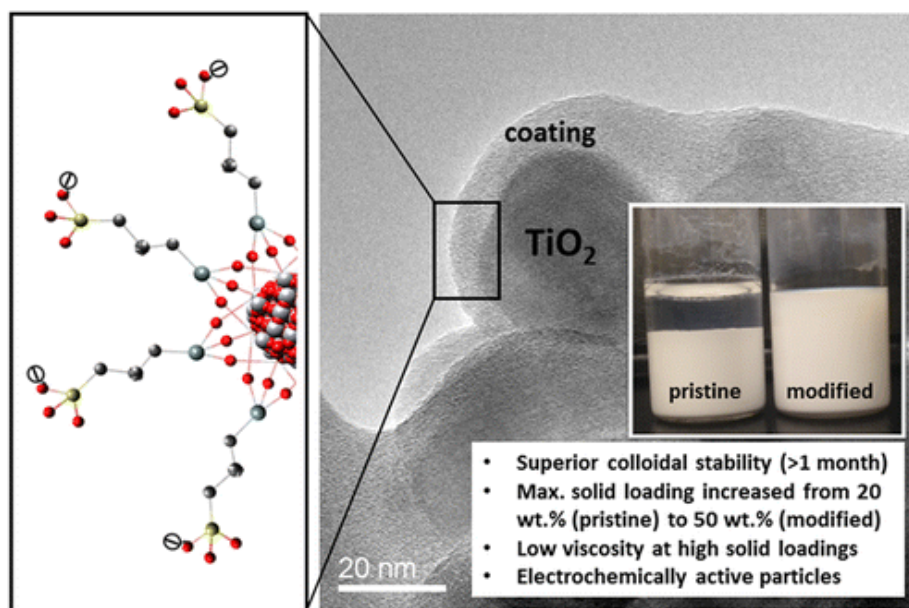


Fig. 5 TiO₂ nanoparticles functionalized to improve it stability in a dispersion⁷⁴. Reprinted (adapted) with permission from (Sen, S. et al. ACS Appl. Mater. Interfaces 7, 20538–20547 (2015)). Copyright (2015) American Chemical Society

A completely different, but very promising approach was published by Park et al. they developed a new multiple redox flow battery system of V-Mn-Ti/V-Mn-Ti ions which in the catholyte produce MnO₂ nanoparticles (70-380nm). It used the same composition of V, Mn and Ti ions for the negative and positive electrolytes but only two ions in each electrolyte participate in the redox reaction. In the negative electrolyte, both V and Ti were active ions, whereas V and Mn behaved as active ions in the positive electrolyte, sulfuric acid was used as electrolyte. The optimized electrolyte concentration was 1.1 M of V, 1.5 M of Mn and 1.5 M of Ti in 1.6 M of H₂SO₄, which exhibited a relatively high energy density of 39.4 Wh·L⁻¹ ⁷⁵. Also related to molecular species with no added capacitive component, Stimming and col. have recently reported another interesting work with POM fluids. They used a 0.2M solution of [SiW₁₂O₄₀]⁴⁻ for anolyte and 1M of [PV₁₄O₄₂]⁹⁻ for catholyte⁷⁶. The cell showed a specific capacity of 10.7 Ah·L⁻¹ with a capacity loss of 0.16% per cycle, with 155 cycles carried out, an open circuit voltage of 1.05 V and a power density of 100 mW·cm⁻².

Finally, it should be noted that in the emerging field of electroactive nanofluids there is a wide dispersion of results. The number of reported systems is limited, and yet, there are examples of both good and bad performance. We have emphasized throughout this paper the importance of cell optimization. We would like to mention a couple of examples which underscore the importance of proper cell design in the final performance. Recently Joseph et al. reported an electroactive nanofluid made of iron oxide synthesized from ferrous sulfate heptahydrate via a facile microwave assisted one-

step route in 1-butyl-4-methylpyridinium chloride. They achieved an efficiency of the charge–discharge process greater than 94% after 100 cycles. However the system only yielded a very low discharge capacity of $0.01 \text{ mAh}\cdot\text{g}^{-1}$ ⁷⁷. We believe that this modest result is not an intrinsic characteristic of the material, but most likely related to a simple cell design with very small effective area (both of the distant current collectors and membrane), leading to poor electronic and ionic transport.

Similarly, the work by Qi et al is a perfect example of the importance of a proper cell design and the electronic percolation issue of solid dispersions. They prepared a full electrochemical cell based on 0.5 vol% LiCoO_2 suspension as cathode and 1 vol% $\text{Li}_4\text{Ti}_5\text{O}_{12}$ suspension as anode in (EC) and (EMC) with EC:EMC = 3:7 by volume ratio with 1.2 M lithium hexafluorophosphate (LiPF_6). Both dispersions where in different reservoirs with magnetic stirring and an Al wire as current collector⁷⁸. Poor Coulombic efficiency was obtained (1.58%) which was justified as due to a low concentration of particles. But low concentration should lead to low charge, not to a large difference between charge and discharge. In our opinion this work is an example of the high difficulty to get a good electrical percolation in this kind of dispersions. In this particular work a non-optimized cell design was used, with Al wire used as current collector probably providing a small active area. Furthermore, the electroactive oxide particles used probably had a poor electrical conductivity, making it necessary to modify them with conductive coating or to add conducting additives to the nanofluid.

Conventional electrochemical cells are just fine for studying and exploiting the electrochemistry of simple molecular species. Yet, in the context of complex materials, electrodes and components, their integration into an efficient device will be key to success. In the same way that a great cell with a bad chemistry will be no good, we should also realize that a great battery chemistry could easily be ruined by a bad cell design. And in this context, nanofluids and nanopastes emerge as bold examples of the need of a joint development of materials chemistries and cell designs.

Perspective and prospective

When it comes to storing large amounts of charge in a battery you can apparently go for using large amounts of active material externalized out of the electrochemical cell or choose a highly concentrated active material. The first approach is the one taken in RFBs whereas the second is characteristic of Li-ion batteries, where ca. 80% of the electrode mass corresponds to active materials. But, why not both? What prevents the design of cells with extensive and at the same time intensive electrode materials?

RFBs have undergone a relatively modest evolution from their initial Cr and Fe ions into the, now mature, all-Vanadium technology, with hybrid systems such as Zn-Br₂ next-in-queue for development. But further breakthroughs of the type provided by ambipolar electrolytes or with highly concentrated solutions are still needed to overcome the poor energy density associated to low solubility limits. Isn't there any highly soluble electroactive species to play with in this respect? Or, even better, wouldn't it be great to count with a bulk electroactive liquid? a pure flowing substance able to reversibly exchange one or maybe two electrons per molecule? As a matter of fact, such a compound exists. We call it water. But again, reversible Fuel Cells are far from being problem-free. Poor kinetics derived from the need of a triple-phase –boundary (electrode-electrolyte-gas) ruins their great thermodynamics. Another unsolved problem is that low temperature Fuel Cells still need to get freed from their well-known platinum addiction.

Actually, none of the electrochemical energy storage technologies explored so far is problem-free. Instead, they all feature complementary advantages and drawbacks. Indeed, many different designs and systems somewhat in between conventional RFBs and conventional solid (Li-ion) batteries have been recently proposed. Among them, the flowing shuttle concept or SSFBs or nanofluids or fluid-confining 2-D materials. Yet, all of them present serious drawbacks. For example, 2D-confined liquids could suffer precisely from over-confinement of the liquid electrolyte in the bulk solid electrode structure, whereas the electronic conductivity of nanofluids could be hindered by the low concentration of solid nanoparticles dispersed in the liquid phase. On the bright side, electroactive fluids and pastes present the advantages of fast ion diffusion, high specific power and tolerance for volume expansion when compared with conventional solid electrodes, because in the latter only a small fraction of the active material is in direct contact with the electrolyte, thus ions have to diffuse from the electrode-electrolyte interphase through the solid electrode material to the active sites. That is a slow process that in addition can lead to defects on the crystalline structure of the active material due to the volume expansion associated to the intercalation of ions. On the other hand, solid

active materials present larger energy densities and larger electrical conductivity in comparison with electroactive fluids or pastes thanks to the direct and constant contact of the particles that conform the electrode.

It seems clear then that improving the electrolyte accessibility to the active electrode sites without loss of electrical conductivity would be key to improving power and cyclability without loss of capacity and energy density. But that is easier said than done, and unexpected difficulties frequently arise. For instance, the nanoconfinement of liquids in 2D solids was proposed to improve ionic transport; yet, it facilitates the electrodes exfoliation upon repeated cycling⁶⁴. But this apparent detrimental consequence could be turned into an advantage within the framework of novel designs of electrodes and devices.

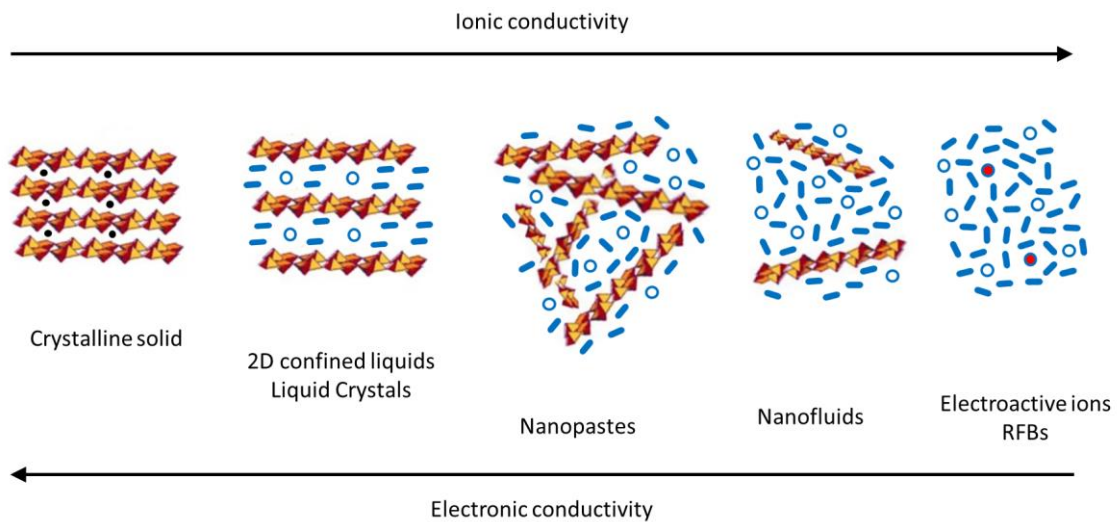


Fig 6. Schematic comparative diagram of several of the stages going from a compact solid electrode material to a dilute nanofluid and a RFB solution. Orange polyhedral denote a generic extended solid phase; blue segments, solvent molecules, open circles, generic ions and red circles electroactive ions.

In this context, the field could evolve towards the design of electroactive bulk nanopastes (Figure 6) which could work as effectively as thick solid electrodes and which, in the best case, would not need to be pumped. This type of alternative design could strongly contribute to lower the manufacturing cost of batteries, and this would be most important within the upcoming framework of battery gigafactories. After all, pastes are well known by the industry when it comes to primary conventional cells. Why not then for rechargeable ones?

The race is on for the development of the ultimate solution in order to make massive energy storage possible. And while none of the contenders seems to have reached optimal performance, both flowing and non-flowing designs could make it; in

which case the answer to the title's question would be to flow AND not to flow, with the various chemistries and cell designs possibly addressing different needs for different niche applications.

Flowing systems could keep breaking records for the energy density of their fluids while nanopaste electrodes could be designed as extra-thick or massive electrodes inaugurating a battery revolution resting more on the integration of materials and components in the devices than on the nature of the materials and components themselves. This means there are plenty of opportunities for interdisciplinary research involving materials chemistry, surface science, nanoscience, electrochemistry and engineering. There is plenty of room at the interface.

References

1. Davis, S. J. *et al.*. *Science* (80-.). **360**, eaas9793 (2018).
2. Thaller, L. H. (1974). Report/Patent Number NASA-TM-X-71540, E-7922
3. Bhushan, M., Kumar, S., Singh, A. K. & Shahi, V. K. *J. Memb. Sci.* **583**, 1–8 (2019).
4. Abdiani, M. *et al.* *J. Power Sources* **424**, 245–253 (2019).
5. Nguyen, T. D. *et al.* *ChemSusChem* **12**, 1076–1083 (2019).
6. Nourani, M. *et al.* *J. Electrochem. Soc.* **166**, A353–A363 (2019).
7. Yang, Y., Zhang, Y., Liu, T. & Huang, J. *J. Power Sources* **415**, 62–68 (2019).
8. Trovò, A. *et al.* *Appl. Energy* **240**, 893–906 (2019).
9. Lim, H., Yi, J. S. & Lee, D. *ChemSusChem* **12**, 1459–1468 (2019).
10. Lim, H., Yi, J. S. & Lee, D. *J. Power Sources* **422**, 65–72 (2019).
11. Soloveichik, G. L. *Chem. Rev.* **115**, 11533–11558 (2015).
12. Huang, Q. & Wang, Q. *Chempluschem* **80**, 312–322 (2015).
13. Park, M., Ryu, J., Wang, W. & Cho, J. *Nat. Rev. Mater.* **2**, (2016).
14. Pan, F. & Wang, Q. *Molecules* **20**, 20499–20517 (2015).

15. Sun, C., Zhang, H., Luo, X. & Chen, N. *Ionics*. **25**, 4219–4229 (2019).
16. Ponce de León, C., Frías-Ferrer, A., González-García, J., Szánto, D. A. & Walsh, F. C. *J. Power Sources* **160**, 716–732 (2006).
17. Li, B. *et al. Nat. Commun.* **6**, 1–8 (2015).
18. Zhu, Y. *et al. J. Power Sources* **417**, 83–89 (2019).
19. Winsberg, J., Hagemann, T., Janoschka, T., Hager, M. D. & Schubert, U. *S. Angew. Chemie - Int. Ed.* **56**, 686–711 (2017).
20. Leung, P. *et al. J. Power Sources* **360**, 243–283 (2017).
21. Lê, A. *et al. Acta* **301**, 472–477 (2019).
22. Chang, Z., Henkensmeier, D. & Chen, R. *J. Power Sources* **418**, 11–16 (2019).
23. Trudgeon, D. P. *et al. J. Power Sources* **412**, 44–54 (2019).
24. Robb, B. H., Farrell, J. M. & Marshak, M. P. *Joule* **0**, (2019).
25. Lee, W., Permatasari, A., Kwon, B. W. & Kwon, Y. *Chem. Eng. J.* **358**, 1438–1445 (2019).
26. Khataee, A., Dražević, E., Catalano, J. & Bontien, A. *J. Electrochem. Soc.* **165**, A3918–A3924 (2018).
27. Chen, R. *ChemElectroChem* **6**, 603–612 (2019).
28. Hagemann, T. *et al. J. Power Sources* **378**, 546–554 (2018).
29. Cao, J., Zhu, Z., Xu, J., Tao, M. & Chen, Z. *J. Mater. Chem. A* **5**, 7944–7951 (2017).
30. Ding, Y., Zhang, C., Zhang, L., Zhou, Y. & Yu, G. *Chem. Soc. Rev.* **47**, 69–103 (2018).
31. Huo, Y., Xing, X., Zhang, C., Wang, X. & Li, Y. *RSC Adv.* **9**, 13128–13132 (2019).
32. Wei, X. *et al. ACS Energy Lett.* **2**, 2187–2204 (2017).
33. Huang, J. *et al. Adv. Sustain. Syst.* **2**, 1700131 (2018).

34. Wei, X. *et al. Adv. Mater.* **26**, 7649–7653 (2014).
35. Rueda-García, D., Dubal, D. P., Hugenin, F. & Gómez-Romero, P. *J. Power Sources* **350**, 9–17 (2017).
36. Kwabi, D. G. *et al. Joule* **2**, 1894–1906 (2018).
37. Armstrong, C. G. & Toghiani, K. E. *Electrochem. commun.* **91**, 19–24 (2018).
38. Hu, B. *et al. Chem. Commun.* **54**, 6871–6874 (2018).
39. Li, X., Li, J., Huang, C. & Zhang, W. *Electrochim. Acta* **301**, 240–250 (2019).
40. Wang, X. *et al. Int. J. Electrochem. Sci.* **13**, 6676–6683 (2018).
41. Wang, X., Xing, X., Huo, Y., Zhao, Y. & Li, Y. *RSC Adv.* **8**, 24422–24427 (2018).
42. Qi, Z. & Koenig, G. M. Review Article: *Mater. Process. Meas. Phenom.* **35**, 040801 (2017).
43. Duduta, M. *et al. Adv. Energy Mater.* **1**, 511–516 (2011).
44. Presser, V. *et al. Adv. Energy Mater.* **2**, 895–902 (2012).
45. Shukla, G. & Franco, A. A. *J. Phys. Chem. C* **122**, 23867–23877 (2018).
46. Campos, J. W. *et al. Electrochim. Acta* **98**, 123–130 (2013).
47. Boota, M. *et al. J. Electrochem. Soc.* **161**, A1078–A1083 (2014).
48. Madec, L. *et al. Chempluschem* **80**, 396–401 (2015).
49. Lee, J., Weingarh, D., Grobelsek, I. & Presser, V. *Energy Technol.* **4**, 75–84 (2016).
50. Narayanan, A., Mugele, F. & Duits, M. H. G. *Langmuir* **33**, 1629–1638 (2017).
51. Tian, M. *et al. J. Power Sources* **364**, 182–190 (2017).
52. Akuzum, B. *et al. J. Electrochem. Soc.* **165**, A2519–A2527 (2018).

53. Hatzell, K. B., Boota, M. & Gogotsi, Y. *Chem. Soc. Rev.* **44**, 8664–8687 (2015).
54. Liu, H., Liao, L., Lu, Y. C. & Li, Q. *Adv. Energy Mater.* **7**, (2017).
55. Hamelet, S. *et al. J. Electrochem. Soc.* **159**, A1360–A1367 (2012).
56. Ruggeri, I., Arbizzani, C. & Soavi, F. *Carbon N. Y.* **130**, 749–757 (2018).
57. Chen, H., Lai, N. C. & Lu, Y. C. *Chem. Mater.* **29**, 7533–7542 (2017).
58. Li, S. *et al. Joule* **3**, 1637–1646 (2019).
59. Ventosa, E. *et al. Chem. Commun.* **51**, 7298–7301 (2015).
60. Huang, Q., Li, H., Grätzel, M. & Wang, Q. *Phys. Chem. Chem. Phys.* **15**, 1793–1797 (2013).
61. Li, G. *et al. J. Power Sources* **378**, 418–422 (2018).
62. Yu, J., Fan, L., Yan, R., Zhou, M. & Wang, Q. *ACS Energy Lett.* **3**, 2314–2320 (2018).
63. Yan, W. *et al. Nat. Commun.* **10**, 2513 (2019).
64. Augustyn, V. & Gogotsi, Y. *Joule* **1**, 443–452 (2017).
65. Sen, S., Chow, C. M., Moazzen, E., Segre, C. U. & Timofeeva, E. V. *J. Appl. Electrochem.* **47**, 593–605 (2017).
66. Fan, F. Y. *et al. Nano Lett.* **14**, 2210–2218 (2014).
67. Rueda-garcia, D. *et al. Electrochim. Acta* **281**, 594–600 (2018).
68. Dubal, D. P., Rueda-Garcia, D., Marchante, C., Benages, R. & Gomez-Romero, P. *Chem. Rec.* 1–10 (2018). doi:10.1002/tcr.201700116
69. Sadeghinezhad, E. *et al. Energy Convers. Manag.* **111**, 466–487 (2016).
70. Kong, C. Y., Qian, W. Z., Zheng, C. & Fei, W. *J. Mater. Chem. A* **3**, 15858–15862 (2015).
71. Vardhan, P. V., Idris, M. B., Manikandan, S., Rajan, K. S. & Devaraj, S. *J. Solid State Electrochem.* **22**, 1795–1800 (2018).

72. Dubal, D. P. & Gomez-Romero, P. *2D Mater.* **3**, 031004 (2016).
73. Lobato, J., Mena, E. & Millán, M. *ChemistrySelect* **2**, 8446–8450 (2017).
74. Sen, S. *et al.* *ACS Appl. Mater. Interfaces* **7**, 20538–20547 (2015).
75. Park, S., Lee, H. J., Lee, H. & Kim, H. *J. Electrochem. Soc.* **165**, A3215–A3220 (2018).
76. Friedl, J. *et al.* *Energy Environ. Sci.* **11**, 3010–3018 (2018).
77. Joseph, A. *et al.* *Chem. Commun.* **55**, 83–86 (2019).
78. Qi, Z., Liu, A. L. & Koenig, G. M. *Electrochim. Acta* **228**, 91–99 (2017).

CHAPTER 2

MOTIVATION AND

OBJECTIVES

2.1 Motivation

The search for new and improved electrical energy storage systems is nowadays one of the biggest challenges of science and technology in order to complete a sustainable energy model and reduce our dependence of fossil fuels.

Batteries are the obvious candidates for this task. But what batteries? Some cells like LIBs bet on condensed, concentrated, intensive materials, concentrated inside enclosed electrodes, whereas others, namely, RFB rest on extensive amounts of active materials stored outside the electrochemical cell.

On the other hand, from the point of view of storage mechanism, current technologies fall mainly in one of two categories: batteries and SCs, which have opposite advantages and drawbacks. Thus, a combination of both technologies could lead to new hybrid technology with the strength of both but without their drawbacks.

SCs are commonly based on carbon electrodes and take advantage of their large active area, electrical conductivity and low price. As a newcomer to the family of carbons, graphene is not the cheapest member of the clan, but, for the same reason, it holds the greatest promise and potential to display new properties and applications.

Thanks to its great electrical conductivity and surface area graphene could lead to a new generation of SCs and novel energy storage devices. Few-layer graphene materials, for instance, could break the distinction between intercalation and adsorption mechanisms for energy storage, and could thus work as an ideal hybrid material.

But from the electrochemical point of view and according to relevant literature, graphene has excelled as a purely capacitive material.

The present Thesis stems from two main motivations,

1.- Couldn't it be possible to design more energy-intensive materials within the framework of extensive devices? That is, how to design flowing materials and flow cells with higher energy density.

2.-How could we develop hybrid electroactive (flowing) systems combining or merging capacitive with faradaic activity.

In addition to graphene, in order to develop hybrid materials or systems with enhanced capacity, two active redox candidates have been chosen: quinones and polyoxometalates (POMs).

Desing of novel electroactive nanofluids for flow cell

Quinones have been deeply studied as electroactive specie for RFBs because of their good kinetics, tuneability and low cost. However, studies have been mainly limited to aqueous electrolytes. We wanted to explore the possible use of quinones in organic solvents in order to take advantage of two factors: i) their greater solubility and ii) their larger voltage range in these media, both factors converging to get solutions with a larger energy density. In addition, quinones could match graphene perfectly well in a hybrid configuration, since both are aromatic compounds and a strong π - π interaction, possibly leading to effective charge transfer between them, could be anticipated.

POMs are ideal model clusters which have been used previously in our group for the development of solid hybrid electrodes and, as such, were ideally suited for extending their study to flowing systems. In the same, well-known category, LiFePO_4 is one of the most extensively studied faradaic (battery) materials and it could provide again a perfect benchmark material. Furthermore, in addition to their similarities (well-known compounds studied in solid electrodes) these two materials provided radically different starting points, i.e. a molecular cluster 1nm in diameter vs. a larger nanoparticulate solid phase.

Finally, concerning the specific motivations for the choice of our materials, we decided to go for the synthesis of truly few-layers graphene by electrochemical exfoliation of graphite in order to be able to produce well-known, controlled materials beyond the uncertainty of commercial ones.

2.2 Objectives

The general objective of the Thesis was to explore new hybrid flowing systems which could eventually contribute to increase the energy density of flow cells.

The specific objectives targeted and pursued to contribute to that general objective were:

- 1.- Study the use of quinones in organic electrolytes to understand their electrochemical behavior.
- 2.-Explore the use of complex hybrid nanofluids for the harnessing of their electrochemical properties as energy storage devices.
- 3.- Demonstrate the possible use of hybrid systems, i.e. combining capacitive and faradaic electrodes, alike Li-ion capacitors but within the framework of flow Cells
- 4.- Study the effect of Graphene (specifically in this work rGO) on the electrochemical cycling of well-known redox and faradaic materials.
- 5.- Develop an improved method for the controlled synthesis of few-layers graphene by means of electrochemical exfoliation of graphite

Despite the apparently very diverse nature of these objectives and the associated research works presented in this Thesis, it is important to note how all of them fully address the questions raised in the above motivation text, delving at the intersection between questions 1 and 2 above.

CHAPTER 3
EXPERIMENTAL
METHODS

3.1 Electrochemical Techniques

3.1.1 General Fundamentals

Electrical energy storage can involve two clear different mechanisms: faradaic, associated to redox processes and capacitive, associated to electrostatic interactions between electrode and electrolyte. Capacitive mechanisms will always be present, but faradic only in the presence of active redox species and will take place simultaneously with the capacitive mechanism. Therefore, it is important to keep in mind that when the electrochemical performance or nature of any material or device is characterized, a capacitive signal will always be present and also that in the study of any redox system there will always be a capacitive contribution. Knowing this and understanding both mechanisms, it is possible to understand and design or adjust models that fit and explain the results obtained and also to use the proper characterization technique. Additionally, it is possible to know or identify the weak points of the material or device in order to improve its performance.

There are mainly two kinds of electrochemical techniques: potentiostatic and galvanostatic used to control the voltage or the current and measure the current or the voltage, respectively. It is important to point out that voltage and current cannot be controlled independently at the same time (when we control one of them we measure the response of the other) and that the resistance of the system, which is usually constant during the experiments, can change if there is a variation of the experimental setup, although it will not change due to the current or voltage applied. Finally, despite the fact that faradaic and capacitive processes deliver direct current (DC), it is possible to apply alternate current (AC) or voltage to them, which is the base of impedance techniques. In this case, the resistance of the system turns into impedance (Z), which has an imaginary component that depends on the frequency applied and the circuit element (resistance, capacitor or inductance) through which current flows. Therefore, in this technique the impedance of system is measured as a function of the frequency applied in a fixed current or voltage¹.

A capacitive energy storage mechanism is based on the charge accumulation on the surface of the electrode. With electrodes in contact with an electrolyte this is possible due to reorganization of the ions of the electrolyte near the electrode in order to balance the charge injected into the electrode with the charge stored at its surface. Polarization of two electrodes will force the movement of electrons (e^-) from one electrode to the other,

therefore one electrode will be charged negatively and the other positively but this is only possible if the charge neutrally is kept at any moment which is what the electrolyte ions do at the electrolyte-electrode interface.

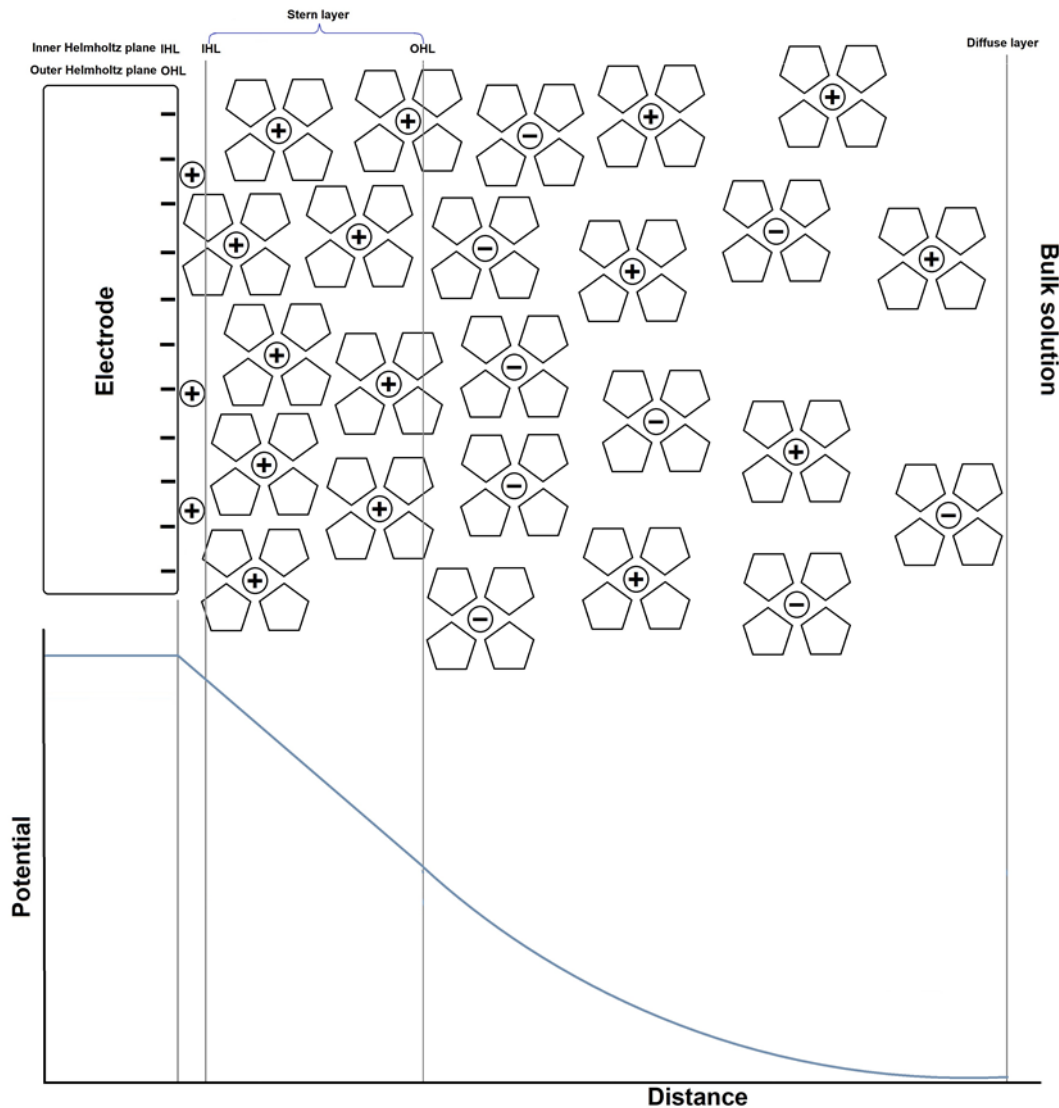


Fig.1 Scheme of EDL and potential profile.

Thus, polarized electrodes in contact with an electrolyte generate what is called an electrical double layer (EDL) when the ions are organized at the electrode's surface storing charge, which is a fast, reversible, efficient and purely electrostatic process (no chemical reactions). Ions can store charge at the electrode's surface in two different states. Firstly, there is adsorption on the electrode's surface, which means the ions are not solvated by the solvent: this first layer of ions is known as the inner Helmholtz layer (IHL) and is ca. 0.2nm thick. Secondly, there are the solvated ions that also contribute to charge storage at the electrode's surface. These define the outer Helmholtz layer (OHL) which has a thickness compressed between 1-10nm. Both layers, IHL and OHL define

the Stern layer (Figure 1), which is the distance at which ions store charge. Beyond the Stern layer, there is a region limited by the diffusive layer, where ions are moved mainly by diffusion (concentration gradient) to the electrode. Behind the diffusive layer is the bulk electrolyte^{2,3}.

A redox reaction involves two processes: one of them is an oxidation process that produces electrons that are consumed by the other process, which is reduction. As a result, there can't be an oxidation without a reduction or a reduction without an oxidation. However, special considerations have to be taken into account in the case of a redox reaction in an electrochemical cell. Common redox reactions take place when the reagents come into contact and the electrons are spontaneously transferred from one species to the other. However, this is not possible in an electrochemical cell: indeed, electrochemical cells are specifically designed in order to avoid the direct reaction. The purpose of an electrochemical cell is to allow the flow of electrons produced by a redox process through an external circuit or to induce a current in the external circuit in order to induce a redox process into the electrochemical cell. That is only possible if the redox processes take place at different and separated electrodes only connected by the external circuit. In order for oxidation and reduction processes to take place at the respective electrodes, ions that maintain electrical neutrality in the electrodes are needed and thus, the electrodes must be in contact with an electrolyte, therefore EDL will be generated, that's the reason why when a redox process takes place in an electrochemical cell, a capacitive process also inevitably takes place at the same time⁴.

Redox processes take place at the electrodes because there is a proper difference between the Fermi levels of the electrodes and the active species, as shown in Figure 2. For a reduction process, the Fermi level of the electrode must be higher than the species in order to be reduced and electrons will move from the electrode to active species where electrons are in a lower energy state. Of course, the active species must be able to receive an electron in order to be reduced. For oxidation it is the opposite case: the Fermi level of the electrode must be lower than the species to be oxidized so that the electrons can move from the active species to the electrode in order to be in a lower energy state. Electrons introduced into the electrode in which the oxidation takes place circulate through the external circuit to the other electrode where would be moved into the species that would be reduced^{5,6}.

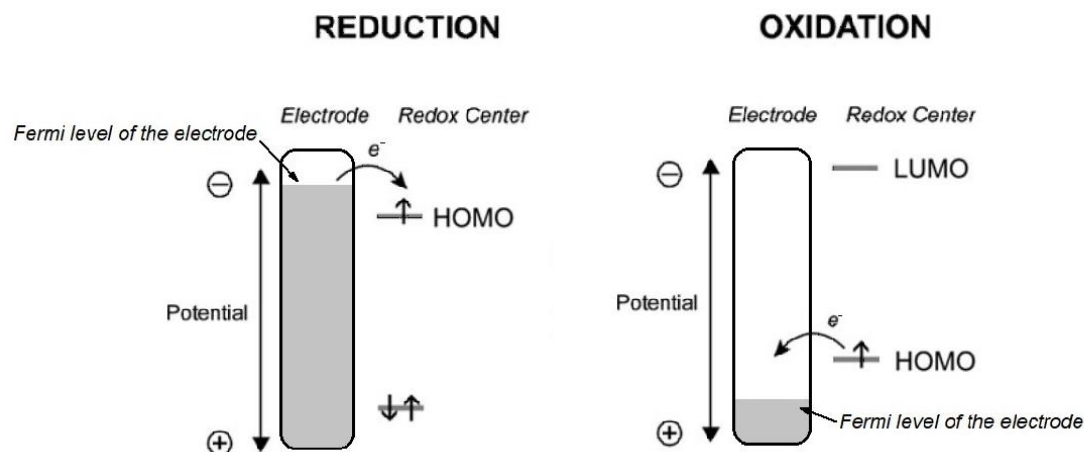


Fig.2 Scheme oxidation and reduction process by an electrode.

It is important to explain that initially, two equal electrodes both have the same Fermi however if there's an active species with a higher Fermi's level in one electrode and a different active species with a lower Fermi's level in the other electrode, a spontaneous electrochemical process will take place until one of the active species is consumed. When voltage is induced between two electrodes there is a modification of Fermi levels: an increase in the negative electrode and a reduction in the positive electrode. Thanks to this modification, it is possible to induce a non spontaneous electrochemical process by adjusting the Fermi levels of the electrodes, as shown in Figure 3.

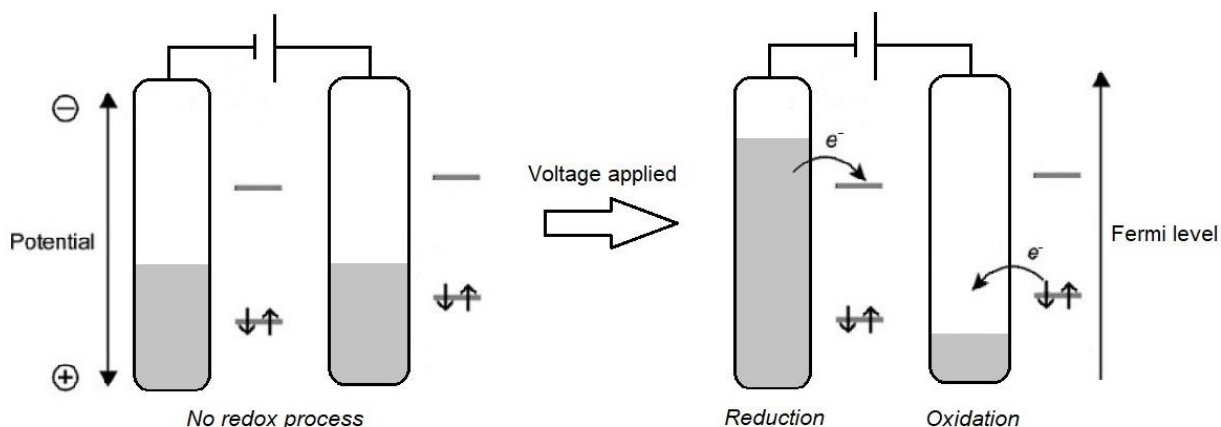


Fig.3 Scheme of induced redox process by a voltage application on the electrodes.

When the Fermi level of the electrode and the active species are equal, a dynamic equilibrium takes place between the reduction and oxidation processes and both processes take place at the same velocity and consequently, the net current measured is 0, as shown in Figure 4. An electrochemical species with very negative equilibrium potential has a very high Fermi level and is thus a very effective reducing agent as it can

be oxidized very easily. Similarly, an electrochemical species with a very positive equilibrium potential makes an effective oxidizing agent because it can be reduced very easily as its low fermi level can be easily filled.

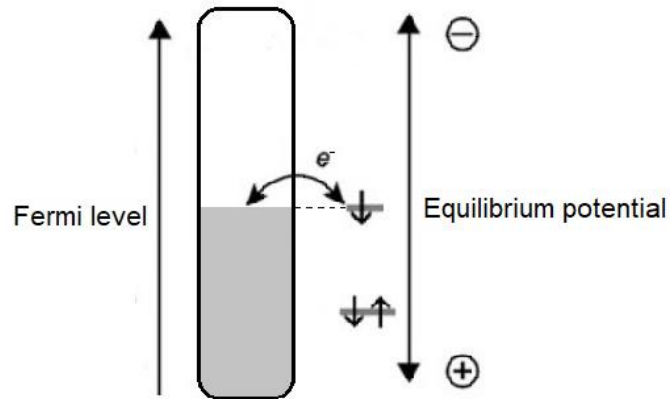


Fig.4 Scheme of an active redox species in equilibrium the electrode potential.

If voltage applied into the electrode is reduced with respect to the equilibrium voltage, the reduction process is favoured until a point in which would be the only electrochemical process, no oxidation would take place into the electrode. Logically, if the voltage is increased with respect to the equilibrium voltage, the same happens with the oxidation process. The currents produced can be described by the following Butler–Volmer equation(single step with n electrons transferred)^{1,4,5,7}:

$$j = j_o \left\{ \exp \left(\frac{n\alpha_a \eta F}{RT} \right) - \exp \left(- \frac{n\alpha_c \eta F}{RT} \right) \right\}$$

where:

- j = electrode current density ($A \cdot m^{-2}$)
- j_o = exchange current density ($A \cdot m^{-2}$) (current in the absence of net electrolysis and at zero overpotential)
- T = temperature (K)
- n = number of electrons involved into the redox process
- F = Farady constant ($C \cdot mol^{-1}$)
- R = universal gas constant ($J \cdot K^{-1} \cdot mol^{-1}$)
- η = overpotential ($E - E_{eq}$) (V)
- α_a = anodic charge transfer coefficient.
- α_c = cathodic charge transfer coefficient

Desing of novel electroactive nanofluids for flow cell

The charge transfer coefficients are the fraction of the interfacial potential at an electrode-electrolyte interface that helps in lowering the free energy barrier for the electrochemical reaction. Thus, they define the overpotential needed to activate the reaction and are related by: $\alpha_a = 1 - \alpha_c$. Therefore, the transfer coefficient is related to the kinetic constants of the electron transfer for the oxidation and reduction processes by the equations:

$$k_r = k_s \exp\left\{\frac{-\alpha n F \eta}{RT}\right\} \quad k_o = k_s \exp\left\{\frac{(1-\alpha)n F \eta}{RT}\right\}$$

where k_s is the standard heterogeneous rate constant. Large values for k_s indicate that following the application of an applied potential, the equilibrium between Ox and Red will be re-established quickly. Small values for k_s indicate slow kinetics and longer time requirement for equilibrium⁸.

Furthermore, it is important to take into account that the equilibrium potential of a redox process is not constant and depends on the temperature and activity of the reduced and oxidized species, as described by Nernst equation:

$$E_{eq} = E^o - \frac{RT}{nF} \cdot \ln \frac{a_{reduced}}{a_{oxidized}}$$

$$a_i = \gamma_i \cdot c_i \quad * \log \gamma_i = -A \cdot z^2 \frac{\sqrt{I}}{1+\sqrt{I}} \quad I = 0.5 \sum c_i z_i^2$$

*Valid for concentrations between 0.01 to 0.1M⁹

where:

- E_{eq} = real equilibrium potential (V)
- E^o = equilibrium potential at standard conditions (1atm, 25 °C)
- R = universal gas constant (J·K⁻¹·mol⁻¹)
- T = temperature (K)
- n = number of electrons involved into the redox process
- F = Faraday constant (C·mol⁻¹)
- a = activity of the reduced or oxidized species
- γ = activity coefficient
- c = concentration of the reduced or oxidized species (mol·L⁻¹)
- z = valence number of the ion
- A = 0.5102 (at 25°C)⁹
- I = ionic strength (mol·L⁻¹)

The equilibrium potential of the redox processes is tabulated against the hydrogen electrode and is measured by calculating the potential difference between the studied process and the process $2\text{H}^+ + 2\text{e}^- \rightarrow \text{H}_2$ in standard conditions, assigning 0 V to this electrode. By determining the equilibrium potential, it is possible to obtain a referenced scale of all the redox processes which allows us to easily determine which of the two species will be oxidized or reduced. Most importantly, the energy difference between them in V, therefore allows us to predict the voltage of a battery or know the voltage needed to be applied in order to induce a non-spontaneous redox process^{1,4,5,7}.

The application of a voltage difference between the two electrodes of an electrochemical cell could induce redox processes if the voltage applied is high enough. Consequently, all the species present in the cell must be carefully chosen depending on the voltage of cell: solvent, salt and current collector must be stable in the working potential. If not, they will provide spurious electrochemical reactions that will distort the results and degrade, damage and even break the electrochemical cell.

3.1.2 Cyclic Voltammetry

Cyclic Voltammetry (CV) is an effective technique for measuring current as a function of potential and is commonly used in electrochemical research studies. With this technique, the potential applied to the working electrode (WE) with respect to a reference electrode (RE) is cyclically swept at a constant sweep rate and the resulting current passing through the WE and an auxiliary counter electrode (CE) is measured and plotted as a function of potential. Conventionally, CV can be performed in two different configurations: using three or two electrodes, in which case it would be preferable to call it cyclic polarization (CP).

While the conventional three-electrode CV is the best way to characterize an electrode, the two-electrodes CP is the simplest configuration to characterize a device. It has some limitations in terms of accuracy for the study of the thermodynamics and kinetics of a redox process, but nevertheless is the most used configuration for the practical, preliminary characterization of electrochemical devices. In a two electrode configuration, the difference of potential between the two electrodes (while passing current through them) is measured, although the position of the working electrode potential in the tabulated potential list is unknown since the counter electrode is also connected as “reference electrode”, see Figure 5.

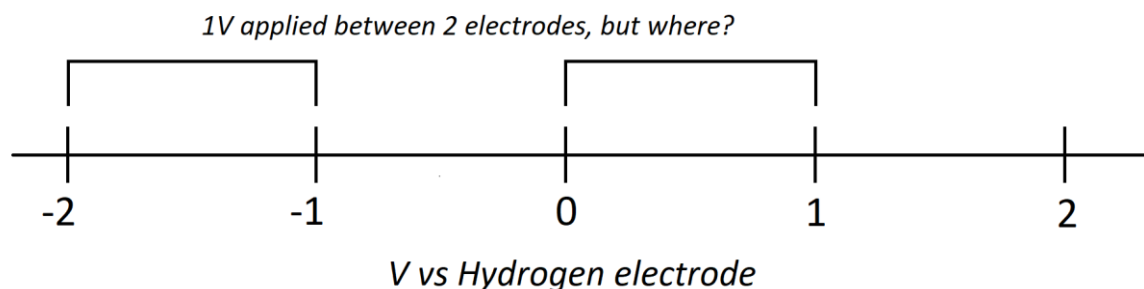


Fig.5 Example of the two electrode voltage issue.

Therefore, with a two electrode configuration it is not possible to apply the potential needed in order to induce or study a specific redox process that takes place at a specific potential. The reason for this is that there is no true reference that can indicate the position of the potential applied between the two electrodes against a standard redox process. Furthermore, as the potential of an electrode depends on the activity of the redox species, the voltage applied between two electrodes can shift against the specific redox process during the experiment.

A three electrode configuration solves this issue, because this configuration includes a specific reference electrode. Voltage is applied between RE and WE and current flows between WE and the current electrode (CE), see Figure 6, left. The RE is a special electrode based on a specific redox process with a fixed potential due to the fact that the reduced and oxidized species are solids (the activity of a solid is 1 if it is a pure compound at 1 atm) and thus can be proven by the Nerst equation that in this case the potential of the electrode will not change. In this type of configuration, it is important to keep the RE as near as possible to the WE in order to minimize the uncompensated solution resistance. Additionally, since the set up potential is just applied between the WE and the RE including this partial potential drop, the actual potential applied to WE is insufficient by the amount of potential drop^{10,11}, see Figure 6 right. Even with a modern potentiostat, such a potential drop cannot be controlled completely.

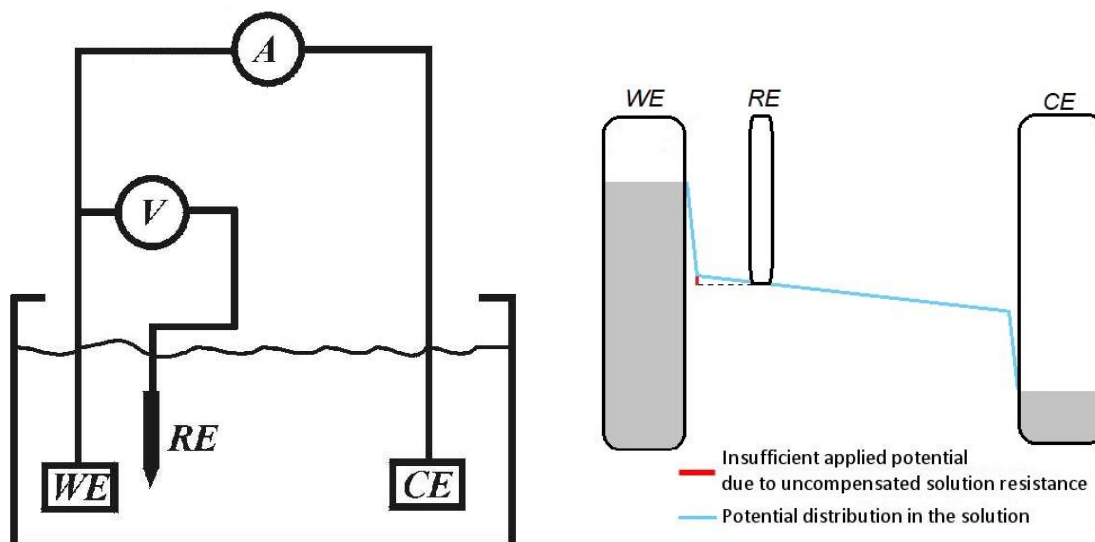


Fig.6 Left 3 electrodes configuration scheme, right uncompensated solution resistance diagram.

Moreover, should be pointed out that in a symmetrical two electrode cell, the potential differences applied to each electrode are equal to each other and are one-half of the values shown on the potential axe of the CV¹². In contrast, in a three electrode configuration the potential applied to WE with the RE, corresponds with potential plotted in the CV.

CV of a capacitive system will show a rectangular profile because the current is not dependent on the voltage since there is no electrochemical reaction. CV applied to a capacitive process can also show deviations from the ideal rectangular profile due to a high resistance, see Figure 7. There are two main reasons for this. First, there is a linear increase or decrease of the current with the voltage, a small slope in the current signal that makes it not constant vs the voltage. This is usually due to variables such as the internal resistance in the system, the electrical conductivity of the electrodes, the distances between them or the effective area in contact. Second, there is the ionic conductivity of the electrolyte: a smaller ionic conductivity results in a worse ionic response to the polarization and consequently the response of the current against the polarization of the electrodes is not fast enough to keep the rectangular profiles of the ideal CV^{2,3}.

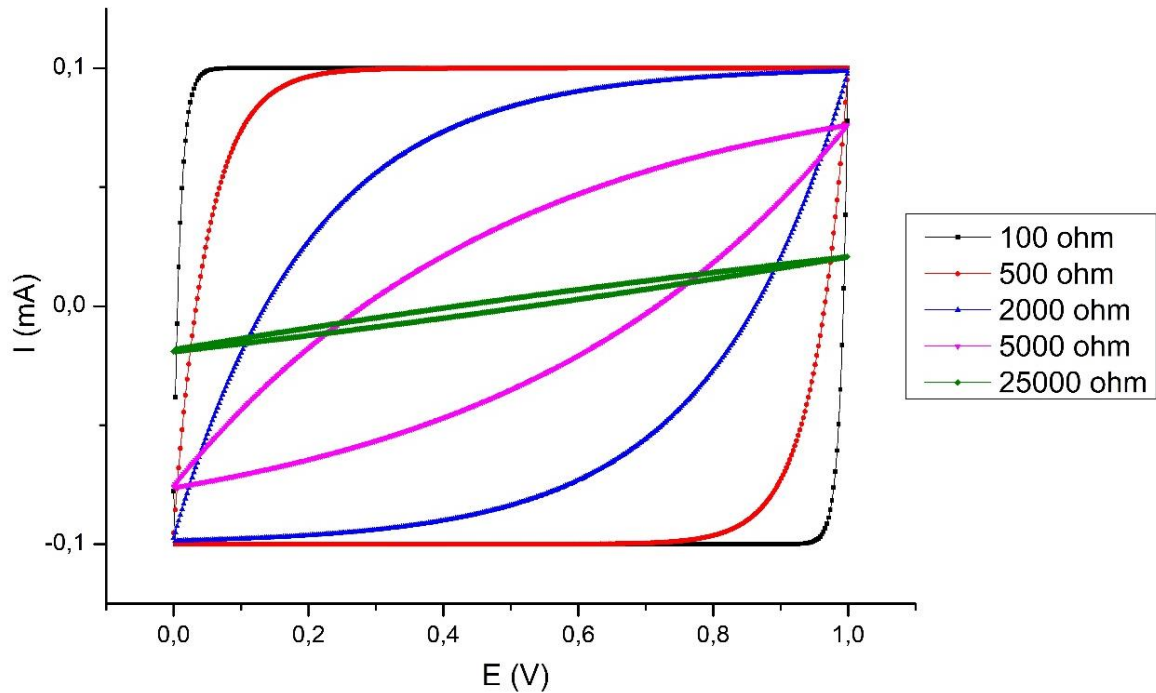


Fig.7 Simulation of a 1mF supercapacitor at 100mV/s at different resistances.

The capacitive current response follows a linear dependence on the scan rate:

$$i_c = v \cdot C,$$

where v is the scan rate ($V \cdot s^{-1}$) and C the capacitance ($A \cdot s \cdot V^{-1}$)¹³.

For a redox process, the CV profile is completely different since the reaction and its associated current only takes place once the potential of the redox process is exceeded: the current suddenly increases until it reaches a maximum and then decreases back to a small but non-zero value. The current decrease after the maximum occurs due to a depletion of the active species needed for the redox process (the redox active species in case of solutions or ions for an intercalation solid electrode) near the electrode and therefore, the velocity of the process is limited by the diffusion process of the active species to the electrode. The velocity of a redox process increases with the overpotential applied as Butler–Volmer equation proves. This equation shows that for an overpotential larger than 250mV a maximum velocity of electron transfer between the electrode and the active species is reached. But maximum velocity of electron transference is usually faster than the velocity at which the active species can reach the electrode to react. As a result, once all the active species near the electrode (inside the diffusive layer) is consumed, due to the redox process being faster than the process of diffusion of the active species from the bulk solution species and thus current measured decreases from the value that corresponds to the velocity of the redox process to a value delimited by diffusion of the active species^{1,4,5}.

Desing of novel electroactive nanofluids for flow cell

Generally, the current intensity of a redox process is notably larger than the current intensity from a capacitive process and consequently, in a CV of a redox process the capacitive current signal used to look like a base line.

For a reversible redox process, two peaks at potentials above and below E_{eq} would appear: an oxidation peak with positive overpotentials and positive currents and a reduction peak with negative overpotentials and negative currents. The separation between these peaks indicates the reversibility of the redox process, see Figure 8. It relates to how much more energy is necessary to charge the electrode compared with the energy returned. When electron transfer kinetics are fast, the redox reaction does not depend on the diffusion process, is electrochemically reversible and is in accordance with the Nernst equation. However, if the electron transfer kinetics are sufficiently slow, the concentration of reactants and products at the electrode surface (and thus the magnitude of the faradaic current) are not what is predicted by the Nernst equation and in this case, the system is electrochemically irreversible^{1,4,5,7}:

$$E_{anodic\ peak} - E_{cathodic\ peak} > 0.05916/n \text{ irreversible}$$

$$E_{anodic\ peak} - E_{cathodic\ peak} = 0.05916/n \text{ reversible}$$

Desing of novel electroactive nanofluids for flow cell

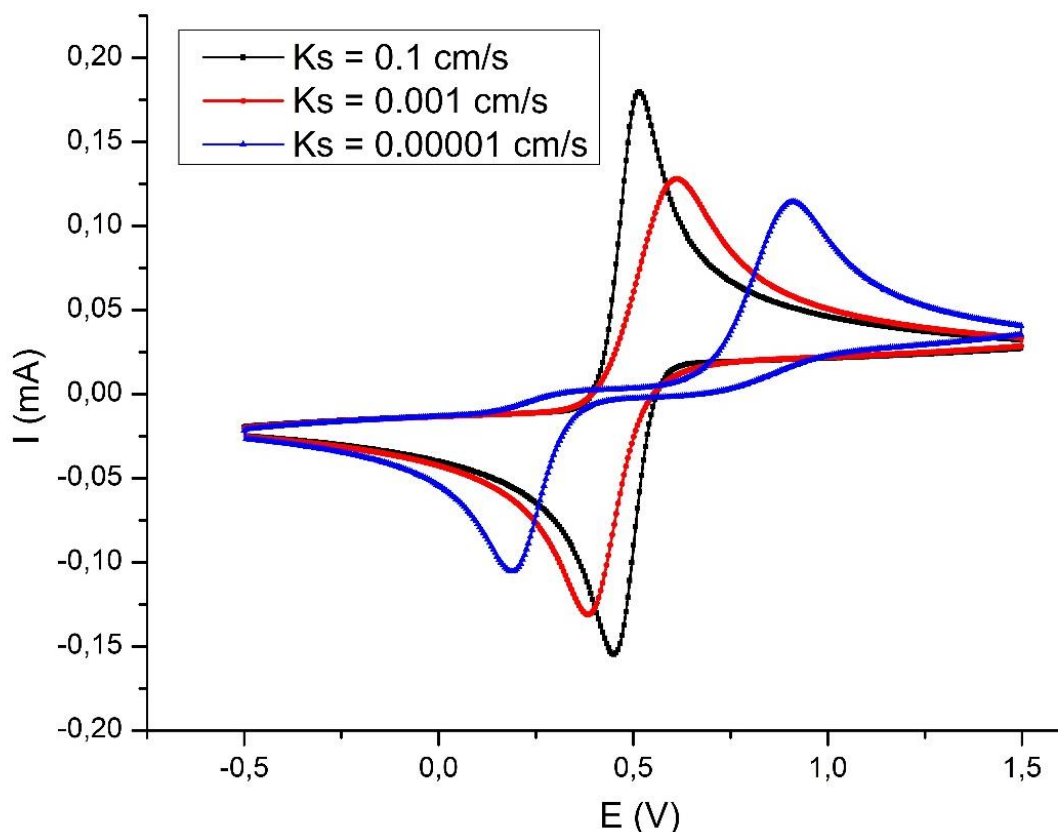


Fig.8 CV simulation of one e^- reversible redox process at different standard heterogeneous rate constant (K_s), only at 0.1cm/s the system is electrochemically reversible

The peak current in a CV, figure 9, is given by the Randles-Sevcik equation^{1,14,15}:

$$i_p = (2.69 \times 10^5) n^{3/2} A D^{1/2} \nu^{1/2} C$$

where:

- i_p = maximum current of the peak (A)
- n = number of electrons of the redox process
- A = area of the electrode (cm^2)
- D = diffusion constant of the reduced or oxidized species ($\text{cm}^2 \cdot \text{s}^{-1}$)
- ν = scan rate ($\text{V} \cdot \text{s}^{-1}$)
- C = concentration of the active species ($\text{mol} \cdot \text{L}^{-1}$)

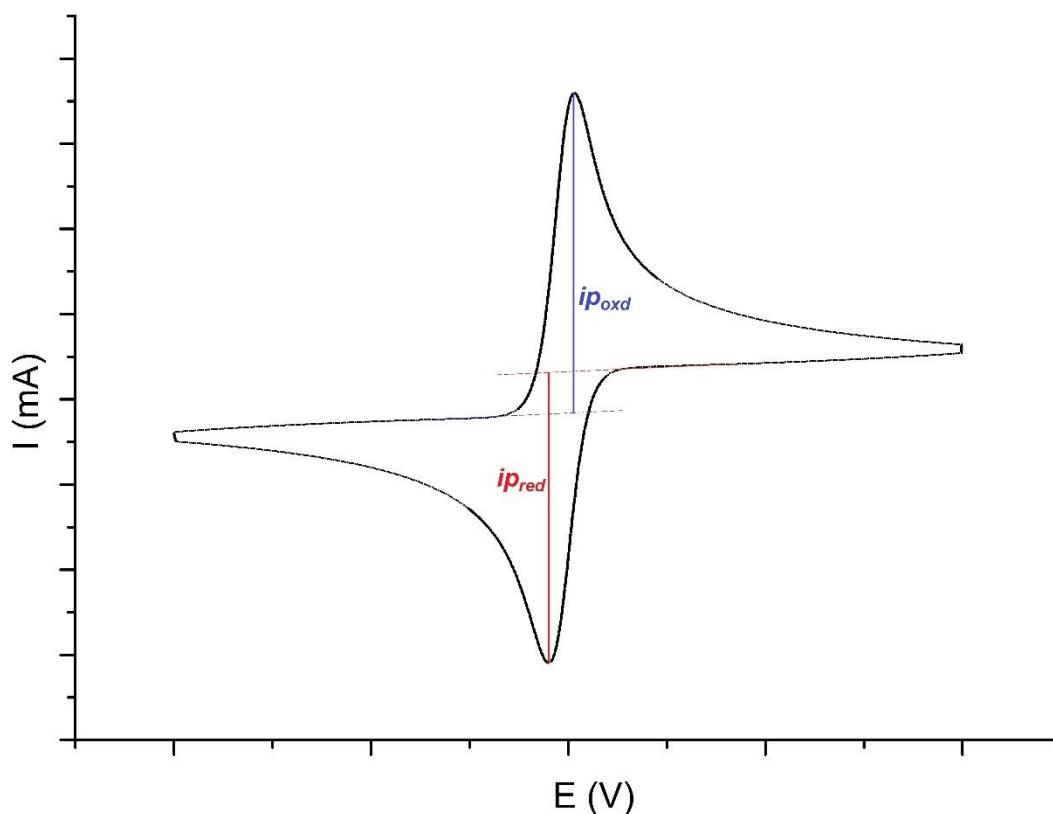


Fig.9 Intensity peaks of a reduction and oxidation process in a CV.

In a non-reversible process oxidation or reduction could be hindered or partially hindered and therefore not all oxidized products would be reduced in a cycle and vice versa. As a consequence, peaks could be unsymmetrical, or, in the limit, only one of the two peaks could be observed in the CV^{8,14,15}, see Figure 10.

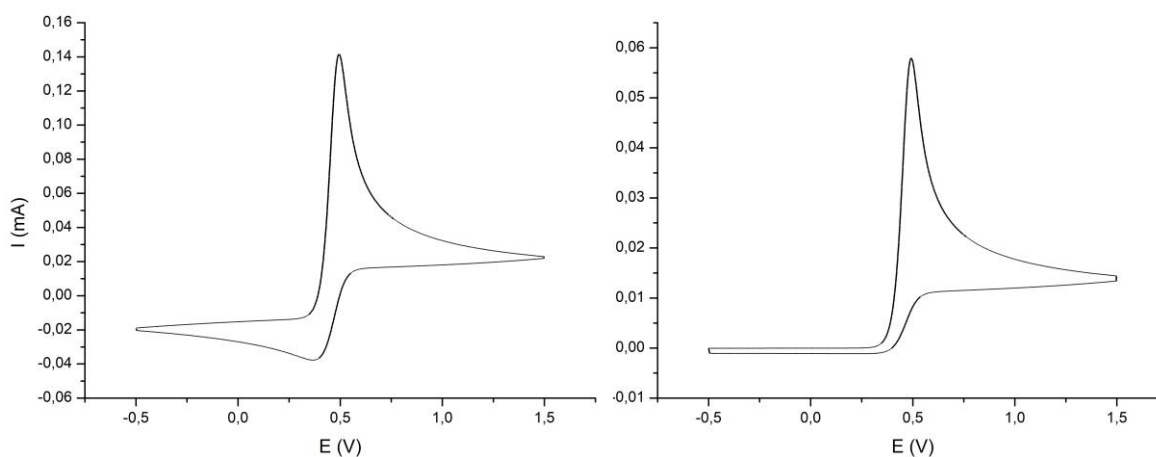


Fig.10 CV simulation of one e^- irreversible redox process, left partially reversible, right completely irreversible.

3.1.3 Chronoamperometry

Chronoamperometry is an electrochemical technique based on the application of a constant potential to the WE which measures current as a function of time. When a chosen potential is applied, the current slowly but continuously decreases as the active redox species is consumed. The current depends on the depletion velocity of the of the active species, which depends in turn, on the capacity of the active species to reach the WE electrode.

There are three possible mechanisms by which an active species can reach the WE: diffusion, convection and migration. Diffusion occurs when the concentration of the active species at the surface of the electrode is different from the concentration in bulk solution. The region of the solution in which diffusion occurs is the diffusion layer and in the absence of other mechanisms of mass transport, the width of the diffusion layer (δ) increases with time. Convection takes place when the solution is mechanically stirred, moving reactants toward the electrode and removing products from the electrode. Finally, migration occurs when a charged particle in solution is attracted to or repelled from an electrode that carries a surface charge by the coulombic force: thus, unlike diffusion and convection, migration only affects the movement of charged particles.

Real movement of species to and from the electrode's surface is a complex function of diffusion, convection and migration. In order to simplify the calculations, it is possible to limit the movement of active species by only diffusion. Migration can be eliminated by a large addition of a support electrolyte due to ions of similar charge are equally attracted to or repelled from the surface of the electrode. Each ion has an equal probability of undergoing migration and thus, a large excess of an inert electrolyte ensures that few reactants or products experience migration, so their contribution is negligible. Eliminating convection can be achieved simply by not stirring the solution. Thus, with only diffusion as the mechanism by which the active species move to the electrode, the current can be described by Fick's law^{1,13}:

$$i = \frac{nFAD(C_{bulk} - C_{x=0})}{\delta}$$

where:

- i = current (A)
- n = number of electrons of the redox process
- F = Faraday constant ($C \cdot mol^{-1}$)
- A = area of the electrode (dm^2)
- D = diffusion coefficient ($dm^2 \cdot s^{-1}$)
- δ = thickness of diffusion layer (dm)
- $C_{x=0}$ = concentration at the electrode's surface ($mol \cdot L^{-1}$)
- C_{bulk} = concentration into the bulk solution ($mol \cdot L^{-1}$)

3.1.4 Galvanostatic Cycling with Potential Limitation (GCPL)

This is a charge-discharge technique in which a constant current is applied and potential is recorded as a function of time. Potential is limited to the charge and discharge state of the studied device. Once the voltage at which the device is charged is reached, an inverse current is applied until it reaches the voltage at which the device is discharged. The process is repeated in order to produce several charge-discharge cycles to allow the study of both performance and stability.

In a battery GCPL experiment, potential remains almost constant during charge and discharge. Potential initially increases at charge or decreases at discharge until the potential needed to carry out the redox process is reached. Thereafter, potential stays constant until the redox process related to the charge or the discharge finish. In a supercapacitor, voltage linearly increases or decreases during charge and discharge, respectively^{7,13}.

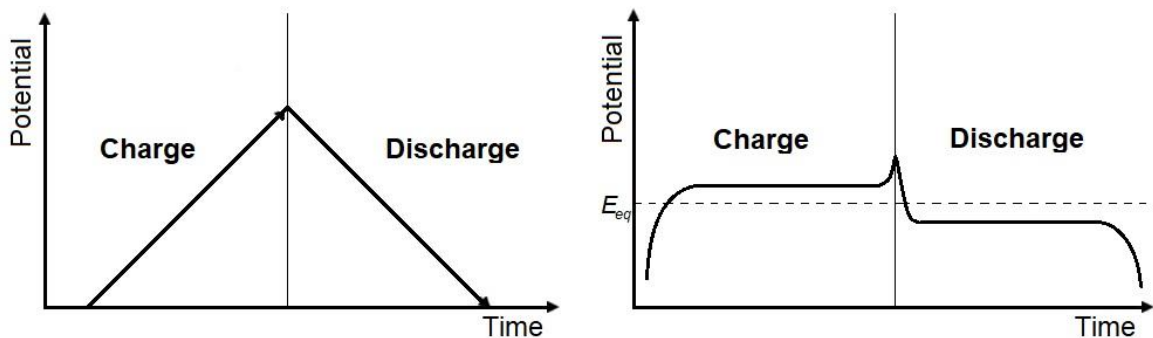


Fig.11 GCPL profiles for a, left a supercapacitor, right a battery.

3.1.5 Potentiostatic Electrochemical Impedance Spectroscopy (PEIS)

PEIS is an AC electrochemical technique in which voltage is fixed and impedance is measured as a function of applied frequency. For this technique, and in general for any electrochemical impedance technique, it is very important to look for a steady state between current and voltage. Thus, for PEIS, once potential is applied, measurements should be taken only when the current has stabilized. This is important because models and functions applied to the electrochemical impedance are built on this assumption and also on the assumption of flat electrodes¹.

AC can be described as two components, E and I phasor, been both components related by a phase angle (Φ) and depending on the circuit element through which current flows^{16,17}:

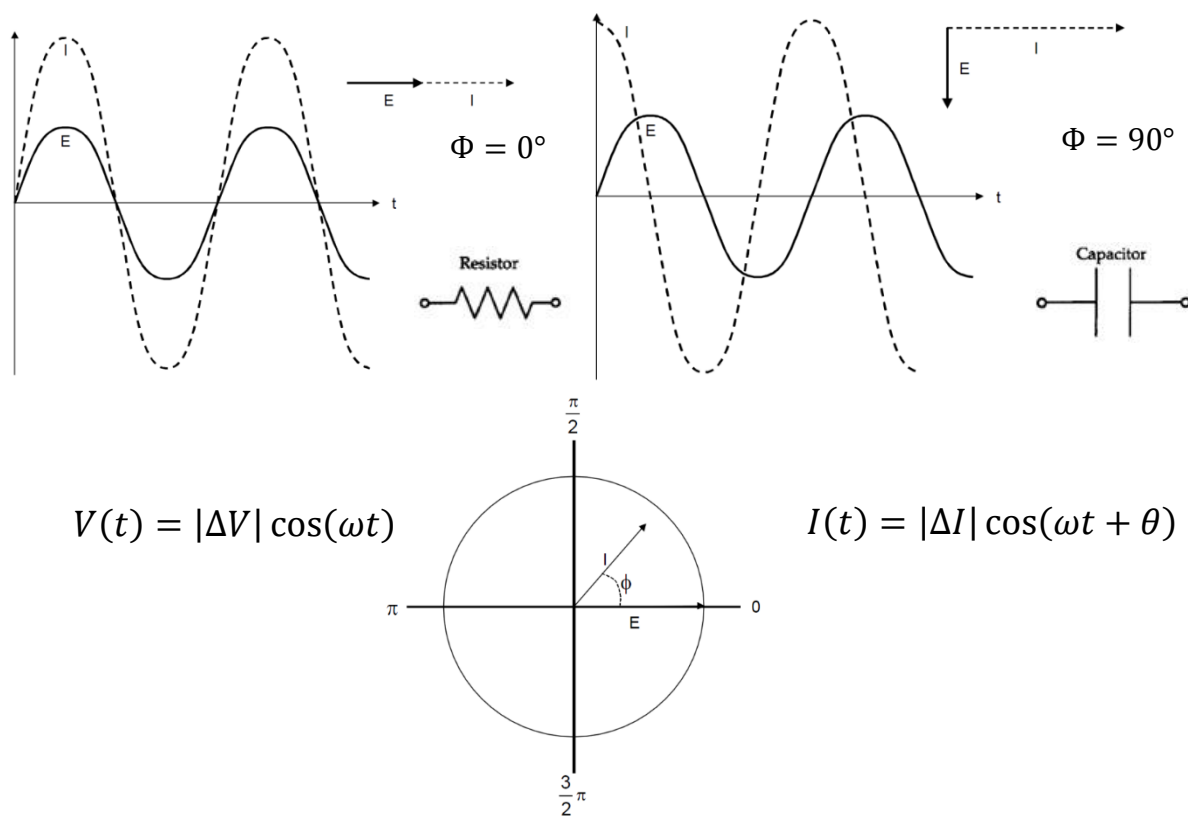


Fig.12 Representation of phase delay between V and I induced by the circuit element.

Desing of novel electroactive nanofluids for flow cell

Impedance techniques provide information about an electrical circuit and therefore, electrochemical system needs to be considered as an electrical circuit to fit the data obtained by the EIS. Three circuit elements can be used to develop the equivalent circuit: resistors, capacitors and inductors. The Z of an electrical circuit can be decomposed into real (Z_r) and imaginary (Z_j) components, the resistor is the only one of these three circuit elements that doesn't have an imaginary component^{1,16,17}, see Figure 13:

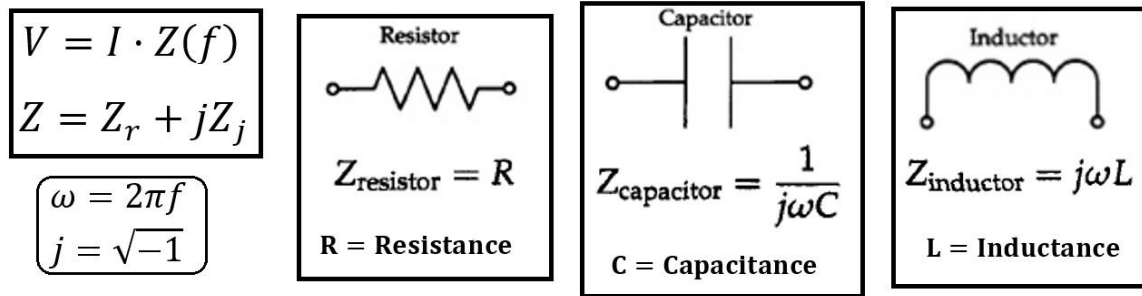


Fig.13 Impedance definition of an electrical circuit and impedance of the three basic circuit elements.

Impedance data is usually represented in a diagram called a Nyquist plot. In this diagram Z_j is the y axis Z_r is the x axis and each point of the diagram represents a specific frequency. Figure 14 shows an example with a simple circuit:

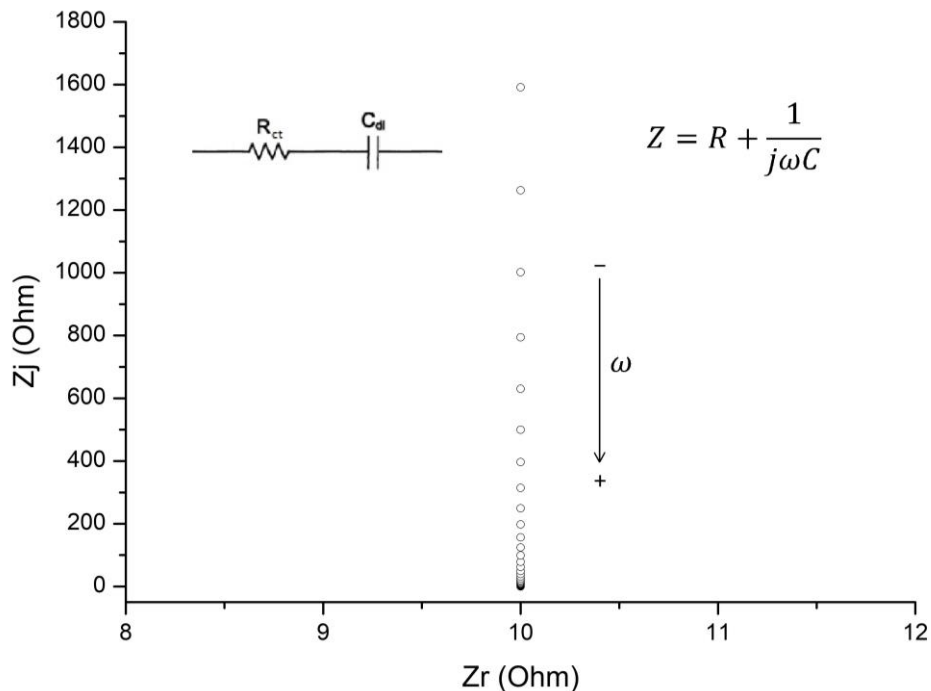


Fig.14. Nyquist plot of a simulation of 10 Ω resistance and 0.1mF capacitor in serial.

Desing of novel electroactive nanofluids for flow cell

For this simple circuit, it can be proved that:

$$Z = R + \frac{1}{j\omega C} = R_{ct} + \frac{\sigma}{\omega^{1/2}} + \frac{\sigma}{j\omega^{1/2}}$$

Part of the impedance that depends on the frequency, called Warburg impedance (Z_w)

Charge transference resistance, depends on i_o and doesn't depend on the frequency.

$$R_{ct} = \frac{RT}{nFi_o} = R - \frac{1}{\omega C}$$

$$\sigma = \frac{RT}{2^{1/2}n^2F^2AD^{1/2}} \left[\frac{1}{C_o} + \frac{1}{C_r} \right]$$

$O + ne^- \rightleftharpoons R$

where:

- R = resistance of the equivalent circuit
- C = capacitance of the equivalent circuit
- R_{ct} = charge transference resistance of a redox process
- σ = Warburg coefficient ($\Omega \cdot s^{-1/2}$)
- n = number of e^- associated with the redox process
- F = Faraday constant
- i_o = faradic current (current from redox process)
- A = Area of the electrode
- C_o = concentration of the oxidized species
- C_r = concentration of the reduced species

In this case, Z can be described as a sum of a real part and an imaginary part that depends on the frequency. This simple circuit provides a very good description of the behavior of redox process in an electrode; large currents in a redox process mean low charge transfer resistances (R_{ct}) and thus, current is limited by the diffusion process. Therefore, in this case R_{ct} is very small and then Z would depend on Z_w . Consequently, Z_w is used to define resistance associated with ionic diffusion. On the other hand, in the case of a redox process with a little current, the R_{ct} is large, thus limits the current of the redox process. In this case R_{ct} is very large and thus Z depends on it^{1,16,17}.

In a real electrode redox and capacitive processes take place simultaneously, considering the redox process just defined, an electrical circuit with it in parallel with a capacitor would describe properly both mechanisms simultaneously:

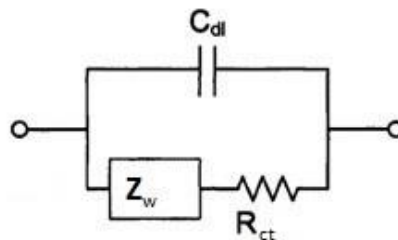


Fig.15 Equivalent circuit of a redox process and ELD

But it may be useful to first study a simpler system in order to properly understand the behavior of a real electrode in the Nyquist plot diagram, Figure 16 illustrates the behavior of a resistance and a capacitor in parallel:

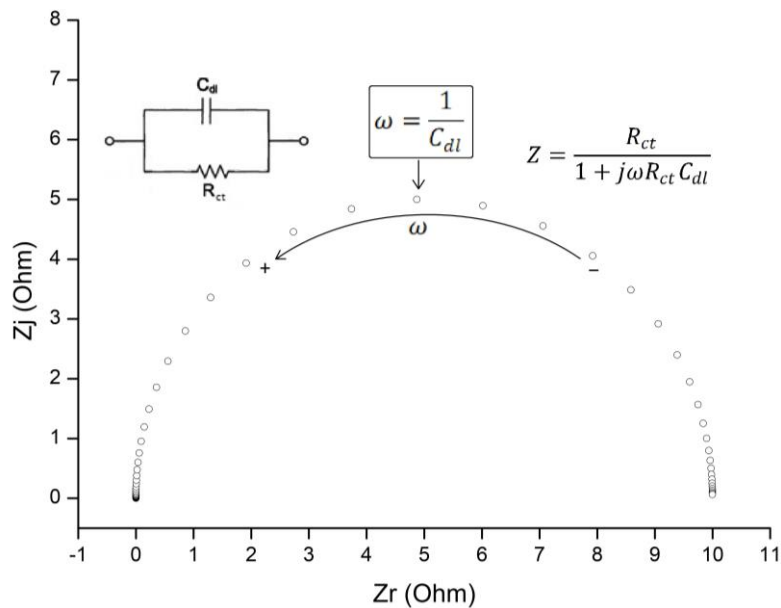


Fig.16 Nyquist plot of a simulation of a 10 Ω resistance and 0.1mF capacitor in parallel

A resistance and a capacitor in parallel generate a perfect semicircle in the Nyquist plot from which the capacitance of the capacitor (C_{dl}) can be easily obtained from the point with the larger Z_j , see Figure 16. This behavior is due to a frequency where the Z_j and Z_r have the same contribution and consequently, the capacitive current (i_c) and the faradaic current (i_r) are also equal at this frequency^{1,16,17}:

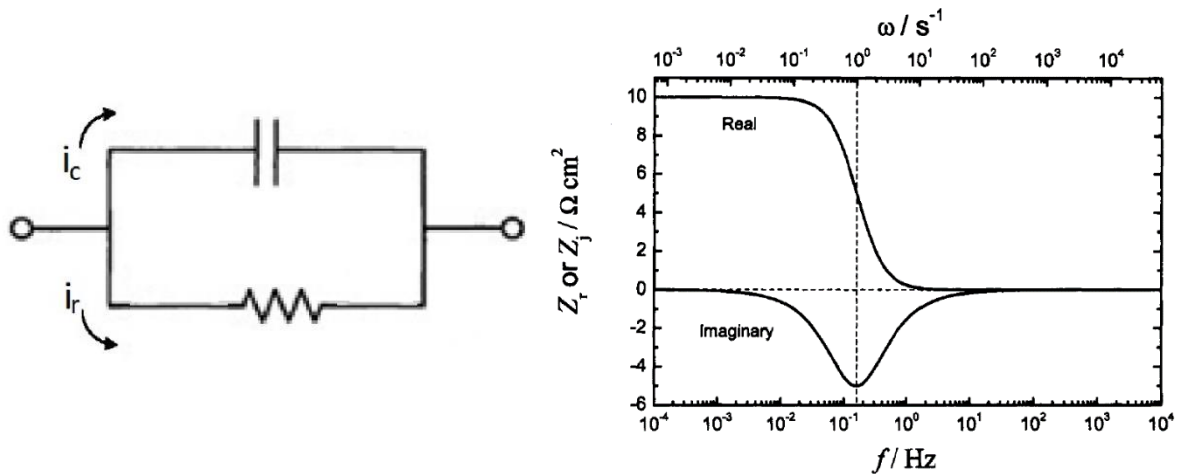


Fig.17 Distribution of the current though a resistance and a capacitor in serial as a function of the frequency.

Desing of novel electroactive nanofluids for flow cell

In order to properly define an electrochemical process, the resistance of the solution (R_s) must be added to the equivalent circuit and placed in serial with the R_{ct} and the C_{dl} . The R_s produces a displacement of the semicircle and starts at the value of the R_s .

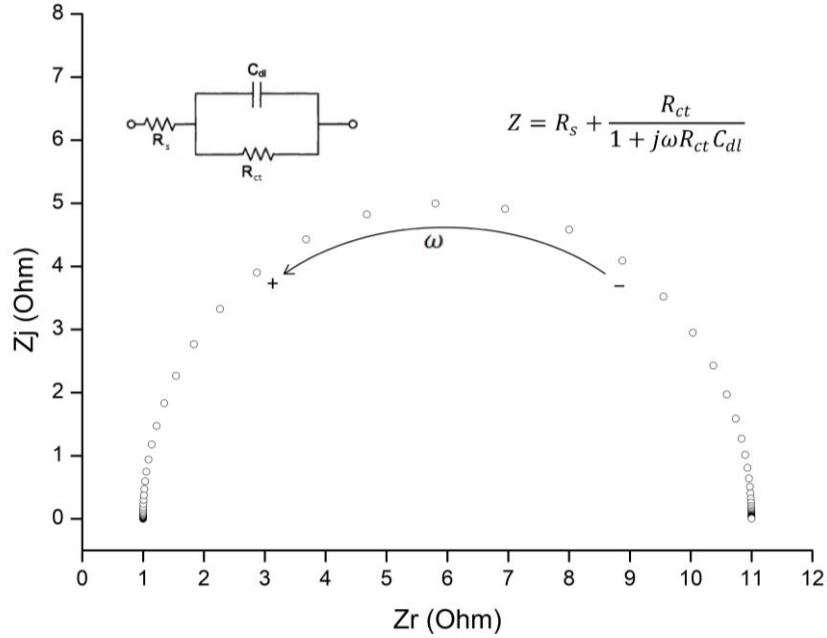


Fig. 18 Nyquist plot of a simulation of a 10 Ω resistance and 0.1mF capacitor in parallel with a resistance of 1Ω in serial of both

Consequently, the equivalent circuit of a redox process is composed of a R_s in serial with C_{dl} in parallel with R_{ct} and Z_w , which is termed a Randles circuit^{1,16,17}:

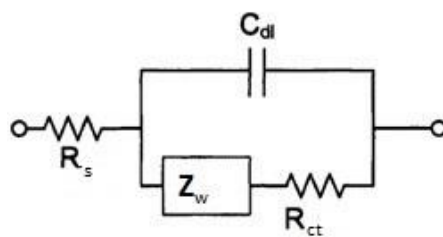


Fig. 19 Randles circuit, equivalent circuit of a simple redox process

Desing of novel electroactive nanofluids for flow cell

The Nyquist plot of a Randles circuit shows linear behavior at low frequencies and the explained semicircle behavior at high frequencies with Z being a complex function^{1,16,17}:

$$Z_r = R_s + \frac{R_{ct} + \sigma\omega^{-1/2}}{(C_{dl}\sigma\omega^{1/2} + 1)^2 + \omega^2 C_{dl}^2 (R_{ct} + \sigma\omega^{-1/2})^2}$$

$$Z_j = \frac{\omega C_{dl} (R_{ct} + \sigma\omega^{-1/2})^2 + \sigma\omega^{-1/2} (\omega^{1/2} C_{dl} \sigma + 1)}{(C_{dl}\sigma\omega^{1/2} + 1)^2 + \omega^2 C_{dl}^2 (R_{ct} + \sigma\omega^{-1/2})^2}$$

For simplicity, Z of the Randles circuit can be expressed depending on the range of frequencies^{1,16,17}:

· At high f ($\omega \rightarrow \infty$):

$$Z_r = R_s + \frac{R_{ct}}{1 + \omega^2 + C_{dl}^2 + R_{ct}^2}$$

$$Z_j = \frac{C_{dl} R_{ct}^2 \omega}{1 + \omega^2 + C_{dl}^2 + R_{ct}^2}$$

Elimination of ω from this pair of equations yields:

$$\left(\frac{R_{ct}}{2}\right)^2 = \left(Z_r - R_s - \frac{R_{ct}}{2}\right)^2 + Z_j$$

Circumference with center $Z_r = R_s + \frac{R_{ct}}{2}$

And radio = $\frac{R_{ct}}{2}$

· At low frequencies ($\omega \rightarrow 0$):

$$Z_r = R_s + R_{ct} + \sigma\omega^{-\frac{1}{2}}$$

$$Z_j = \sigma\omega^{-\frac{1}{2}} + 2\sigma^2 C_{dl}$$

Elimination of ω from this pair of equations yields:

$$Z_j = Z_r - R_s - R_{ct} + 2\sigma^2 C_{dl}$$

Straight with slope 1, cut Z_r in $R_s + R_{ct} - 2\sigma^2 C_{dl}$

Desing of novel electroactive nanofluids for flow cell

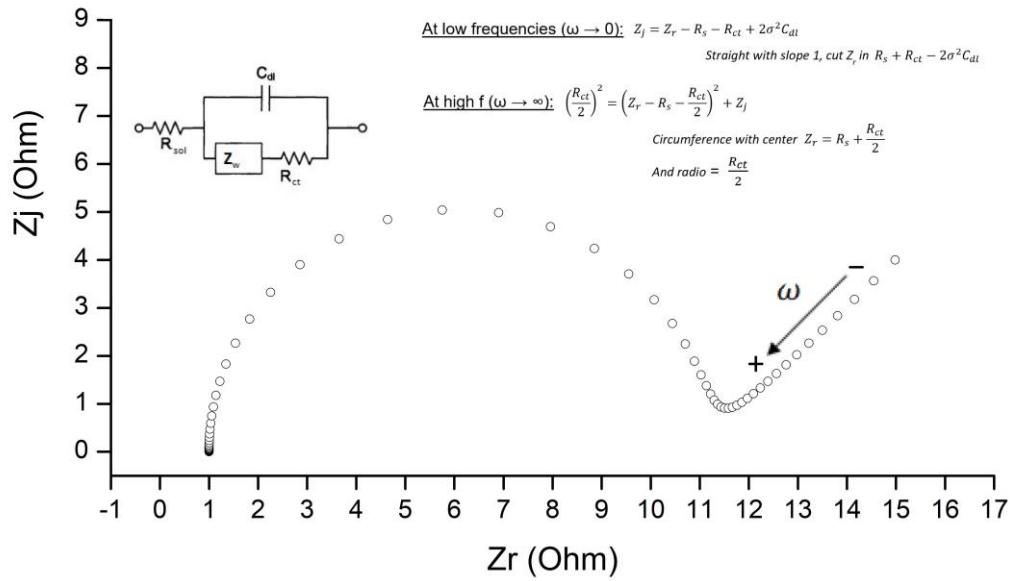


Fig.20 Simulation of a Randles circuit with 1Ω of R_s , 10Ω of R_{ct} , 0.1mF of C_{dl} and $10\Omega \cdot s^{-1/2}$ of σ .

This different behavior at different frequencies is because in an impedance technique, the processes observed depend on the frequency. High frequencies allow observation of fast processes like the DLC generation or charge transference between an active redox species and the electrode, whereas low frequencies allow observation of slow processes like diffusion to the electrode^{1,16,17}.

As a result, a Randles circuit provides a good description of a simple redox electrochemical process, Figure 21. However, for more complex systems more complex equivalent circuits are needed. For instance, inductors are used in the equivalent circuit to describe the generation of coatings on the electrode surface. In this case, the profile in the Nyquist plot is extended to negative values in the Z_j as a partial semicircle^{16,17}, Figure 22.

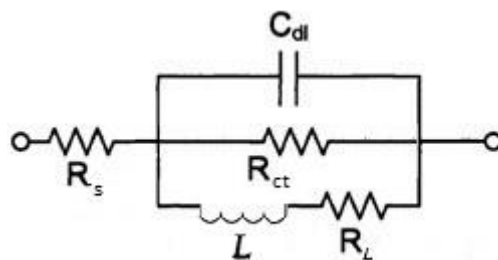


Fig.21 Example of an equivalent circuit for an electrode in which a coating process takes place.

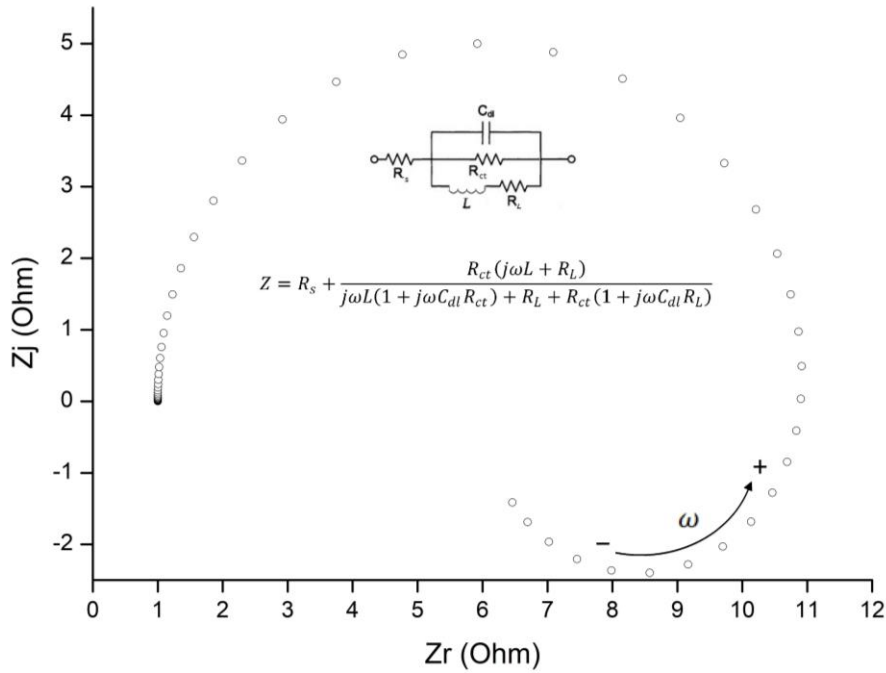


Fig.22 Simulation of the equivalent circuit of the fig 21. R_s 1Ω, C_{dl} 0.1mF, R_{ct} 10Ω, L 1 henry (H) and R_L 10Ω.

Equivalent circuit design is crucial for PEIS or any impedance technique, is basic to design or find a circuit that fits the experimental data but that also have physical sense with what is taking place in the electrode (there are a lot of equivalent circuits that can fit the same data, but only a few have physical meaning). Therefore, in every case, the equivalent circuit should be carefully chosen, especially in complex systems^{1,16,17}.

3.2 Spectroscopic Techniques

3.2.1 Energy Dispersive X-ray Spectroscopy (EDX)

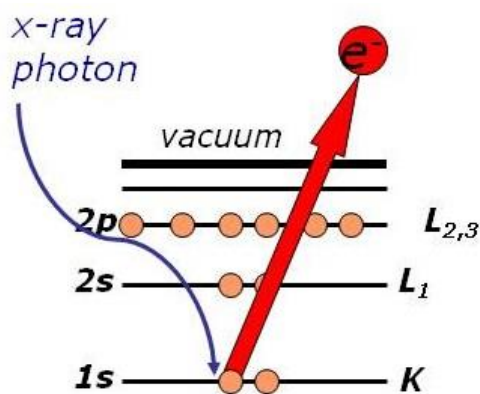
This technique records the energy and intensity of the x-rays generated by the impact of an electron beam on the surface of a sample for a qualitative and quantitative elemental analysis.

An electron beam ejects core electrons from the atom of the sample leaving the atom in an ionized state and an electron vacancy in the core, which is immediately filled by an upper-shell electron and consequently an x-ray is emitted. The energy between electronic levels is characteristic of each element and therefore, by measuring the energy of the x-rays produced by the sample, it is possible to obtain the elemental composition of the sample. Quantitative analysis can be performed by comparison of the relative peak intensity of the peaks of different elements. Nevertheless, for an accurate quantification, a standard compound with known stoichiometry is required¹⁸.

3.2.2 X-ray Photoelectron Spectroscopy (XPS)

In this technique, electrons are ejected from the sample surface by excitation caused by x-ray radiation.

For elemental analysis, chemical state and a quantitative analysis of the sample can be performed by measuring kinetic energy and counting the electrons emitted by the sample because each element and chemical state has a unique electron energy¹⁹.



XPS analysis in the present study was carried out using a Perkin-Elmer system, equipped with cylindrical analyzer and a highly monochromatic Al K α (1486.6 eV) X-ray source.

3.2.3 Raman Spectroscopy

In this spectroscopic technique, the sample is excited with visible light and the inelastic photons emitted by the sample are measured. When a sample is excited, electrons can move to a virtual upper state, which they leave immediately by the emission of a photon. If the electron returns to the same state, then an elastic interaction takes place and the emitted photons have the same energy as the absorbed, which is the most probable process and is called Rayleigh dispersion. But if the electron returns to a different state, then inelastic interaction take place. This is very improbable in comparison with Rayleigh scattering, which is $10^6 - 10^7$ larger than inelastic interaction. If an electron returns to a higher energy state than the initial state, the photons emitted have lower energy than the absorbed photons, which is called Raman Stokes scattering. If the electron returns to a lower energy state, compared with its initial state, the emitted photons have a larger energy than the absorbed photons and this is referred to as anti-Stokes Raman scattering. Anti-Stoke signals are less intense than Stoke signals because they are less probable²⁰.

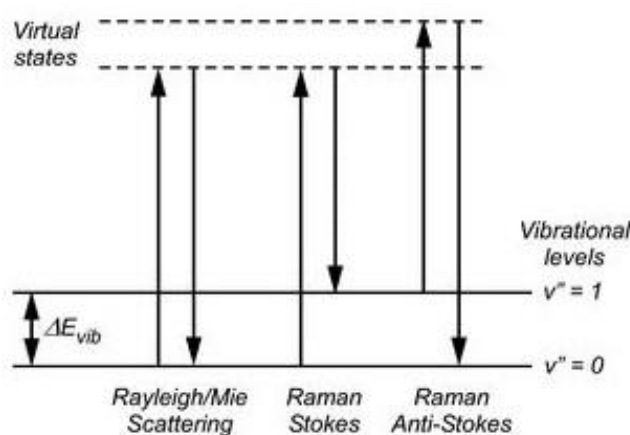


Fig.24 Scheme of different electronic transitions

Raman scattering occurs as a result of a molecular vibration or a phonon that generates a change in polarizability: in contrast, infrared scattering is produced by vibration modes that cause a permanent dipole²⁰.

Raman spectroscopy has been used to characterize graphene, it usually presents 3 bands and their exact position depends on the laser used to excite the sample²¹:

- D band $\approx 1350 \text{ cm}^{-1}$
- G band $\approx 1580 \text{ cm}^{-1}$
- 2D band $\approx 2700 \text{ cm}^{-1}$

Pure one-layer graphene will only show the G and 2D bands, being the 2D the most intense. As the number of layers increases, the intensity of the 2D decreases: at 5-10 layers, the intensity of the G and 2D are about equal. Above 10 layers, the G band is the most intense peak. The D band is produced due to graphene defects, so oxidized materials like rGO or GO use to present a strong D band, but in bulk graphene its contribution is small and related to its edges.²²

3.2.4 Ultraviolet-Visible Absorption Spectroscopy

This technique works on the principle of photon absorption that promotes bonding and non-bonding electrons to excited states by a light source of 200-800nm. The energy needed for this electronic transition is unique for each molecule and this technique therefore allows identification of molecules and also the study of electronic properties like the band gap. The main electronic transitions are:

- $\sigma \rightarrow \sigma^*$: promotion of an electron in a σ bonding orbital to an anti-bonding σ^* orbital, are very energetic transitions due to affects to the most stable valence electrons, $\lambda < 150\text{nm}$.
- $n \rightarrow \sigma^*$: promotion of non-bonding electrons (pair of free electrons) to an anti-bonding σ^* orbital, are also very energetic because the σ^* is a very energetic orbital, $\lambda < 150\text{-}200\text{nm}$.
- $n \rightarrow \pi^*$ and $\pi \rightarrow \pi^*$: These are the most common and studied transitions, from non-bonding and π orbitals to anti-bonding π^* orbitals and take place at λ 200-700 nm. These transitions correspond to the promotion of electrons from double, triple bonds and ligands.

Spectra is recorded as absorbance (A_λ) vs wavelength (λ), absorbance is a measure of the attenuation of light after passing through a material defined as:

$$A_\lambda = -\log_{10} \left(\frac{I}{I_0} \right)$$

where I_0 is the intensity of the light before passing through the sample and I is the intensity after passing through the sample. Bands tend to be wide in the A_λ vs λ diagram because electrons from excited vibrational and rotational states are also promoted too²³.

But it can also be recorded as transmittance (T_λ) vs λ , where T_λ is:

$$A_\lambda = -\log_{10} T_\lambda$$

By the Beer–Lambert law, it is possible to determine the concentration of a solution by using the equation:

$$A_\lambda = lc\varepsilon$$

where l is the length of the light path (cm), c is the analyte concentration ($\text{mol}\cdot\text{L}^{-1}$) and ε is the molar absorptivity coefficient ($\text{L}\cdot\text{mol}^{-1}\cdot\text{cm}^{-1}$)

3.3 Transmission Electron Microscopy (TEM)

To characterize the morphology of NPs or nanostructures, the size or number of graphene layers and also do chemical and crystallographic analysis in situ TEM is needed. In this technique, a thin specimen is crossed by an electron beam (electrons are unable to cross trough a thick sample) and higher atomic elements will appear darker in TEM images because of their higher electron density.

Electrons are used to generate the image because in order to see in the atomic scale, a wavelength with the same scale is needed and electrons have a De Broglie wavelength (size of particles that will interact with the radiation) of less than 1 Å. The resolution of any optical system is defined by the Abbe's equation²⁴:

$$d = \frac{\lambda}{2n \sin \theta}$$

where:

- d = minimum resolvable distance
- λ = wavelength
- n = refractive index
- θ = aperture angle of the objective lens

X-ray radiation also fits the wavelength requirements, but electrons interact stronger with atoms, so electrons are the best option to obtain images at atomic scale.

TEM works by monoenergetic electrons, magnetic lenses and a fluorescence screen or a CCD sensor everything under ultravacuum conditions and can work in two modes: image and diffraction depending on the aperture^{24,25}, Figure 25.

Diffraction patterns are used to identify the crystallographic structures of a sample thanks to constructive and destructive interferences produced by the crystal structure of a material. Furthermore, TEM analysis capacity has been improved by the integration of other techniques in the device and techniques like EDX and electron energy loss spectroscopy (EELS) ²⁴

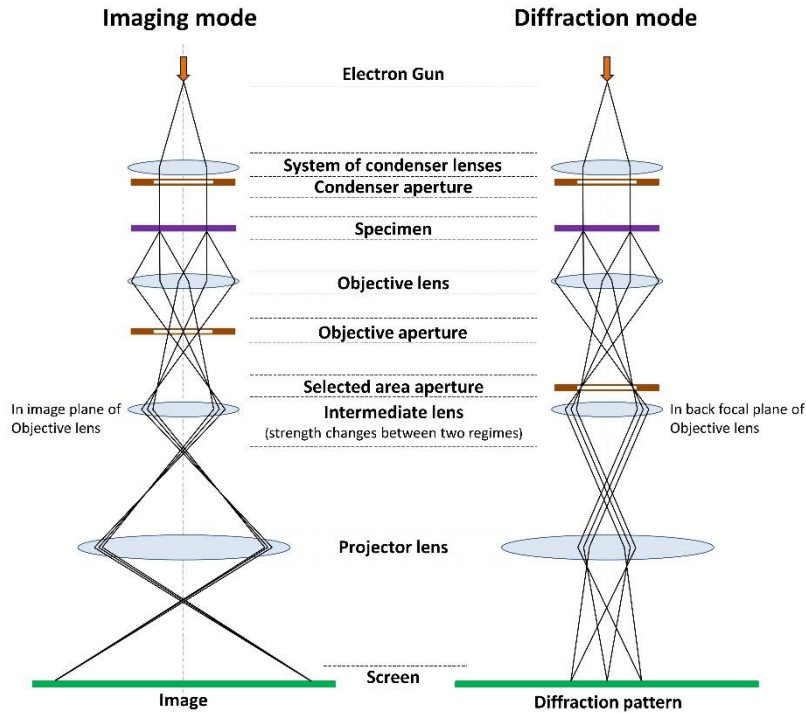


Fig.25 Scheme of TEM in image and diffraction mode

3.3.1 Selected Area Electron Diffraction (SAED)

SAED is a crystallographic technique that can be implemented in the diffraction mode of a TEM to identify and study crystalline phases. In this technique, the sample is first examined by the image mode of the TEM to determine the concrete area to study. The microscope is then switched to diffraction mode by inserting the proper aperture, which blocks almost all the electrons from the beam except for the small fraction that are scattered by the sample due to its crystalline structure²⁴.

Interplanar distance can be directly determined by the separation of the diffraction spots (figure 26), thanks to Bragg's law and the camera length (L):

$$2d \sin \theta = \lambda$$

Desing of novel electroactive nanofluids for flow cell

where λ is the wavelength of the electrons, d is interplanar space and 2θ is the scattering angle of the electrons caused by the diffraction process.

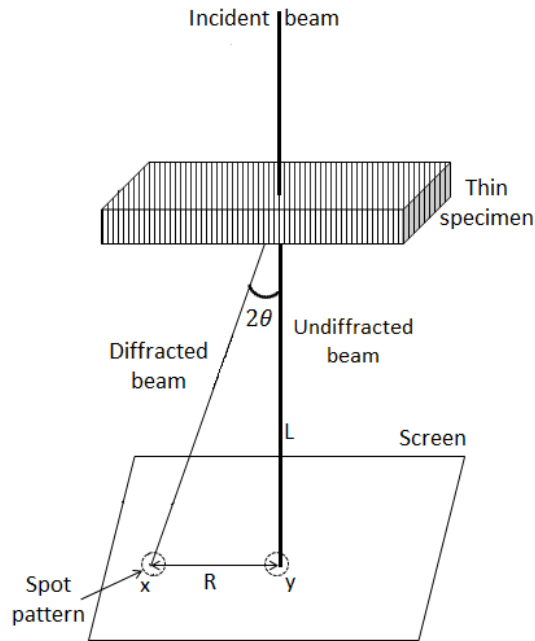


Fig.26 Scheme of the geometry of the diffraction pattern

Because electron wavelength is very small, the diffraction angle is also very small and thus, diffracted electrons are almost parallel to the electron beam. For instance, for a low energy beam of 100 KeV, λ is 0.037Å and $\theta \approx 1^\circ$. Consequently, for a small angle of diffraction²⁶

$$\sin \theta \approx \tan \theta \approx \frac{1}{2} \tan(2\theta) \quad (1)$$

By the geometry of figure 26

$$\tan(2\theta) = \frac{R}{L} \quad (2)$$

and using Bragg's law can be expressed as:

$$2d \frac{1}{2} \frac{R}{L} = \lambda \quad (3)$$

and

$$Rd = \lambda L \quad (4)$$

Equation 4 allows to determine the interplanar space from the separation of the diffraction points (R), provided λL , the “camera constant” ($\text{\AA}\cdot\text{cm}$), is known.

3.4 Scanning Electron Microscopy (SEM)

This technique allows to characterize the surface morphology and microstructural characteristics of a sample, but also can provide information about the elemental composition. SEM works by the scanning of the sample with a focused beam of electrons, the electrons can get scattered through an elastic (negligible energy loss) or inelastic mechanism, then are collected to generate the picture, thus the sample must be electrically conductive in order to be able to scatter the electrons.

Inelastic scattered electrons ejected from the valence band of the sample with low energy ($< 50\text{eV}$) are called secondary electrons. They emerge from the immediate sample surface (few nanometers below the surface), thus these electrons provide an excellent topological information. On the other hand, elastic scattered electrons can also be used to generate a picture of the sample. In that case topological details will be worse than those obtained from secondary electrons because elastically scattered electrons come from a deeper part of the sample. However, since elastic scattering depends on the mass of the atoms, in this case important information related to composition of the sample can be obtained²⁷.

3.5 X-ray Diffraction (XRD)

XRD is a technique that allows the crystal structure or structures of a sample to be determined and even, with a proper pattern, a quantitative analysis of the different phases in a complex mixture can also be performed, thanks to the intensity and thickness of peaks in the diffraction pattern.

X-rays are used because their wavelength fits with the interplanar distances of the crystalline structures, and monochromatic x-ray radiation is used. Diffraction peaks are generated when the scattered x-ray from a set of lattice planes in the crystal satisfies Bragg’s law. Thus, scanning a powder sample through a range of 2θ angles, all possible diffraction directions of the lattice can be attained due to the random orientation of the powdered material. Because each crystalline phase has a unique interplanar distance, it is possible to identify the various phases that form a material from the conversion of the

peaks recorded in the diffractogram to the corresponding interplanar distance. This is usually done by comparison of the peak position and intensity with those of standard database patterns²⁸.

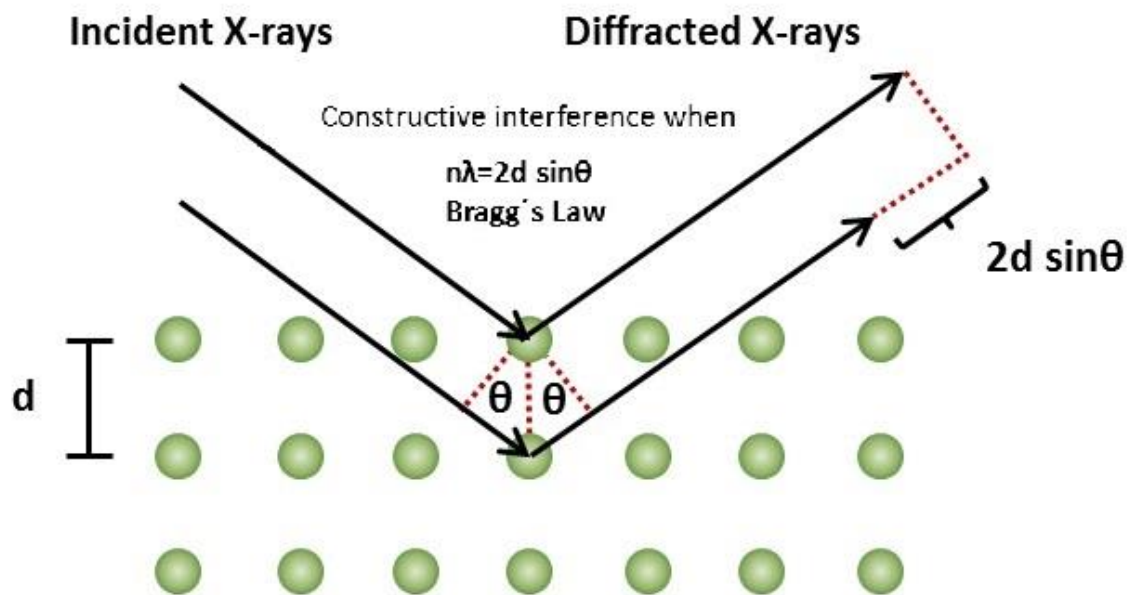


Fig.27 Scheme of x-ray diffraction process

3.6 Specific Surface Area (SSA)

This technique measures N_2 adsorption and desorption at different pressures on the surface of a material to determine its SSA and pore size by the multipoint Brunauer-Emmett-Teller (BET) method. The concept behind this method is an extension of the Langmuir theory, which is a theory for monolayer to multilayer molecular adsorption with the following hypotheses: (a) gas molecules physically adsorb on a solid in layers infinitely; (b) there is no interaction between each adsorption layer; and (c) the Langmuir theory can be applied to each layer²⁹.

IUPAC pore size classification:

- Macroporous: pores larger than 50 nm.
- Mesoporous: pores between 2-50 nm.
- Microporous: pores smaller than 2nm.

Gas adsorption is a complex process that depends on chemical composition, physical interactions and the surface structure. Thus, inert gasses at low temperatures are used to make physical interactions. A large part of the porous structures are complex, with different pore sizes and channels of different sizes, which produce different kinds of adsorption-desorption curves. One of the classifications more widely accepted is that proposed by IUPAC²⁹:

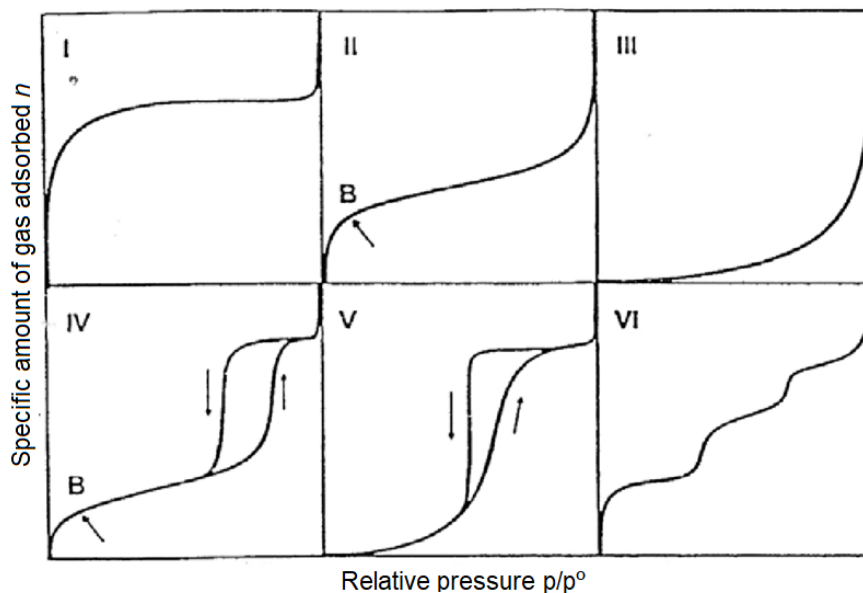


Fig.28 IUPAC adsorption-desorption curves classification

Type I: A typical curve of microporous materials: high adsorption energy of micropores allows gas adsorption at low pressures.

Type II: This curve is obtained with a non-porous or microporous adsorbent and represents unrestricted monolayer-multilayer adsorption. Point B, the beginning of the almost linear middle section of the curve, is often taken to indicate the stage at which monolayer coverage is complete and multilayer adsorption is about to begin.

Type III: This type of curve, which is not commonly found, indicates a weak interaction between the gas and material.

Type IV: A typical curve of mesoporous materials: at low pressures it acts as type II but at high pressures, it shows a hysteresis cycle.

Type V: This is like a type III curve indicating a low interaction between gas and material. This is also not a common kind of curve.

Type VI: This curve is associated with an adsorption layer by layer that is homogeneous with respect to the gas. These are the least common adsorption curves.

3.7 Rheology

Rheology is the discipline dealing with deformation and flow of matter. Viscosity is one of the building blocks of rheology. Viscosity is a measure of the flow resistance of a fluid. When a fluid starts to flow under the action of a force, a shearing stress arises everywhere in the fluid that tends to oppose the motion. As one layer of the fluid moves past an adjacent layer, the fluid's molecules interact to transmit momentum from the faster layer to the slower layer, tending to resist motion³⁰. In this thesis work, rheology experiments were carried out using a RheoStress 600 from Hacker at the Institut de Ciència de Materials de Barcelona (ICMAB).

3.8 Materials Preparation

3.8.1 Reduced Graphene Oxide (RGO)

Graphene oxide (GO) was synthesized from natural graphite using the modified Hummers method. Briefly, 2.5 g of NaNO₃ and 125 ml of H₂SO₄ were added to 2.5 g of graphite and stirred for 30 min in an ice bath. 12.5 g of KMnO₄ was added to the resulting solution, and then the solution was stirred at 50 °C for 2 h. 500 ml of deionized water and 15 ml of H₂O₂ (35%) were then slowly added to the solution, and the solution was washed with dilute HCl. The GO product was washed again with 250 ml of concentrated HCl (37%). The reduced graphene oxide (RGO) was prepared by high temperature treatment of the GO sample at 800 °C under nitrogen for 1 h.

3.8.2 RGO-Polyoxometalate (RGO-POM)

Hybrid materials were prepared based on rGO-phosphomolybdic acid (rGO-PMO₁₂) and RGO-phosphotungstic acid (RGO-PW₁₂). Briefly, 0.25 g of rGO was dispersed in 100 ml of deionized water with a probe sonicator (1000 watts) for 30 min. 10 mM of the chosen POM was then added to the pre-sonicated 100 ml RGO dispersion. This suspension was further sonicated (bath sonicator 200 watts) for 2 h and kept at room temperature for 24 h. Afterwards, the product was filtered off and dried in a vacuum oven at 80 °C overnight.

3.8.3 LiFePO₄

A LiFePO₄ sample was prepared by a reflux method. Stoichiometric amounts (0.03 mmol) of Li(CH₃COO)·2H₂O (3.0606 g), Fe(C₂O₄)·2H₂O (5.3907 g) and 85 %v/v H₃PO₄ (2.05 mL) were dissolved in 70mL of ethylene glycol. The liquid reaction mixture was placed in a round-bottom flask connected to a condenser and refluxed vigorously for 72 h at 200°C. The final pH of this solution was 7. The resulting solid was filtered-off, washed several times with deionized water and then ethanol. The sample was dried under vacuum at 80°C overnight, preheated at 350°C for 5 h and then sintered at 700°C for 10 h under nitrogen atmosphere. 3.4214 g of green powder were collected, which amounts to a 92% yield.

3.8.4 Electrochemically Exfoliated Few Layers Graphene

A cell with a novel horizontal geometry was designed and built in order to directly exfoliate graphite powders (20 µm of average size). Graphite powder (Sigma Aldrich 282863-1KG) was placed at the bottom of the cell as the negative electrode and a Pt sheet was placed on top of it as the positive electrode. The whole system was submerged in the electrolyte, 0.1M (NH₄)₂SO₄, to carry out the exfoliation process.

After the exfoliation process, the electrochemical cell was cleaned with water and acetone over a filtration setup with a 0.2 µm pore size PTFE filter to deposited on it the exfoliated product. Which was washed with water and acetone several times to remove the electrolyte.

The product obtained was weighed and dispersed in DMF, 3g/L, and sonicated for 5 minutes in an ultrasound bath. After 24 h the stable dispersion was extracted from the precipitated non exfoliated product, which was filtrated and weighed in order to calculate the yield of the exfoliation process.

3.8.5 Graphene Film Preparation

Graphene film was prepared from the stable graphene dispersions produced by the electrochemical exfoliation of carbon powder. LiClO₄ was added up to 1M to the stable graphene dispersions to induce a flocculation process to precipitate the graphene. Next, the excess solvent was removed and deposited on a Kapton substrate placed on a watch glass to avoid leaking at the edges. After a week, samples were dried, and the graphene and LiClO₄ were deposited on the Kapton substrate. Finally, samples were carefully cleaned with acetone to only remove the LiClO₄.

References

1. Bard, A. J. & R. Faulkner, L. *Electrochemical methods, fundamentals and applications. Journal of Chemical Education* (2000).
2. Kurzweil, P. *Electrochemical Double-layer Capacitors. Electrochemical Energy Storage for Renewable Sources and Grid Balancing* (Elsevier B.V., 2015). doi:10.1016/B978-0-444-62616-5.00019-X
3. Kotz, R. & Carlen, M. Principles and applications of Caps. *Electrochim. Acta* **45**, 2483–2498 (2000).
4. Linden, D. & Reddy, T. B. *Handbook of Batteries, third edition. McGraw-Hill* (2002). doi:10.1016/0378-7753(86)80059-3
5. Daniel, C. *Electrochemical Technologies for Energy Storage and Conversion Electrocatalysis of Direct Methanol Fuel Cells Nanotechnology for the Energy Challenge Lithium Ion Rechargeable Batteries Hydrogen and Fuel Cells Handbook of Fuel Cells High Energy Density Lit.* (2012).
6. Goodenough, J. B. & Park, K. S. The Li-ion rechargeable battery: A perspective. *J. Am. Chem. Soc.* **135**, 1167–1176 (2013).
7. Winter, M. & Brodd, R. J. What are batteries, fuel cells, and supercapacitors? *Chem. Rev.* **104**, 4245–69 (2004).
8. Zhou, H. & Dong, S. Determination of the standard heterogeneous rate

- constant in polyelectrolyte using steady state microdisk voltammograms. *J. Electroanal. Chem.* **425**, 55–59 (1997).
9. Bleam, W. Water Chemistry. in *Soil and Environmental Chemistry* 189–251 (Elsevier, 2017). doi:10.1016/B978-0-12-804178-9.00005-7
 10. Madjarov, J. *et al.* Revisiting methods to characterize bioelectrochemical systems: The influence of uncompensated resistance (iRu-drop), double layer capacitance, and junction potential. *J. Power Sources* **356**, 408–418 (2017).
 11. Van Der Vliet, D. *et al.* On the importance of correcting for the uncompensated Ohmic resistance in model experiments of the Oxygen Reduction Reaction. *J. Electroanal. Chem.* **647**, 29–34 (2010).
 12. Stoller, M. D. & Ruoff, R. S. Best practice methods for determining an electrode material's performance for ultracapacitors. *Energy Environ. Sci.* **3**, 1294–1301 (2010).
 13. Shao, Y. *et al.* Design and Mechanisms of Asymmetric Supercapacitors. *Chem. Rev.* **118**, 9233–9280 (2018).
 14. Sandford, C. *et al.* A Synthetic Chemist's Guide to Electroanalytical Tools for Studying Reaction Mechanisms. *Chem. Sci.* (2019). doi:10.1039/C9SC01545K
 15. Elgrishi, N. *et al.* A Practical Beginner's Guide to Cyclic Voltammetry. *J. Chem. Educ.* **95**, 197–206 (2018).
 16. Orazem, M. E. & Tribollet, B. *Electrochemical Impedance Spectroscopy*. (John Wiley & Sons, Inc., 2008). doi:10.1002/9780470381588
 17. Snook, I. & Barnard, A. *Impedance Spectroscopy. America* (John Wiley & Sons, Inc., 2005). doi:10.1002/0471716243
 18. Tsuji, K. Grazing-exit electron probe X-ray microanalysis (GE-EPMA): Fundamental and applications. **60**, 1381–1391 (2005).
 19. Bluhm, H. X-ray photoelectron spectroscopy (XPS) for in situ characterization of thin film growth. in *In Situ Characterization of Thin Film*

- Growth* 75–98 (Elsevier, 2011). doi:10.1533/9780857094957.2.75
20. Dietzek, B., Cialla, D., Schmitt, M. & Popp, J. Introduction to the Fundamentals of Raman Spectroscopy. in *Springer Series in Surface Sciences* **66**, 21–42 (2010).
 21. Ferrari, A. C. *et al.* Raman spectrum of graphene and graphene layers. *Phys. Rev. Lett.* **97**, 1–4 (2006).
 22. Das, A., Chakraborty, B. & Sood, A. K. Raman spectroscopy of graphene on different substrates and influence of defects. *Bull. Mater. Sci.* **31**, 579–584 (2008).
 23. De Caro, C. A. & Haller, C. *UV-VIS Spectrophotometry - Fundamentals and Applications*. (Mettler-Toledo, 2015).
 24. Williams, D. B. & Carter, C. B. *Transmission Electron Microscopy: A Textbook for Materials Science*. (Springer US, 1996). doi:10.1007/978-1-4757-2519-3
 25. Meyer, J. C. Transmission electron microscopy (TEM) of graphene. in *Graphene* 101–123 (Elsevier, 2014). doi:10.1533/9780857099334.2.101
 26. Fultz, B. & Howe, J. *Transmission Electron Microscopy and Diffractometry of Materials*. (Springer Berlin Heidelberg, 2008). doi:10.1007/978-3-540-73886-2
 27. Zhou, W., Apkarian, R., Wang, Z. L. & Joy, D. Fundamentals of Scanning Electron Microscopy (SEM). in *Scanning Microscopy for Nanotechnology* 1–40 (Springer New York, 2006). doi:10.1007/978-0-387-39620-0_1
 28. Jenkins, R. & Snyder, R. L. *Introduction to X-ray Powder Diffractometry. Chemical Analysis - volume 138* (John Wiley & Sons, Inc., 1996). doi:10.1002/9781118520994
 29. K.S., W. S. Reporting physisorption data for gas/solid systems with Special Reference to the Determination of Surface Area and Porosity. *Pure Appl. Chem.* **57**, 603–619 (1985).
 30. *Rheology of Complex Fluids*. (Springer New York, 2010).

doi:10.1007/978-1-4419-6494-6

CHAPTER 4

Molecular Flowing Systems. Quinones in Organic Electrolytes

4.1 Context

This first research chapter is centered on a well-known family of electroactive molecular compounds, i.e. quinones. In principle, simple organic molecules able to reversibly exchange two electrons per molecule in solution with good kinetics and a well-known mechanism in aqueous media. As a consequence, the overwhelming majority of work related to the use of quinones in flow cells dealt with aqueous electrolytes. As a matter of fact, this made it necessary for these aromatic molecules to be tuned, e.g. sulfonated, in order to reach acceptable concentrations in water to be used as an energy storage system.

In principle, the use of organic solvents would lead to greater solubility of quinones, to a wider working voltage range and therefore to a greater energy density. In the other hand, quinone redox mechanisms would be needed to be studied due to their high dependence of the media and in order to understand and avoid secondary spurious reactions.

For this study we chose CH_3CN as solvent because its low viscosity, 0.34 mPa·s, and good dielectric constant, 38, make it an excellent option for a system that must flow and thus, its final efficiency will depend not only on the electrochemical performance but also on the cost of pumping the electroactive solutions into the electrochemical cell. We chose a Li salt to work with quinones because we tried to change the two electrochemical semireversible steps that are used to present quinones in organic electrolytes, for an electrochemical mechanism similar to that in water in which Li^+ would act in a similar way to H^+ . Furthermore, working with Li^+ is interesting because it allows to study the potential of quinones as cathodes for Li-ion battery technology. Finally, we chose methyl-p-benzoquinone (MBQ) as the main quinone in this work because, due to its size and steric hindrance, it allows to show more clearly these effects on the electrochemical performance in comparison with the other quinones also studied and reported in this work.

4.2 Introduction

Quinones are the perfect example of reversible redox organic molecules. They are key pieces in natural and synthetic chemistry, from biological processes such as the mitochondrial ATP synthesis or the photosynthetic reaction center to their use as active materials in energy storage applications.¹ In both cases their effectiveness rests on their well-known reversible aqueous electrochemistry with good kinetics and a high electrochemical equivalent (two electrons per molecule of quinone).

In the field of energy storage quinones have been increasingly studied as active molecular materials for redox flow batteries (RFBs) and they count with all the characteristics necessary to conform the next generation of this type of cells. On the other hand, quinones have most frequently been used in aqueous solutions for this type of applications. Indeed, a recent series of works have described the successful use of sulfonated quinone derivatives to demonstrate their potential in aqueous electrolytes²⁻⁴. This may seem paradoxical since these organic molecules are most soluble in a variety of organic solvents rather than in water. As a matter of fact, the effective use of anthraquinone in aqueous solutions requires the sulfonation of the aromatic moiety. Thus, a plausible alternative would be to explore the use of quinones in organic electrolytes as active fluid materials for RFBs. In our group we have worked along that direction but have found several hurdles which we report here, as well as two alternative solutions to circumvent those hurdles

Two distinct mechanisms for the reduction of quinones have been proposed depending on the medium. For protic media the redox reactions take place in a single step involving the transference of two electrons. In this case the nature of intermediate species depends on the pH⁵. In aprotic media the redox mechanism involves two one-electron steps with a radical being generated in the first step^{1,5,6}, and with a second process that usually is not completely reversible.

In aprotic media, the addition of a proton source (Bronsted acid) results in an intermediate situation^{5,7,8} with hydrogen-bond formation leading to a redox mechanism similar to that in protic media⁹⁻¹¹.

In any event, the behavior of quinones in aprotic media is quite varied and complex because it depends on the polarity of the solvent, the support electrolyte, the quinone structure and, as explained above, the presence of protons in the media. Furthermore, the redox chemistry of quinones in aprotic media involves several possible intermediate adducts formed through weak interactions between two quinone molecules.

These adducts could be anionic ($[QQ]^{2-}$, $[QQ]^-$) or radical species ($[QQ]^{\bullet}$)^{7,12-14} that modify the mechanism leading to an irregular reversibility of the second redox process. The variable redox behavior of quinones with solvent polarity^{15,16} is due to the selective stabilization of some of these adduct species in different solvents. Similarly, the support electrolyte modulates the redox mechanism due to the interaction between the electrolyte cation and the different quinone anions¹⁴⁻¹⁸.

Other important issue of the redox chemistry of quinones in aprotic media is a distinct trend to undergo dimerization. Indeed, the radical generated in the first redox process can react with a neutral quinone molecule, a quinone-anion or other radical leading to dimer generation¹⁹⁻²². Finally, we should mention the formation of polymers as another characteristic feature of quinone electrochemistry in aprotic media. The resulting polymers can be grown as thin films on the electrode surface,²³⁻²⁵ and can present conductivity and reversible redox processes, thus making them potentially useful as catalysts or electrodes. A common approach to foster these polymerization processes is the use of quinones with amino or carboxylic acid groups. For example, poly-1,5-diaminoanthraquinone is one of the most frequently studied quinone polymers as a thin film supercapacitor electrode²⁶⁻²⁸, but it has also been studied as electrocatalyst for O_2 reduction^{29,30}.

A vast number of articles have been published on the electrochemistry of quinones. Yet, a substantial majority of them dealt with aqueous media, where the redox mechanism is better understood. As we have just discussed, the chemistry and electrochemistry of quinones in organic media is more difficult to predict, but precisely because of that it should deserve more attention.

In this work we report a detailed study of a specific combination of quinone (methyl-p-benzoquinone (MBQ)), solvent (CH_3CN) and electrolyte ($LiClO_4$). Acetonitrile was selected for this study due to its large dielectric constant, 38, and low viscosity, 0.34 mPa·s, together with a wide electrochemical stability window. Also we decided to work with a Li electrolyte to its widespread use and good performance in redox process applied to energy storage. Under our experimental conditions MBQ only shows a couple of redox peaks and the reversibility of its redox process depends on the concentration of $LiClO_4$, with best results for larger concentrations of $LiClO_4$. These facts made us consider the hypothesis that Li^+ could induce a behavior similar to that of protons in the redox mechanism of MBQ.

The work reported here was carried on in order to confirm this hypothesis and understand the corresponding redox mechanisms. On the other hand, during the

electrochemical reduction of MBQ a green layer was systematically generated onto the working electrode (regardless of the working electrode used and the presence of O₂ in solution). We have proven and show here how this layer prevents the MBQ redox processes from taking place, and how it can lead to a quinone polymerization process which can be reversed by the application of a positive overpotential. Similar behavior was observed for p-benzoquinone and 1,4-naphthoquinone but not for anthraquinone.

4.3 Experimental Section

Reagents from Sigma Aldrich: 1,4-naphthoquinone (97%), acetonitrile (≥99.9%), anthraquinone (97%), lithium perchlorate (>95%), methyl-p-benzoquinone “MBQ” (98%), p-benzoquinone (98%), tetraethylammonium tetrafluoroborate (99%).

A VMP3 potentiostat-galvanostat from BioLogic with the EC-Lab 10.44 version was used for the electrochemical measures. Glassy carbon disk of 3 mm diameter from CH Instruments Inc. (CHI 104) electrode and a Pt sheet were used as working (WE) electrode, a Pt mesh as a counter electrode (CE). We used a non-aqueous reference electrode (RE) Ag/Ag⁺ from BAS Inc. (013394), based on a solution of 0.1 M tetrabutylammonium perchlorate (TBAP) and 0.01 M AgNO₃ in CH₃CN.

Cyclic Voltammetry and Potentiostatic Electrochemical Impedance Spectroscopy (PEIS) experiments were performance with the same 3 electrodes configuration, working frequencies were from 10 kHz to 100 mHz. Before each PEIS measure was made a chronoamperometry experiment of 10 minutes to obtain a current with low variation front time, was not possible apply a longer time in the chronoamperometry experiments by large volatility of the solution to obtain a better constant current, a longer time would promote a significant concentration difference between the experiments. Also before each experiment the glassy carbon electrode was polished.

UV-Vis spectra were recorded as a function of the potential applied on the working electrode. These in-situ studies were carried out with an Autolab PGSTAT30 potentiostat/galvanostat. Chromogenic analyses were performed concomitantly with the electrochemical experiments using a USB4000 spectrophotometer (Ocean Optics Inc) equipped with an LS1 tungsten halogen light source and fiber optic cables with a diameter of 600 μm.

4.4 Results and Discussion

Cyclic voltammetry experiments of MBQ solutions in $\text{LiClO}_4 / \text{CH}_3\text{CN}$ electrolytes showed an apparently single (or two unresolved) redox couple process in contrast to the typical behavior of quinones in aprotic solvents, which show two well-resolved processes. Figure 1 compares CVs for the same MBQ in two different acetonitrile electrolytes, showing the remarkable difference between LiClO_4 and tetraethylammonium tetrafluoroborate (TEATFB).

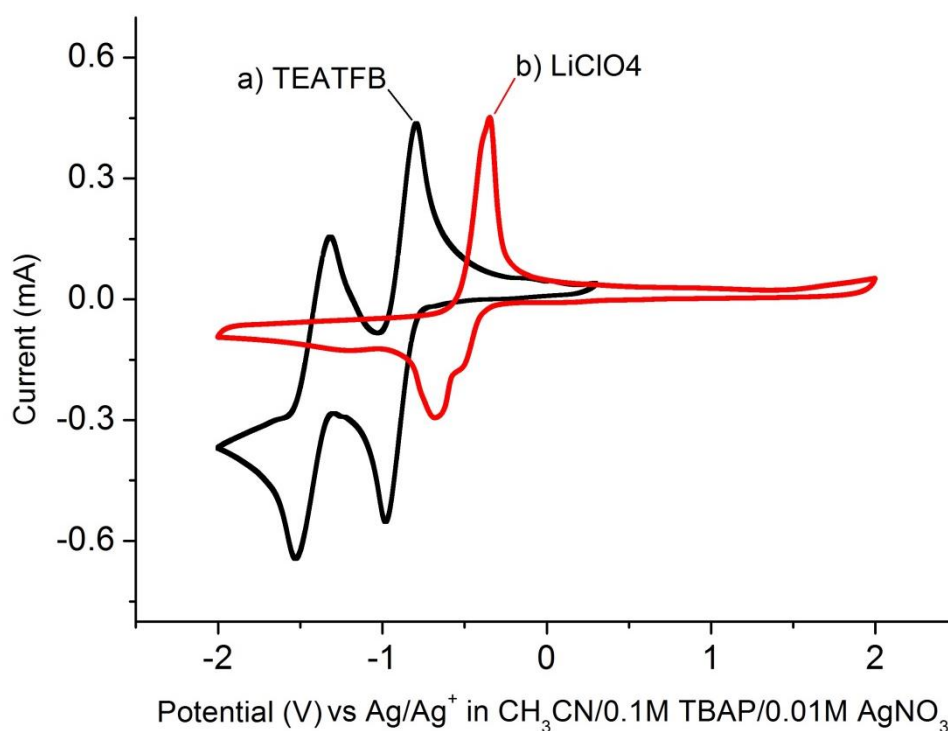


Fig.1 Cyclic voltammetry with glassy carbon WE at 100 mV s^{-1} of 0.01M MBQ solution in CH_3CN , a) 1.5M LiClO_4 b) 1M TEATFB.

Another remarkable difference between the electrochemistry of MBQ in TEATFB and in LiClO_4 electrolytes is the generation of a bright green coating upon application of negative potentials associated to the reduction of MBQ. This green coating, which will be discussed in detail below (Figure 3d) is formed regardless of the working electrode, scan rate and electrolyte concentration used. Indeed, we found it in every experiment we run.

But before dealing with this conspicuous green layer, we need to discuss another important element of this work, namely, the effect of Li^+ concentration on the electrochemistry of MBQ. Figure 2 shows CVs of MBQ with various concentrations of LiClO_4 in acetonitrile electrolytes recorded at 100 mV s^{-1} . The separation between

oxidation and reduction peaks of MBQ (indicative of the reversibility of the redox potentials) depends on the concentration of LiClO_4 . Low concentration of salt leads to a wide and weaker oxidation peak which is shifted to higher potential, indicating a poorly reversible oxidation process (figure 2a). As the concentration of LiClO_4 is increased the oxidation peak gets better resolved and shifts to lower potentials (figure 2b). Thus, the larger concentration of LiClO_4 used led to the minimum distance between oxidation and reduction peaks by a displacement of the oxidation peak to more negative potentials (figure 2c).

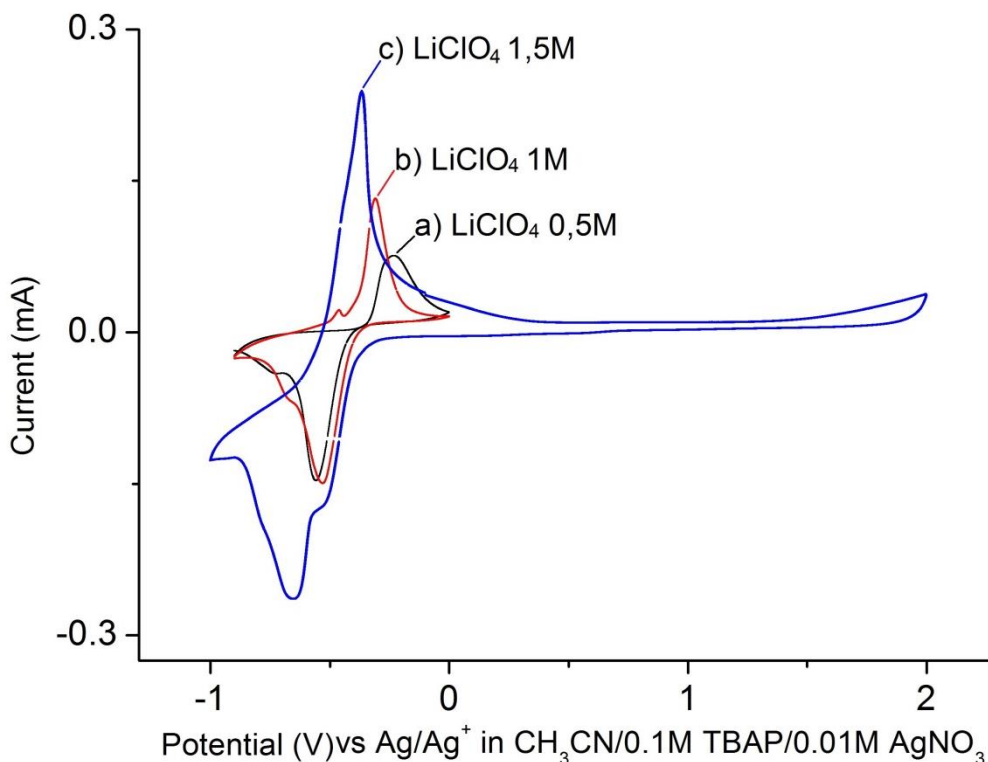


Fig.2 Cyclic voltammetry with glassy carbon WE at 100 mV s^{-1} of 0.01M MBQ solution in CH_3CN , a) 0.5M LiClO_4 b) 1M LiClO_4 c) 1.5M LiClO_4 .

Thus, an increase of the LiClO_4 concentration increases the reversibility of the redox process of MBQ. This indicates that Li^+ ions stabilize the MBQ anions generated by the reduction process. Accordingly, any possible irreversible reaction which MBQ anions could undergo for low lithium concentrations are minimized with high lithium concentrations, thus allowing the generation of a reduced product able to be reoxidized. Furthermore, it should be noted that the oxidation process is composed of two individual steps, as indicated by the shoulder in the oxidation peak in figure 2c. That indicates that the redox of MBQ in our conditions takes place in two steps at very close potentials, implying the presence of a radical species in the MBQ redox mechanism.

Desing of novel electroactive nanofluids for flow cell

Cyclic voltammetry experiments at lower scan rates (10 mV s^{-1}) show a decrease of the intensity in each cycle (figures 3a-c) with a faster collapse for the oxidation peak. That behavior is associated to the very conspicuous and fast generation of a green layer coating the WE. That coating was generated at negative potentials corresponding to the reduction of MBQ and was formed regardless of Li^+ concentration, scan rate or materials used as WE (figure 3d), in our case, Pt, Au Ni and Cu, as well as various carbon electrodes, including glassy carbon. Remarkably, it was possible to remove this coating, produced by the reduction of the MBQ, with the application of a positive overpotential, but this reoxidation is a slower process than the reductive coating process as is proved by the experiments at 10 mV s^{-1} .

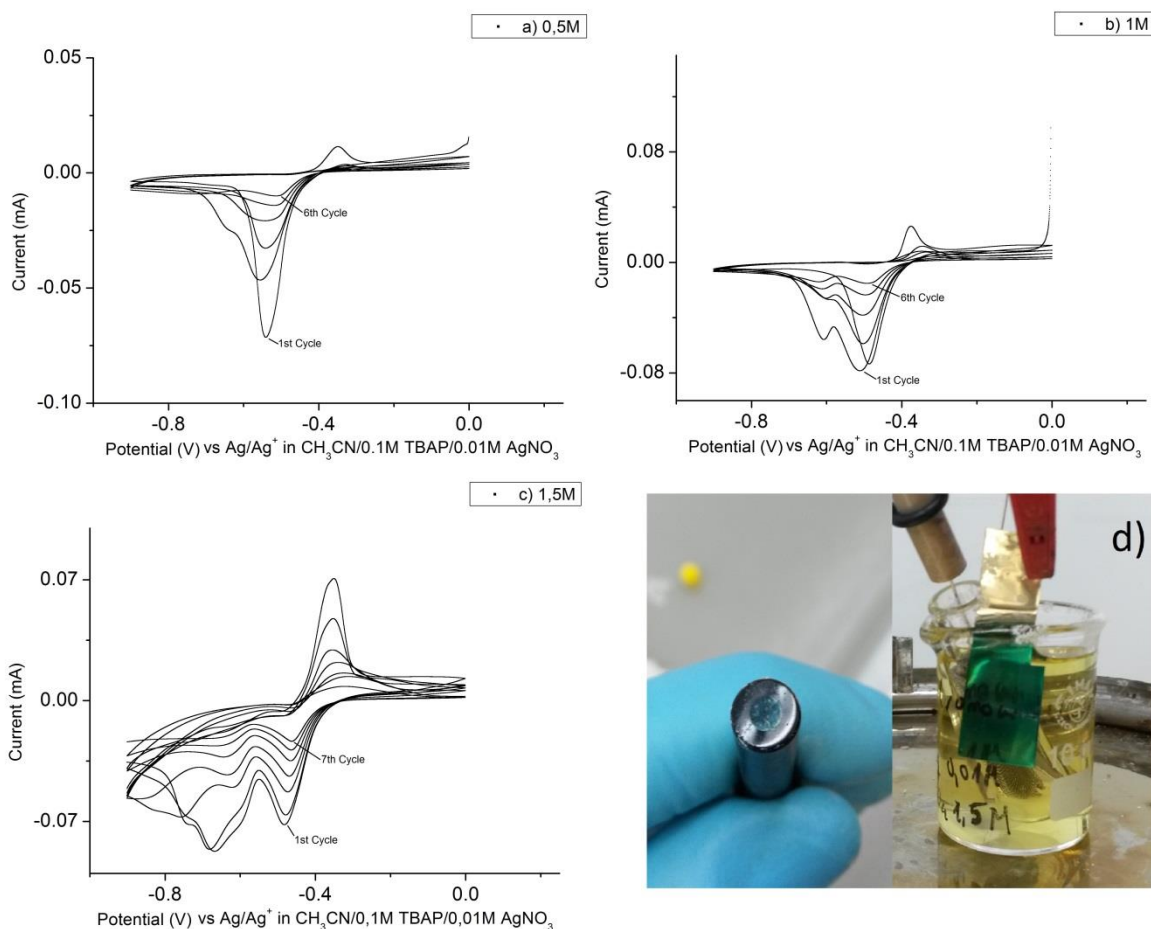


Fig.3 Cyclic voltammetry with glassy carbon WE at 10mV s^{-1} of 0.01M MBQ solution in CH_3CN , a) 0.5M LiClO_4 b) 1M LiClO_4 c) 1.5M LiClO_4 , d) Glassy carbon and Pt sheet as WE covered by the MBQ reduction.

The electrode passivation at low scan rate indicate that the reduction process is faster than oxidation. The progressive collapse of CV waves upon cycling indicates that the coating generated on the surface of the electrode by the reduction process increases in each cycle, with the resistance of the electrode increasing at the same time. This is consistent with a polymerization process taking place on the surface of the electrode. This electropolymerization process is clearly associated to the reduction peak appearing at the more negative potentials on the CVs (figure 2c). That peak is much better resolved in the CV of figure 2c than in 2a,b. The reason is that the former CV was run up to a large positive potential, thus allowing enough time for the green coating to dissolve after each cycle (a dissolution which was ascertained by visual inspection). This resulted in the polymerization process to start anew in each cycle leading to a well-defined electropolymerization peak. This hypothesis is supported by results at low scan rate, figures 3a-c, where the most negative peaks disappear faster than the other reduction peaks upon cycling.

Impedance studies corroborate the mechanism proposed by the CV experiments. The impedance experiments were performance at five different potentials in order to study the different processes taking place on the electrode surface. Figure 4a shows Nyquist plots recorded at each of those potentials, and figure 4b presents the corresponding polarization curve. A glassy carbon disk electrode was used as WE in all the PEIS experiments.

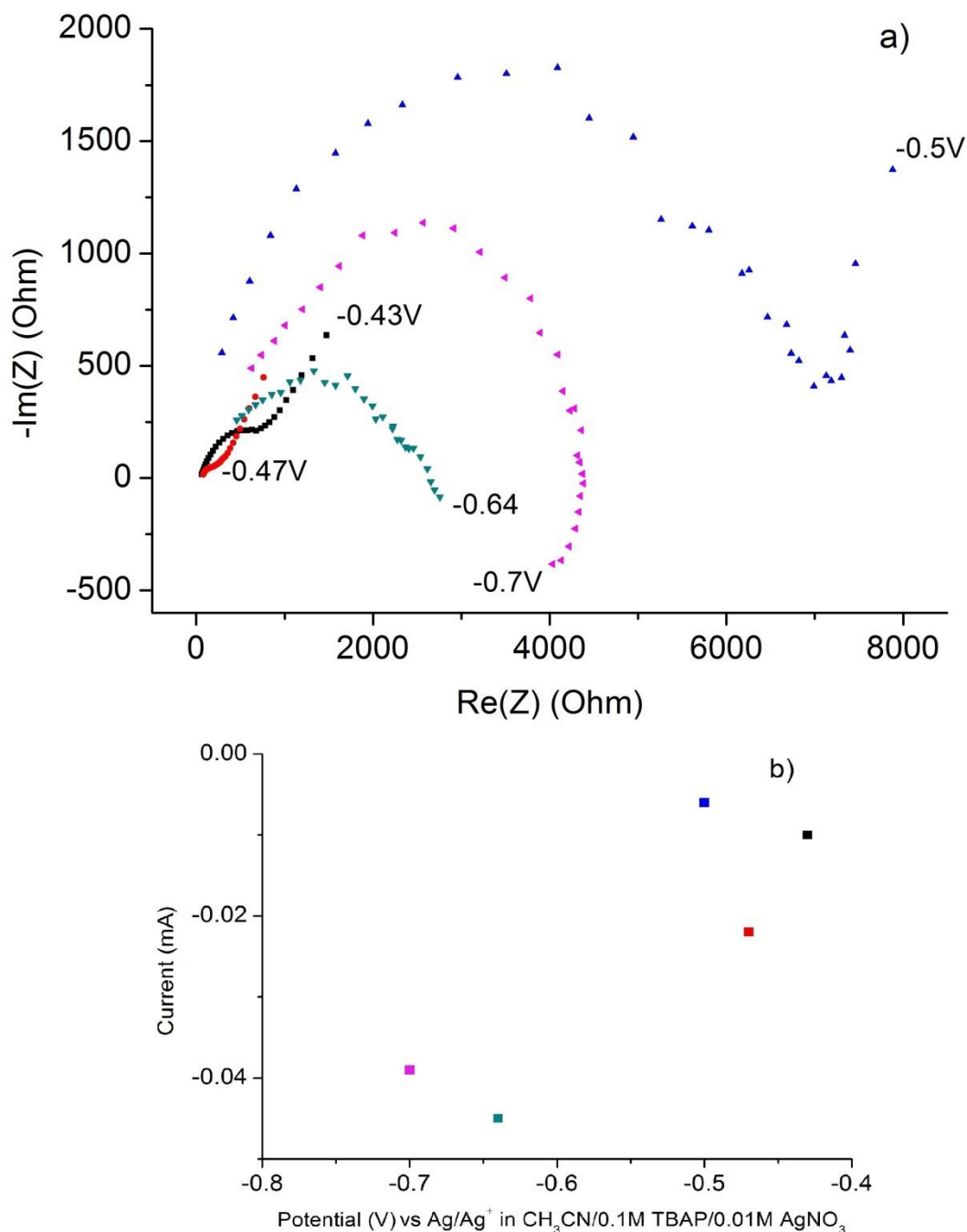


Fig.4 a) Nyquist plot of the different potentials applied, b) Polarization curve.

The first point was recorded at -0.43V, a potential less negative than the reduction peak of MBQ. The corresponding series in the Nyquist plot shows the typical behavior for a simple electrochemical redox process, a semicircle at high frequencies due to the electron transfer and a 45° straight line at low frequencies due to mass transport. The second point (-0.47V) corresponds to the first reduction peak, corresponding to the reversible reduction of MBQ. It also shows the behavior of a simple electrochemical redox process. In this case the resistance associated to electron transfer decreases and

the current increases due to the application of a larger overpotential allowing for a maximum velocity for electron transfer between MBQ and the electrode. It should be noted that no green coating was detected on the electrode surface after these two PEIS experiments.

The third point (-0.5V) is located between the peak of reversible reduction of MBQ and the second reduction peak that we assign to a polymerization process. At this potential the resistance associated with the electron transfer is the largest of all the potentials studied and, correspondingly, the current is the lowest. The shape in the Nyquist plot changes radically with respect to the two previous cases. The semicircle can be considered completed but it is irregular and is followed by a line with larger slope than in the two previous cases at less negative potentials discussed above. The large semicircle clearly indicates that the resistance for the redox process of MBQ increases substantially. On the other hand, the large slope after the semicircle indicates a capacitive behavior which is compatible with the adsorption of MBQ on the electrode and not diffusing to the solution. Indeed, at the end of this experiment, the green coating was apparent on the surface of the electrode, thus confirming the MBQ adsorption. All these observations conform to a picture in which the application of a potential negative enough (-0.5V), leads to a faster reduction of MBQ, which results in an increased concentration of the reduced product on the electrode surface; a concentration high enough to lead to the formation of the green coating, which in turn blocks the surface to the reduction of the remaining MBQ in solution. This blocking barrier (not yet an insoluble polymer) is responsible for the largest resistance observed and the very small current associated.

The fourth point (-0.64V) is integrated in the second reduction peak. As mentioned before, this potential was associated to the growth of a blocking polymer leading to the collapse of intensity of CVs at low scan rate (Fig. 3). At this potential the shape of the Nyquist plot is similar to that of the third point (at -0.5V) but the resistance associated to the electron transfer is much smaller (Fig 4 a). Furthermore, the series for this fourth point shows negative values of the imaginary component of impedance for the last three points. Finally, this point presents the largest intensity value despite having a larger resistance than the first and second points. This large intensity confirms that an electropolymerization process is effectively taking place. The larger resistance of the electrode compared to the two first points indicates that it is covered, so the process involved at this potential takes place on the coating not on the electrode surface and the product resulting from that process is characterized by a lower resistance than the (green) coating produced at the third voltage point. This means that a new product is generated on the electrode surface. It should be noted that after this experiment the

electrode was coated with a darker material, which was more difficult to remove from the electrode than the green coating formed at the third potential point. Thus, the green coating grown at -0.5V could be easily removed by dissolution in acetonitrile whereas the darker coating of this fourth point (-0.64V) could not be dissolved in a similar way and needed scratching the electrode surface to be removed.

The fifth point (-0.7V) was fixed after the second reduction point. As it could be expected for the continuing growth of the polymer coating, the intensity decreases and the resistance increases with respect to the values found for the fourth point. The shape on the Nyquist plot is still not well defined but shows a semicircle on the negative imaginary impedance zone that indicates an inductance due to the larger thickness of the coating on the working electrode. To a lesser extent this behavior can also be appreciated on the fourth point (the last three points extending to the negative zone of the imaginary impedance component).

All the experiments described so far were carried out in air. In order to establish the possible involvement of oxygen in the formation of the described coatings, a series of parallel experiments in deaerated electrolytes under argon were carried out. These experiments were necessary since it is well known that reduced quinone species and polymers can reduce oxygen³¹.

Figure 4 shows the CV of a solution of MBQ in deaerated acetonitrile and under Ar flow (5a) and in air, as above (5b). Despite the obvious similarities we note that the solution without oxygen, 4a, shows more intense and better resolved oxidation peaks. This can be explained by a larger concentration of reduced species in each cycle thanks to the absence of dissolved oxygen, which could otherwise oxidize part of the reduced MBQ.

Desing of novel electroactive nanofluids for flow cell

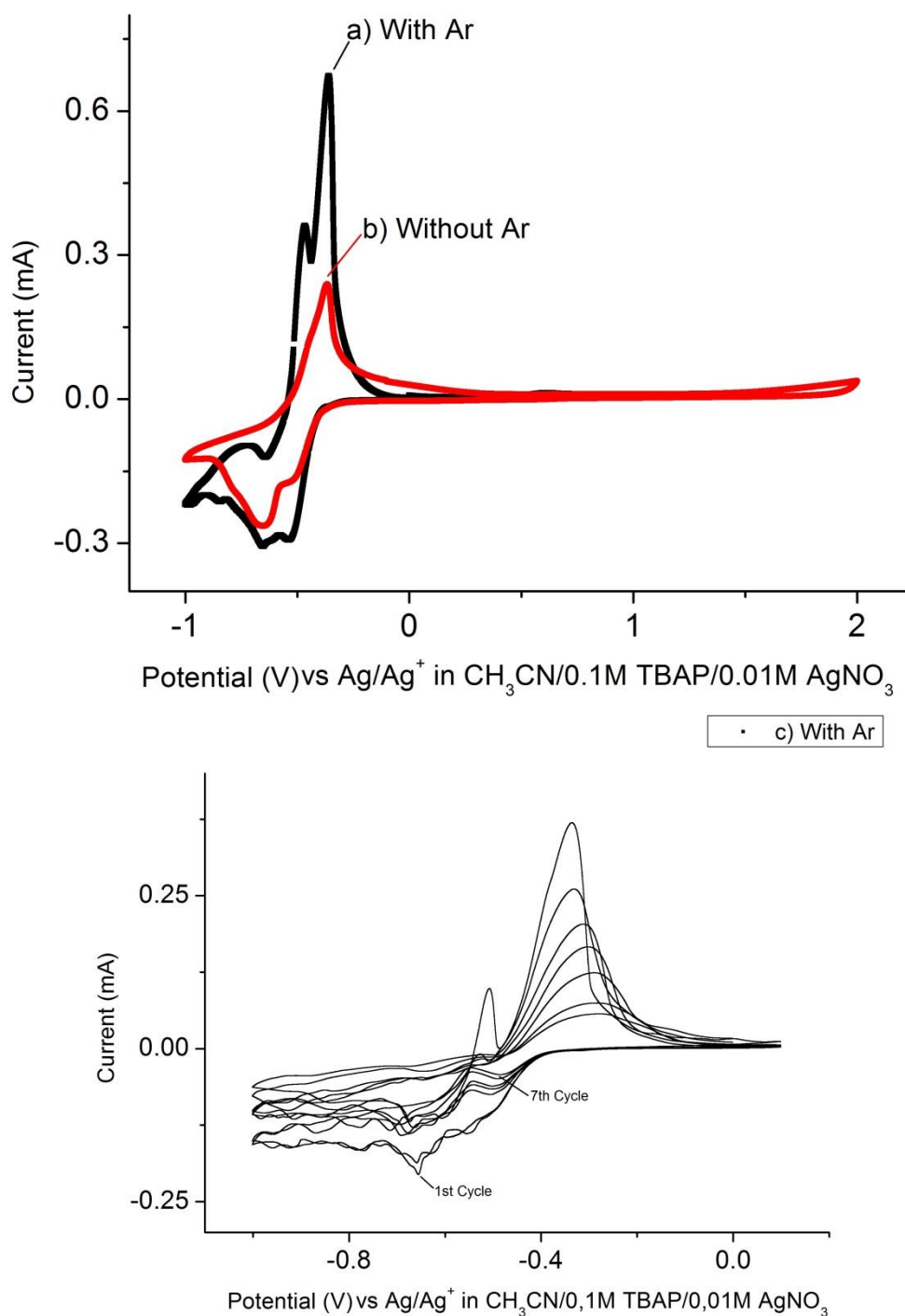


Fig.5 Cyclic voltammetry with glassy carbon WE at 100 mV s^{-1} of 0.01M MBQ , 1.5M LiClO_4 solution in CH_3CN , a) with Ar flux, b) at ambient conditions, c) at 10 mV s^{-1} with Ar flux.

On the other hand, all redox peaks appear at the same potentials. And, most importantly, the green layer that was formed under air is also formed in the absence of air. Here, again, the green coating is formed on the electrode surface at negative overpotentials, and it forms much faster than it dissolves. Thus, both with and without oxygen, the green coating quickly appears, even within the timescale of a fast CV, but it needs longer times to disappear at positive potentials. Also, both with and without

oxygen, the green coating passivates the electrode surface thus blocking the reversible redox process of MBQ. This can be ascertained from figure 5c, where several cycles were recorded at low scan rate. The peak at ca. -0.35 V, corresponding to the reversible oxidation of MBQ, gets collapsed upon cycling due to the accumulation of the green coating, similarly to what happened in air (figure 3c).

So, the generation of the green layer is a process independent of the presence of oxygen in solution. However, this will not be so for the ensuing processes following further reduction of the green layer, as we will show below. The first hint towards this conclusion comes from the very complex pattern systematically recorded on the CVs at negative overpotentials. Indeed, all Ar-deaerated CVs showed an apparently noisy signal after the negative redox peak, below ca. -0.6V (figure 5c). Our first hypothesis of an instrumental artefact was ruled out by the systematic reproducibility of these apparently irreproducible traces, characterized by a chaotic component. Figure 6 shows one experiment intended to probe the extent of this behavior in a wide potential range. Indeed, the aleatory appearance of the trace goes down to -2.0 V in contrast with the behavior in air.

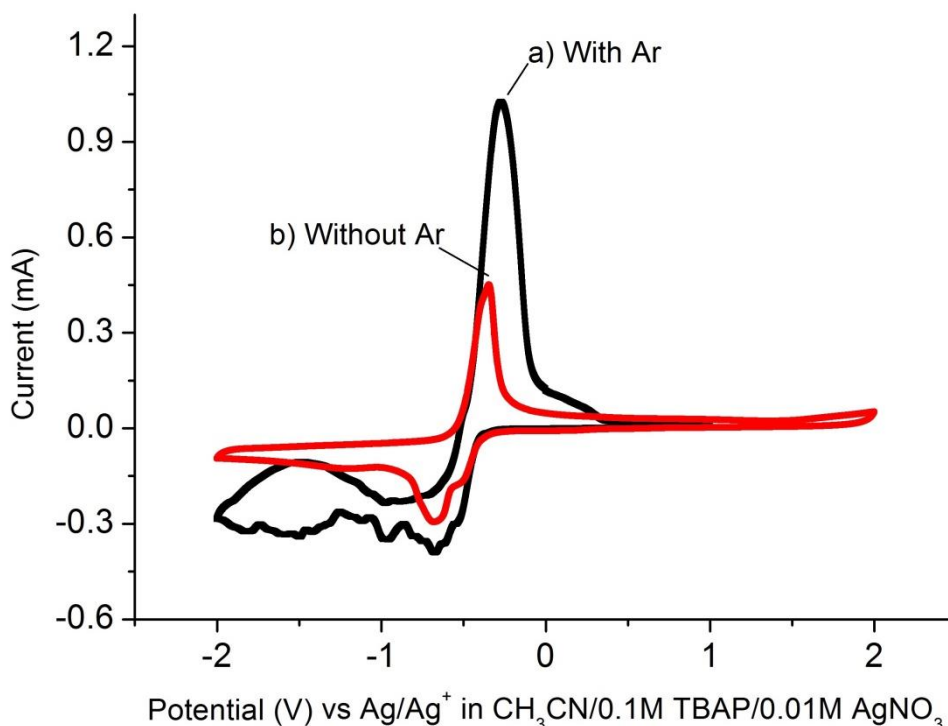


Fig.6 Cyclic voltammetry with glassy carbon WE at 100 mV s^{-1} of 0.01M MBQ, 1.5M LiClO_4 solution in CH_3CN , a) with Ar flux, b) at ambient conditions.

Complex Impedance measurements were also performed for this oxygen-free series at voltages similar to the series run in air. Thus, figure 7 collects the corresponding Nyquist plots and polarization curve for this series, which show a different behavior under Ar, even at the potential corresponding to the first redox peak (-0.5V), thus confirming the dependence of this process on the presence of oxygen in solution.

For the first potential point (-0.495), placed right before the first reduction peak, PEIS results under Ar show a simple electrochemical redox process as the experiment in air. And, as in air, with no signal of the green coating. In the second potential point (-0.536V), which corresponds to the first reduction peak, there is already inductive behavior just after the formation of the green coating on the working electrode surface. In the experiment with air there was no green layer generated at this point, which can be explained by the presence of O₂ lowering the concentration of reduced MBQ. That is also the reason for the different trend observed for the first three points of the polarization curve in Ar versus air: the coverage process starts before reaching the potential of the peak for the reversible MBQ reduction.

The third potential point (-0.6V) is located between the two reduction peaks. In this case the impedance shows a capacitive behavior (high slope line) and the working electrode gets the green coating layer. This different behavior with respect to the experiments in air confirms that the polymerization mechanism depends on the presence of O₂. The fourth potential point (-0.66V) corresponds to the second reduction peak, the Nyquist plot shows a complete semicircle with a very low resistance followed by a straight line with a large slope. That may indicate that a redox process takes place but not involving diffusion of molecular species to the electrode and with the product generated on the electrode still acting as a capacitor. Again that behavior is completely different from that observed in the solution with air, where the resistance was reduced in the second redox peak potential but never with a smaller value than for the first and second points. The large current and low resistance at this point confirm that there is a very favored process, but despite being at a very similar potential to the second reduction peak in the experiments with O₂ is not the same process.

Finally, the last point (-1.0V) shows large resistance in the Nyquist plot and low current values, confirming the growth of a passivating product on the electrode.

Desing of novel electroactive nanofluids for flow cell

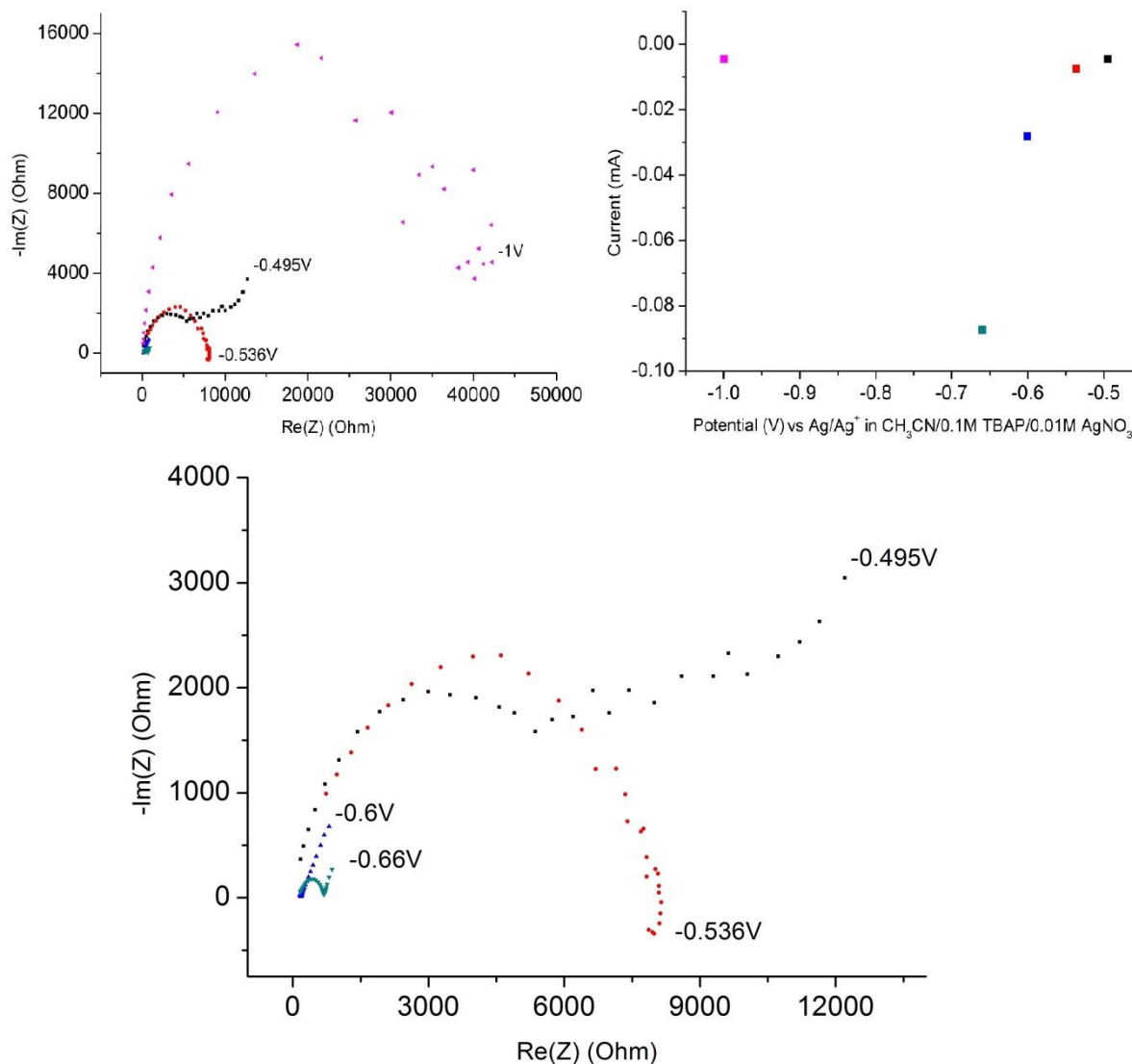


Fig.7 Nyquist plot of the different potentials applied with Ar flux (second diagram is focus on the small impedance values) and it polarization curve.

In an attempt to identify and characterize the products growing and passivating the working electrodes, in situ spectroscopy analyses were carried out. Thus, UV-Vis spectra were recorded in real time using a transparent Indium Tin Oxide (ITO) working electrode as it was polarized to record a CV (Fig 8). Figure 8b shows the evolution of absorbances measured at four different wavelengths as successive cyclic voltammeteries were carried out (five CV cycles are shown). Two well-resolved maxima are initially detected in the time evolution line. They are clearly correlated to the two reduction waves detected in the first CV (Fig 8a). This agrees with our hypothesis that the initial coating leads to the generation of a second product by a polymerization process. As CV cycles go on the first maximum (associated to the formation of the green coating) is eventually buried by the growing second maximum (corresponding to polymer formation). As the number of cycles grow the maximum absorbance of the second process grows and the

polymer formed on the surface of the electrode under reduction is not completely dissolved upon oxidation, thus initiating the passivation of the electrode.

The results of this in-situ experiments clearly confirm the successive generation of two different products, as proposed in our mechanism. It should be noted that although the electrochemical signal of MBQ on an ITO electrode is worse than on glassy carbon, it still shows the two reduction peaks and the decrease of redox peaks upon cycling.

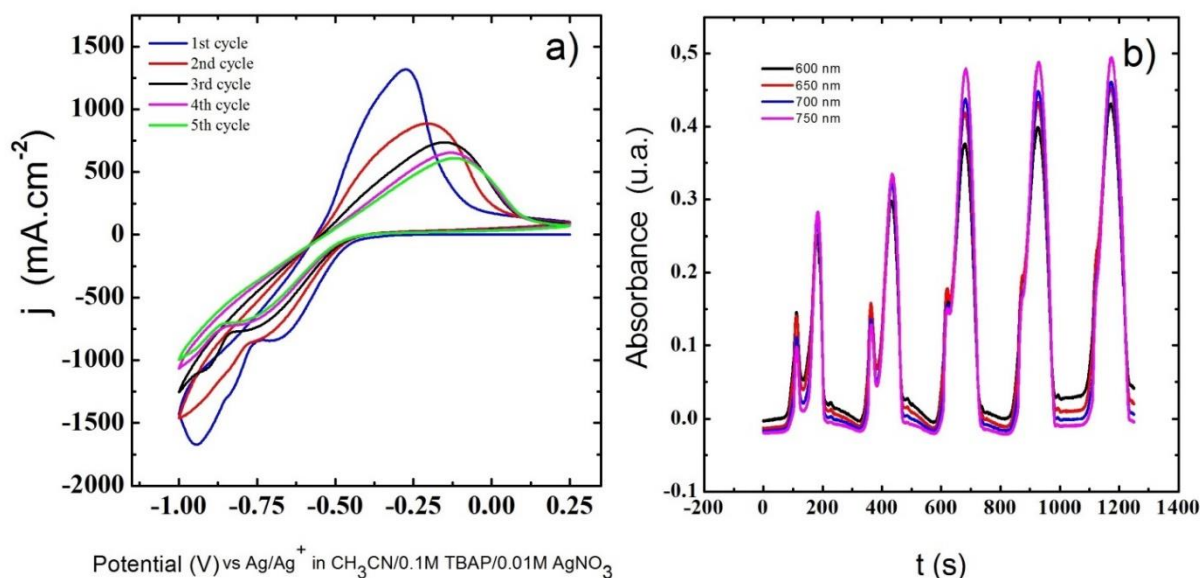


Fig.8 Real time spectroscopy of an ITO working electrode at 10 mV s^{-1} of 0.01M MBQ and 1.5M LiClO_4 in CH_3CN solution (in air). a) CVs of the first 5 cycles, b) Evolution of the absorbance at various visible wavelengths of the ITO working electrode.

So far we have been able to prove the electrochemical growth of the green coating (both in the presence and absence of oxygen) and the subsequent formation of passivating layers whose nature depends on the presence of oxygen. In order to determine whether these layers form exclusively through electrochemical processes we carried out an experiment consisting on the chemical reduction of solutions of MBQ in acetonitrile using metallic lithium as reducing agent.

Figure 9 includes a digital photograph showing the formation of the green layer on the surface of metallic lithium, thus proving that this compound can also be formed chemically as long as lithium is present. It should be noted that the green product grows on the surface of lithium but can be easily dispersed to the solution by just a very gentle shaking. Remarkably, the final color of the solution was not green but orange, corresponding to the typical color of free reduced quinone anions, indicating the metastable nature of the green species. This result can contribute to an understanding of the structure of the green product, which must be formed by reduced quinone

molecules with the implication of Li (the green layer was not formed in TEA⁺ TFB⁻ electrolytes).



Fig.9 Metal lithium on a 0.01M MBQ solution on CH₃CN. The green layer formed on the surface of metallic lithium is apparent in this photograph.

With all the data at hand we propose the structure depicted in figure 10 (left structure), in which Li atoms bridge different reduced quinone molecules in an arrangement which is not purely ionic (only possible at reducing potentials) and only possible on the vicinity of the reducing electrode with a relatively large ratio of reduced quinone to lithium. The lack of covalent bonding between quinones would explain the low stability of this product, which upon stirring gets dissolved into the (Li⁺ rich) bulk electrolyte solution yielding the red-orange reduced Li₂MBQ species.

A combined analysis of CV, PEIS and UV-Visible spectroscopy results allows us to propose a mechanism for the transformation (in air) of the green layer into a secondary product with an improved conductivity (shown by PEIS data) which eventually grows into a passivating coating on the surface of the WE. Starting from the green product (left structure), figure 10 shows the mechanism for further reduction. We relate the second reduction peak of the CV with a polymerization process, made possible by the catalytic reduction of O₂ by the green product^{31,32}, a process obviously not possible in the absence of air. That process generates a polymer with a conductive structure that explains the reduction of the resistance on the PEIS experiments with respect to the initial green coating.

For experiments under Ar the green coating accumulates faster on the electrode thanks to the absence of O_2 that could otherwise oxidize part of the reduced MBQ. Thus, the polymerization process starts before, even at less negative potentials and there isn't a decrease of the current in the polarization curve between the MBQ redox and the polymerization processes. The final outcome is also a passivating layer. However, impedance data show that is not the same polymer obtained in air. Furthermore, the chaotic oscillation of current in the reduction area of the CV indicates that the electrode passivation doesn't follow a well-defined polymerization process as with O_2 . In this case different reactions could take place, including Diels-Alder reaction or Michael addition³⁰. A wide variety of structures could be generated in these processes, not only by reaction among quinone molecules but also possibly by heterogeneous reactions of quinones with the carbon electrode leading to covalent bonding. That fact could explain the widening oxidation peak and its shoulder in the CVs of deaerated solutions (figure 5) as well as the chaotic reduction currents. Unfortunately, the wide possibilities for these processes do not allow for the proposal of a single plausible mechanism in the absence of oxygen.

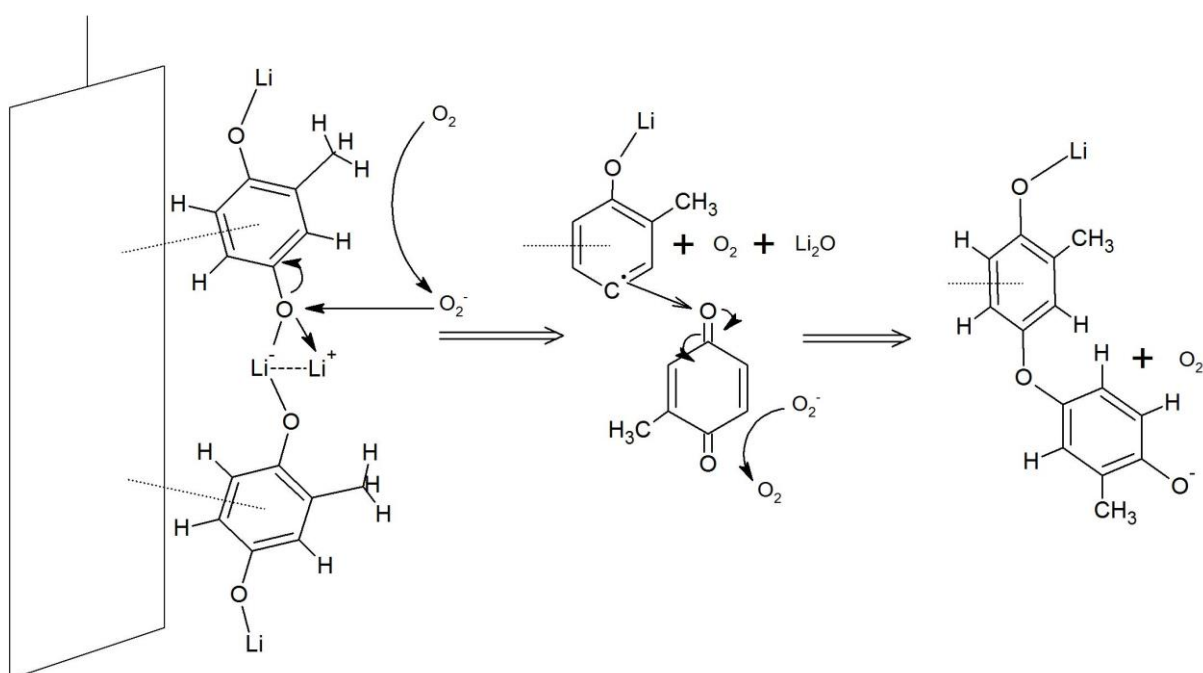
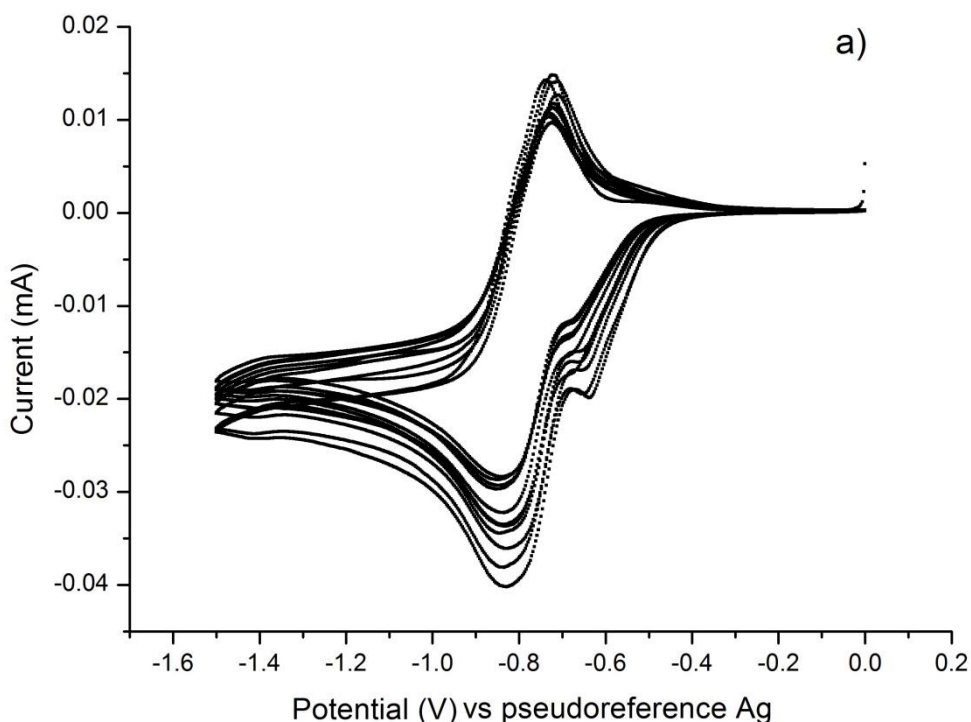


Fig.10 Proposed mechanism for the MBQ polymerization process at ambient conditions.

The same kind of coating process described above was observed not only for MBQ but also for other quinones like p-benzoquinone (BQ) and 1,4-naphthoquinone (NQ). On the other hand, the electrochemical reduction of anthraquinone (AQ) did not yield the green layer nor any passivating polymer. These facts reinforce our hypotheses because BQ and NQ could lead to polymerizations but anthraquinone would be too large and bulky and would present an important steric hindrance which would prevent the formation of structures like the ones depicted in figure 10. Figures 11 and 12 gathers CV data for both AQ (Figure 11) and BQ (Figure 12). AQ CVs feature reversible ideal redox waves, they don't show any decrease in intensity upon repeated cycles at any scan rate and the CVs do not show the second reduction peak, which we have related to the passivating polymerization process. On the other hand, the CVs of the totally unhindered BQ (Figure 12) show even at 100 mV s⁻¹ a decrease in the intensity upon cycling and also show the second reduction peak related to the polymerization process which, for this unsubstituted quinone generates new and more complex species (figure 12).



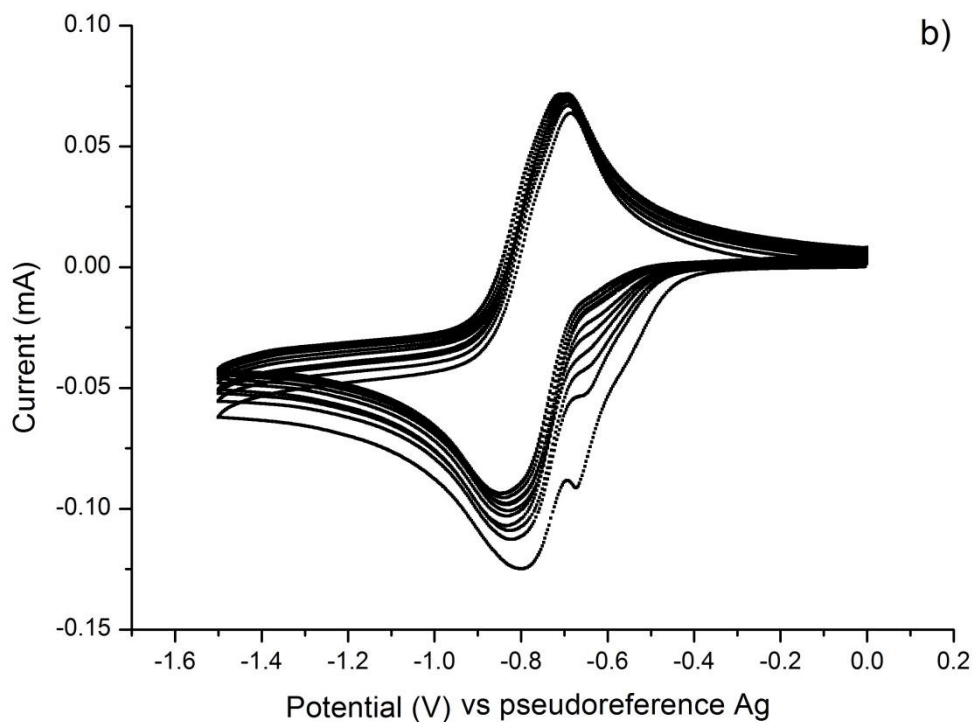
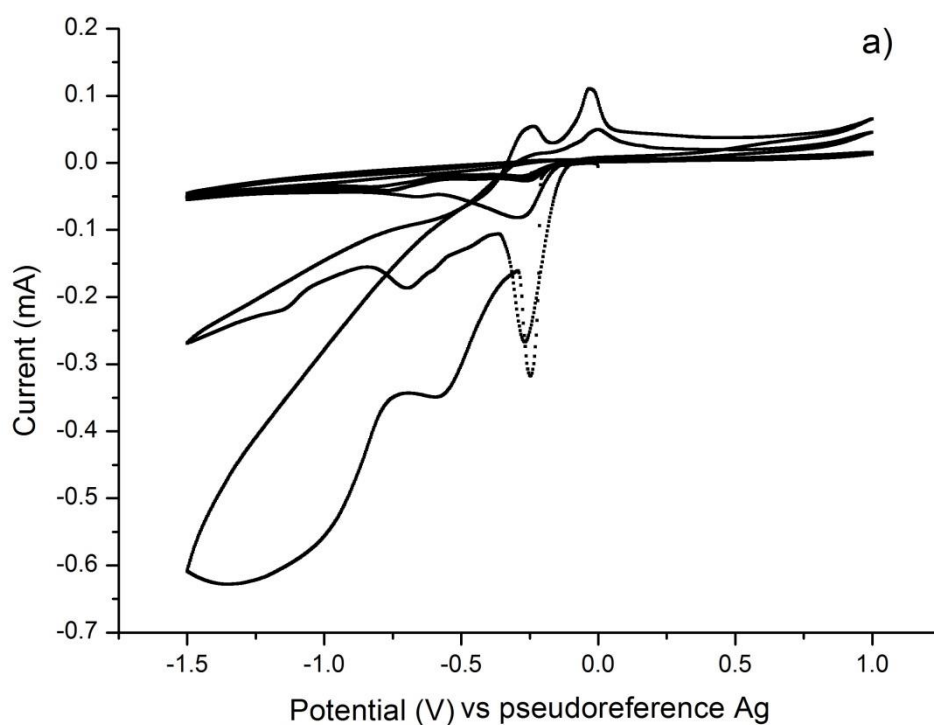


Fig.11 Cyclic voltammety of anthraquinone (AQ) solutions 0.05 M, 1M LiClO₄ in CH₃CN solution, with glassy carbon WE at a) 10 mV s⁻¹ b) 100 mV s⁻¹.



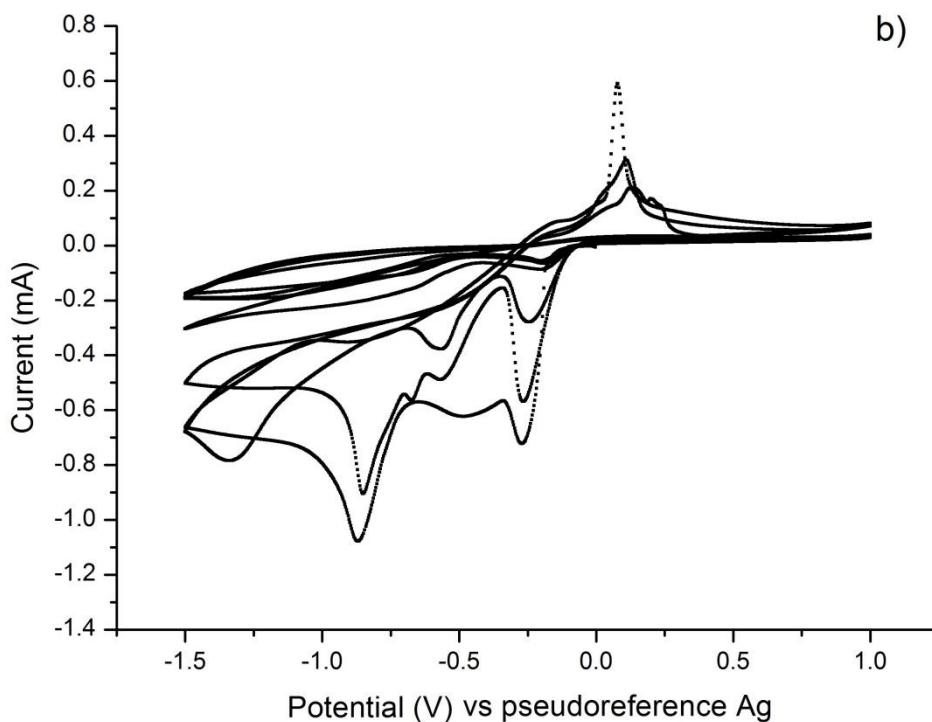


Fig. 12 Cyclic voltammetry of benzoquinone (BQ) solutions 0.05 M, 1M LiClO₄ in CH₃CN solution, with glassy carbon WE at a) 10 mV s⁻¹ b) 100 mV s⁻¹.

In addition to the green coating issue described, Li-organic electrolytes present another problem in order to work with quinones: low solubility in organic solvents of the reduced Li-quinone product, which tends to crystallize even outside of the electrochemical cell Figure 13.



Fig. 13 Digital pictures of quinone crystallization outside of different electrochemical cells.

4.5 Conclusions

The possible use of quinones in organic lithium electrolytes for application in Redox Flow Batteries could benefit from wider stability windows and higher solubility in organic media. However, a high concentration of quinones on the electrode-electrolyte interphase is precisely one of the conditions leading to the type of passivating coatings that we have reported here.

Our results show the large influence of Li^+ on the MBQ redox mechanism, showing mainly a couple of redox peaks and increasing the electrochemical reversibility of the MBQ redox process.

On the other hand, we have proven the systematic and reversible generation of a green coating that increases the resistance of the electrode and prevents the regular redox process of MBQ to take place, regardless of the presence of O_2 in solution and the nature of the electrode material. We have proven the involvement of Li in the formation of this green coating by showing its growth by chemical reduction with Li metal in CH_3CN and its absence when other electrolytes such as $\text{TEA}^+ \text{TFB}^-$ were used. That green product is not stable and easily disassembles into individual reduced Li-MBQ molecules. We have also shown the generation of new and different products on this first coating that increase notably the resistance of the electrode, and which nature depends on the presence or absence of O_2 . All of these coatings have a detrimental effect for the use of quinones in organic electrolytes. On the other hand, we have found that larger quinones such as anthraquinone can be reversibly cycled without formation of the passivating layers, whereas quinones with no steric impediments quickly yield these coatings on the current collector.

Thus, our work allows us to conclude that in order to apply quinones for energy storage in RFBs making use of organic media, two main guidelines should be considered. Large, sterically hindered quinones should be used instead of simpler quinones prone to polymerization in the presence of Li^+ . Otherwise, organic electrolytes not containing Li^+ would be preferable.

Despite the hurdles found in our research, the intrinsic but potential advantages of organic quinone electrolytes (wider working voltage, greater quinone solubility) make it worth it to further investigate their possible application in RFBs in the light of the present results. We hope that the work reported here will help in preventing some of the drawbacks of these systems, thus contributing to setting the path for organic quinone electrolytes to be applied in redox flow batteries.

References

1. Guin, P. S., Das, S. & Mandal, P. C. Electrochemical Reduction of Quinones in Different Media: A Review. *Int. J. Electrochem.* **2011**, 1–22 (2011).
2. Chen, Q., Eisenach, L. & Aziz, M. J. Cycling Analysis of a Quinone-Bromide Redox Flow Battery. *J. Electrochem. Soc.* **163**, A5057–A5063 (2016).
3. Huskinson, B. *et al.* A metal-free organic-inorganic aqueous flow battery. *Nature* **505**, 195–8 (2014).
4. Qing Chen, Michael R. Gerhardt, Lauren Hartle, M. J. A. A Quinone-bromide Flow Battery with 1 W/cm² Power Density. *J. Chem. Inf. Model.* **53**, 160 (1989).
5. Quan, M., Sanchez, D., Wasylikiw, M. F. & Smith, D. K. Voltammetry of Quinones in Unbuffered Aqueous Solution: Reassessing the Roles of Proton Transfer and Hydrogen Bonding in the Aqueous Electrochemistry of Quinones. *J. Am. Chem. Soc.* **129**, 12847–12856 (2007).
6. Alizadeh, K. & Shamsipur, M. Calculation of the two-step reduction potentials of some quinones in acetonitrile. *J. Mol. Struct. THEOCHEM* **862**, 39–43 (2008).
7. Gupta, N. & Linschitz, H. Hydrogen-bonding and protonation effects in electrochemistry of quinones in aprotic solvents. *J. Am. Chem. Soc.* **119**, 6384–6391 (1997).
8. Tonholo, J. *et al.* Electrochemical properties of biologically active heterocyclic naphthoquinones. *J. Braz. Chem. Soc.* **9**, 163–169 (1998).
9. Macías-Ruvalcaba, N. a., González, I. & Aguilar-Martínez, M. Evolution from Hydrogen Bond to Proton Transfer Pathways in the Electroreduction of α -NH-Quinones in Acetonitrile. *J. Electrochem. Soc.* **151**, E110 (2004).
10. Alligrant, T. M. & Alvarez, J. C. The Role of Intermolecular Hydrogen Bonding and Proton Transfer in Proton-Coupled Electron Transfer. *J. Phys. Chem. C* **115**, 10797–10805 (2011).
11. Alligrant, T. M., Hackett, J. C. & Alvarez, J. C. Acid/base and hydrogen bonding effects on the proton-coupled electron transfer of quinones and hydroquinones in acetonitrile: Mechanistic investigation by voltammetry, ¹H NMR and computation. *Electrochim. Acta* **55**, 6507–6516 (2010).
12. Nikitina, V. a., Nazmutdinov, R. R. & Tsirlina, G. a. Quinones electrochemistry in room-temperature ionic liquids. *J. Phys. Chem. B* **115**, 668–677 (2011).
13. Guin, P. S., Das, S. & Mandal, P. C. Electrochemical reduction of sodium 1,4-dihydroxy-9,10- anthraquinone-2-sulphonate in aqueous and aqueous dimethyl formamide mixed solvent: A cyclic voltammetric study. *Int. J. Electrochem. Sci.* **3**, 1016–1028 (2008).

14. Electroanal, J., Russel, C. & Jaenicke, W. Heterogeneous electron exchange of quinones in aprotic solvents, part III. *Electroanalysis* **199**, 139–151 (1986).
15. Bao, D. *et al.* Electrochemical reduction of quinones: Interfacing experiment and theory for defining effective radii of redox moieties. *J. Phys. Chem. B* **114**, 14467–14479 (2010).
16. Seto, K., Nakayama, T. & Uno, B. Formal redox potentials of organic molecules in ionic liquids on the basis of quaternary nitrogen cations as adiabatic electron affinities. *J. Phys. Chem. B* **117**, 10834–10845 (2013).
17. T.Fujinaga, K.Izutsu, T. N. Effect of metal ions on the polarographic reduction of organic compounds in dipolar aprotic solvents. *Electroanal. Chem. INTERFACIAL Electrochem. Elsevier Sequoia S.A., Lausann* **29**, 203–209 (1971).
18. Choi, D. *et al.* Electrochemical recognition of ammonium and alkali metal cations with calix[4]arenequinone. *J. Electroanal. Chem.* **387**, 133–134 (1995).
19. Cheng, W. X. *et al.* Investigation on the π -dimer/ σ -dimer of 1,8-dihydroxy-9,10- anthracenedione in the process of electrochemical reduction by using IR spectroelectrochemical cyclic voltabsorptometry and derivative cyclic voltabsorptometry. *J. Phys. Chem. C* **117**, 3940–3948 (2013).
20. Li, D., Cheng, L. & Jin, B. Investigation on PCET-accompanied Dimerization of 5-hydroxy-1, 4-naphthoquinone in the Process of Electrochemical Reduction by in Situ FT-IR Spectroelectrochemistry and Density Functional Calculation. *Electrochim. Acta* **130**, 387–396 (2014).
21. Macías-Ruvalcaba, N. A. & Evans, D. H. Association reactions of the anion radicals of some hydroxyquinones: Evidence for formation of π - And σ -dimers as well as a neutral-anion radical complex. *J. Phys. Chem. C* **114**, 1285–1292 (2010).
22. Rieke, R. D., Saji, T. & Kujundzic, N. Vo Itammetric measurements Electrochemical synthesis of diduroquinone. **102**, 397–405 (1979).
23. Algharaibeh, Z. & Pickup, P. G. Charge trapping in poly(1-amino-anthraquinone) films. *Electrochim. Acta* **93**, 87–92 (2013).
24. Balasubramaniam, E. *et al.* Electrochemical Preparation of Anthraquinone and Zinc Porphyrin Coated Electrodes - Redox Activity and Film Stability. *J. Mater. Chem.* **5**, 625–629 (1995).
25. Yamamoto, T. & Etori, H. Poly(anthraquinone)s Having a π -Conjugation System along the Main Chain. Synthesis by Organometallic Polycondensation, Redox Behavior, and Optical Properties. *Macromolecules* **28**, 3371–3379 (1995).
26. Suematsu, S. & Naoi, K. Quinone-introduced oligomeric supramolecule for supercapacitor. *J. Power Sources* **97-98**, 816–818 (2001).
27. Naoi, K., Suematsu, S., Hanada, M. & Hideaki, T. Enhanced Cyclability of π - π Stacked Supramolecular (1,5-Diaminoanthraquinone) Oligomer as an

- Electrochemical Capacitor Material. *J. Electrochem. Soc.* **149**, A472 (2002).
28. Naoi, K., Suematsu, S. & Manago, A. Electrochemistry of poly(1,5-diaminoanthraquinone) and its application in electrochemical capacitor materials. *J. Electrochem. Soc.* **147**, 420–426 (2000).
 29. Gao, M., Yang, F., Zhang, G., Liu, L. & Wang, X. Effects of poly-1,5-diaminoanthraquinone morphology on oxygen reduction in acidic solution. *Electrochim. Acta* **54**, 2224–2228 (2009).
 30. Dongmo, S., Witt, J. & Wittstock, G. Electropolymerization of quinone-polymers onto grafted quinone monolayers: A route towards non-passivating, catalytically active film. *Electrochim. Acta* **155**, 474–482 (2015).
 31. Newton, L. a. a., Cowham, E., Sharp, D., Leslie, R. & Davis, J. Plumbagin: a natural product for smart materials? *New J. Chem.* **34**, 395 (2010).
 32. Ardakani, M. M., Karami, P. E., Zare, H. R. & Hamzehloo, M. Electrocatalytic reduction of oxygen on the surface of glassy carbon electrodes modified with plumbagin. *Microchim. Acta* **159**, 165–173 (2007).

CHAPTER 5

***Hybrid Nanofluids Made
of Reduced Graphene
Oxide and
Polyoxometalates***

5.1 Context

Previous work in our group proved the feasibility of using reduced graphene oxide (rGO) dispersed in acidic electrolytes as electroactive nanofluids. Indeed, these rGO dispersions act as supercapacitors, showing an ultrafast response (being able to show a capacitive response in Cyclic Voltammograms recorded at very fast rates, up to $10 \text{ V}\cdot\text{s}^{-1}$). These rGO nanofluids also showed specific capacitance per gram of active material ($169 \text{ F}\cdot\text{g}^{-1}$) comparable with the corresponding electrodes in solid devices even at very small mass loads (0.025 wt%) which means and stunning electrical percolation capability of the dispersed rGO, which indeed is acting as an electrode in whole volume of the electroactive nanofluids.

In this work we explore the performance as nanofluids of hybrid materials formed by polyoxometalates adsorbed onto rGO (rGO-POMs), and dispersed in the same acidic electrolyte and conditions used with rGO dispersions. The redox activity of POMs turns these materials into hybrids with the possibility of combined faradaic and capacitive energy storage. These hybrid materials had been studied previously as solid electrodes in our group but these were the first studies exploring the feasibility of their use in the form of nanofluids.

5.2 Introduction

The field of hybrid materials is a field with many trees.¹⁻³ In just a few decades it has evolved into a lush and fertile landscape with a large variety of endemic species as well as new blossoming ones. Describing this evolution with agricultural metaphors is most fitting in a field that made words like *hybrid* or *grafting* part of its own identity. And along this line it is most appropriate to highlight the seminal work seeded by prof. Ruiz-Hitzky and his group.

Indeed, three decades ago Ruiz-Hitzky's group was already publishing inspiring communications in high-impact journals⁴⁻⁹[1-5] reporting how to graft organic branches into inorganic phases^{4, 10} or the possibility to use the hybrid approach to develop improved ionic conductors.^{9, 11} Our group was not working on solid electrolytes but on electrode materials at the time. And the group's approach was not to work with covalent but with ionic bonding in hybrids. But those works were inspiring and inviting and conveyed the full strength of the hybrid approach: wise design of complex materials integrating organics and inorganics at the molecular level in order to get the best of both worlds, leading even to synergy^{12, 13}.

Nowadays the hybrid concept impregnates all areas subareas and little corners of materials science¹⁴⁻²⁰. Our own crop of hybrid materials, developed with energy storage applications in mind, grew on different grounds from Ruiz-Hitzky's and other pioneers^{8, 14-20}. Our group explored several varieties of hybrids for energy storage, mainly those dispersing organic into inorganic components (i.e. Conducting Organic Polymers into transition metal oxides)^{21, 22} and vice versa, those integrating smaller inorganic components into organic matrices. Among the latter we have tried nanoparticles and nanostructures,²³ smaller polyoxometalates²⁴⁻²⁷ and molecular species²⁸⁻³⁰ into conducting but also non-conducting organic polymers³¹ as well as onto carbons³²⁻³⁶. These materials were used in symmetric³²⁻³⁵ and asymmetric³⁶ supercapacitors with enhanced energy density.

The present work presents a new way to deliver nanostructured hybrid materials for energy storage, namely, in the form of nanofluids.

Nanofluids are homogeneous dispersions of nanoparticles in conventional base fluids which constitute an emerging type of unique liquid materials within the field of Nanoscience and Nanotechnology. Several applications of nanofluids have been explored with very special prominence on magnetic (ferrofluids) or thermal properties for heat-transfer applications³⁷. However, they have never been proposed as possible

electroactive materials. A few recent investigations have suggested the use of thick slurries as electrodes for energy storage in flow cells. For instance, Gogotsi et al.³⁸ reported an electrochemical flow capacitor (EFC) using a flowable carbon slurry improving upon the concept introduced by Kastening et al³⁹. Very recently we have also reported graphene nanofluids featuring ultrafast charge transfer⁴⁰. Yet, all of these recent reports were on flowing materials with a purely capacitive storage mechanism

We present here the first examples of the use of hybrid electroactive nanofluids (HENFs) with the potential to be used as liquid electrode in flow electrochemical cells by combining redox as well as capacitive double-layer mechanisms.

5.3 Experimental Section

We used $\text{H}_3\text{PMo}_{12}\text{O}_{40}$ ($\geq 99.9\%$) and $\text{H}_3\text{PW}_{12}\text{O}_{40}$ ($\geq 99.9\%$) electroactive clusters from Sigma Aldrich.

Graphene oxide (GO) was synthesized from graphite using a modified Hummers method. Briefly, 5 g NaNO_3 and 225 ml H_2SO_4 were added to 5 g graphite and stirred for 30 min in an ice bath. 25 g KMnO_4 was added to the resulting solution, and then the solution was stirred at 50 °C for 2 h. 500 ml deionized water and 30 ml H_2O_2 (35%) were then slowly added to the solution, and the solution was washed with dilute HCl. Next, the GO product was washed again with 500 ml concentrated HCl (37%). The reduced graphene oxide (rGO) was prepared by high temperature treatment of the GO sample at 800 °C.

We first prepared solid nanocomposite hybrid materials based on redox-active polyoxometalates (POMs) supported on reduced Graphene Oxide nanosheets (rGO), the latter providing a double-layer capacitive storage mechanism. In particular, we used phosphomolybdic acid ($\text{H}_3\text{PMo}_{12}\text{O}_{40}$) and phosphotungstic acid ($\text{H}_3\text{PW}_{12}\text{O}_{40}$) electroactive clusters.

In order to prepare the corresponding HENFs, rGO-POMs hybrid materials were dispersed in different proportions in aqueous electrolyte (1 M H_2SO_4) to be directly used as liquid electrodes for charge storage in flow cells. Interestingly, this type of hybrid nanofluids combines the faradaic storage capabilities of redox POMs clusters with the high power provided by the electric double layer (EDL) mechanism of rGO. The HENFs reported here were able to store electricity through both mechanisms, as the parent solid-

electrode supercapacitors, except that in the present case the electrode is a liquid, stored externally and flowing through a flow electrochemical cell.

5.4 Results and Discussion

In order to confirm the effective anchoring of POMs on the surface of 3D open porous rGO nanosheets, multiple morphological characterizations were carried out. Figure 1 (a, b) presents SEM images of rGO-PMo₁₂ and rGO-PW₁₂ hybrid materials with the corresponding elements mapping and EDAX spectra. It is interesting to note that, rGO preserves its 3D open porous structure even after heavy deposition of PW₁₂ and PMo₁₂ clusters, which is highly beneficial to enhance the electron transport while keeping good ionic conductivity within each solid particle. EDS mapping and elemental analyses of rGO-POM hybrid samples evidently confirm the homogeneous and efficient anchoring of PW₁₂ and PMo₁₂ clusters onto the rGO nanosheets. Figure 2 (a-c) shows STEM images of rGO, rGO-PW₁₂ and rGO-PMo₁₂ samples, respectively. It is clearly seen that the surface of rGO nanosheets is blank and free from tiny spots (Figure 2 a) while in great contrast the surface of rGO-POMs hybrids is abundantly decorated with nanometer-sized PW₁₂ and PMo₁₂ dots (Figure 2 b-c) (see also EDS mapping with STEM in Figure 4). It is also interesting to note that the POM clusters are evenly distributed at a strictly molecular level without any agglomeration.

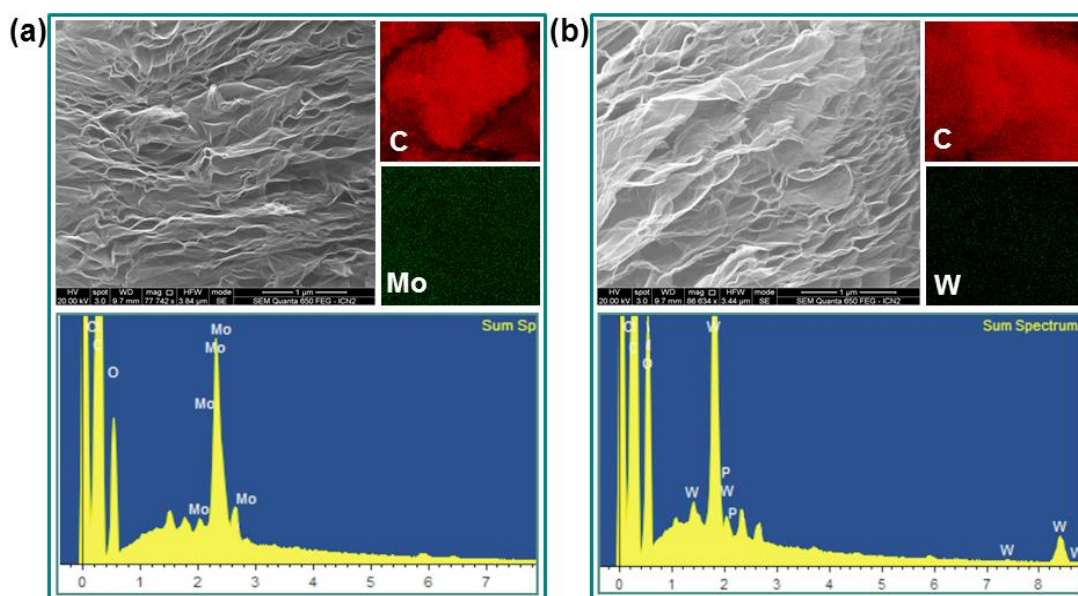


Fig.1 SEM images of (a) rGO-PW₁₂ and (b) rGO-PMo₁₂ hybrid materials with corresponding mapping images and EDX elemental spectrum which suggests mooring ofPOM clusters to rGO nanosheets showing characteristic molybdenum and tungsten peaks in the spectrum.

It is very important to note the utterly dispersed nature of the electroactive centers in this hybrid material. These POM clusters have a stable structure and size (1nm diameter), with all twelve W or Mo moieties on the surface of the cluster (there is no “bulk”). Therefore, the present hybrid configuration is ideal for fast (diffusion-free) faradaic processes added to the inherently fast capacitive polarization of graphene. Furthermore, it should be noted that rGO-PW₁₂ and rGO-PMo₁₂ exhibit high surface areas of 237 m²/g and 231 m²/g, respectively (Figure 3). The slight decrease in the active surface for rGO-PW₁₂ is attributed to the inclusion of the PW₁₂ nanoparticles, which contribute heavily to the total mass of the hybrid. Even with this slight decrease the specific BET surface area of rGO-PW₁₂ is considerably larger than many recently reported carbon/metal oxide hybrid materials⁴¹⁻⁴².

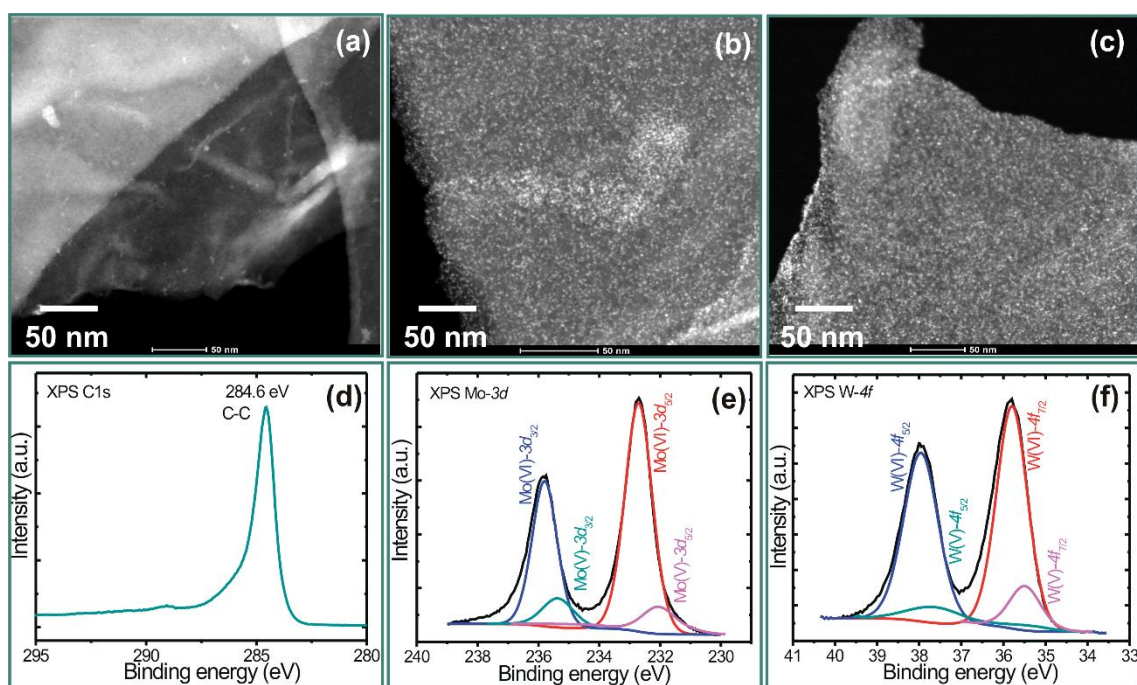


Fig.2 (a–c) Scanning transmission electron micrographs (STEM) of rGO, rGO-PW₁₂, rGO-PMo₁₂ hybrid, respectively (d–f) core-level C1s, Mo3d and W4f spectra of rGO-PMo₁₂ and rGO-PW₁₂ material.

Figure 2d-f shows core level XPS spectra of C1s, Mo3d and W4f, respectively. The detection of Mo3d peaks at 232.3 eV (Mo3d_{3/2}) and 235.4 eV (Mo3d_{5/2}) unambiguously confirms the presence of PMo₁₂ in rGO-PMo₁₂ hybrid with a predominance of Mo(VI) oxidation state Figure 2e^{43, 44} while core-level W4f spectrum shows two peaks at 37.54 eV (W4f_{5/2}) and 35.4 eV (W4f_{7/2}) with spin-orbit splitting of 2.14 eV (with a peak ratio 4:3). The position and shape of these peaks are representative of W atoms with an oxidation state of W(VI) further confirming the presence of PW₁₂ in rGO-PW₁₂ hybrid (Figure 2f)^{45, 46}.

Desing of novel electroactive nanofluids for flow cell

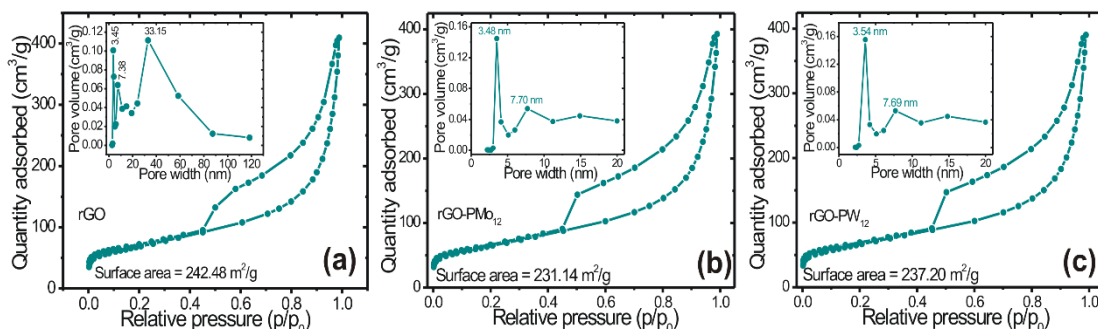


Fig.3 (a-c) Nitrogen adsorption-desorption curves and the corresponding pore size distribution plots for rGO, rGO-PMo₁₂ and rGO-PW₁₂ samples, respectively. The shape of the hysteresis loop is characteristic of mesoporous materials. BET analyses of these data showed that all the samples exhibit high surface areas of 242.48 m²/g, 231.14 m²/g and 237.20 m²/g. The slight decrease in the active surface for rGO-POMs sample is attributed to the inclusion of the POM nanoparticles, which contribute heavily to the total mass of the hybrid.

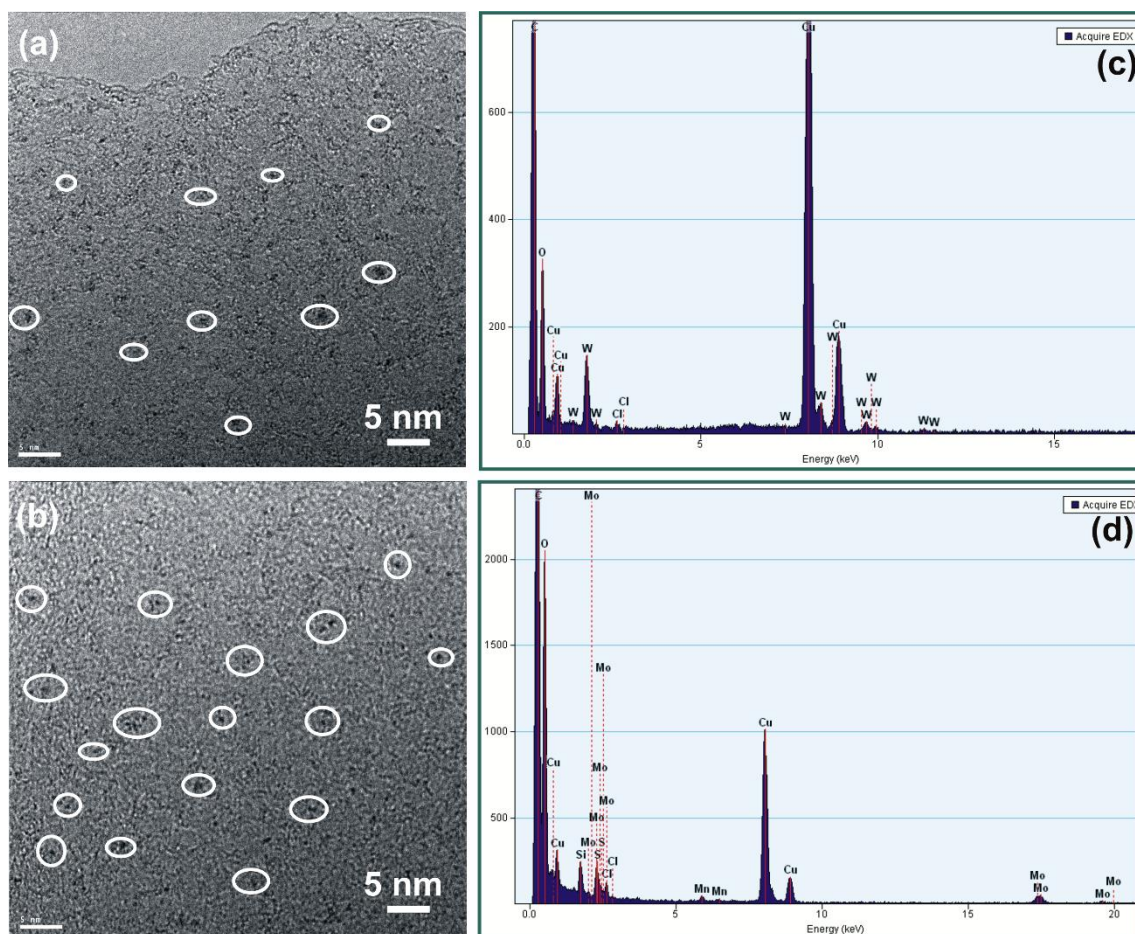


Fig.4 (a, b) shows HRTEM images of rGO-PW₁₂ and rGO-PMo₁₂ hybrid, respectively. As seen in Figure, few parts are highlighted with circles to realize the presence of PW₁₂ and PMo₁₂ clusters however that is not only the part covered by POMs. (c, d) EDS spectra of rGO-PW₁₂ and rGO-PMo₁₂ hybrid materials. EDX analysis explicitly confirmed the mooring of PW₁₂ and PMo₁₂ clusters to rGO nanosheets showing characteristic tungsten and molybdenum peaks in the spectrum.

Desing of novel electroactive nanofluids for flow cell

The electrochemical characterization of rGO-POMs HENFs was carried out both under static and continuous flow conditions using a specially designed flow cell (Figure 5a-b). Hybrid Electroactive Nanofluids (HENFs) of rGO-POMs were prepared by direct mixing of different proportions of rGO-POMs (rGO-PMo₁₂ or rGO-PW₁₂) (0.025 %, 0.1 % and 0.4 %) in 1 M H₂SO₄ aqueous solution (where, H₂SO₄ acts as an electrolyte). These dispersions of rGO-POMs HENFs were directly used as liquid electrodes in electrochemical flow cells (see Figure 5c).

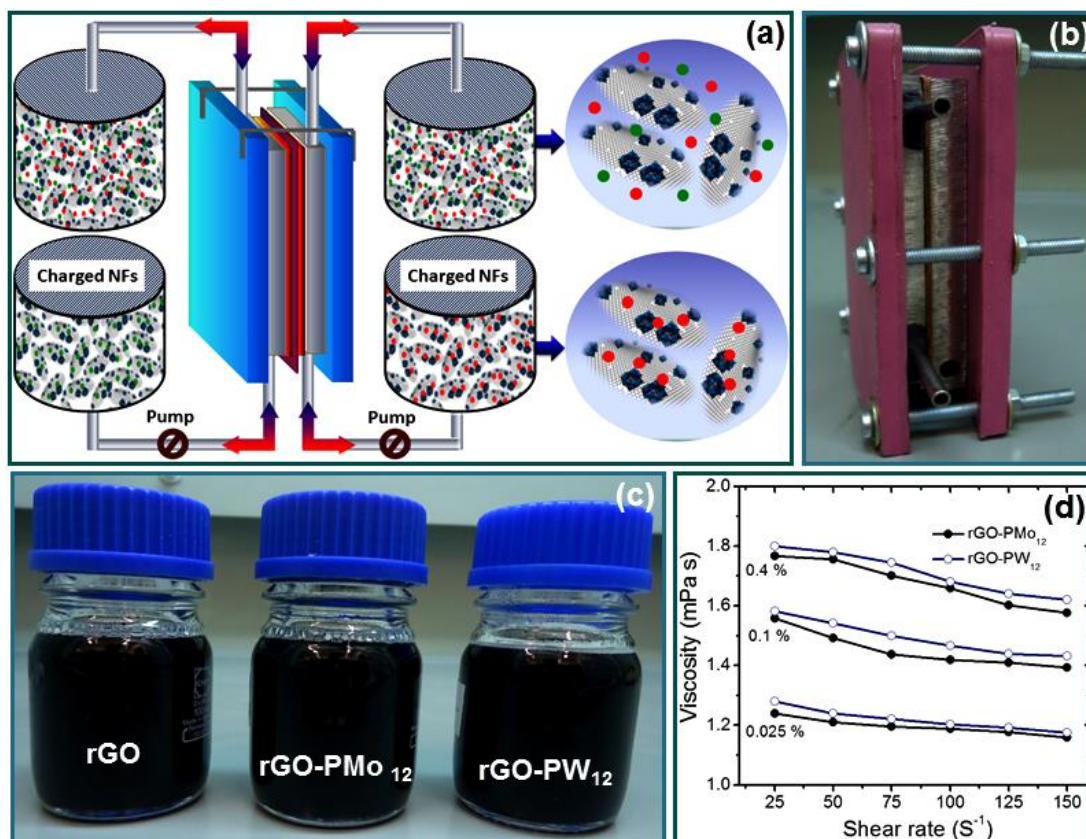


Fig.5 (a) Schematic diagram of the flow cell setup used in this work in which charged and discharged nanofluids are stored in separate containers. Two peristaltic pumps with automatic control of flow direction and flow rate were used, (b) Digital photograph of our home-made flow cell which consists of stainless-steel current collectors (7 cm x 6cm x 1 cm) with a carved serpentine, polyvinylidene fluoride (PVDF) membrane as a separator and oil paper as a gasket enclosed together using hard plastic plates and screws, (c) Actual photographs of rGO, rGO-PMo₁₂ and rGO-PW₁₂ HENFs (0.025% in 1 M H₂SO₄ aqueous solution) showing stable and uniform sols, (d) The viscosity of rGO, rGO-PMo₁₂ and rGO-PW₁₂ HENFs of different concentrations with shear rate *Electrochemical performance of rGO-POMs Hybrid Electroactive Nanofluids (HENFs).*

The rheological properties of rGO-POMs HENFs were measured under variable shear rates ranging from 25/s to 150/s. In the present study, the base fluid composed of water with surfactant (0.5 % triton X-100) and electrolyte (1 M H₂SO₄) showed Newtonian behavior with a viscosity of approximately 1 mPa s, in the shear rate range of 25-150 /s at room temperature (25°C), essentially identical to the theoretical value of water (1 mPa s)⁴⁷. The viscosities of rGO-POMs HENFs of different concentrations with shear rate

were determined and are plotted in Figure 5d. There are two kinds of viscosity variations for rGO-POMs HENFs are observed with increase in shear rate: Newtonian and shear-thinning behaviors. As seen in Figure 5d, the viscosity of rGO-POMs HENFs decreases slightly with shear rate, showing the shear-thinning behavior. It is further seen that with an increase in the concentration of solid nanoparticles the viscosities of the rGO-POMs HENFs increase but are in all cases between 1.2 to 1.8 mPa s, very close to that of water (1 mPa s)⁴⁸. These low values are far better than those for carbon-slurry based electrodes (ca. 2000 mPa s)^{38, 49}. These results undoubtedly ascertain the suitability of rGO-POMs HENFs to be used as liquid electrodes in electrochemical flow cells without any flowing or clogging problems.

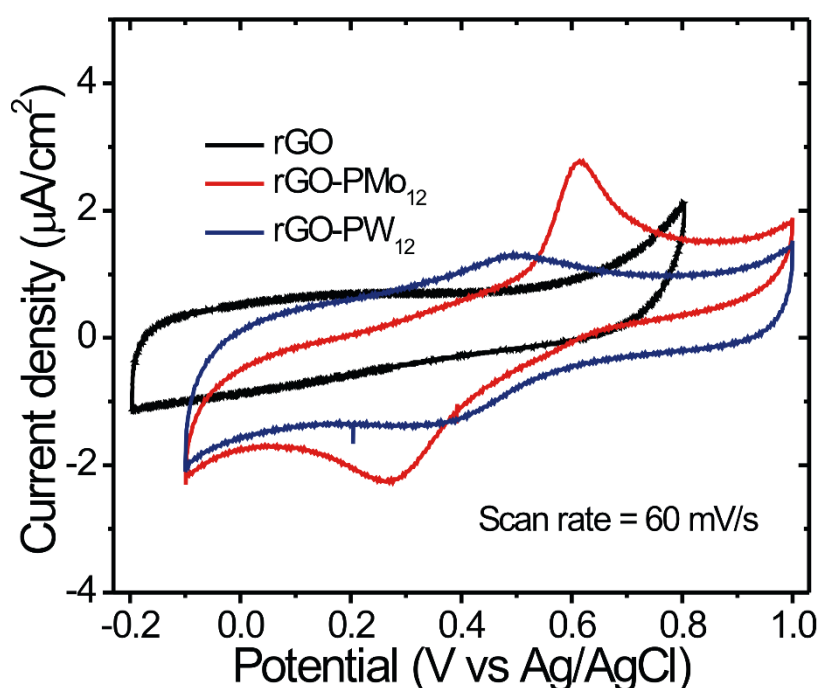


Fig.6 CV curves of rGO and rGO-POMs HENFs at 60 mV/s scan rate with conventional three electrode set-up comprising glassy carbon, platinum wire and Ag/AgCl as working, counter and reference electrodes, respectively.

Before exploring their final application in flow cells, we tested the electrochemical properties of rGO and rGO-POMs HENFs in conventional three-electrode cells comprising glassy carbon, platinum wire and Ag/AgCl as working, counter and reference electrodes, respectively. Figure 6 shows CV curves of rGO and rGO-POMs HENFs at 60 mV/s scan rate. The CV curve for rGO nanofluid exhibits a featureless rectangular shape characteristic of double layer capacitive mechanism whereas CV curves for rGO-POMs hybrid nanofluids show quasi-rectangular capacitive behavior but with well-defined redox peaks on top, confirming both EDL and faradaic charge storing mechanism. This test definitely confirmed our successful preparation of hybrid

electroactive nanofluids. CV curves for rGO and rGO-POMs HENFs at different scan rates are shown in Figure 7.

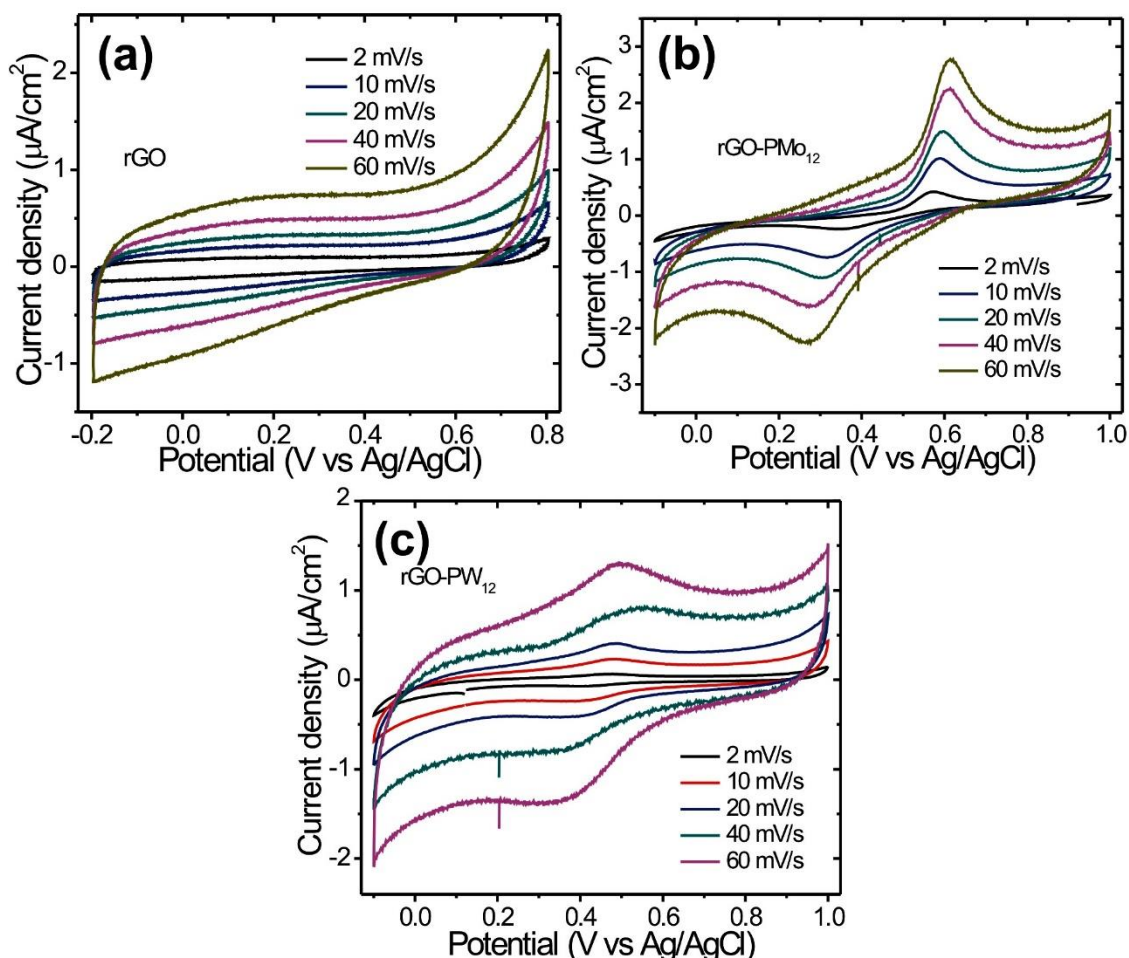


Fig.7 (a-c) CV curves of rGO, rGO-PMo₁₂ and rGO-PW₁₂ hybrid electroactive nanofluids with conventional three electrode set-up comprising glassy carbon, platinum wire and Ag/AgCl as working, counter and reference electrodes, respectively at different scanning rates.

In order to demonstrate the practical application of these rGO-POMs HENFs, their electrochemical performance was tested in flow cells under static and flowing conditions using the cell described above. Figure 8a-b shows the Cyclic polarization curves of symmetric rGO-PW₁₂ and rGO-PMo₁₂ HENFs cells at different scanning rates under static conditions. It is worth noting that, the shape of CV curves for rGO-POMs HENFs is different than that for rGO nanofluid with extensive improved current densities (Figure 9). Furthermore, CV curves up to very high scan rate of 5 V/s (5000 mV/s) for rGO-POMs HENFs were recorded (Figure 10). Most remarkably, the rectangular CV shape was maintained even at a very high scan rate of 5000 mV/s, indicating rGO-POMs HENFs exhibit excellent rate capabilities as needed for high-power supercapacitors. This is an extremely fast scan rate, much greater than values reported to have been used in CV measurements of any capacitive flow cell⁵⁰. It should be noted that the shape of CV

Desing of novel electroactive nanofluids for flow cell

curves becomes more and more rectangular with increase in scan rate. This indicates an increasingly important relative contribution of capacitive (Double Layer) energy storage vs. pseudocapacitive (faradaic) energy storage at high rates. Again, this could be expected for any conventional solid carbon based hybrid electrode, given the slower rates of redox reactions and electron transfer processes when compared with electrophysical double layer polarization.

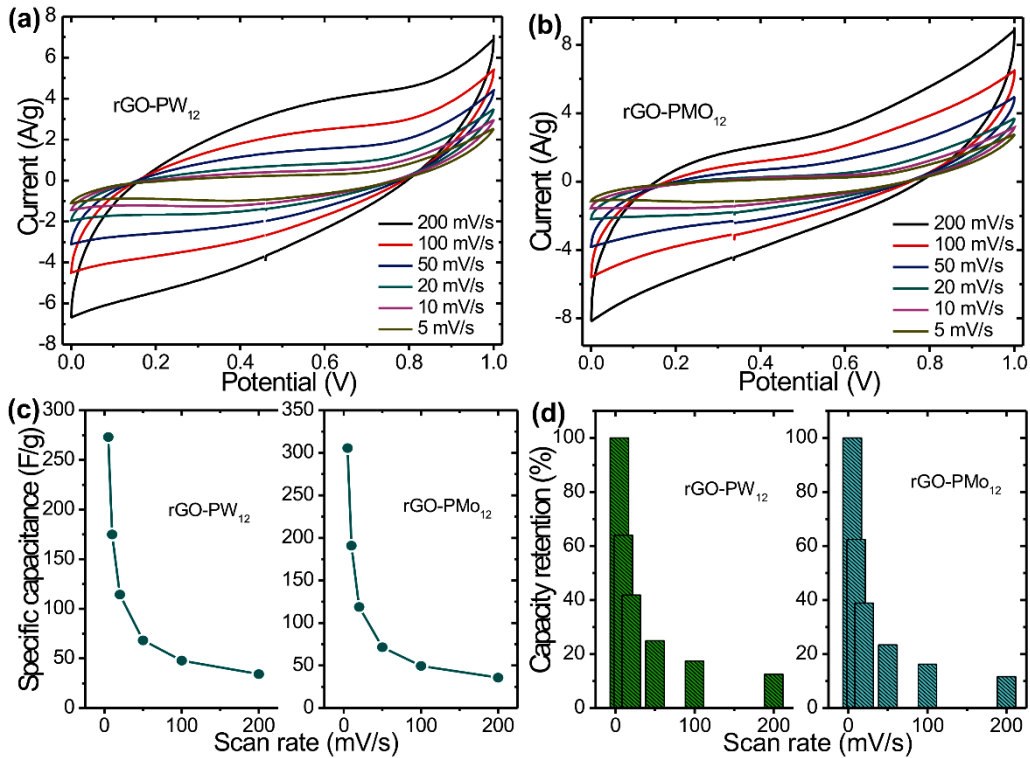


Fig.8 (a–b) CV curves of rGO-PW₁₂ and rGO-PMO₁₂ HENFs of 0.025% concentration at different scanning rates, respectively (c) Variation of specific capacitance with scan rates for rGO-POMs HENFs, (d) Plot of capacity retention with scan rate for rGO-POMs HENFs.

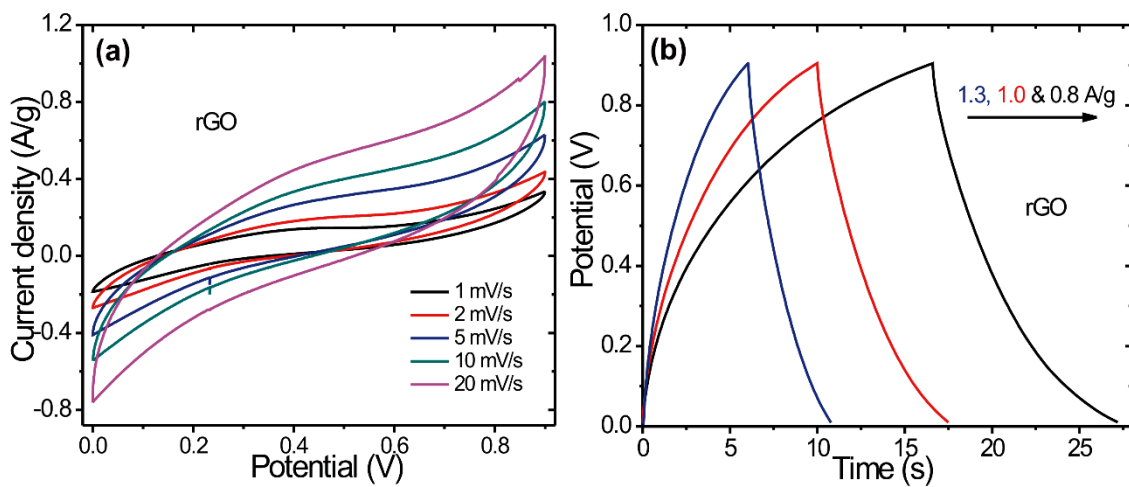


Fig.9 (a–b) Cyclic voltammetry and galvanostatic charge discharge curves of rGO nanofluids at different scanning rates and different current densities, respectively.

Desing of novel electroactive nanofluids for flow cell

The specific capacitances of the cell for rGO-POMs HENFs were calculated from the CV curves for 0.025 % concentration at different scanning rates.

From cyclic voltammetry, the capacitance was calculated using the following equation:

$$C_{sp} = \frac{2 \int idV}{v \cdot m \cdot \Delta E} \quad (1)$$

where ΔE is the voltage window, i the discharge current, V the voltage, v scan rate, and m the mass of rGO in one electrode. The factor of 2 accounts for the two electrode setup, where the charge is evenly distributed between two capacitors in series. Note that the specific capacitances were normalized by the mass of rGO in one electrode (not the total weight of nanofluids).

The specific capacitance C_{sp} was calculated from galvanostatic cycling using this equation:

$$C_{sp} = \frac{2i}{m \cdot \left(\frac{dV}{dt} \right)} \quad (2)$$

where dV/dt is the slope of the discharge curve.

Initially, the cell was discharged for 15 min (at 0 V) then the cell was charged to certain cell potential for 5 min and then discharged to 0 V for 5 min. Integration of the discharge curve directly yielded the charge of the two-electrode setup. The capacitance was extracted from the discharge curves of chronoamperometry experiments using the following equation:

$$C_{sp} = \frac{2 \int idt}{m \cdot \Delta E} \quad (3)$$

The coulombic efficiency was determined according to the following equation and corrected for leakage current:

$$\varepsilon_C = \left| \frac{\int I_{discharge} dt}{\int I_{charge} dt} \right| \cdot 100\% \quad (4)$$

Desing of novel electroactive nanofluids for flow cell

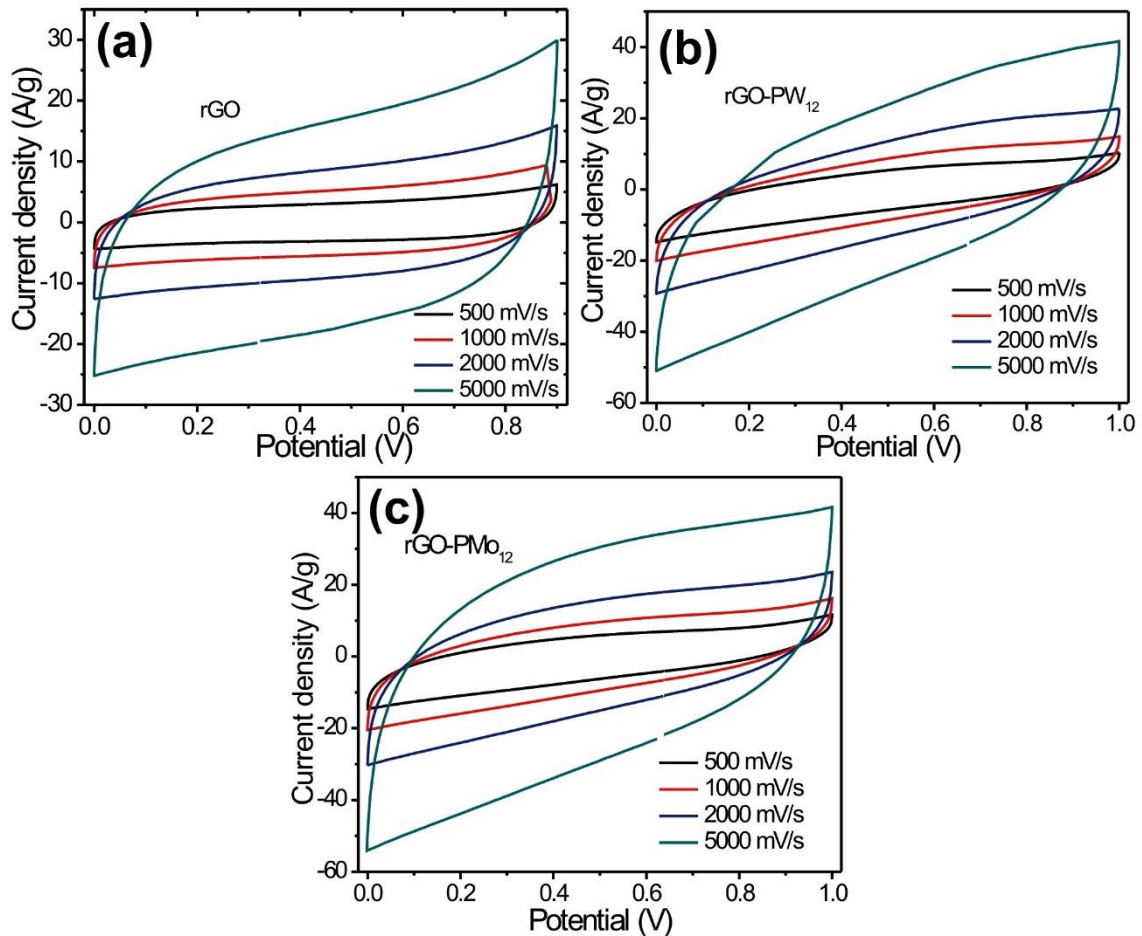


Fig. 10 (a-c) Cyclic voltammetry curves of rGO, rGO-PW₁₂ and rGO-PMo₁₂ hybrid electroactive nanofluids at very high scan rates, respectively.

As expected, specific capacitances decrease gradually with increasing scan rate (Figure 8c). Maximum specific capacitance values of 273 F/g(rGO-PW₁₂) and 306 F/g(rGO-PMo₁₂) were obtained for 0.025 % rGO-POM HENFs at a scan rate of 5 mV/s. Here again, in order to store that amount of charge on rGO-POMs HENFs within the flow cell, the rGO flakes must be electrically connected to the external load via a conductive pathway. Unlike conventional supercapacitors in which solid film electrodes benefit from well-defined fixed conduction paths, our cell utilizes a 'liquid electrode' in which charge must percolate through a dynamic network of conductive particles. Figure 8d shows the capacity retention with scan rate. It is observed that about 12-14 % of specific capacitance is retained for rGO-POMs HENFs as scan rate increases from 5 mV/s to 200 mV/s, suggesting good rate capability of the material in flow cell. The values of specific capacitances obtained in this work are very much comparable or even higher than the values reported for thicker carbon slurries as well as solid carbon-POM based electrodes. For instance, Presser et al.³⁸ prepared a thick carbon slurry of carbide-derived carbon powder obtained from titanium carbide (TiC: CDC) and 1 M Na₂SO₄ with

compositions of 3:1 and 4:1 (electrolyte: carbon by mass). The highest specific capacitance reported for toothpaste-like TiC:CDC slurry (3:1, electrolyte: carbon) was 109 F/g at the scan rate of 2 mV/s. Furthermore, Zhang et al.⁵⁰ reported a specific capacitance of 154 F/g at 2 mV/s in 1 M H₂SO₄ for a thick slurry of porous carbon spheres with concentration ranging from 16 wt% to 23 wt%. Moreover, our recent investigation on activated carbon-PMo₁₂ and activated carbon-PW₁₂ solid electrodes showed a specific capacitance of 183 F/g and 254 F/g respectively.^{32, 33}. And our recent reports on solid graphene-polyoxometalate electrodes³⁴⁻³⁶ also showed high specific capacitance and long cyclability. Our present study provides promising preliminary data supporting the use of this type of materials in a novel liquid electrode format, namely that of hybrid electroactive nanofluids (HENFs) and supports the potential of HENFs in general and of rGO-POMs HENFs in particular for energy storage applications.

The electrochemical performance of rGO-POMs HENFs was further studied by galvanostatic charge/discharge test in static conditions as shown in Figure 11a-b. The shapes of charge-discharge curves are not symmetrically triangular showing a great contribution from the redox species of POMs molecular clusters. The maximum values of specific capacitance obtained for the 0.025 % rGO-POMs HENFs were 207.7 F/g(rGO-PW₁₂) and 222.8 F/g(rGO-PMo₁₂) at current density of 4 A/g, respectively. This capacitance corresponds to specific energy values of 28.85 Wh/kg(rGO-PW₁₂) and 30.95 Wh/kg(rGO-PMo₁₂) and specific power of 2-8 kW/kg(rGO-POMs) as shown in Figure 11c. The values obtained for rGO-POMs HENFs are remarkably higher than those measured for rGO nanofluids (13.1 Wh/kg(rGO)) which can be due to the synergetic combination of rGO and POMs redox clusters. Moreover, the values of specific energy are significantly higher than those previously reported for slurries (for example, 5.6-8.2 Wh/kg for carbon beads slurry⁴⁹). Furthermore, the galvanostatic charge/discharge cycling performance was tested at different current densities for 2000 cycles. The rGO-POMs HENFs were found to be remarkably stable, with cycle efficiencies greater than about 94-95 % after 2000 charge/discharge cycles (Figure 11d). This confirms the stable attachment of the POMs redox clusters to the graphene sheets.

Desing of novel electroactive nanofluids for flow cell

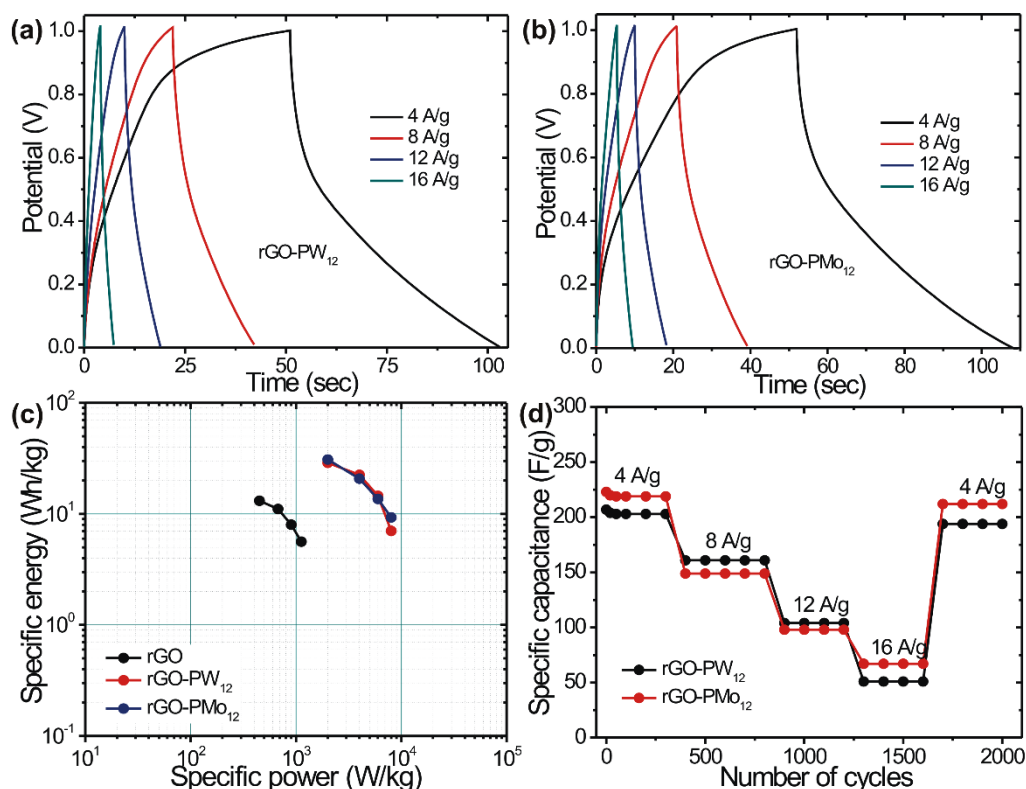


Fig. 11 (a–b) Galvanostatic charge-discharge curves for rGO-PW₁₂ and rGO-PMo₁₂ HENFs of 0.025% at different current densities in static condition, (b) Plot of specific energy versus specific power in Ragone plot for rGO, rGO-PW₁₂ and rGO-PMo₁₂ in flow cell (d) Galvanostatic charge/discharge cycling test for rGO-POMs HENFs of 0.025% at different current densities for 2000 cycles.

Figure 12a-b shows a series of chronoamperometry experiments carried out for rGO-PW₁₂ and rGO-PMo₁₂ HENFs under static conditions. Initially, the cell was completely discharged for a period of 15 min and then charged to different potentials such as 0.4, 0.6, 0.8 and 1.0 V. While charging was associated with additional leakage current, the integration of the discharge current versus time plot directly yields the charge for a given cell voltage (as plotted in Figure 12c). The flow cell capacitances were calculated by simply dividing by the cell voltage and are displayed in Figure 12d. When compensating for the leakage current, this translates into device capacitances of 0.70-0.72 F for rGO-POMs HENFs. Moreover, the coulombic efficiency of the rGO-POMs nanofluid cell was found to be 95.3 % (a large value since we did include the leakage current).

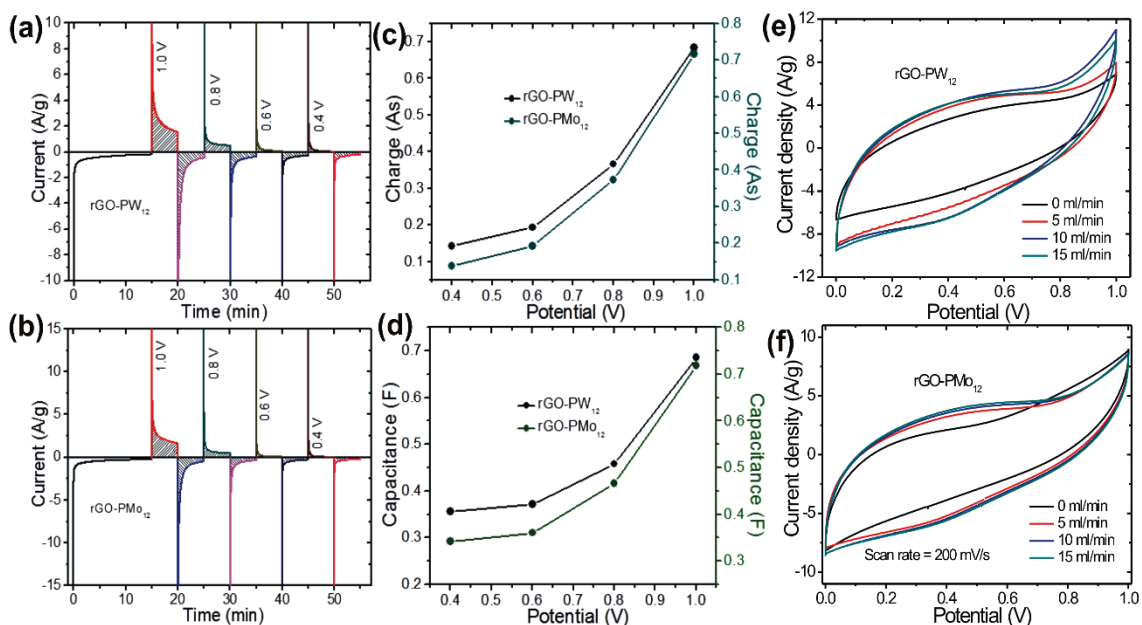


Fig. 12 (a–b) Chronoamperometry test for rGO-PW₁₂ and rGO-PMo₁₂ HENFs (0.025%) under static condition at different applied voltages such as 0.4, 0.6, 0.8 and 1.0 V which shows high coulombic efficiency of 95.3% when charged to a cell potential of 1.0 V and subsequently discharged to 0 V, (c) Plot of charge extracted by integrating discharge curves with given potential, (d) Plot of device capacitance versus given potential for rGO-PMOs HENFs in flow cell, (e–f) CV curves of rGO-PW₁₂ and rGO-PMo₁₂ for different flow rates at scan rate of 200 mV/s, respectively.

Energy storage of rGO-POMs HENFs under flowing condition

As a final test for the use of our nanofluids in flow cells, we tested the electrochemical properties of rGO-POMs HENFs under continuous flow conditions. Indeed, it is interesting to note that the shape of the CV curves slightly changes for the different flow rates used, which may be due to the migration of the redox electroactive clusters (see Figure 12 e-f). However, the current under the curve slightly increases with increase in flow rate from 0 to 10 ml/min but then remains constant for flow rates > 10 ml/min. This initial increase in current density may be attributed to the flow of fresh rGO-POMs nanoparticles taking part in charge storage. However, at high flow rates, and under the experimental conditions used, the residence time for rGO-POMs nanoparticles in the flow channels will eventually be insufficient for completing the expected redox reactions of all the dispersed material, consequently leading to the saturation in current density. In addition, CV curves of rGO-POMs at different flowing rates for different scan rates are presented (see Figure 13).

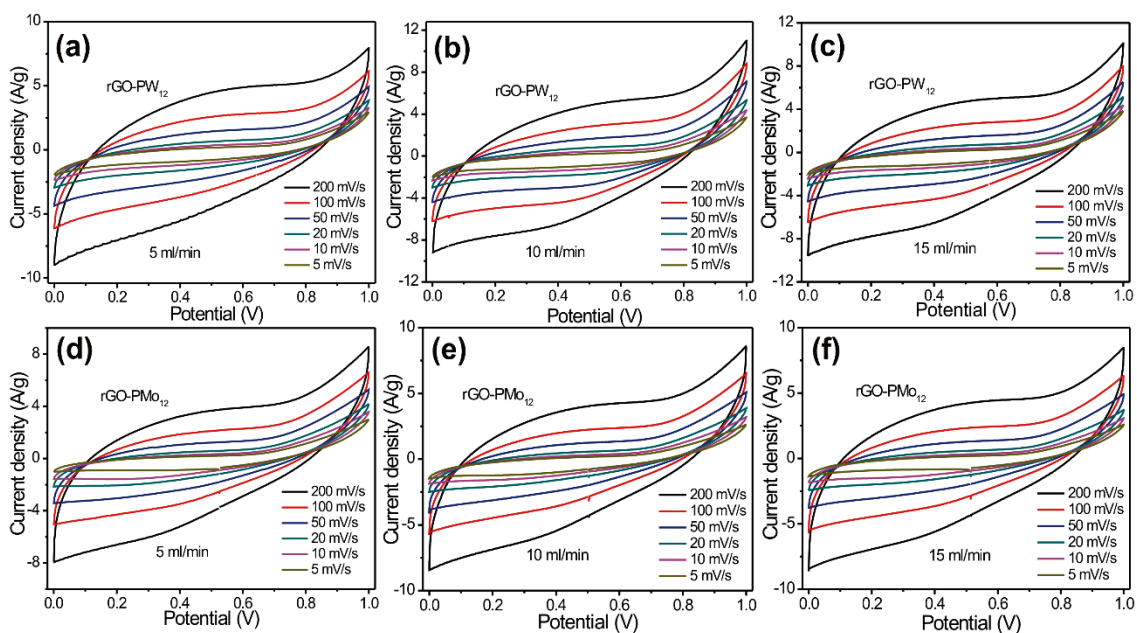


Fig. 13 CV curves for (a-c) rGO-PW₁₂ and (d-f) rGO-PMo₁₂ hybrid electroactive nanofluids (HENs) at different scan rates for different flow rates (5 ml/min, 10 ml/min and 15 ml/min), respectively.

5.5 Conclusions

Our present investigation has established the first successful example of the possible use of hybrid electroactive nanofluids for energy storage in electrochemical flow cells. In particular, our work provides proof of this breakthrough concept by demonstrating the use of hybrid rGO-POMs nanofluids for dual energy storage through a hybrid (faradaic-capacitive) mechanism parallel to hybrid solid electrodes⁵¹ but in this case, for the first time, in the form of a nanofluid.

The results certainly confirmed that these rGO-POMs HENFs electrodes exhibit excellent electrochemical performances, including high capacitance and energy density as well as high rate performance and long cycle life. Most strikingly, our study shows full electrochemical utilization of both components of the hybrid (rGO and POMs) in the bulk nanofluid, even at very fast rates, thus showing effective charge percolation in a material that behaves as a true liquid electrode. The studies described here have been performed with model low-concentration nanofluids and certainly more concentrated systems will be necessary. But our work provides data on the intrinsic potential of these rGO-POMs HENFs as truly flowing electrodes for Electrochemical Flow Cells. Further investigations are already in progress concerning both improved engineering design and improved active materials, a combination which should lead to efficient, low-cost and scalable flow cells based on Electroactive Nanofluids (ENFs).

References

1. P. Gomez-Romero, C. Sanchez, *Functional Hybrid Materials*. Editor, Wiley-VCH, **2004**.
2. G. Kickelbick, *Hybrid Materials: Synthesis, Characterization, and Applications*. Editor, Wiley-VCH, **2007**.
3. S. A. Kumar, *Eco-Friendly Nano-Hybrid Materials for Advanced Engineering Applications*. Editor, CRC Press, **2017**.
4. E. Ruizhitzky, J. M. Rojo, *Nature* **1980**, *287*, 28-30 10.1038/287028a0.
5. E. Ruizhitzky, P. Aranda, *Advanced Materials* **1990**, *2*, 545-547 10.1002/adma.19900021108.
6. J. M. Amarilla, B. Casal, J. C. Galvan, E. Ruizhitzky, *Chemistry of Materials* **1992**, *4*, 62-67 10.1021/cm00019a015.
7. P. Aranda, E. Ruizhitzky, *Chemistry of Materials* **1992**, *4*, 1395-1403 10.1021/cm00024a048.
8. E. Ruizhitzky, *Advanced Materials* **1993**, *5*, 334-340 10.1002/adma.19930050503.
9. E. Ruizhitzky, R. Jimenez, B. Casal, V. Manriquez, A. S. Ana, G. Gonzalez, *Advanced Materials* **1993**, *5*, 738-741 10.1002/adma.19930051011.
10. A. J. Aznar, J. Sanz, E. Ruizhitzky, *Colloid and Polymer Science* **1992**, *270*, 165-176 10.1007/bf00652183.
11. P. Aranda, J. C. Galvan, B. Casal, E. Ruizhitzky, *Electrochimica Acta* **1992**, *37*, 1573-1577 10.1016/0013-4686(92)80114-2.
12. P. Gomez-Romero, *Advanced Materials* **2001**, *13*, 163-174.
13. P. Gomez-Romero, C. Sanchez, *New Journal of Chemistry* **2005**, *29*, 57-58 10.1039/b416075b.
14. E. Ruiz-Hitzky, B. Casal, P. Aranda, J. C. Galvan, *Reviews in Inorganic Chemistry* **2001**, *21*, 125-159.
15. E. Ruiz-Hitzky, M. Darder, P. Aranda, K. Ariga, *Advanced Materials* **2010**, *22*, 323-336 10.1002/adma.200901134.
16. L. Rozes, C. Sanchez, *Chemical Society Reviews* **2011**, *40*, 1006-1030 10.1039/c0cs00137f.
17. E. Ruiz-Hitzky, P. Aranda, M. Darder, M. Ogawa, *Chemical Society Reviews* **2011**, *40*, 801-828 10.1039/c0cs00052c.

18. M. C. Orilall, U. Wiesner, *Chemical Society Reviews* **2011**, *40*, 520-535
10.1039/c0cs00034e.
19. C. Sanchez, P. Belleville, M. Popall, L. Nicole, *Chemical Society Reviews* **2011**, *40*, 696-753 10.1039/c0cs00136h.
20. K. Naoi, W. Naoi, S. Aoyagi, J. Miyamoto, T. Kamino, *Accounts of Chemical Research* **2013**, *46*, 1075-1083.
21. M. Lira-Cantu, P. Gomez-Romero, *Journal of Solid State Chemistry* **1999**, *147*, 601-608.
22. M. Lira-Cantu, P. Gomez-Romero, *Journal of the Electrochemical Society* **1999**, *146*, 2029-2033.
23. O. Ayyad, D. Munoz-Rojas, J. Oro-Sole, P. Gomez-Romero, *Journal of Nanoparticle Research* **2010**, *12*, 337-345 10.1007/s11051-009-9620-3.
24. P. Gomez-Romero, M. Lira-Cantu, *Advanced Materials* **1997**, *9*, 144-147.
25. M. Lira-Cantu, P. Gomez-Romero, *Chemistry of Materials* **1998**, *10*, 698-704.
26. P. Gomez-Romero, M. Chojak, K. Cuentas-Gallegos, J. A. Asensio, P. J. Kulesza, N. Casan-Pastor, M. Lira-Cantu, *Electrochemistry Communications* **2003**, *5*, 149-153 10.1016/s1388-2481(03)00010-9.
27. D. P. Dubal, B. Ballesteros, A. A. Mohite, P. Gomez-Romero, *Chemsuschem* **2017**, *10*, 731-737 10.1002/cssc.201601610.
28. P. Gomez-Romero, G. Torres-Gomez, *Advanced Materials* **2000**, *12*, 1454-1456.
29. G. Torres-Gomez, S. Skaarup, K. West, P. Gomez-Romero, *Journal of the Electrochemical Society* **2000**, *147*, 2513-2516.
30. G. Torres-Gomez, E. M. Tejada-Rosales, P. Gomez-Romero, *Chemistry of Materials* **2001**, *13*, 3693-3697.
31. P. Gomez-Romero, J. A. Asensio, S. Borros, *Electrochimica Acta* **2005**, *50*, 4715-4720 10.1016/j.electacta.2005.02.029.
32. V. Ruiz, J. Suarez-Guevara, P. Gomez-Romero, *Electrochemistry Communications* **2012**, *24*, 35-38 10.1016/j.elecom.2012.08.003.
33. J. Suarez-Guevara, V. Ruiz, P. Gomez-Romero, *Journal of Materials Chemistry A* **2014**, *2*, 1014-1021 10.1039/c3ta14455k.
34. J. Suarez-Guevara, V. Ruiz, P. Gomez-Romero, *Physical Chemistry Chemical Physics* **2014**, *16*, 20411-20414 10.1039/c4cp03321c.

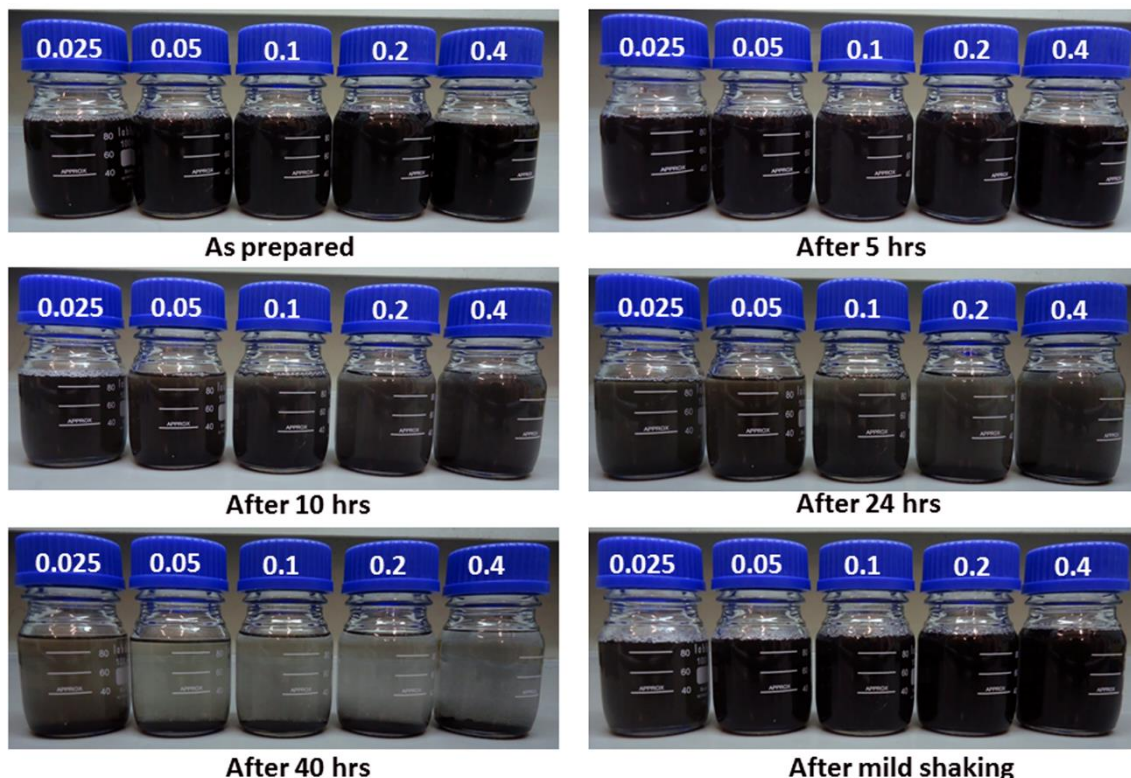
35. D. P. Dubal, J. Suarez-Guevara, D. Tonti, E. Enciso, P. Gomez-Romero, *Journal of Materials Chemistry A* **2015**, *3*, 23483-23492 10.1039/c5ta05660h.
36. D. P. Dubal, N. R. Chodankar, A. Vinu, D. H. Kim, P. Gomez-Romero, *Chemsuschem* **2017**, *10*, 2742-2750 10.1002/cssc.201700792.
37. Taylor, R. J. *J. Appl. Phys.* **113**, 011301 (2013).
38. Presser, V. *et al. Adv. Energy Mater.* **2**, 895-902 (2012).
39. Kastening, B. Boinowitz, T. Heins, M. J. *Appl. Electrochem.* **27**, 147-152 (1997).
40. Dubal, D. P. and Gomez-Romero, P. *2D-Materials*, **3**, 031004 (2016).
41. Ji, Y. Huang, L. Hu, J. Streb, C. Song, Y. F. *Energy Environ. Sci.*, **8**, 776-789 (2015)
42. Chen, H. Y. *et al. Nanoscale*, **7**, 7934-7941 (2015).
43. Ma, A. *et. al. J. Electrochem. Soc.*, **161**, F1224-F1230 (2014).
44. Bajwa, G., Genovese, M. Lian, K. Multilayer *ECS J. Sol. State Sci. Tech.*, **2**, M3046-M3050 (2013).
45. Barreca, D. *et al. Surf. Sci. Spectra*, **8**, 258 (2001).
46. Weinhardt, L. *et al.* Electronic surface level positions of WO₃ thin films for photoelectrochemical hydrogen production. *J. Phys. Chem. C*, **112**, 3078-3082 (2008).
47. Pastoriza-Gallego, M.J. Casanova, C. Legido, J. L. Pineiro, M. M. CuO in water nanofluid: Influence of particle size and polydispersity on volumetric behaviour and viscosity. *Fluid Phase Equilibr.* **300**, 188-196 (2011).
48. Hong, R.Y. Rheological properties of water-based Fe₃O₄ ferrofluids. *Chem. Eng. Sci.* **62**, 5912-5924 (2007).
49. Campos, J. W. *et al.* Investigation of carbon materials for use as a flowable electrode in electrochemical flow capacitors. *Electrochim. Acta* **98**, 123-130 (2013).
50. Zhang, C. *et al. Carbon*, **77**, 155-164 (2014).
51. Dubal, D. P. Ayyad, O. Ruiz, V. Gomez-Romero, P. *Chem. Soc. Rev.* **44**, 1777-1790 (2015).

CHAPTER 6

***From hybrid Nanofluid
to hybrid cells. The
rGO/DABA-LiFePO₄
system***

6.1 Context

The rGO-POM nanofluids described in the previous chapter showed great performance, however their stability left room for improvement. After 10h a clear change in the opacity due to the precipitation of rGO was observed, and after 40h almost all the rGO had been precipitated despite the use of surfactants. In order to improve the stability of the rGO dispersions we developed a new kind of nanofluid.



Using the π - π interaction between rGO and a solvated aromatic molecule we aimed at a definitive improvement of the stability of rGO in nanofluids without using surfactants, thus without an increase of the viscosity and most important, without affects to it electronic transference capability though the solution. For this propose we chose the 3,4 diaminobenzoic acid (DABA) as the aromatic solved molecule which will “hold” the rGO through the π - π interaction.

But in addition to new strategies to stabilize nanofluids, the work reported in this article was trying to answer the question of how to harness the electroactivity of a well-known conventional solid phase widely used in batteries when “transplanted” to a nanofluid. LiFePO_4 was selected as the model battery material and dispersed as nanosheets in a series of nanofluids with increasing complexity, but always based in the interaction with the dispersed rGO which allows the charge transference between the

LiFePO₄ nanosheets and the current collector due to the nanosheets have a poor diffusion capability because it large size in comparison with a molecule or ion.

Thus, the fundamental question was how to enable charge transfer in these nanomaterials and we could determine the role of rGO as enabler of this process. Another interesting technological derivation of the work could be the combination of a purely capacitive nanofluid electrode with a redox-active nanofluid in an unprecedented hybrid flow cell.

6.2 Introduction

Electrochemical Energy Storage is the midst of a regenerative resurgence. Batteries, Supercapacitors (SCs), Fuel Cells (FCs) or Redox Flow Batteries (RFBs) are markedly complementary technologies and are all called to play a role within the forthcoming sustainable energy model. From load-leveling devices to wearable electronics, to the development of smart grids to electric vehicles or to renewable energy storage. Exploring conceptual frontiers between batteries, supercapacitors, redox flow batteries (RFBs) and fuel cells (FCs) could provide new opportunities to get the best of each of those technologies.

Redox Flow Batteries (RFBs) for instance could indeed be considered as laying halfway between conventional solid-electrode batteries and FCs. Unlike traditional batteries, energy density and power density are effectively detached in RFBs. Energy is proportional to the size of the external reservoirs and power to the number of cells and area of the electrodes. This technology does not suffer memory effect and benefits from a long cycle life. These are important advantages related to the fact that active materials are ions solvated in the flowing electrolyte media. On the other hand, RFBs have drawbacks like low energy density and low specific energy due to the solubility limit of the active redox species.

Different types of mechanisms have been proposed for flow cells in water and in organic media, as discussed in a very recent review¹ All organic RFBs have been typically developed using benzoquinone and anthraquinone. Some works combining organic and inorganic solutions (for instance anthraquinone and ferricyanide as electrolytes) have been published in order to develop organic-inorganic redox flow cells. Also a combination of Li metal (deposited on the anode) and an organic molecule as

catholyte has been frequently used for organic – inorganic hybrid flow batteries in organic media.

In the same review¹ a full comparative discussion of the various types of flow cells is included. Concerning energy densities, flow batteries with organic molecules in aqueous media report values below 20 Wh·L⁻¹. For hybrid organic-inorganic redox flow batteries the energy densities increase but always to values below 40 to 50 Wh·L⁻¹ for aqueous and organic solvents respectively. The largest value of energy density reported so far (200 Wh·L⁻¹) corresponds to a flow cell combining metallic Li anode and a TEMPO catholyte. This device however presents serious stability problems and has only been subject to 20 cycles¹

Among well-established systems, All-Vanadium cells constitute the most developed type of RFBs and have an energy density of 40 Wh·L⁻¹ and a specific energy of 25 Wh·Kg⁻¹ and operate between 1.6V and 1.3V^{2, 3}. Those values are far away from current Li-Ion Batteries (LIBs), 150-200 Wh·Kg⁻¹ at 3.7V⁴. Aside from the higher voltage attained in organic LIBs, the primary reason why RFBs do not achieve the energy density values of LIBs is the low concentration of active material due to limited solubility^{5, 6}. Furthermore, the chemical stability of the active species is limited in some cases by the enhancement of spurious reactions at high concentrations^{5, 7}. Finally, there is one more factor that affects both the energy and power densities of many RFBs, namely, relatively low voltages due not only to thermodynamic but also to kinetic factors, such as the high internal resistance associated to electrolyte diffusion through selective membrane separators.

The recent proposal of Semisolid Flow Batteries (SFBs) tries to solve these drawbacks by using heterogeneous mixtures of electroactive species with surfactant and carbon particles. For example, Chiang and coworkers described a so-called semi-solid lithium flow battery⁸. And Gogotsi and coworkers described a similar system for a capacitive system⁹. A so-called *flowable* carbon-electrolyte mixture was used as the active material for capacitive energy storage and was handled in a similar way to flow or semi-solid batteries. In 2014, Nair and collaborators also reported a flow capacitor device based on a graphene dispersion in organic electrolyte, with improved energy density (14.3 W·h·L⁻¹) with respect to graphite (0.422 W·h·L⁻¹)¹⁰. 3D interconnected hybrid materials (RGO@CS) were used to prepare an EFC. When tested as *flowable* electrodes, the composition with a 1:2 ratio of GO to CS exhibited the highest capacitance of 200 F·g⁻¹ and an improved rate performance¹¹. In general, this approach

has been quite popular and highly concentrated semisolid catholytes based on LiCoO_2 , $\text{LiNi}_{0.5}\text{Mn}_{1.5}\text{O}_4$ and $\text{Li}_4\text{Ti}_5\text{O}_{12}$ suspensions, have been developed¹².

More recently, Tarascon et al. focused on the performance of a $\text{LiFePO}_4/\text{LiPF}_6$ EC-DMC/Li redox flowable half-cell¹³. As a result, power densities of $328 \text{ mW}\cdot\text{cm}^{-2}$ at $104 \text{ mA}\cdot\text{cm}^{-2}$ were achieved with specific energy of $50 \text{ Wh}\cdot\text{kg}^{-1}$. It is important to mention, however, the use of intermittent flow conditions with the values reported being measured under static conditions¹³.

A procedure described as “intermittent flow” was used that allowed the slurry to rest on the electrodes prior to and during measurements. Under those conditions the process of cycling of the active material could be closer to that of a solid battery electrode rather than to a flowing one.

Lu et al reported a silicon-carbon nanocomposite semi-solid anolyte, achieving a high reversible capacity ($>1200 \text{ mAh g}^{-1}$) and stable cycle life (>100 cycles), although the experiments were also made under interment flow conditions¹⁴.

SFBs usually need a significant amount of dispersed conducting particles such as carbon particles, which can transform the electrolyte solution into a slurry electrode that allows for electrical conduction by percolation in all the volume of the electrode⁹. On the other hand, these conducting particles often need a surfactant to generate a stable dispersion¹⁵. This large amount of carbon particles and the use of surfactant are responsible for a detrimental increase in the viscosity of semisolid electrodes. Finally, the nature of the carbon used is another crucial point since it determines the electrical conductivity and thus the effectiveness of the percolation effect^{16, 17}.

High viscosity is not compatible with flow cells, which need a pumping system to flow the solutions from the reservoirs to the electrochemical cell and vice versa, with a corresponding decrease in overall efficiency. Thus, a significant increase in viscosity of the fluids is highly undesirable, because the extra energy needed to circulate the pastes could cancel out the possible intrinsic advantages of the active materials, or at least reduce dramatically the overall efficiency of the system.

On the other hand, a different approach to the harnessing of electroactive solid particles in flow cells has been proposed by Grätzel and collaborators by introducing the concept of shuttle redox molecular solutions with suitable redox potentials, solubility, stability and kinetics to transfer the charge to solid particles stored in a separate reservoir¹⁸.

Other approach using nanofluids was proposed by Timofeeva and col. in 2015. They developed a scalable one-step surface modification procedure for functionalizing TiO₂ nanoparticles with a monolayer coverage of propyl sulfonate groups¹⁹. With this new formulation the nanofluids had a high solid loading and low viscosity, while retaining the surface activity of nanoparticles.

Our approach has been to use graphene instead of activated carbon as the key material to provide an electrical percolation effect on the solution. This approach is backed by preliminary results showing extraordinary charge percolation even in dilute graphene nanofluids²⁰. Thus, a stabilized dispersion of rGO in aqueous sulfuric acid solution can provide energy storage capacities similar to those of solid electrode supercapacitors (169 F·g⁻¹(rGO)) but working up to much faster rates (from 1 mV·s⁻¹ to the highest scan rate of 10 V·s⁻¹) in nanofluids²⁰.

Our efforts to create graphene-based nanofluids led to the development of two new hybrid materials (rGO-phosphomolybdate, rGO-PMo₁₂ and rGO-phosphotungstate, rGO-PW₁₂), dispersed with the aid of a surfactant in 1 M H₂SO₄ aqueous electrolyte to yield highly stable hybrid electroactive nanofluids (HENFs) of low viscosity which were tested in a home-made flow cell under static and continuous flowing conditions. Remarkably, even low concentration rGO-POMs HENFs (0.025 wt%) exhibited high specific capacitances of 273 F/g(rGO-PW₁₂) and 305 F/g(rGO-PMo₁₂) with high specific energy and specific power per mass of active material²¹.

Indeed, RGO must be properly dispersed in electrolytes in order to be used as a nanofluid. This has been attempted both in aqueous and organic solvents. For example Xu et al. reported a successful production of stable high-concentration graphene dispersions in low-boiling-point, low-polarity conventional organic solvents by liquid-phase noncovalent exfoliation of graphite assisted using polyethylene (HDPE) as the stabilizer²². Other example of RGO dispersion, this time in water, is the report of an imidazolium-modified hexa-*peri*-hexabenzocoronene derivative (HBC-C₁₁-MIM[Cl⁻]⁵) designed and synthesized as a stabilizer to disperse RGO. The resulting RGO/HBC-C₁₁-MIM[Cl⁻] hybrid can reach stable concentrations of 5.0 mg·mL⁻¹ (rGO) in water²³. In these two examples the stabilization of the rGO is achieved by a solvated aromatic molecule that keeps rGO in suspension.

On the other hand, LiFePO₄ has been intensely studied as cathode material for LIBs since the seminal work of Goodenough in 1997²⁴. It has made it from the labs to the market thanks to its low cost, abundant raw materials, safety, low toxicity, structural stability and excellent electrochemical properties. The active material can be reversibly

charged and discharged with a stable voltage at 3.45 V vs. Li⁺/Li with a very small change in unit cell parameters during the LiFePO₄/FePO₄ phase transition. It needs, however, conducting additives or coatings in order to display its full potential. As part of the extensive research on LiFePO₄ Bonaccorso, reported a battery with a graphene and LiFePO₄ electrodes and an energy density of 190 Wh·Kg⁻¹ ²⁵.

In this work we want to demonstrate the feasibility of reversibly transferring charge to/from nanoparticles of an electroactive phase (in this case, model LiFePO₄) dispersed in an electrolyte by means of the presence of rGO in a stabilized nanofluid, with rGO providing effective charge percolation.

In this work, we have used 3,4-diaminobenzoic acid (DABA) to generate a stable rGO dispersion in water and lithium iron phosphate (LiFePO₄) nanoparticles with a 2D layered morphology to demonstrate the high rate of charge transfer throughout the graphene dispersion in low concentration and in the absence of conventional surfactants. Just small amounts of rGO dispersed in aqueous Li₂SO₄ electrolyte lead to nanofluids with low viscosity while allowing effective charge/discharge of redox LiFePO₄ nanoparticles.

6.3 Experimental Section

LiFePO₄ sample was prepared by a reflux method. Stoichiometric amounts (0.03 mmol) of Li(CH₃COO)·2H₂O (3.0606 g), Fe(CO₂CO₂)·2H₂O (5.3907 g) and 85 %v/v H₃PO₄ (2.05 mL) were dissolved in 70 mL of ethylene glycol. The liquid reaction mixture was placed in a round-bottom flask connected to a condenser and refluxed vigorously for 72 h at 200 °C. The final pH of this solution was 7. The resulting solid was filtered-off, washed several times with deionized water and then ethanol. The sample was dried under vacuum at 80°C overnight, preheated at 350°C for 5 h and then sintered at 700°C for 10 h under nitrogen atmosphere. We collected 3.4214 g of green powder which amounts to 92% yield.

Graphite oxide (GO) was prepared from natural graphite using a modified Hummers method as follows²⁶: NaNO₃ (5g) and H₂SO₄ (225mL) were added to graphite (5g) and stirred for 30 min in an ice bath. KMnO₄ (25g) was added to the resulting solution, and then the solution was stirred at 50°C for 2 h. Deionized (DI) water (500 mL) and H₂O₂ (30 mL, 35%) were then slowly added to the solution. Concentrated HCl (500 mL, 37%) was added and then a final washing with 750 mL of 10% HCl, followed by dialysis until pH 6-7 and a final drying under vacuum at 70°C, afforded the GO product

as a powder. The amount of powder recovered was 4.1381g, which represents a 16% yield. Reduced graphene oxide (rGO) was prepared by high temperature treatment of this GO sample at 800°C under N₂ atmosphere for 1 hour.

The electroactive nanofluids discussed in this article were prepared using 1M solutions of Li₂SO₄·H₂O as base fluid and different DABA concentrations. RGO was then dispersed in this electrolyte solution, and sonicated for 5 minutes. The mass ratio of DABA to rGO was optimized in order to get a stable dispersion with a maximum amount of rGO. It is important to mention that pH 7 is needed for these electroactive nanofluids. To adjust the pH, LiOH·H₂O was added before adding LiFePO₄. Finally, layered LiFePO₄ was added and the mixture sonicated for 35 minutes. Different amounts of rGO and LiFePO₄ were tested and will be discussed through the article.

The viscosity for DABA/rGO (40:1)) nanofluid is 1.055 (10) mPa·s at 20.1°C. This value is very similar to the viscosity of water at the same temperature (1.002 mPa·s). The electroactive nanofluid based on sample e LiFePO₄ 1.4 g/L (DABA/RGO (40:1)) has a viscosity of 1.72 mPa·s, at 20.1°C with a shear rate of 2880 s⁻¹. This electroactive nanofluid has a higher viscosity than water and the base nanofluid, the higher viscosity is a result of the addition of the LiFePO₄ particles. However, this value is still reasonably low and perfectly compatible with low-energy pumping in a flow cell system.

Physical Characterization. The phase purity and crystal structure of the samples were confirmed by X-ray diffraction (XRD) using PANalytical X' Pert PRO diffractometer using a Cu K α radiation source ($\lambda = 1.5418 \text{ \AA}$) in the angular range $10^\circ \leq 2\theta \leq 70^\circ$ at a scan rate of 0.017° per second. The morphology of the particles was studied by Scanning Electron Microscopy (SEM) and Transmission Electron Microscopy (TEM, Tecnai G2 F20 HRTEM) operated at an acceleration voltage of 200 keV. For TEM studies, samples were dispersed in absolute ethanol, and a drop was then put onto a holey carbon coated Cu grid and allowed to evaporate slowly under ambient conditions before being introduced for TEM characterization. Raman scattering (RS) spectra were recorded on a HORIBA Scientific LabRAM HR Raman spectrometer system using Ar laser. Rheology experiments were carried out at the Institut de Ciencia de Materials de Barcelona (ICMAB) with a Haake RheoStress 600.

Cyclic voltammograms were carried out from -0.2 V to 1.2V vs Ag/AgCl 3.5M KCl. Pt was used as counter and working electrode during the electrochemical tests of the nanofluids. Potentiostatic electrochemical impedance spectroscopy (PEIS) experiments were carried out over a frequency range of 5000 kHz and 100000 mHz, with an amplitude of 10 mV. Before the PEIS experiments, the cell was keep at constant voltage for 10

Desing of novel electroactive nanofluids for flow cell

minutes. The voltages of the experiments were 0.0 V vs. Ag/AgCl or 0.9 V vs. Ag/AgCl the electrochemical tests were carried out with a Biologic VMP3 potentiostat/galvanostat.

A commercial Electrolysis Cell was used (BASi Bulk). A container with a porous glass frit of 4-6 μm pore diameter was used for the charge and discharge test. In the glass frit only $1.4 \text{ g}\cdot\text{L}^{-1}$ of LiFePO_4 DABA/rGO (40:1) nanofluid was placed. A DABA-rGO (40:1) dispersion was used as counter electrode in the 75 mL glass cell with an Ag/AgCl KCl 3.5M reference electrode immersed in it. The cell was cycled between -0.2V to 1V vs. Ag/AgCL KCl 3.5M at 1C. The dispersion was stirred during the experiment. It is important to mention that we balanced the amounts of active materials in each nanofluid electrode ($1.4 \text{ g}\cdot\text{L}^{-1}$ of LiFePO_4 DABA/rGO (40:1) sample and the DABA/rGO (40:1) sample) to balance their charge. For instance, we used 75 mL of DABA/rGO (40:1) nanofluid and 1.3 mL of the LiFePO_4 DABA/rGO nanofluid. The calculation was based on data from a symmetric cell with DABA/rGO (40:1) electrodes Figure 1.

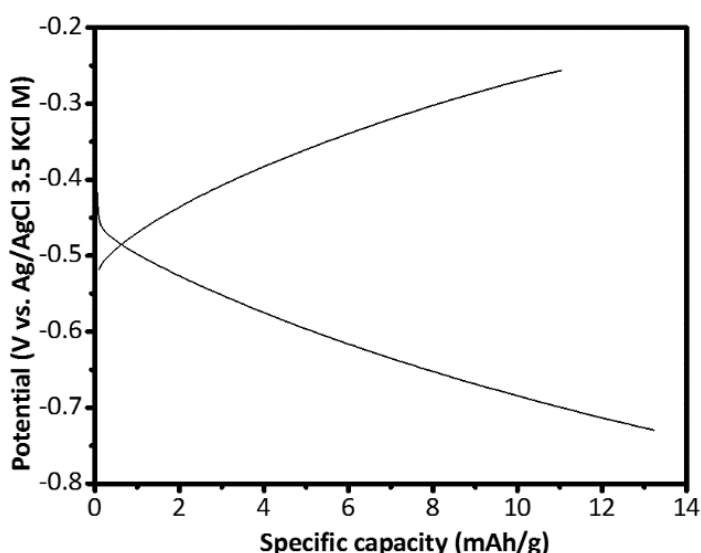


Fig.1 Capacity vs. Potential profile of symmetric capacitor cell with DABA/rGO (40:1) electrodes. Cycle at 500 mA for one hour. Both the anolyte and the catholyte were DABA/RGO (40:1).

Physical Characterization. The phase purity and crystal structure of the samples were confirmed by X-ray diffraction (XRD) using PANalytical X' Pert PRO diffractometer using a $\text{Cu K}\alpha$ radiation source ($\lambda = 1.5418 \text{ \AA}$) in the angular range $10^\circ \leq 2\theta \leq 70^\circ$ at a scan rate of 0.017° per second. The morphology of the particles was studied by Scanning Electron Microscopy (SEM) and Transmission Electron Microscopy (TEM, Tecnai G2 F20 HRTEM) operated at an acceleration voltage of 200 keV. For TEM studies, samples were dispersed in absolute ethanol, and a drop was then put onto a holey carbon coated Cu grid and allowed to evaporate slowly under ambient conditions before being

introduced for TEM characterization. Raman scattering (RS) spectra were recorded on a HORIBA Scientific LabRAM HR Raman spectrometer system using Ar laser. Rheology experiments were made in the Institute de Ciencia de Materials de Barcelona (ICMAB) with a Haake RheoStress 600.

For the solid-electrode test the cathodes were prepared by pressing a mixture of the active materials with Carbon Super-P (Timcal) and Polyvinylidene fluoride (PVDF) binder in a weight ratio 85/10/5. They were mixed in a mortar for 5 minutes and then dispersed in N-Methyl-2-pyrrolidone and coated onto Al foil.

6.4 Results and Discussion

Behera et al. have reported that reduced graphene oxide has a better dispersibility in a pH range of 7 to 11²⁷. Guyomard and collaborators reported that LiFePO₄ has an initial pH near 7 in a water dispersion; they conclude that the stability and the electrochemical performance is better when the initial pH is not altered²⁸. Furthermore, DABA solubility has a strong dependence on the pH, with decreased solubilities in acidic media (Table 1 and Table 2) probably due to the protonation of its carboxylic acid moiety. Therefore, LiOH·H₂O was used in order to adjust the pH at 7; this compound was selected to avoid the presence of other ions in solution.

DABA concentration	LiOH.H ₂ O	pH	Solubility
12 g·L ⁻¹	N/A	4	no
12 g·L ⁻¹	1.6 g·L ⁻¹	6	partially
12 g·L ⁻¹	2.8 g·L ⁻¹	7	yes
12 g·L ⁻¹	3.6 g·L ⁻¹	10	yes

Table 1 DABA experimental solubility

As a preliminary step for the formulation of our final nanofluids, we optimized the DBA/rGO concentration in aqueous media. Three different DABA/rGO mass ratios were tested: 20:1, 30:1 and 40:1 (see Table 1 for concentration). As it is shown in Table 1, the more stable dispersion of DABA and rGO was the one with the mass ratio DABA/rGO 40 to 1.

Desing of novel electroactive nanofluids for flow cell

pH	Concentration (g·L ⁻¹)
1	263
2	30
3	5.2
4	2.7
5	4
6	18
7	161
8	1000
9	1000
10	1000

Table 2 Theoretical solubility of DABA at 25 ° C ^(a)

(a) Calculated using Advanced Chemistry Development (ACD/Labs) Software V11.02 (© 1994-2017 ACD/Labs)

For comparison, pure rGO was dispersed in the Li₂SO₄ aqueous electrolyte at a nominal concentration of 0.29 g·L⁻¹. However, at this concentration RGO precipitates immediately, although a grey-colored dispersion was maintained (Table 3). This means that, although some graphene flakes remain in solution thanks to the polar oxygen groups remaining in the structure of rGO, in the absence of DABA, the solubility limit for rGO is much lower.

Desing of novel electroactive nanofluids for flow cell

Sample	Aspect	Stability	Complete precipitation of the dispersion (hours)
RGO (0.29 ng/L)	Translucent grey	immediate ppt	N/A
Diaminobenzoic acid / RGO (20:1) (0.6 g·L ⁻¹ RGO)	Translucent	Precipitation starts after 4 hrs.	7
Diaminobenzoic acid / RGO (30:1) (0.4 g·L ⁻¹ RGO)	(orange) Decrease with time	Precipitation starts after 27 hrs.	56
Diaminobenzoic acid / RGO (40:1) (0.3 g·L ⁻¹ RGO)	(orange) Decrease with time	Precipitation starts after 97 hrs.	120
Diaminobenzoic acid / RGO (40:1)/ 0.4 g·L⁻¹ LiFePO₄	Brown	Precipitation starts after ca. 24 hours	36
Diaminobenzoic acid / RGO (40:1)/ 1 g·L⁻¹ LiFePO₄	Almost Black	N/A	Around 24
Diaminobenzoic acid / RGO (40:1)/ 1.4 g·L⁻¹ LiFePO₄	Almost black	N/A	Around 24
Diaminobenzoic acid / RGO (40:1)/ 2 g·L⁻¹ LiFePO₄	Black	N/A	More than 12 less than 24

Table 3 Stability of the nanofluids (12 mg/mL DABA, 2.8 mg/mL LiOH.H₂O, 1M of Li₂SO₄.H₂O, pH 7).

The stabilization of rGO by DABA could be explained through solvation by this aromatic molecule that keeps rGO in suspension by π - π interactions, with the introduction of functional groups providing a steric effect that maintains the rGO layers apart. Indeed, DABA is an amphiphilic molecule with an aromatic core and polar groups. This must be at the heart of its capacity to stabilize rGO in water. The fact that a large excess of molecules is needed for this suggest that a simple single-layer coating of both sides of rGO sheets by DABA is not enough to explain this stabilization. Instead, we propose a multilayer structure of DABA molecules with orientations parallel to rGO sheets in the first-layer sphere (with π - π interactions) turning into loosely perpendicular orientations after a few DABA layers, with carboxylate and $-NH_2$ groups hydrogen-bonding water molecules. Of course, this appealing hypothesis would need to be confirmed by further studies, possibly through molecular simulation.

Desing of novel electroactive nanofluids for flow cell

After optimization of the DABA/rGO ratio (optimal mass ratio 40:1 DABA/rGO), we proceeded to develop an electroactive nanofluid incorporating platelet LiFePO_4 as redox electroactive species to test the rGO/DABA dispersion. Different amounts of LiFePO_4 were tested to optimize the amount of redox active material load in the nanofluid (Table 3). The sample with $0.4 \text{ g}\cdot\text{L}^{-1}$ of LiFePO_4 was the most stable, however samples containing $1 \text{ g}\cdot\text{L}^{-1}$ and $1.4 \text{ g}\cdot\text{L}^{-1}$ of LiFePO_4 exhibited a stability that could be considered good enough to develop a nanofluid. Unfortunately, the sample with $2 \text{ g}\cdot\text{L}^{-1}$ of LiFePO_4 layer did not show good stability. Depending on the particle concentration and the strength of particle–particle interactions, a dispersion/agglomeration equilibrium is established in the particle suspension. Large concentrations of LiFePO_4 platelets induce agglomeration and precipitation. On the other hand, it should be noted that even gentle stirring prevents precipitation of these more concentrated nanofluids.

The electrochemical characterization of optimized nanofluids included cyclic voltammetry (CV) and impedance (PEIS) studies, as well as Galvanostatic Charge-Discharge (GCD) tests. As shown in Fig.2a, the CV of DABA shows an important change on its electrochemical signal when rGO is added. DABA alone did not show any special electrochemical response. There is an apparent wave at both ends of the selected scan range, the separation between the peaks is ca. 0.7 V vs. Ag/AgCl . The difference between these E_{p_a} and E_{p_c} , is a useful diagnostic test of a Nernstian reaction. In this case it is quite far from the value of 0.059 V at 25°C ²⁹ expected for a reversible reaction.

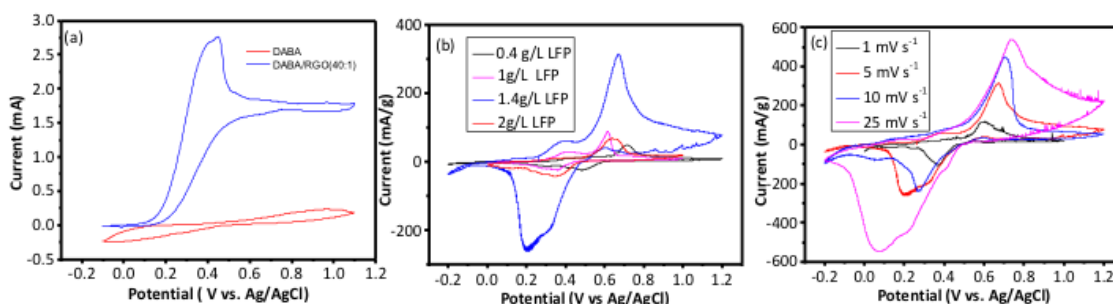


Fig.2 (a) Cyclic Voltammograms of DABA (12 g L^{-1}) (red trace) and DABA/rGO (12 g L^{-1} and 0.3 g L^{-1} respectively) (blue) showing a characteristic irreversible oxidation wave of DABA enabled by rGO. Scan rate 5 mV s^{-1} (b) Cyclic Voltammograms of LiFePO_4 (DABA-rGO (40/1)) (concentrations of LiFePO_4 0.4 g L^{-1} , 1 g L^{-1} , 1.4 g L^{-1} , 2 g L^{-1}). Scan rate 5 mV s^{-1} . (c) Cyclic Voltammetry at different scan rates of LiFePO_4 (1.4 g L^{-1}). Inset shows the CV of a 1 g L^{-1} LiFePO_4 in DABA/rGO (40/1) in which the characteristic wave from DABA is still apparent.

But the addition of RGO leads to the appearance of an oxidation wave at 0.3 V vs Ag/AgCl. Thus, rGO seems to promote an irreversible oxidation process. It is important to mention that the rGO dispersion shows a capacitive behavior rather than a faradaic redox process, Figure 3a.

Fig.2b shows cyclic voltammograms of nanofluids with various LiFePO₄ concentrations with DABA/rGO as additive at constant concentration (40/1 mass ratio). They show the expected LiFePO₄ redox waves at 0.65 V vs Ag/AgCl and 0.19 V vs. Ag/AgCl with intensities increasing as LiFePO₄ concentration increases up to 1.4 g·L⁻¹. The acknowledged redox process for LiFePO₄ is the following ^{24, 30}:

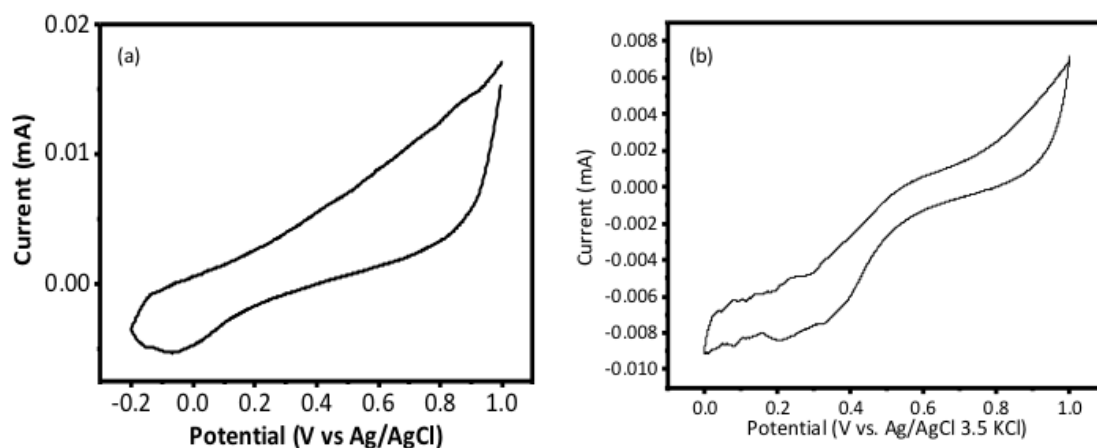


Fig.3 Cyclic voltammograms of (a) rGO (b) 1.4g/L of LiFePO₄ in an aqueous electrolyte. The electrolyte is 1M Li₂SO₄ with 1.4 gL⁻¹ of LiFePO₄. The scan rate was 5 mVs⁻¹.

Finally, a redox wave associated to DABA was also detected at 0.3 V vs Ag/AgCl.

The sample with 1.4 g·L⁻¹ of LiFePO₄ led to the best electrochemical performance, although its dispersion in the nanofluid is not as long-lasting as that of more dilute sample (i.e. 0.4 g·L⁻¹). Thus, the 1.4 g·L⁻¹ was further used to explore in detail the electrochemical characteristics of these nanofluids. The decrease in the current intensity for the nanofluid with a LiFePO₄ concentration of 2 g/L is a result of a co-precipitation of rGO and LiFePO₄ nanoparticles.

Fig.2c shows the electrochemical behavior of the selected sample (1.4 g/L LiFePO₄ nanofluid) at different scan rates. The intensity of the Fe(II)/Fe(III) peak from LiFePO₄ increases as the scan rate is increased. On the other hand, the peak corresponding to DABA appears as a shoulder at low scan rates and nearly disappears as the scan rate is increased up to 25 mV·s⁻¹. It should be noted that the order for recording these CVs was from fastest to slowest. Thus, the disappearance of the DABA

signal cannot be due to full consumption of the chemical. Instead, it can be attribute to a slow kinetic of the DABA reaction. This observation allows us to conclude that at fast scan rates this reaction does not contribute significantly to the electrochemistry of this system. The concentration of LiFePO_4 also has an effect. Thus, as we can see in Figure 4, the CV of the sample with $1 \text{ g}\cdot\text{L}^{-1}$ of LiFePO_4 at $25 \text{ mV}\cdot\text{s}^{-1}$ shows a small peak corresponding to DABA oxidation. These experiments show a decrease of the DABA signal induced both by the addition of LiFePO_4 and by an increase of the scan rate. That behavior suggests that the electrochemical redox processes of LiFePO_4 are much faster than the oxidation of DABA.

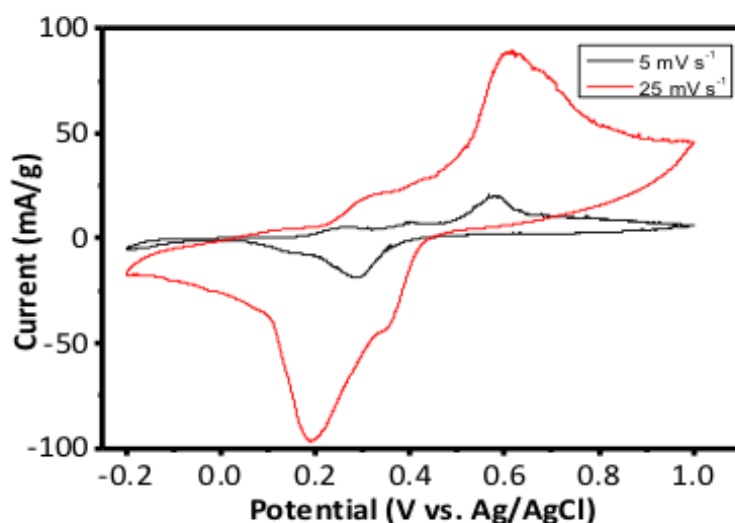


Fig.4 Cyclic voltammograms of 1g/L of LiFePO_4 in DABA/RGO (40:1).

On the other hand, it is well known that LiFePO_4 electroactivity is hindered by its poor electronic conductivity ($10^{-9} \text{ S}\cdot\text{cm}^{-1}$) and slow lithium diffusion³¹. Increasing the conductivity by coating the LiFePO_4 surface with carbon^{30, 32} or conducting polymers^{33, 34} have been two of the most popular approaches to improve the capacity and rate performance of LiFePO_4 in LIBs. Similarly, our experiments show that in the absence of rGO the Cyclic Voltammogram of LiFePO_4 does not show a well-defined electrochemical signal (Figure 3b). This behavior changes dramatically when the nanofluid contains DABA-stabilized rGO in addition to LiFePO_4 , with well-defined and intense redox peaks unambiguously assigned to LiFePO_4 (Figure 4). This indicates that the water-dispersed rGO allows for an effective charge-transfer percolation between the current collector and the uncoated LiFePO_4 nanosheets.

PEIS experiments were carried out for the $1.4 \text{ g}\cdot\text{L}^{-1}$ LiFePO_4 nanofluid and the corresponding Nyquist plots for the system in its reduced ($0.0 \text{ V vs. Ag/AgCl}$) (Fig.5a)

and oxidized (0.9 V) (Fig.5b) states. The results fit the Randles equivalent circuit (inset Fig.5b) typical for a simple electrochemical process. In this equivalent circuit, there is a resistance associated to the electrolyte and the external circuit, which in the Nyquist plot corresponds to the point in the real axes where the semicircle begins. This point is the same for the oxidation and reduction processes of the sample. The value of this resistance is negligible compared to the resistance associated with the charge transfer, discussed below.

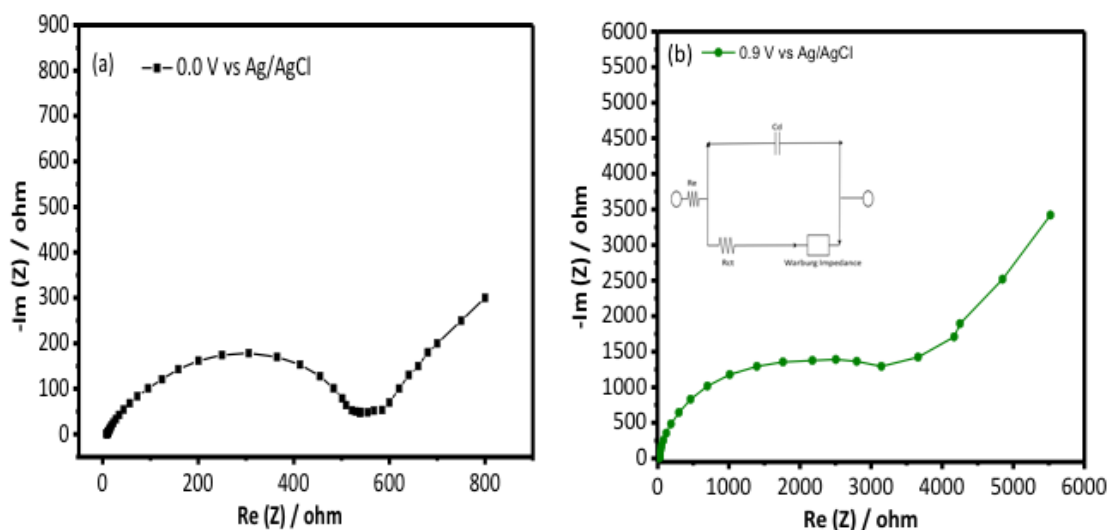


Fig.5 PEIS impedance spectra of LiFePO_4 (1.4 g L^{-1}) in DABA/RGO (40:1) (a) recorded at 0.0V (reduced) and (b) at 0.9 V (oxidized).

The charge transfer resistance related to the redox process can be measured by the width of the semicircle observed in the real axes of the Nyquist plot. The semicircle is larger for the oxidation than for the reduction process in LiFePO_4 . This agrees with other publications, where they found that LiFePO_4 is more stable than FePO_4 ³⁵. This also means that the de-intercalation process is less favorable than the intercalation process in this system.

The inclined line in the low frequency zone of the plot represents the Warburg impedance (Z_w), which is customarily associated to lithium-ion diffusion in the material³⁶. This process is associated with a mass transfer control.

Fig. 6a shows the performance of a full cell with the LiFePO_4 (1.4 g L^{-1}) - DABA/rGO (40:1) nanofluid as positive electrode and the DABA/rGO (40:1) nanofluid as negative electrode cycled at 1C. The discharge capacity of the cell is ca. $140 \text{ mA}\cdot\text{h}\cdot\text{g}^{-1}(\text{LiFePO}_4)$ at 1 C.

Desing of novel electroactive nanofluids for flow cell

The Coulombic efficiency of the cell increases continuously from 65% (1st cycle) up to ca. 90% (5th cycle). This is not an intrinsic behavior of the electroactive phases in the nanofluids. We believe the initial lower efficiency could be related to some irreversible (but minor) reaction taking place during the first few cycles of charge. Finally, the results show a high utilization of the LiFePO₄.

Fig. 6b shows a plot of the potential of the working electrode vs. capacity for a single representative cycle (5th cycle). The charge capacity is only slightly larger than the discharge capacity, in agreement with the evolution of the coulombic efficiency shown in Figure 6Fig. a. The profile of the cell shows a clear plateau around 0.35 V (discharge) and 0.55 V (charge) vs Ag/AgCl.

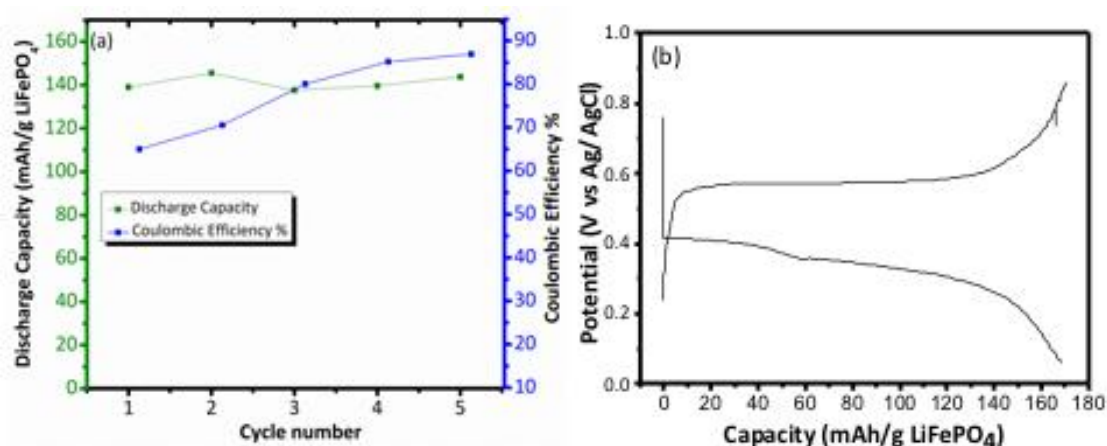


Fig. 6 (a) Evolution of discharge capacity and coulombic efficiency of a two-nanofluid cell with LiFePO₄ (1.4 g L⁻¹)-DABA/RGO (40/1) as positive and DABA/RGO (40/1) as negative electrodes. Full cell cycled at 1C. (b) Charge and Discharge profiles (cell Voltage vs. charge) of the full Nanofluids cell.

Material characterization

The LiFePO₄ material prepared presents the expected olivine phase as confirmed by powder XRD (Figure 7a) with high purity. All diffraction peaks are indexed to orthorhombic LiFePO₄ (JCPDS card number 081-1173, space group Pnma), with no impurities detected. The average primary crystallite size, as determined from the peak width at 23.2 θ by the Scherrer equation, was 38 nm, substantially smaller than the average size of the plates which was found to be 138 nm.

Desing of novel electroactive nanofluids for flow cell

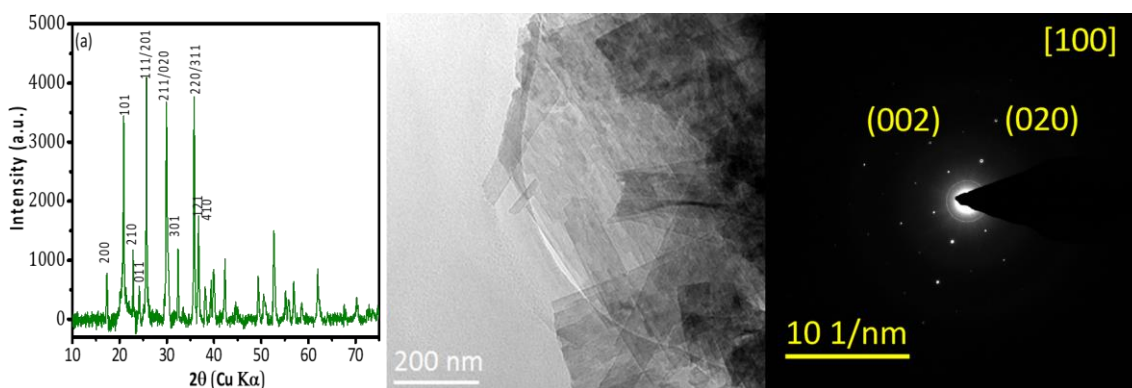


Fig.7 (a) XRD pattern (indexes shown only up to 37°) (b) TEM image showing the flake microstructure and (c) Selected Area Electron Diffraction (SAED) pattern; all corresponding to our solid LiFePO_4 material.

On the other hand, the synthesis procedure reported here for LiFePO_4 leads to a striking, unusual morphology and agglomeration of thin plates Figure 7b. This sample is well crystallized, single-crystals according to their Selected Area Electron Diffraction (SAED) patterns, Figure 7c. This analysis of the SAED pattern, obtained from the isolated nanoparticle shows in the inset of this figure, shows that this particle has a plane axis of [100]. The inset shows a TEM image of the particle used to obtain the SAED. The planes show by this nanoparticle can be index 101 and 020, corresponding to the bc plane. These axes are listed in a JCPDS card number 081-1173 of LiFePO_4 .

In the absence of such a conducting coating, the maximum discharge capacity obtained for this material in half cells vs. Li was around $100 \text{ mA}\cdot\text{h}\cdot\text{g}^{-1}$ at 0.10C, decreasing progressively at higher rates down to $30 \text{ mA}\cdot\text{h}\cdot\text{g}^{-1}$ at 5C and ca. $10 \text{ mA}\cdot\text{h}\cdot\text{g}^{-1}$ at 10C (Figure 8b).

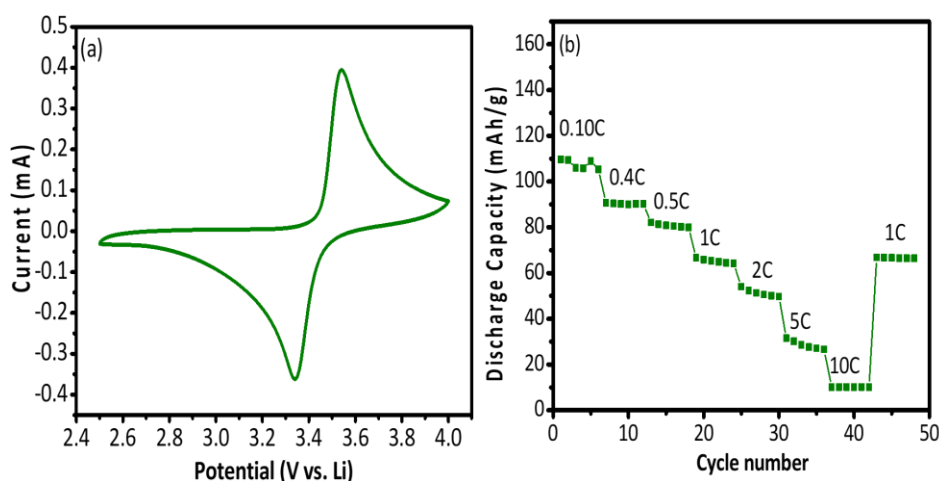


Fig.8 (a) Cyclic Voltammetry of LiFePO_4 scan rate $0.5 \text{ mV}\cdot\text{s}^{-1}$ (b) Rate Capability of the half-cell $\text{Li}/\text{LiFePO}_4$ from Galvanostatic Charge-Discharge measurements at various current densities.

Figure 9a shows micrographs of representative rGO sheets at different scales. These sheets are very thin and segregated, although their preparation for TEM results in wrinkles and partial overlap with each other. The SAED pattern of the sheet shown in the top inset (Figure 9a) shows a typical hexagonal symmetry but with strongly distorted elongated spots, which is representative of single-crystalline graphene layers with a high degree of distortions.

Raman scattering is one of the most widely used techniques to characterize the structural and electronic properties of carbon materials. Figure 9b shows the Raman spectrum of our rGO with a D band at 1355.2cm^{-1} and a G band at 1595.3cm^{-1} . The D band is related to the degree of disorder and its intensity shows the degree of edge chirality. Thus, the intensity ratio of G and D band (I_D/I_G) of rGO indicates the degree of the disorder. As shown in Figure 9b, the I_D/I_G ratio of rGO is 0.99. This spectrum shows that this sample has 2 other bands at 2716.3 and 2953.9cm^{-1} . The bands correspond to 2D (2953.9cm^{-1}), a combination scattering peak^{37, 38}; a second order overtone of a different in plane vibration D + G (2716.3cm^{-1})³⁷.

D and G Raman bands can be deconvoluted using four Gaussians or Gaussian-Lorentzian lines in order to estimate the ratio of sp^2 to sp^3 type carbon.[38] We have fitted the Raman intensity profiles using four Gaussian lines, see Figure 9b, and have estimated intensity ratio $I_{\text{sp}^2}/I_{\text{sp}^3} = (I_{1270} + I_{1610}) / (I_{1100} + I_{1510})$. For RGO sample, we found a value for $I_{\text{sp}^2}/I_{\text{sp}^3} = 3.2$.

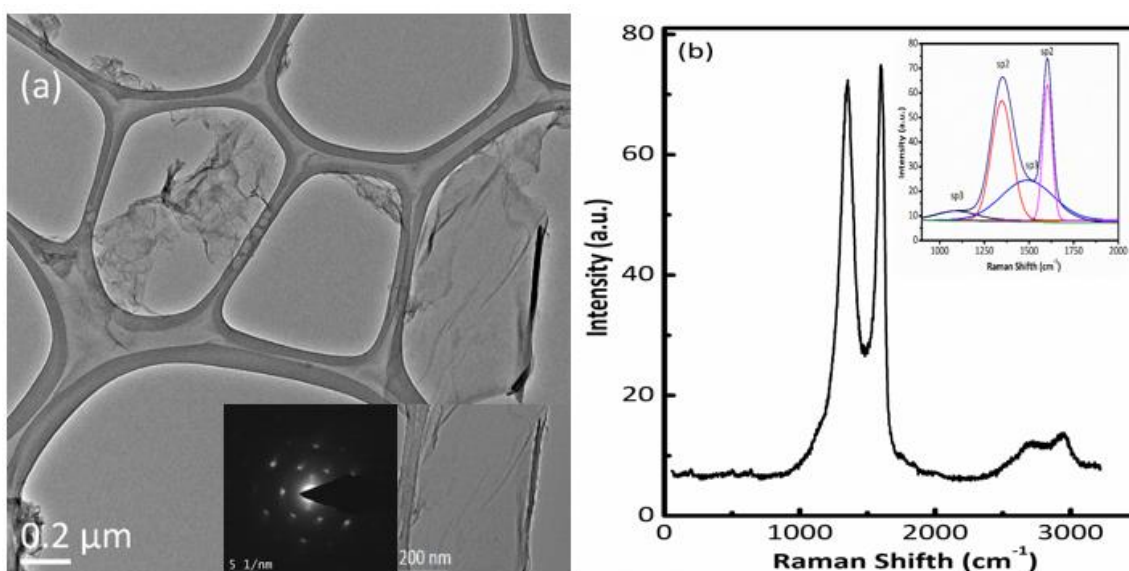


Fig.9 (a) RGO HRTEM image, inset SAED and TEM image (b) Raman spectra of GO (bottom) and RGO (top) (inset shows RGO D and G band deconvolution)

6.5 Conclusions

We successfully developed a stable dispersion of rGO in water thanks to the addition of DiAminoBenzoic Acid (DABA). This aromatic but polar molecule interacts with rGO through π - π forces equivalent to a solvating effect. As a consequence of this interaction rGO was maintained in water as stable dispersions. Furthermore, the steric effect of the functional groups of the DABA preclude the restacking of rGO layers, which remain separated in the dispersion.

Our results show the strong effect of adding rGO-DABA to a nanofluid containing LiFePO₄ allowing for an effective charge-transfer percolation between the current collector and the uncoated LiFePO₄ nanosheets. The latter were used as a model electroactive nanoparticulate phase and showed an improvement of its redox performance in the nanofluid with respect to their use in a solid electrode. It should also be noted that our base nanofluid (rGO-DABA) does not disturb the electrochemical signal of this LiFePO₄, despite the enhancement by rGO of a redox process of DABA (not observed with pristine DABA). In this respect, we must conclude that the relatively much faster and reversible LiFePO₄ electrochemistry precludes the process of irreversible oxidation of DABA, especially at fast rates. Finally, our work shows how to harness the electroactivity of LiFePO₄ integrated in a freely flowing nanofluid. It should be noted that LiFePO₄ nanosheets in the nanofluid were not coated with any conducting material. Yet, they performed better than similarly uncoated nanoparticles integrated in a conventional electrode. This improved performance must be assigned to the efficient charge-transfer from current collectors mediated by rGO in the nanofluid.

We feel our present work represents one end of a research line connecting i) well-dispersed nanofluids (sols) with low viscosity but low energy density (this work) and ii) the many paste formulations with higher energy density but poor flowing characteristics reported in the literature. It is our opinion that a whole new world of opportunities lies in between: the world of nanopastes, with heavy loads of solid nanoparticles dispersed in liquids, yet with the particles stabilized to avoid agglomeration, thus keeping the interface between solid and liquid domains effectively active at the nanodimension.

References

1. P. Leung, A.A. Shah, L. Sanz, C. Flox, J.R. Morante, Q. Xu, M.R. Mohamed, C. Ponce de León, F.C. Walsh, Recent developments in organic redox flow batteries: A critical review, *J. Power Sources*, 360 (2017) 243-283.
2. Q. Huang, Q. Wang, Next-Generation, High-Energy-Density Redox Flow Batteries, *ChemPlusChem*, 80 (2015) 312-322.
3. G.L. Soloveichik, Flow Batteries: Current Status and Trends, *Chem. Rev.*, 115 (2015) 11533-11558.
4. Z. Yang, J. Zhang, M.C.W. Kintner-Meyer, X. Lu, D. Choi, J.P. Lemmon, J. Liu, Electrochemical Energy Storage for Green Grid, *Chem. Rev.*, 111 (2011) 3577-3613.
5. L. Hooper-Burkhardt, S. Krishnamoorthy, B. Yang, A. Murali, A. Nirmalchandar, G.K.S. Prakash, S.R. Narayanan, A New Michael-Reaction-Resistant Benzoquinone for Aqueous Organic Redox Flow Batteries, *J. Electrochem. Soc.*, 164 (2017) A600-A607.
6. M.O. Bamgbopa, Y. Shao-Horn, S. Almheiri, The potential of non-aqueous redox flow batteries as fast-charging capable energy storage solutions: demonstration with an iron-chromium acetylacetonate chemistry, *Journal of Materials Chemistry A*, 5 (2017) 13457-13468.
7. D. Rueda-García, D.P. Dubal, F. Huguenin, P. Gómez-Romero, Hurdles to organic quinone flow cells. Electrode passivation by quinone reduction in acetonitrile Li electrolytes, *J. Power Sources*, 350 (2017) 9-17.
8. M. Duduta, B. Ho, V.C. Wood, P. Limthongkul, V.E. Brunini, W.C. Carter, Y.-M. Chiang, Semi-Solid Lithium Rechargeable Flow Battery, *Advanced Energy Materials*, 1 (2011) 511-516.
9. V. Presser, C.R. Dennison, J. Campos, K.W. Knehr, E.C. Kumbur, Y. Gogotsi, The Electrochemical Flow Capacitor: A New Concept for Rapid Energy Storage and Recovery, *Advanced Energy Materials*, 2 (2012) 895-902.
10. S. Sasi, A. Murali, S.V. Nair, A.S. Nair, K.R.V. Subramanian, The effect of graphene on the performance of an electrochemical flow capacitor, *Journal of Materials Chemistry A*, 3 (2015) 2717-2725.
11. M. Boota, K.B. Hatzell, M. Alhabeab, E.C. Kumbur, Y. Gogotsi, Graphene-containing flowable electrodes for capacitive energy storage, *Carbon*, 92 (2015) 142-149.
12. M. Duduta, B. Ho, V.C. Wood, P. Limthongkul, V.E. Brunini, W.C. Carter, Y.M. Chiang, Semi - Solid Lithium Rechargeable Flow Battery, *Advanced Energy Materials*, 1 (2011) 511-516.
13. S. Hamelet, T. Tzedakis, J.-B. Leriche, S. Sailler, D. Larcher, P.-L. Taberna, P. Simon, J.-M. Tarascon, Non-Aqueous Li-Based Redox Flow Batteries, *J. Electrochem. Soc.*, 159 (2012) A1360-A1367.

14. H. Chen, N.-C. Lai, Y.-C. Lu, Silicon–Carbon Nanocomposite Semi-Solid Negolyte and Its Application in Redox Flow Batteries, *Chem. Mater.*, 29 (2017) 7533-7542.
15. L. Madec, M. Youssry, M. Cerbelaud, P. Soudan, D. Guyomard, B. Lestriez, Surfactant for Enhanced Rheological, Electrical, and Electrochemical Performance of Suspensions for Semisolid Redox Flow Batteries and Supercapacitors, *ChemPlusChem*, 80 (2015) 396-401.
16. M. Boota, K.B. Hatzell, M. Beidaghi, C.R. Dennison, E.C. Kumbur, Y. Gogotsi, Activated Carbon Spheres as a Flowable Electrode in Electrochemical Flow Capacitors, *J. Electrochem. Soc.*, 161 (2014) A1078-A1083.
17. J.W. Campos, M. Beidaghi, K.B. Hatzell, C.R. Dennison, B. Musci, V. Presser, E.C. Kumbur, Y. Gogotsi, Investigation of carbon materials for use as a flowable electrode in electrochemical flow capacitors, *Electrochim. Acta*, 98 (2013) 123-130.
18. Q. Huang, H. Li, M. Gratzel, Q. Wang, Reversible chemical delithiation/lithiation of LiFePO₄: towards a redox flow lithium-ion battery, *PCCP*, 15 (2013) 1793-1797.
19. S. Sen, V. Govindarajan, C.J. Pelliccione, J. Wang, D.J. Miller, E.V. Timofeeva, Surface Modification Approach to TiO₂ Nanofluids with High Particle Concentration, Low Viscosity, and Electrochemical Activity, *ACS Applied Materials & Interfaces*, 7 (2015) 20538-20547.
20. D.P. Dubal, P. Gomez-Romero, Electroactive graphene nanofluids for fast energy storage, *2D Materials*, 3 (2016) 031004.
21. D.P. Dubal, D. Rueda - Garcia, C. Marchante, R. Benages, P. Gomez - Romero, Hybrid Graphene - Polyoxometalates Nanofluids as Liquid Electrodes for Dual Energy Storage in Novel Flow Cells, *The Chemical Record*, 0.
22. L. Xu, J.-W. McGraw, F. Gao, M. Grundy, Z. Ye, Z. Gu, J.L. Shepherd, Production of High-Concentration Graphene Dispersions in Low-Boiling-Point Organic Solvents by Liquid-Phase Noncovalent Exfoliation of Graphite with a Hyperbranched Polyethylene and Formation of Graphene/Ethylene Copolymer Composites, *The Journal of Physical Chemistry C*, 117 (2013) 10730-10742.
23. H. Wei, Y.-Y. Li, J. Chen, Y. Zeng, G. Yang, Y. Li, Dispersion of Reduced Graphene Oxide in Multiple Solvents with an Imidazolium-Modified Hexa-perihexabenzocoronene, *Chemistry – An Asian Journal*, 7 (2012) 2683-2689.
24. A.K. Padhi, K.S. Nanjundaswamy, J.B. Goodenough, Phospho - olivines as Positive - Electrode Materials for Rechargeable Lithium Batteries, *J. Electrochem. Soc.*, 144 (1997) 1188-1194.
25. J. Hassoun, F. Bonaccorso, M. Agostini, M. Angelucci, M.G. Betti, R. Cingolani, M. Gemmi, C. Mariani, S. Panero, V. Pellegrini, B. Scrosati, An Advanced Lithium-Ion Battery Based on a Graphene Anode and a Lithium Iron Phosphate Cathode, *Nano Lett.*, 14 (2014) 4901-4906.
26. N.J. Dudney, Thin Film Micro-Batteries, *Electrochem. Soc. Interface*, 17 (2008).

27. S. Kashyap, S. Mishra, S.K. Behera, Aqueous Colloidal Stability of Graphene Oxide and Chemically Converted Graphene, *Journal of Nanoparticles*, 2014 (2014) 6.
28. W. Porcher, P. Moreau, B. Lestriez, S. Jouanneau, D. Guyomard, Is LiFePO₄ Stable in Water?: Toward Greener Li-Ion Batteries, *Electrochem. Solid-State Lett.*, 11 (2008) A4-A8.
29. A.J. Bard, L.R. Faulkner, *Electrochemical Methods: Fundamentals and Applications*, Wiley, New York, 2001.
30. Z. Cabán-Huertas, O. Ayyad, D.P. Dubal, P. Gómez-Romero, Aqueous synthesis of LiFePO₄ with Fractal Granularity, *Scientific Reports*, 6 (2016) 27024.
31. Y.-N. Xu, S.-Y. Chung, J.T. Bloking, Y.-M. Chiang, W.Y. Ching, Electronic Structure and Electrical Conductivity of Undoped LiFePO₄, *Electrochem. Solid-State Lett.*, 7 (2004) A131-A134.
32. N. Ravet, Y. Chouinard, J.F. Magnan, S. Besner, M. Gauthier, M. Armand, Electroactivity of natural and synthetic triphylite, *J. Power Sources*, 97–98 (2001) 503-507.
33. A. Fedorková, A. Nacher-Alejos, P. Gómez-Romero, R. Oriňáková, D. Kaniansky, Structural and electrochemical studies of PPy/PEG-LiFePO₄ cathode material for Li-ion batteries, *Electrochim. Acta*, 55 (2010) 943-947.
34. A.V. Murugan, T. Muraliganth, A. Manthiram, Microwave-Irradiated Solvothermal Synthesis of LiFePO₄ Nanorods and their Nanocomposites for Lithium Ion Batteries, *ECS Transactions*, 16 (2009) 49-56.
35. P. Tang, N.A.W. Holzwarth, Y.A. Du, Comparison of the electronic structures of four crystalline phases of FePO₄, *Physical Review B*, 76 (2007) 174118.
36. A. Fedorkova, R. Orinakova, A. Orinak, M. Kupkova, H.D. Wiemhofer, J.N. Audinot, J. Guillot, Electrochemical and XPS study of LiFePO₄ cathode nanocomposite with PPy/PEG conductive network, *Solid State Sciences*, 14 (2012) 1238-1243.
37. R. Saito, A. Jorio, A.G. Souza Filho, G. Dresselhaus, M.S. Dresselhaus, M.A. Pimenta, Probing Phonon Dispersion Relations of Graphite by Double Resonance Raman Scattering, *Phys. Rev. Lett.*, 88 (2001) 027401.
38. R. Saito, M. Hofmann, G. Dresselhaus, A. Jorio, M.S. Dresselhaus, Raman spectroscopy of graphene and carbon nanotubes, *Adv. Phys.*, 60 (2011) 413-550.

CHAPTER 7

New and Improved Cell and Method for the production of Graphene by Electrochemical Exfoliation of Graphites

7.1 Context

All graphene nanofluids previously described are actually based on reduced graphene oxide (rGO) dispersed in aqueous acidic electrolytes. As it was described in the chapter of quinones nanofluids, organic electrolytes can provide larger working voltages and therefore greater energy densities. However, we could no stabilize rGO in organic solvents. As a consequence, we decided to use graphene instead rGO. But in order to have a fine control of the nature of the graphene obtained (in terms of number of layers, absence or concentration and type of defects and oxygen), we decided to produce it by electrochemical exfoliation of graphite. This task turned out to be more challenging and at the same time more fruitful than anticipated and led us to a simple but original design and procedure which merited the filing of a European patent, described in this chapter.

7.2 State of the art

Great advances are being made in several fields like energy generation and storage, electronics, photonics, composites, sensors and bio applications thanks to the extraordinary properties of graphene^{1,2}, but these advances need the implementation of procedures for large scale synthesis of graphene with truly controlled purity and structural and physical properties³.

Electrochemical exfoliation emerged as a prominent method able to produce large quantities of high quality few layers graphene⁴ (FLG) and other materials like graphite oxide^{5,6}, graphene quantum dots^{7,8} or functionalized graphene^{9,10}. Although much research has been carried out related to the electrochemical exfoliation of graphene¹¹, reported studies have focused mainly on the electrolyte and potential applied, whereas the influence of the C precursor has been generally ignored^{4,10-15}.

The strategy followed when using aqueous electrolytes is generally based on an anodic exfoliation with a Pt current collector. O₂ gas generation in the anode promotes the exfoliation process by the oxidation of (at least) the edges of the graphene layers that induce an expansion of the interlayer space so that ions can get into graphite more easily^{10,16,17}.

Neutral sulfate electrolytes have been widely used because they show the best exfoliation yield although they also lead to a high concentration of oxygen and defects

on the product^{10,16,18,19}. Actually, several different electrolytes have been studied in order to prevent the oxidation of graphene, using additives that inhibit graphene oxidation^{20,21}, surfactans²² or using alternative electrolytes^{10,11,14,23}.

On the other hand, electrochemical exfoliation of graphite in organic electrolytes generally produces better quality graphene with less defects and oxygen than for aqueous electrolytes. With organic electrolytes, in addition to anodic exfoliation²⁴ cathodic exfoliation is also used²⁵, furthermore simultaneous anodic and cathodic exfoliation have been also studied^{26,27} proving that the product generated in the cathode presents less defects and less oxygen than the product generated in the anode²⁸.

Organic electrolytes have typically included salts of large ions^{24,25,28-31}, but also with ionic liquids^{27,32} and even molten salts^{33,34}.

On the other hand, the effect of the precursor carbon materials used has received little attention in comparison with the exfoliation mechanism and conditions. Indeed, there are very few works focusing on the carbon precursor³⁵ or studying in a systematic way the influence of different carbon precursors under the same experimental conditions^{15,23,36,37}. There are even some reports in which it is not properly specified which was the carbon material used^{5,21,38,39}, which shows the little importance that in general it receives as a variable to consider for the exfoliation process.

As it will be shown in this work, the influence of the type of graphite material used as precursor for the exfoliation is huge, and affects the conditions needed for the exfoliation, the yield of the exfoliated material and the quality of the product. Consequently, a soft and thin graphite will be prone to exfoliation under a wider range of experimental conditions, whereas a compact, rigid and thick electrode would need extremely harsh conditions to be exfoliated, thus resulting in final graphene products with more oxygen and defects.

J.M.D. Tascon and col.³⁶ tackled this issue by studying the effect of four different carbon materials under anodic exfoliation, the materials were: Highly Oriented Pyrolytic Graphite (HOPG), rigid C flake, flexible C foil and C pellets made by compression of graphite powder with a hydraulic press in 0.1M K₂SO₄ aqueous electrolyte at 10V. By SEM analysis before and after the exfoliation of the materials they observed that HOPG and rigid C flake present a clearly more compact structure and consequently low expansion and delamination of the materials were observed. On the other hand, flexible C foil and C pellets showed larger expansion and delamination as a result of their lower compaction. In addition, flexible C foil showed greater exfoliation than the C pellet. This was explained considering that the small particles conforming the pellet lost the electrical

Chapter 7. New and Improved Cell and Method for the production of Graphene by Electrochemical Exfoliation of Graphites

contact due to its expansion at a very early step of the exfoliation process. Consequently, exfoliation processes were faster and thus more effective for C pellets (3 min) and flexible C foil (15 min) than rigid C flake and HOPG (60min each). Moreover, C pellets showed the lowest oxygen content (determined by XPS) and the lower amount of defects (determined by Raman) followed by flexible C foil, rigid C flake and finally HOPG. It should be noted the large amount of defects that shows the rigid C flake and particularly HOPG which D band is the most intense band in its Raman spectra. Another important result showed by J.M.D Tascon and col. is the increase of the oxygen content in the products as exfoliation time increases.

In a more recent paper by the same group,²³ Munuera et al. reported the exfoliation of graphene with halide aqueous electrolytes looking for a non-oxidative electrolyte. In this work they used HOPG, rigid graphite flake, and flexible C foil. They found that under those conditions the exfoliation process only works with flexible C foil. A SEM analysis of the materials before and after the exfoliation showed that due to the more compacted structure of HOPG and rigid graphite flake they were not able to be expanded and thus exfoliated by the electrolytes tested.

7.3 Patent

Reference	Application No./Patent No. 18382798.9 - 1108
Applicant/Proprietor Fundació Institut Català de Nanociència i Nanotecnologia, et al	

Designation as inventor - communication under Rule 19(3) EPC

You have been designated as inventor in the above-mentioned European patent application. Below you will find the data contained in the designation of inventor and further data mentioned in Rule 143(1) EPC:

DATE OF FILING : 12.11.18
PRIORITY : //
TITLE : ELECTROLYTIC CELL AND PROCEDURE FOR THE PREPARATION OF GRAPHENE BY MEANS OF ELECTROCHEMICAL EXFOLIATION
DESIGNATED STATES : AL AT BE BG CH CY OZ DE DK EE ES FI FR GB GR HR HU IE IS IT LI LT LU LV MC MK MT NL NO PL PT RO RS SE SI SK SM TR

INVENTOR (PUBLISHED = 1, NCT PUBLISHED = 0):

1/Gómez Romero, Pedro/C/Bassa 1, casa 14/08290 Cerdanyola/ES
1/Rueda García, Daniel/C/Rocafort 44, 5° 1ª/08015 Barcelona/ES

DECLARATION UNDER ARTICLE 81 EPC:

The applicant(s) has (have) acquired the right to the European patent as employer(s).

Receiving Section



Awarded in the Open Innovation Nanotech of Tokyo with the Technology Transfer award as part of CSIC portfolio awarded

Brief description of the invention

The present invention solves the problems described above, since it refers an electrolytic cell with a horizontal arrangement of the electrodes and a procedure for the fabrication of graphene from any type of graphite, including soft cheap graphitic materials such as powdered graphite.

This allows for an exfoliation process needing much less energy and time than those required for more compact materials which in turn implies a process less aggressive leading to a product with very small amounts of defects and oxygen and at a reduced cost.

Thus, in a first embodiment, the present invention refers to an electrolytic cell for the fabrication of graphene by means of electrochemical exfoliation of graphite (hereafter the electrolytic cell of the present invention), comprising a first electrode and a second electrode linked through a circuit, and separated by a given distance between each other, and being both first and second electrodes immersed in a liquid electrolyte contained in a vessel, characterized in that the first electrode and the second electrode are arranged in horizontal parallel planes as a functional condition for the fabrication of graphene, in which the first electrode is placed in a plane above the second electrode, with the second electrode presenting a confinement zone where the graphite to be exfoliated will be contained, with the mentioned confinement zone being bounded by a confining non-conducting material (such as a polymeric circular ring).

In a particular embodiment of the present invention, the confinement zone comprises a compacting element arranged in a plane parallel to the second electrode and in contact with the graphite to be exfoliated. More in particular, the compacting element is constituted by a porous non-conducting material, more in particular being a porous polymeric film. In a more particular embodiment the compacting element is made of filter paper.

In a particular embodiment of the present invention the first and second electrodes of the electrolytic cell of the present invention are arranged in parallel planes. More in particular the first and second electrodes of the electrolytic cell of the present invention are arranged at a distance between them of at least 1mm.

The electrodes of the present invention can be made of any conducting material as long as they are not oxidized at high voltages. In a particular embodiment, the first and second electrodes of the electrolytic cell of the present invention are made of the same material. More in particular, the first and second electrodes of the electrolytic cell

of the present invention are made of platinum. In another particular embodiment of the present invention, the first and second electrodes of the electrolytic cell of the present invention are made of glassy carbon.

In another particular embodiment of the present invention, the graphite to be exfoliated in the electrolytic cell of the present invention is graphite powder.

In another particular embodiment of the present invention, the graphite powder is mixed with solid particles of a non-oxidizable conducting material. More in particular, the solid particles of non-oxidizable material are selected from glassy carbon and platinum. More in particular, the mixture of graphite powder with solid particles of non-oxidizable material contains between 5-95% (in volume) of graphite powder. In another particular embodiment of the present invention, the graphite powder is contained in a conducting porous material resistant to oxidation at high voltages. In another particular embodiment of the present invention the electrolyte is an electrolyte not leading to a stable dispersion of graphene.

When we refer to an electrolyte in the present invention we mean organic and/or aqueous electrolytes.

In a second embodiment, the present invention refers to a procedure for the fabrication of graphene by means of the electrochemical exfoliation of graphite in an electrolytic cell as described in the present invention (hereafter procedure of the present invention), characterized by the following steps:

- a) Place the material to be exfoliated in the confinement zone on the second electrode.
- b) Apply a voltage to initiate the electrolytic process, in a more particular embodiment a voltage comprised between 3-15V is applied for a time comprised between 0.5-120 minutes during which the reactor is purged with a flow of inert gas in order to eliminate the possible gases generated during the reaction.
- c) Wash the product obtained after the electrolysis of step b in order to eliminate the electrolyte. In a more particular aspect the washing is made by filtering.

In a particular embodiment, voltage is applied in the form of pulses. More in particular, voltage is applied in the form of long pulses (10s to 1 min) of small voltages (1-5V) alternating with short pulses (1-10s) of high voltages (10-15V).

Description of the figures

Figure 1 is a schematic view showing the elements forming one of the embodiments of the electrolytic cell of the present invention.

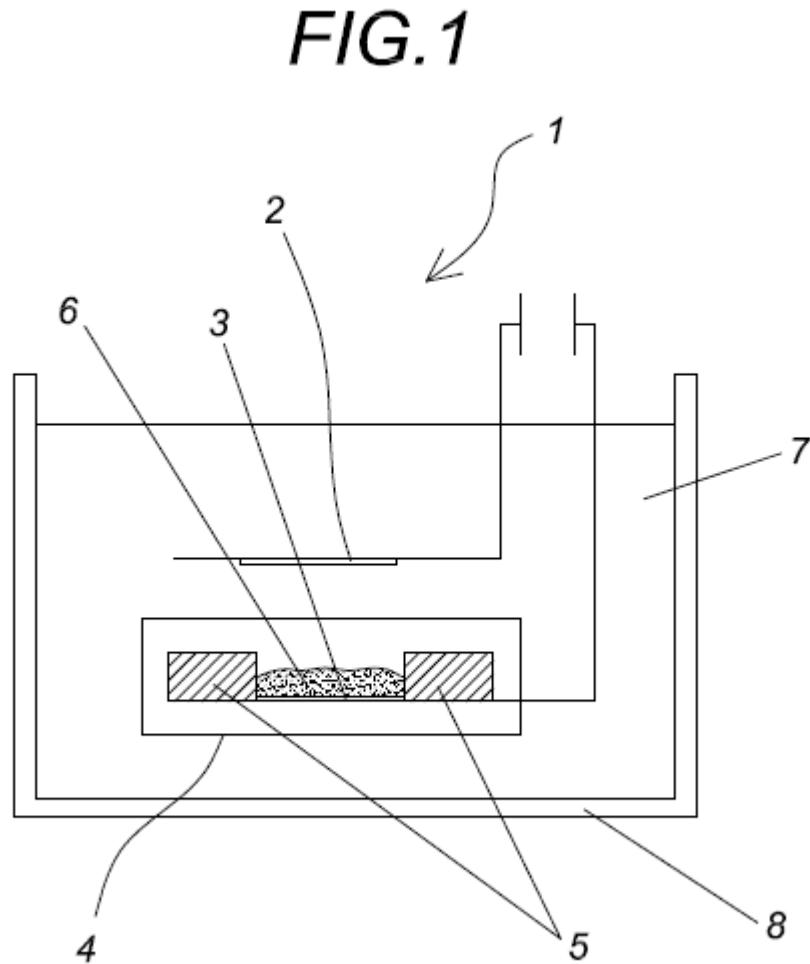


Figure 1

Figure 2 is a schematic view showing the elements forming one of the embodiments of the electrolytic cell of the present invention including the compacting element (9).

FIG.2

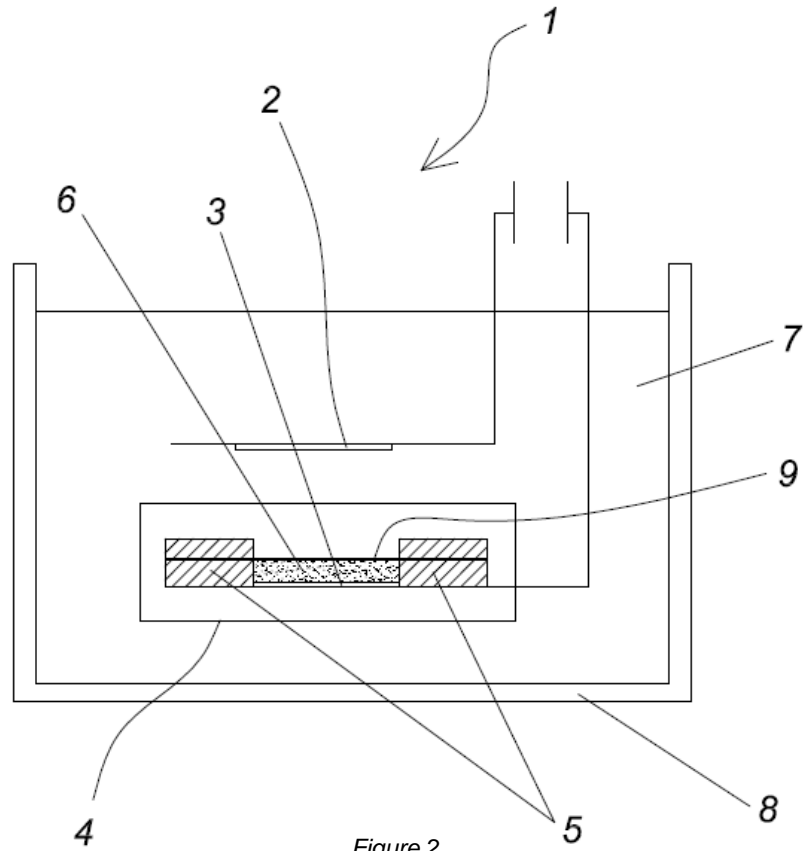


Figure 2

Figure 3 is a schematic view showing the elements forming one of the embodiments of the electrolytic cell of the present invention including the compacting element (9) and the graphite powder mixed with non-oxidizable solid particles.

FIG.3

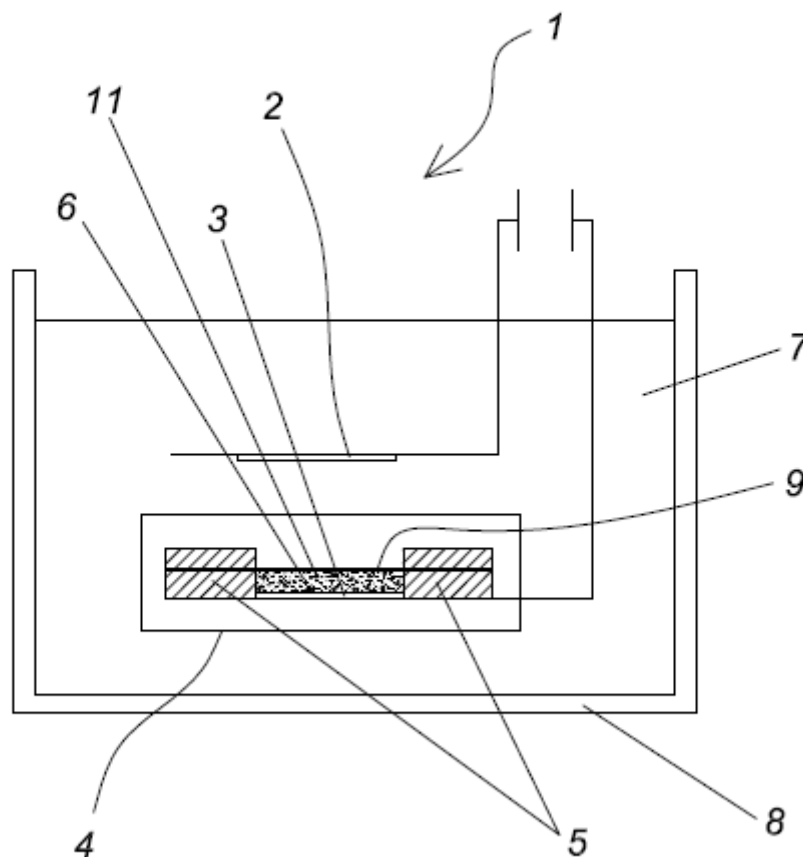


Figure 3

Description of a preferred embodiment of the invention

According to one form of realization, the electrolytic cell (1) for the fabrication of graphene by electrochemical exfoliation of graphite (6) comprises essentially a first electrode (2) a second electrode (3) linked and separated from each other, being both first and second electrodes (2), (3) immersed in a liquid electrolyte (7) contained in a vessel (8) made of a suitable material.

The first electrode (2) and the second electrode (3) are arranged horizontally as a functional condition to obtain graphene in which the first electrode (2) is placed in a plane above the second electrode (3).

In a more detailed description of the second electrode (3), the second electrode (3) presents a confinement zone (4) where the graphite to be exfoliated (6) is placed, with that confinement zone (4) bounded by a confining non-conducting material (5).

Desing of novel electroactive nanofluids for flow cell

Preferably, the graphitic material to be exfoliated (6) is graphite powder, although any other suitable material could be used for the same end.

As shown in figure 1, the first electrode (2) and the second electrode (3) are linked (through the external circuit) and separated by at least a 1 mm gap, with the first electrode (2) placed in a plane above the second electrode (3) an arranged in parallel planes. Both electrodes (2, 3) must be made of a conducting material resistant to oxidation at high voltages, with both electrodes (2, 3) made of platinum in this particular embodiment.

The system described in the present invention assures the obtention of few-layers graphene from graphite powder, using substantially lower voltages than those published in the literature and in a period of time much shorter, all of which represents a great reduction in the overall energy needed to carry out the process. Furthermore, thanks to the low voltages and short processing times needed, the concentrations of oxygen and defects in the final graphene are minimal. This is made possible thanks to the horizontal arrangement of the electrode on which the graphite powder is deposited, since in this configuration graphite particles are always in contact with the current collector.

The specific design of the electrolytic cell of the present invention allows for the use of graphite powder in such a way that during the electrochemical exfoliation process a flow of material from the electrode is generated, with larger, heavier particles being deposited by gravity in the confinement zone, in contact with the second electrode, whereas the lighter exfoliated material is displaced to the surface.

Thus, in addition to reducing the use of energy, time and production costs, the cell and procedure of the present invention allows for an automatic reutilization of poorly exfoliated material without any pre-treatment through a feedback system which could lead to yields close to 100%.

Abstract

The present invention relates to an electrolytic cell (1) for obtaining graphene by electrolytic exfoliation of graphite (6), comprising a first electrode (2) and a second electrode (3) linked and spaced apart, and both electrodes submerged in a liquid electrolyte (7) contained in a vessel (8), where both electrodes (2, 3) are arranged parallel and in a horizontal plane in a functional condition where graphene is obtained, in which the first electrode (2) is located right above the second electrode (3), the second electrode (2) presenting a confinement zone (4) (materialized by a confining non-conductive material(5)) in which the graphite (6) to be exfoliated is contained,. The invention also relates to the process for obtaining few-layers graphene in said electrolytic cell

Claims

1. Electrolytic cell (1) for the fabrication of graphene by electrochemical exfoliation of graphite (6), comprising a first electrode (2) and a second electrode (3) linked and separated and being both first and second electrode (1), (2) immersed in a liquid electrolyte (7) contained in a vessel (8), characterized in that the first electrode (2) and the second electrode (3) are arranged in a horizontal plane as a functional condition for the obtention of graphene, in which the first electrode (2) is placed in a plane above de second electrode (3), with the second electrode (3) featuring a confinement zone (4) in which the graphite (6) to be exfoliated can be placed, with that confinement zone (4) being delimited by a confining non-conducting material (5).

2. Electrolytic cell (1) according to claim 1, in which the confinement zone includes a compacting element (9) arranged in a plane parallel to the second electrode (3) and in contact with the graphite (6) to be exfoliated.

3. Electrolytic cell (1) according to any of the claims 1-2, in which the first and second electrodes (2), (3) are arranged in planes parallel between them.

4. Electrolytic cell (1) according to any of the claims above, in which the electrodes are separated by a distance of at least 1mm.

5. Electrolytic cell (1) according to any of the claims above, in which the first electrode (2) and/or the second electrode (3) are made of platinum.

6. Electrolytic cell (1) according to any of the claims above, in which the graphite to be exfoliated is in the form of graphite powder.

Desing of novel electroactive nanofluids for flow cell

7. Electrolytic cell (1) according to claim 6, in which the graphite powder is mixed with solid particles of a conducting non-oxidizable material.

8. Electrolytic cell (1) according to any of the claims above, in which the electrolyte leads to a non-stable dispersion of graphene.

9. Procedure for the fabrication of graphene by electrolytic exfoliation of a graphitic material in an electrolytic cell (1) according to any of the claims 1-8, characterized by comprising the following steps:

- a) place the material to be exfoliated (6) in the confinement zone (4) on the second electrode (3),
- b) apply a voltage leading to the electrolytic process,
- c) wash or purify the product obtained after the electrolysis carried out in step b).

10. Procedure for the fabrication of graphene according to claim 9, in which the material to be exfoliated (6) is graphite powder.

11. Procedure for the fabrication of graphene according to any of the claims 9-10, in which in step b) a voltage comprised between 3-15 V, is applied for a period of time comprised between 0.5-120 minutes,

13. Procedure for the fabrication of graphene according to any of the claims 9-11, in which the voltage is applied in the form of pulses.

7.4 Results

Exfoliation of graphite powder in the electrolytic cell with a compacting element and conducting particles mixed with the graphite powder to be exfoliated.

In an example of realization, an electrolytic cell (1) was set up, formed by a first electrode (2) and a second electrode (3) (in the present case the positive electrode) both made of platinum and arranged in a planar configuration separated by 10 mm, both immersed in a container filled with an electrolyte made of a 0.1M $(\text{NH}_4)_2\text{SO}_4$ aqueous solution. A compacting element (9) was included in the confinement zone as shown in figure (3). The confined zone contained 0.05g of graphite powder mixed with 0.2g of small glassy carbon.

Next, a 3 V voltage was applied, and 3 electrolysis times were tested: 3, 5 and 10 minutes. The products were then filtered off using a PTFE filter (0.2 μm pore size) and washed with water and acetone to remove remaining electrolyte salt, then weighed.

As an additional procedure, the better exfoliated fraction was separated from the rest by extraction with DMF, DMAc or NMP as it is described in the literature. In the present case the product was dispersed in DMF and left to stand for 24h in such a way that only few-layer graphene did not precipitate.

Finally, the precipitated fraction was collected, dried and weighed in order to determine the amount of few-layer graphene produced by weight difference.

The by-product not fully exfoliated could be used again as starting material for a new exfoliation process without the need of any special treatment.

Product characterization

Few drops of the stable graphene dispersion where dropped on a Ni (with also a bit of Cu) holey carbon grid, after one night all the DMF was evaporated and then samples where exanimated in the TEM:

3V 3min:

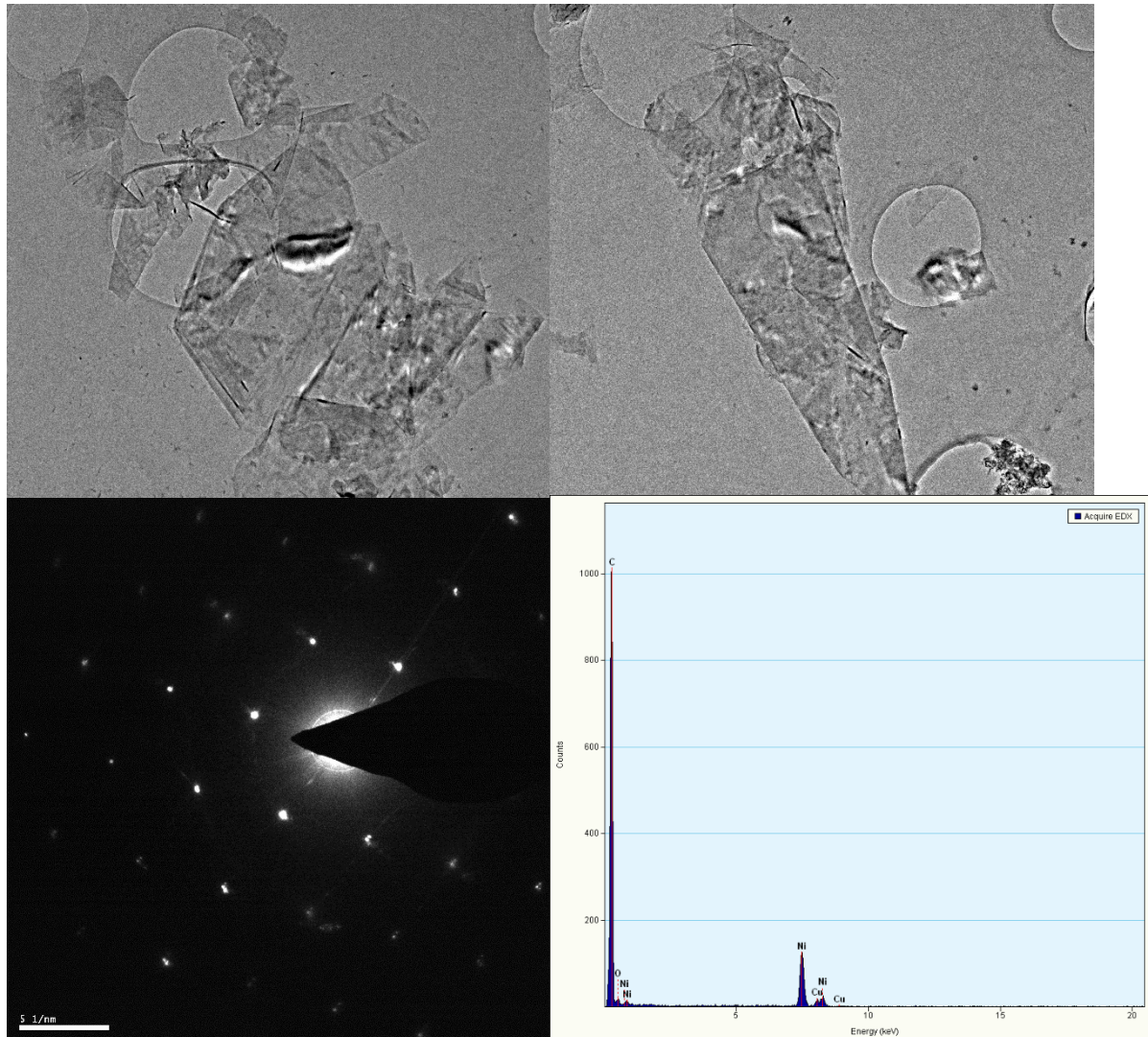


Fig.4 Up TEM images, left-bottom SAED image, right-bottom in situ EDX of the few layers graphene produced at 3V in 3min.

3V 5min:

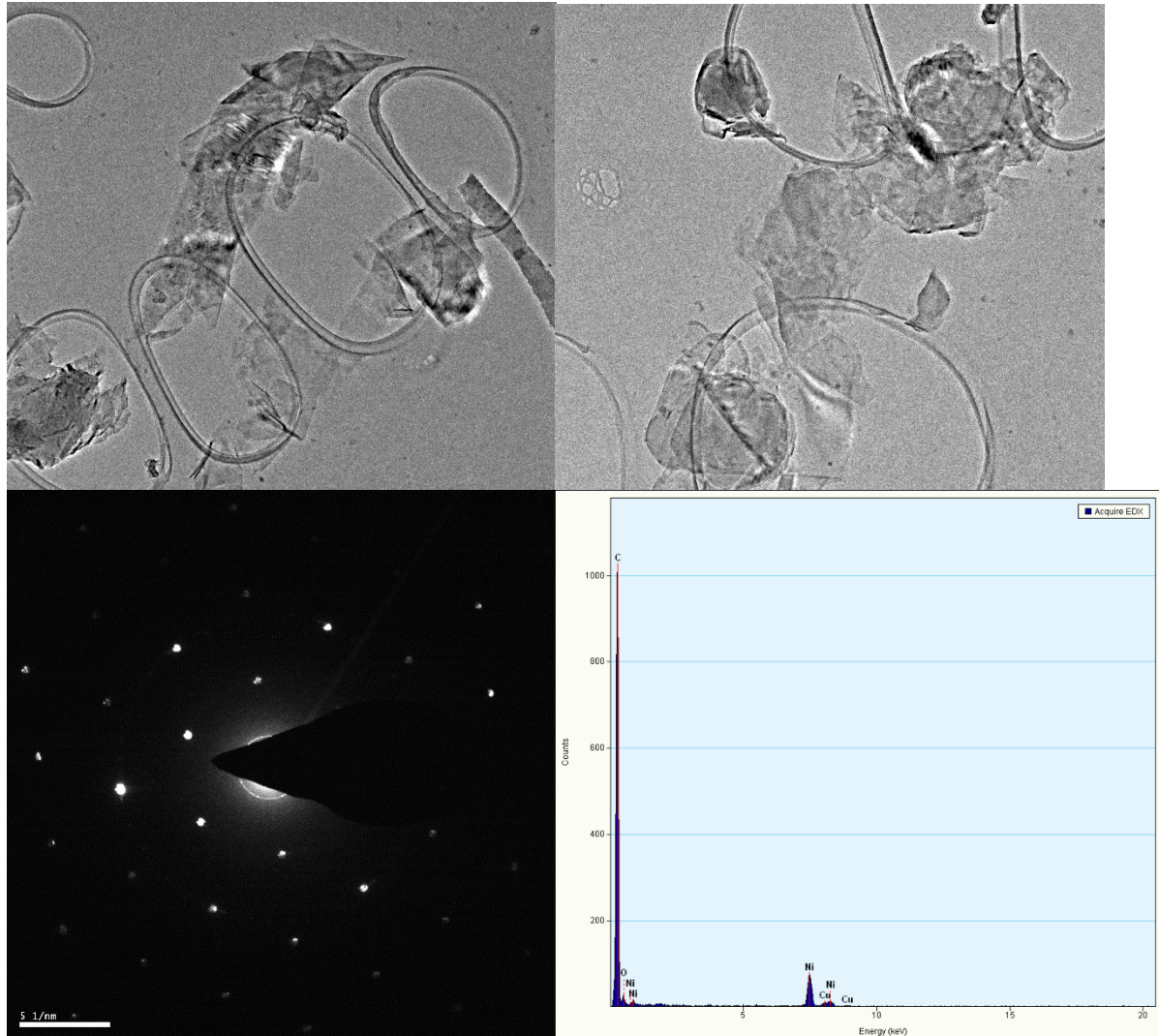


Fig.5 Up TEM images, left-bottom SAED image, right-bottom in situ EDX of the few layers graphene produced at 3V in 5min.

3V 10 min:

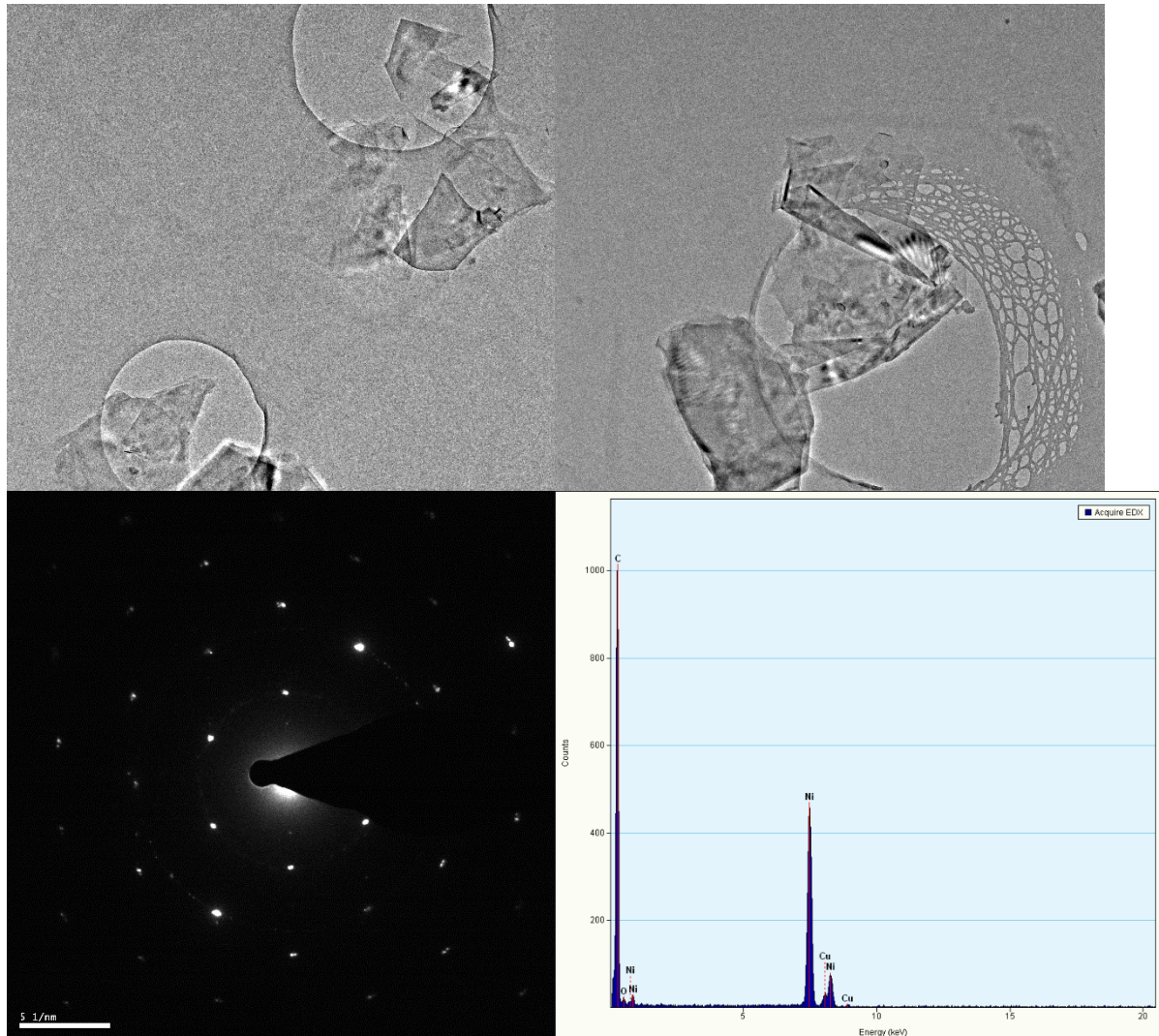


Fig.6. Up TEM images, left-bottom SAED image, right-bottom in situ EDX of the few layers graphene produced at 3V in 10min.

Desing of novel electroactive nanofluids for flow cell

TEM analysis confirms that the product obtained is few-layers graphene, whereas in situ EDX proves that the product was not oxidized during the electrochemical exfoliation.

In order to do Raman and XRD measurements the products were deposited on a Kapton substrate by a new sample preparation method specifically designed. To prepare the samples, LiClO_4 was added to the dispersions up to 1M to induce a flocculation process in the graphene, after 24h all the graphene had been precipitated. Next the excess of solvent was removed and the precipitated graphene deposited on a Kapton substrate placed on a watch glass to avoid leaking at the edges. After a week samples are dried, graphene and LiClO_4 were deposited on the Kapton substrate, finally, samples were very carefully cleaned with acetone to remove LiClO_4 .

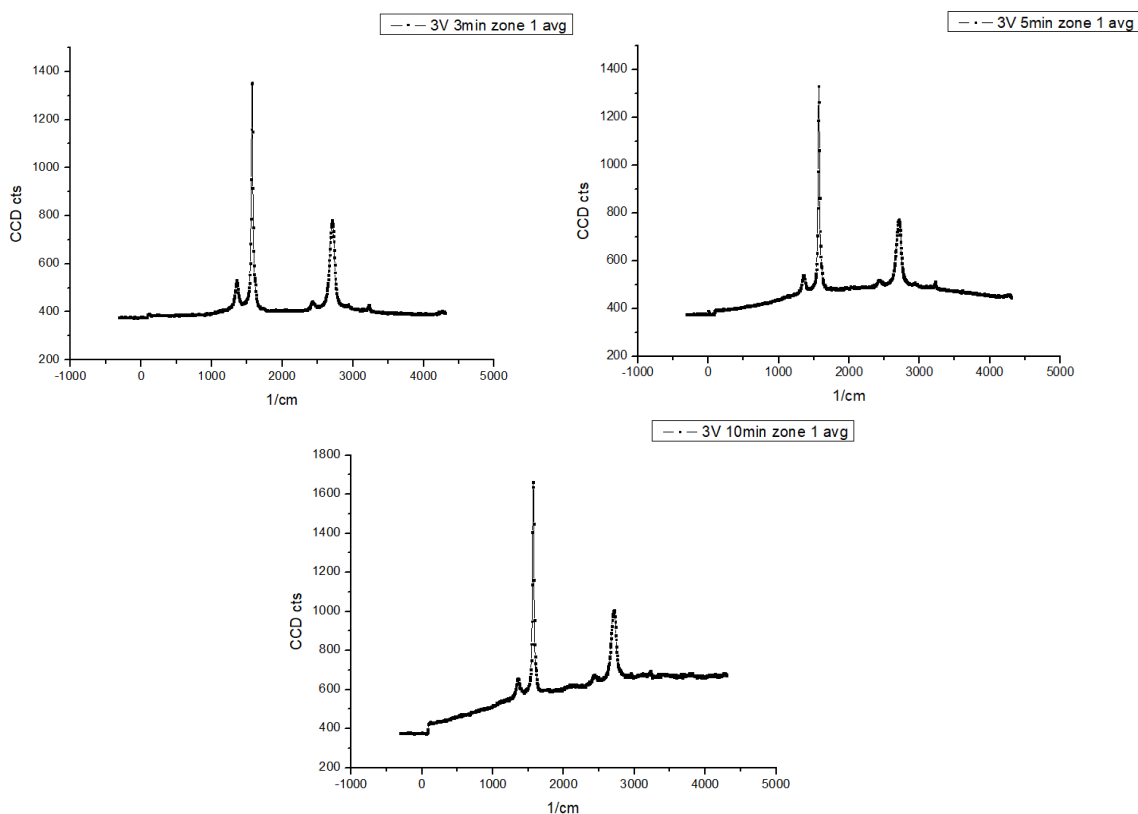


Fig.7 Raman spectra of the electrochemical exfoliation products: top-left 3v 3min, top-right 3V 5min, bottom 3V 10 min.

Raman spectra show that our product is virtually free of defects. The D band is very weak, in good agreement with TEM results⁴⁰. The weak D band could be just resulting from the edges of the graphene layers⁴¹.

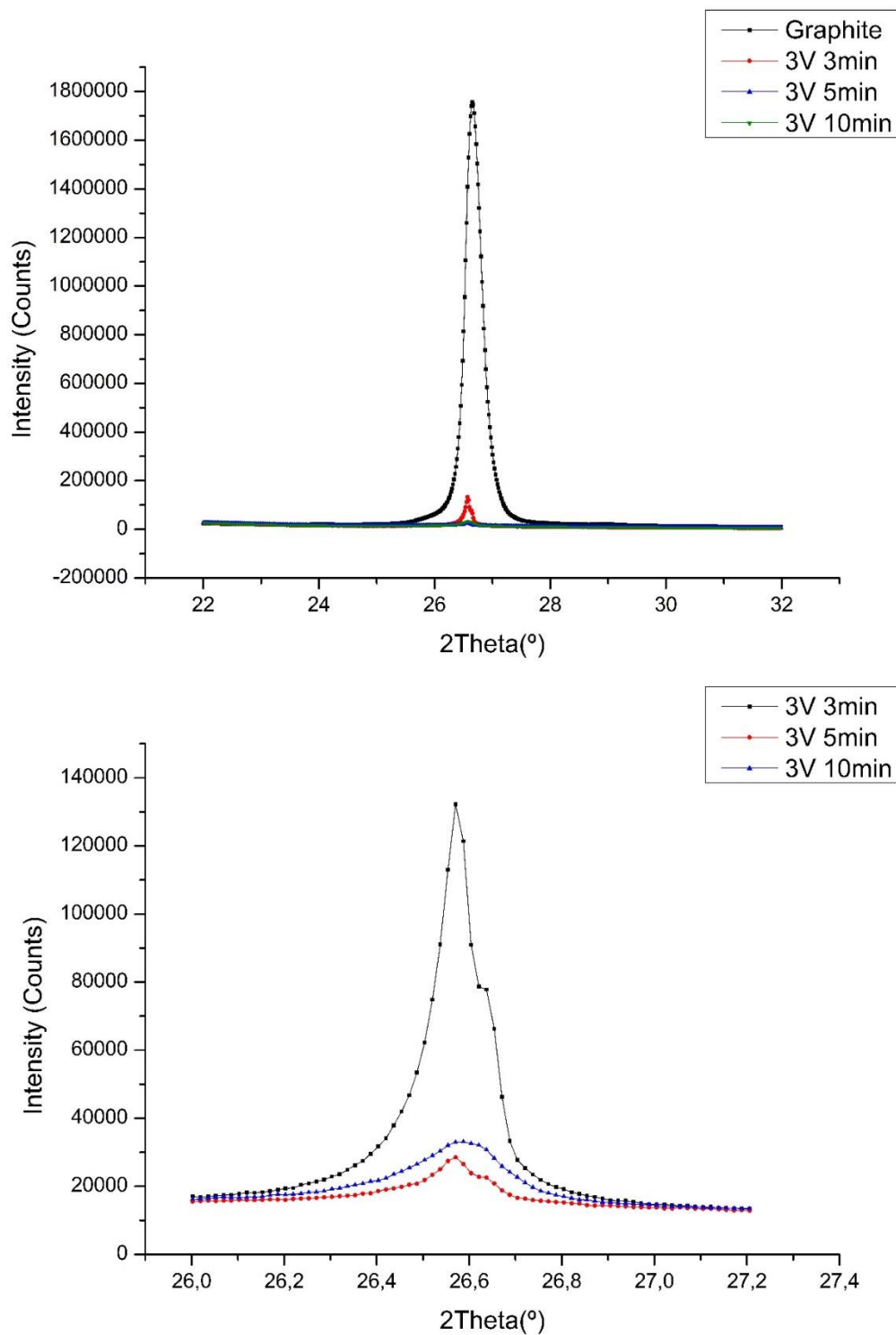


Fig.8 XRD of graphene samples and graphite base product, bottom picture is an inset of the graphene diffractograms.

XRD results show a small, but clear, displacement of the 002 peak in graphite to slightly smaller angles in graphene (from 26.65° in the graphite sample to 26.57° in the graphene samples). In addition, a shoulder can be appreciated in the graphene peaks at the same position of the graphite peak. These results prove that the inter-planar spacing in the graphene samples is a bit larger than in graphite⁴² this suggest a different microcrystalline structure in graphene⁴³. In addition the shoulder of the graphene peaks at the same position than the peak of the graphite suggest that the graphene produced have also part of the same structure than graphite, thus it present a non-uniform multilayer distribution^{44,45}.

These results fit with the data of the Raman spectra and the TEM/EDX that shows no defects and oxidation in our graphene. If our graphene would be oxidized and/or present a high concentration of defects on its structure the displacement of the 002 peak in the XRD would be clearly larger, more than 10° for GO, and peak width would be clearly larger^{46,47}.

Moreover, it should also be pointed out that for the recording of the XRD of graphene produced, a similar mass to that of graphite was used and it was also measured on a Kapton film. Therefore, the big difference in intensity recoded between graphite and graphene samples is not due to a large difference in mass, which could corroborate that our product has few layers.

Our current prototype should be improved because it doesn't allow to keep under a minimum pressure the graphite powder, which is not completely sealed into the cell (figure 9). As a consequence, poor electrical conductivity between carbon particles still limits the efficiency of the exfoliation process

Desing of novel electroactive nanofluids for flow cell

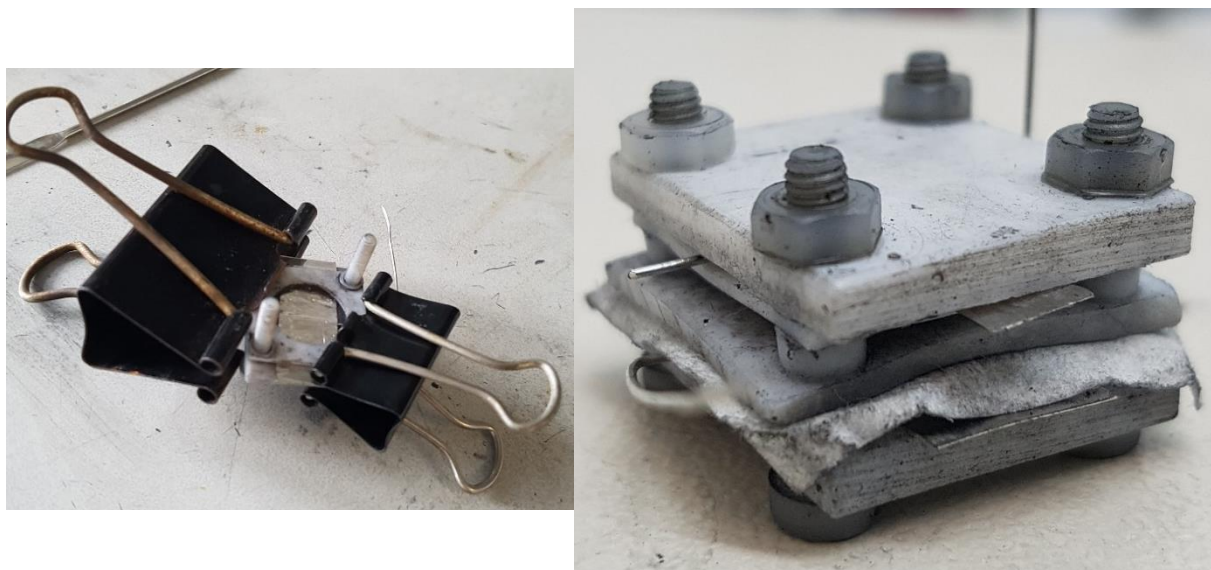


Fig.9 Prototype of the electrochemical cell patented, could be observed that is a very simple cell with important issue in order to be assembled and to keep seal and under pressure the graphite to be exfoliate.

Due to the limitations of the current prototype no significant differences in yield were observed between the 3 times tested, yield was measured by two methods:

- Weight difference between the product collected from the exfoliation process and the product initially precipitated after dispersion in DMF (after 24h).
- Transmittance measurements of the stable dispersions obtained

However, there is one order of magnitude of difference between these two methods, probably because the small amounts of sample obtained induces big errors in the weigh process.

By weigh difference the concentration of the graphene dispersions obtained where:

- 3 minutes: $0.48 \text{ g}\cdot\text{L}^{-1}$
- 5 minutes: $0.79 \text{ g}\cdot\text{L}^{-1}$
- 10 minutes: $0.88 \text{ g}\cdot\text{L}^{-1}$

And the concentration calculated by the Beer–Lambert law ($\epsilon = 1390 \text{ L}\cdot\text{g}^{-1}\cdot\text{m}^{-1}$)⁴⁸:

- 3 minutes: $0.05 \text{ g}\cdot\text{L}^{-1}$
- 5 minutes: $0.08 \text{ g}\cdot\text{L}^{-1}$
- 10 minutes: $0.04 \text{ g}\cdot\text{L}^{-1}$

We are confident that with the optimization of the design mentioned above and the scaling up of the set-up and procedure these values will improve substantially in the future.

References

1. Bonaccorso, F. *et al.* Graphene, related two-dimensional crystals, and hybrid systems for energy conversion and storage. *Science (80-.)*. **347**, (2015).
2. Novoselov, K. S. *et al.* A roadmap for graphene. *Nature* **490**, 192–200 (2012).
3. Zhong, Y. L., Tian, Z., Simon, G. P. & Li, D. Scalable production of graphene via wet chemistry: Progress and challenges. *Mater. Today* **18**, 73–78 (2015).
4. Low, C. T. J., Walsh, F. C., Chakrabarti, M. H., Hashim, M. A. & Hussain, M. A. Electrochemical approaches to the production of graphene flakes and their potential applications. *Carbon N. Y.* **54**, 1–11 (2013).
5. Ambrosi, A. & Pumera, M. Electrochemically Exfoliated Graphene and Graphene Oxide for Energy Storage and Electrochemistry Applications. *Chem. - A Eur. J.* **22**, 153–159 (2016).
6. Sorokina, N. E., Maksimova, N. V. & Avdeev, V. V. Anodic oxidation of graphite in 10 to 98% HNO₃. *Inorg. Mater.* **37**, 360–365 (2001).
7. Huang, H. *et al.* Electrochemical Cutting in Weak Aqueous Electrolytes: The Strategy for Efficient and Controllable Preparation of Graphene Quantum Dots. *Langmuir* **34**, 250–258 (2018).
8. Wang, X., Sun, G., Li, N. & Chen, P. Quantum dots derived from two-dimensional materials and their applications for catalysis and energy. *Chem. Soc. Rev.* **45**, 2239–2262 (2016).
9. Chuang, C. H. *et al.* A green, simple and cost-effective approach to synthesize high quality graphene by electrochemical exfoliation via process optimization. *RSC Adv.* **5**, 54762–54768 (2015).
10. Paredes, J. I. & Munuera, J. M. Recent advances and energy-related applications of high quality/chemically doped graphenes obtained by electrochemical exfoliation methods. *J. Mater. Chem. A* **5**, 7228–7242 (2017).
11. Wu, W., Zhang, C. & Hou, S. Electrochemical exfoliation of graphene and graphene-analogous 2D nanosheets. *J. Mater. Sci.* **52**, 10649–10660 (2017).
12. Yu, P., Lowe, S. E., Simon, G. P. & Zhong, Y. L. Electrochemical exfoliation of graphite and production of functional graphene. *Curr. Opin. Colloid Interface Sci.* **20**, 329–338 (2015).
13. Abdelkader, A. M., Cooper, A. J., Dryfe, R. A. W. & Kinloch, I. A. How to

- get between the sheets: A review of recent works on the electrochemical exfoliation of graphene materials from bulk graphite. *Nanoscale* **7**, 6944–6956 (2015).
14. Yang, S., Lohe, M. R., Müllen, K. & Feng, X. New-Generation Graphene from Electrochemical Approaches: Production and Applications. *Adv. Mater.* 6213–6221 (2016). doi:10.1002/adma.201505326
 15. Coroş, M. *et al.* Simple and cost-effective synthesis of graphene by electrochemical exfoliation of graphite rods. *RSC Adv.* **6**, 2651–2661 (2016).
 16. Parvez, K., Wu, Z., Li, R., Liu, X. & Graf, R. Exfoliation of Graphite into Graphene in Aqueous Solutions of inorganic salts. *J. Am. Chem. Soc.* (2014). doi:10.1021/ja5017156
 17. Hofmann, M., Chiang, W. Y., D Nguyn, T. & Hsieh, Y. P. Controlling the properties of graphene produced by electrochemical exfoliation. *Nanotechnology* **26**, (2015).
 18. Wu, L. *et al.* Powder, paper and foam of few-layer graphene prepared in high yield by electrochemical intercalation exfoliation of expanded graphite. *Small* **10**, 1421–1429 (2014).
 19. Su, C. Y. *et al.* High-quality thin graphene films from fast electrochemical exfoliation. *ACS Nano* **5**, 2332–2339 (2011).
 20. Chen, C. H., Yang, S. W., Chuang, M. C., Woon, W. Y. & Su, C. Y. Towards the continuous production of high crystallinity graphene via electrochemical exfoliation with molecular in situ encapsulation. *Nanoscale* **7**, 15362–15373 (2015).
 21. Yang, S. *et al.* Organic Radical-Assisted Electrochemical Exfoliation for the Scalable Production of High-Quality Graphene. *J. Am. Chem. Soc.* **137**, 13927–13932 (2015).
 22. Alanyalıoğlu, M., Segura, J. J., Oró-Sol, J. & Casañ-Pastor, N. The synthesis of graphene sheets with controlled thickness and order using surfactant-assisted electrochemical processes. *Carbon N. Y.* **50**, 142–152 (2012).
 23. Munuera, J. M. *et al.* Electrochemical Exfoliation of Graphite in Aqueous Sodium Halide Electrolytes toward Low Oxygen Content Graphene for Energy and Environmental Applications. *ACS Appl. Mater. Interfaces* **9**, 24085–24099 (2017).
 24. Najafabadi, A. T. & Gyenge, E. High-yield graphene production by electrochemical exfoliation of graphite: Novel ionic liquid (IL)-acetonitrile electrolyte with low IL content. *Carbon N. Y.* **71**, 58–69 (2014).
 25. Yang, Y. *et al.* Electrochemically triggered graphene sheets through cathodic exfoliation for lithium ion batteries anodes. *RSC Adv.* **3**, 16130–16135 (2013).
 26. Chakrabarti, M. H. *et al.* One-pot electrochemical gram-scale synthesis of graphene using deep eutectic solvents and acetonitrile. *Chem. Eng. J.*

- 274**, 213–223 (2015).
27. Lu, J. *et al.* One-Pot Synthesis of Fluorescent Carbon Graphene by the Exfoliation of Graphite in Ionic Liquids. *ACS Nano* **3**, 2367–2375 (2009).
 28. Najafabadi, A. T. & Gyenge, E. Synergistic production of graphene microsheets by simultaneous anodic and cathodic electro-exfoliation of graphitic electrodes in aprotic ionic liquids. *Carbon N. Y.* **84**, 449–459 (2015).
 29. Cooper, A. J., Wilson, N. R., Kinloch, I. A. & Dryfe, R. A. W. Single stage electrochemical exfoliation method for the production of few-layer graphene via intercalation of tetraalkylammonium cations. *Carbon N. Y.* **66**, 340–350 (2014).
 30. Abdelkader, A. M., Kinloch, I. A. & Dryfe, R. A. W. Continuous electrochemical exfoliation of micrometer-sized graphene using synergistic ion intercalations and organic solvents. *ACS Appl. Mater. Interfaces* **6**, 1632–1639 (2014).
 31. Xia, Z. Y. *et al.* Synergic exfoliation of graphene with organic molecules and inorganic ions for the electrochemical production of flexible electrodes. *Chempluschem* **79**, 439–446 (2014).
 32. Abdelkader, A. M., Patten, H. V., Li, Z., Chen, Y. & Kinloch, I. A. Electrochemical exfoliation of graphite in quaternary ammonium-based deep eutectic solvents: a route for the mass production of graphene. *Nanoscale* **7**, 11386–11392 (2015).
 33. Kim, H. K., Kamali, A. R., Roh, K. C., Kim, K. B. & Fray, D. J. Dual coexisting interconnected graphene nanostructures for high performance supercapacitor applications. *Energy Environ. Sci.* **9**, 2249–2256 (2016).
 34. Kamali, A. R. & Fray, D. J. Large-scale preparation of graphene by high temperature insertion of hydrogen into graphite. *Nanoscale* **7**, 11310–11320 (2015).
 35. Sharief, S. A., Susantyoko, R. A., Alhashem, M. & Almheiri, S. Synthesis of few-layer graphene-like sheets from carbon-based powders via electrochemical exfoliation, using carbon black as an example. *J. Mater. Sci.* **52**, 11004–11013 (2017).
 36. Munuera, J. M. *et al.* High quality, low oxygen content and biocompatible graphene nanosheets obtained by anodic exfoliation of different graphite types. *Carbon N. Y.* **94**, 729–739 (2015).
 37. Marković, Z. M. *et al.* Semi-transparent, conductive thin films of electrochemically exfoliated graphene. *RSC Adv.* **6**, 39275–39283 (2016).
 38. Liu, Z. *et al.* Ultraflexible In-Plane Micro-Supercapacitors by Direct Printing of Solution-Processable Electrochemically Exfoliated Graphene. *Adv. Mater.* **28**, 2217–2222 (2016).
 39. Bakhshandeh, R. & Shafiekhani, A. Ultrasonic waves and temperature effects on graphene structure fabricated by electrochemical exfoliation method. *Mater. Chem. Phys.* **212**, 95–102 (2018).

40. Seehra, M. S., Narang, V., Geddam, U. K. & Stefaniak, A. B. Correlation between X-ray diffraction and Raman spectra of 16 commercial graphene-based materials and their resulting classification. *Carbon N. Y.* **111**, 380–385 (2017).
41. Ni, Z., Wang, Y., Yu, T. & Shen, Z. Raman spectroscopy and imaging of graphene. *Nano Res.* **1**, 273–291 (2008).
42. Barnakov, C. N., Khokhlova, G. P., Popova, A. N., Sozinov, S. A. & Ismagilov, Z. R. XRD characterization of the structure of graphites and carbon materials obtained by the low-temperature graphitization of coal tar pitch. *Eurasian Chem. J.* **17**, 87–93 (2015).
43. Li, Z. Q., Lu, C. J., Xia, Z. P., Zhou, Y. & Luo, Z. X-ray diffraction patterns of graphite and turbostratic carbon. *Carbon N. Y.* **45**, 1686–1695 (2007).
44. Andonovic, B., Ademi, A., Grozdanov, A., Paunović, P. & Dimitrov, A. T. Enhanced model for determining the number of graphene layers and their distribution from X-ray diffraction data. *Beilstein J. Nanotechnol.* **6**, 2113–2122 (2015).
45. Andonovic, B. *et al.* Laue functions model vs scherrer equation in determination of graphene layers number on the ground of XRD data. *J. Chem. Technol. Metall.* **49**, 545–550 (2014).
46. June, P., Eq, A. & Eq, A. An Introduction to Graphene Plasmonics Erratum. 1–2 (2016).
47. Seehra, M. S., Geddam, U. K., Schwegler-Berry, D. & Stefaniak, A. B. Detection and quantification of 2H and 3R phases in commercial graphene-based materials. *Carbon N. Y.* **95**, 818–823 (2015).
48. Hernandez, Y. *et al.* Liquid Phase Production of Graphene by Exfoliation of Graphite in Surfactant/Water Solutions. *J. Am. Chem. Soc.* **131**, 3611–3620 (2009).

CHAPTER 8
CONCLUSIONS

General conclusions

In this thesis, a wide variety of materials have been studied with the common goal of improving the capability of flow cells fluids to store energy. Given this variety that spans from molecular species (both organic and inorganic) to extended phases (inorganic and carbons) it might seem difficult to extract a general conclusion. Nevertheless, when we consider the knowledge gained as a result of our work, we could make some general statements about the different approaches that could be taken in order to improve a parameter in principle so simple as the solubility of the active species. Indeed, both for quinones and for POMs and for LiFePO_4 we were aiming at increasing the concentration of our fluids and found many unexpected problems, like spurious reactions of bare quinones or limited stability of LiFePO_4 dispersions. It should be stressed though, that in all cases our work led to the proposal of alternative ways to guide the path to this final objective (steric protection in quinones, stabilization with DABA of rGO-LiFePO_4 in the latter case). Furthermore, a very important general conclusion of this Thesis is that we have been able to demonstrate how to utilize electroactive solid phases, properly dispersed in electrolyte solutions (in itself a difficult task), for energy storage in a novel type of flow cells. A proof of concept with important implications.

Specific conclusions. In addition to the conclusions published in each of the articles, we present here an extended list of more detailed conclusions for each of the works described. Since the last article presented (Energies, 2019) is itself an extended overview and discussion of our research work in graphene nanofluids, no specific conclusions have been written corresponding to this article.

Organic quinone solutions

- Lithium ion has a strong impact in the electrochemical mechanism of quinones in aprotic solvents. Contrary to the behavior previously reported for other cations, the two electrons involved in the reduction of the quinone molecule are transferred at almost the same potential. This represents a mechanism very similar to that found in protic solvents, and leads to an improved electrochemical reversibility.
- When small non-hindered quinones are reduced in organic Li electrolytes, a reversible green coating is formed on the electrode at negative overpotentials. It is due to the formation of an ionic pair between reduced quinones and Li⁺, which can be dissolved in the solution with mild stirring.
- The same green coating was obtained by the chemical oxidation of Li metal with a solution of small unhindered quinones.
- The rate of formation of the green coating is proportional to the quinone hindrance. Smaller quinones with no steric hindrance present the highest generation speed, whereas large and bulky quinones will not generate the green coating.
- The green coating acts as a passivating layer and prevents the completion of quinone reduction on the electrode. Larger negative overpotentials induce a polymerization process of the quinones on the green layer, leading to an insoluble product with a resistance lower than the initial green layer, but larger than the electrode.
- The formation of the green coating does not depend on the presence of oxygen. On the other hand, the mechanism of the subsequent redox polymerization is different in the presence or absence of oxygen.
- Despite an improved electrochemical reversibility of quinones in aprotic Li⁺ electrolytes (reduced separation of redox waves as Li⁺ concentration increases), effective reoxidation does not take place due to the precipitation of a large fraction of the reduced quinone-Li₂ generated.
- Larger and bulky quinones can be used in electroactive solutions to avoid the unwanted processes described and to ensure good stability over time. However, large and bulky quinones have poorer solubility in polar solvents. The combination of these two factors is at the heart of the difficulties to use quinones as active species for energy storage in organic electroactive fluids.

Hybrid rGO-POM nanofluids

- Hybrid rGO-POM materials have a homogenous distribution of POMs on the rGO layers, POMs are not crystallized on the rGO.
- rGO and rGO-POMs aqueous dispersions have a small viscosity, in the range 1.2-1.8 mPa·s, close to the value of water (1.0 mPa·s).
- The nanofluids with 0.025 wt% of rGO-POM (both for P_{Mo12} and P_{W12}) showed greater long-term stability as compared with 0.1 and 0.4 wt%.
- These nanofluids showed high values of specific capacitance both when studied by CV (Maximum specific capacitance values of 306 F/g(rGO-P_{Mo12}) and 273 F/g(rGO-P_{W12}) for 0.025% rGO-POM at a scan rate of 5 mV/s) as well as through charge discharge cycles (223 F/g(rGO-P_{Mo12}) and 208 F/g(rGO-P_{W12}) at current density of 4 A/g). These values are comparable or even better than those found for related solid electrodes.
- Flowing improves the specific capacitance per gram of active material with respect to static conditions. 10ml/min was found to be the optimal flow rate, although this parameter would heavily depend on the cell design.
- rGO aqueous dispersions in acidic electrolytes showed very fast charge transfer (could cycle up to 10V/s and charge and discharge at 16 A/g) utilizing all of the active material dispersed, thus, performing as conventional supercapacitors but with flowing design.
- POM addition to rGO allows to increase the working potential window, thus increasing the power density of the nanofluid (specific power between 2-8 kW/kg_{rGO-POM}) (with specific power for rGO between 0.45-1.0 kW/ kg_{rGO}).
- POM addition to rGO increases the capacity and as a result the energy density of the nanofluid increases. (between 8-29 Wh/kg_{rGO-POM} as compared to between 5-15 Wh/kg_{rGO} for the parent rGO)
- Good cyclability was observed, cycle efficiency was 77-79% after 2000 charge discharge cycles at different current densities.
- Relative low stability of the dispersion was observed despite low content of active material and use of surfactant, precipitation begins after 10h.
- Despite the good intrinsic performance, the low effective concentration of solid active nanoparticles results in nanofluids with low volumetric and mass energy density.

DABA-rGO and DABA-rGO-LiFePO₄ nanofluids

- rGO was successfully dispersed in water by addition of DABA. The optimal dispersion, with a ratio DABA:rGO of 40:1, showed a great stability and low viscosity (1.055 mPa·s), starting to precipitate after 97h.
- DABA and rGO interact through π - π interactions, thus solved DABA molecules hold graphene dispersed and preclude rGO restacking.
- rGO enhances an irreversible oxidation process of DABA, not observed for pure DABA. This constitutes a proof of the strong interaction between DABA and rGO.
- DABA-rGO nanofluids showed an excellent charge transfer capability, allowing for an effective and complete charge-discharge of pure LiFePO₄ NPs added to the nanofluid. Those particles showed no electrochemical response with no DABA-rGO in the nanofluid.
- The addition of LiFePO₄ NPs to the nanofluid reduced and even made disappear (depending on the scan rate velocity, DABA peak is reduced as the scan rate increases) the redox peak of DABA enhanced by rGO. We believe that is because the fast and reversible redox process of LiFePO₄ precludes the irreversible redox process of DABA, which in turn is only possible thanks to rGO.
- We have demonstrated the feasibility to fully charge and discharge insulating nanoparticles such as LiFePO₄ (not coated by carbon or any other conductive agent) dispersed into the nanofluid. This confirms that a percolation effect exists between rGO layers which allows to transfer charge through all the volume.
- Addition of LiFePO₄ reduces the stability of the nanofluid to 24 h approximately, even when low concentrations of NPs were used. As a result, our nanofluid has a low volumetric and mass energy density, since greater concentrations of LiFePO₄ would result in unstable dispersions.
- An asymmetric balanced cell was setup with DABA-rGO as negative and DABA-rGO-LiFePO₄ as positive electrodes (electrolyte...) demonstrating the feasibility to combine purely capacitive nanofluids with hybrid capacitive-faradaic ones.

Graphene from the electrochemical exfoliation of graphite

- The type of graphite used as graphene precursor is the most important variable to consider in an electrochemical exfoliation to fabricate graphene. Even under the same exfoliation conditions (i.e. voltage, electrolyte and time), different precursors can lead to very different products (i.e. number of layers and amount of oxygen/defects) and very different exfoliation yields.
- Harder exfoliation conditions will promote more oxygen and defects in the exfoliated products. However, these hard conditions would not ensure high exfoliation yields because it would depend on the precursor.
- Hard and thick carbon precursors would be very difficult to exfoliate; only harsh conditions would exfoliate this kind of materials. As a consequence of this harsh conditions, large amounts of oxygen and defects would be present on the exfoliated product. Consequently, the resulting products could be considered closer to a reduced graphene oxide in the best cases and graphene oxide in the worst.
- On the other hand, soft and thin carbon precursors would be very easy to exfoliate at any conditions. Due to the low energy needed to exfoliate this kind of precursors, very few defects and oxygen will be present into the exfoliated product. Moreover, for these precursors exfoliation processes would be faster than for hard and thick precursors.
- Conventional electrochemical exfoliation setups (based on the electrode positioned vertically and immersed in the electrolyte) present the serious drawback of the loss of non-exfoliated material resulting from the breaking and detachment of part of the electrodes during the exfoliation process.
- Graphite powder can be directly exfoliated into graphene. As a matter of fact, it can be the precursor more easily exfoliated, needing lower voltages and times and thus, consuming less energy and time, and leading altogether to a product with a minimum amount of oxygen and defects.
- Nevertheless, a powder cannot be exfoliated in available electrochemical cells because it would just get dispersed in the electrolyte. A new and specific electrochemical cell has been designed in order to allow for the exfoliation of powders.
- A horizontal cell configuration has been demonstrated as an effective configuration to exfoliate powders. Specifically, a suitable current collector was placed on the bottom of a cavity in which the powder to be exfoliated was placed.

Desing of novel electroactive nanofluids for flow cell

- Carbon powders have a deficient contact between the particles during the exfoliation. As a consequence, two solutions were implemented in the horizontal cell design in order to improve the electrical conductivity between carbon particles. First, a cover/holder was added to the cavity that at the same time allowed for an applied pressure to the powder, compacting it in the cavity. Second, the carbon powder to be exfoliated was mixed with glassy carbon macro-microscopic particles in order to get conductive particles that would not be exfoliated and could provide electrons from the current collector during all the exfoliation process.

APPENDIX
RESUMEN EN
CASTELLANO

Desarrollo de nuevos nanofluidos electroactivos para celdas de flujo

Las celdas de flujo van camino de convertirse en una pieza clave para el almacenamiento de energía eléctrica (EES) gracias a su idoneidad como dispositivos de nivelación de carga, contribuyendo así al desarrollo de una red inteligente que pueda compensar la intermitencia de las fuentes de energía renovables. Hasta hace poco, las celdas de flujo se habían limitado a las baterías de flujo redox (RFB), donde el almacenamiento de energía está dado por las reacciones redox de los iones disueltos. Muy recientemente, se han propuesto nuevos tipos de electrodos líquidos basados en un mecanismo de almacenamiento capacitivo (condensadores de flujo electroquímicos o EFC). Nuestro grupo ha sido uno de los laboratorios pioneros en este tipo de nuevas celdas de flujo basadas en nanofluidos electroactivos. La presente Tesis ha tenido como objetivo aprovechar la actividad de especies electroactivas bien conocidas (quinonas, grafeno, polioxometalatos, LiFePO_4) en nuevos nanofluidos electroactivos. Una parte importante de nuestra estrategia ha sido el diseño de formulaciones y sistemas híbridos que pudieran combinar mecanismos de almacenamiento faradaico (redox) y capacitivo (doble capa) para mejorar el rendimiento de las celdas de flujo resultantes.

En la introducción de esta tesis se ha realizado una revisión y perspectiva ampliadas de las tecnologías de celdas de flujo electroquímicas y sus posibles líneas de evolución. Con esto se presentan el estado del arte, los problemas a resolver y las diferentes soluciones propuestas para estas tecnologías. Además, también mostramos nuestro punto de vista y perspectivas para estas tecnologías y el almacenamiento de energía eléctrica en general. Por ello esta parte constituye la parte principal de la introducción y una parte fundamental de esta tesis para entender los objetivos, motivaciones y el trabajo realizado.

En el capítulo 4 se estudiaron los fundamentos electroquímicos de las quinonas en electrolitos orgánicos con sal de litio. Los mecanismos electroquímicos de las quinonas se han descrito ampliamente en la bibliografía pero en medios acuosos. En este trabajo, los estudiamos en un electrolito orgánico en un intento de aprovechar la mayor solubilidad y las ventanas de potencial más amplias disponibles en este medio. Encontramos y describimos en detalle varios problemas que impiden el funcionamiento reversible de las quinonas en los electrolitos orgánicos con Li^+ que, a su vez, impiden su uso en celdas de flujo en esas condiciones.

En el capítulo 5 se describe la síntesis, caracterización y rendimiento electroquímico de materiales híbridos basados en óxido de grafeno reducido (rGO) y

polioxometalatos dispersos en un electrolito acuoso (H_2SO_4) para producir un nanofluido. Estos nanofluidos presentan baja viscosidad y muestran una respuesta electroquímica ultrarrápida e híbrida, con contribución tanto capacitiva del rGO como faradaica de los polioxometalatos. Demostrando así su funcionamiento como fluidos de almacenamiento de energía con plena carga y descarga de todo el material sólido disperso.

El sexto capítulo presenta un nuevo tipo de nanofluido basado en rGO. En lugar de usar tensioactivos convencionales como en el capítulo descrito anteriormente, disolvimos una molécula aromática capaz de estabilizar el rGO en un electrolito acuoso mediante interacciones de tipo π - π . Con este enfoque logramos un gran aumento en la estabilidad del nanofluido. Además, este nuevo nanofluido también mostró una gran capacidad de transferencia de carga, como lo demuestra el hecho de que permite que se produzca actividad redox de nanopartículas de LiFePO_4 (sin recubrimiento conductor) simplemente dispersas en el nanofluido. Por lo tanto, gracias a la presencia de rGO en el nanofluido, los electrones podrían alcanzar las nanopartículas dispersas y, por lo tanto, cargarse y descargarse de manera efectiva y completa, algo que no es posible en nanofluidos que contienen solo nanopartículas de LiFePO_4 .

La síntesis de grafeno también se ha estudiado en profundidad en esta tesis tal y como se puede ver en el capítulo 7, dado que el objetivo final es producir materiales que se puedan usar en aplicaciones reales, asegurarse de que los materiales con los que se trabaja se pueden producir en cantidades grandes, mediante métodos escalables y elementos abundantes es también importante. Como resultado, se ha desarrollado y patentado un nuevo método para la producción de grafeno por exfoliación electroquímica de grafito. En esta tesis se presenta la patente, un resumen de los resultados obtenidos y el estado del arte del método de exfoliación electroquímica de grafeno.

En esta tesis hemos demostrado el potencial de los nanofluidos en el almacenamiento de energía electroquímica. A partir de los resultados mostrados aquí, podemos inducir conclusiones generales importantes sobre los efectos extendidos de pequeñas cantidades de sólidos en todo el volumen del nanofluido. Hemos demostrado que las dispersiones estables de rGO en agua pueden transferir la carga a través de todo el volumen de nanofluidos, lo que hace que todo el nanofluido actúe como un electrodo supercondensador que almacena la carga a través de un mecanismo capacitivo. De hecho, el nanofluido acuoso rGO mostró una transferencia de carga extremadamente rápida, pudiendo realizar ciclos a $10\text{V}\cdot\text{s}^{-1}$. Gracias a esta rápida

transferencia de carga, pudimos cargar y descargar por completo nanopartículas activas redox dispersas de LiFePO_4 y detectar claramente picos redox incluso a $25 \text{ mV}\cdot\text{s}^{-1}$. Además, al dopar el rGO con especies redox activas moleculares como los polioxometalatos, desarrollamos sistemas híbridos con potencia y capacidad mejoradas con respecto al nanofluido rGO puro. Finalmente, demostramos que los nanofluidos de rGO acuosos pueden mejorar su estabilidad al disolver una molécula aromática (DABA) capaz de estabilizar rGO mediante interacciones π - π manteniendo su buena conductividad eléctrica. Todo esto ha sido posible manteniendo la viscosidad de los nanofluidos desarrollados muy cerca de los disolventes originales, lo que facilitará su aplicación final en dispositivos de flujo real. Por otro lado, la baja concentración de nanopartículas de grafeno podría ser una desventaja para la aplicación de estos materiales en dispositivos de alta densidad de energía. Por lo tanto, aumentar la carga de nanopartículas electroactivas es un objetivo importante.

En resumen, hemos diseñado y preparado nanofluidos basados en grafeno pero también en híbridos de grafeno. Hemos mostrado en esta descripción general cómo estos novedosos materiales de nanofluidos pueden presentar rendimientos sobresalientes incluso en el caso de sistemas muy diluidos. Hemos demostrado efectos no lineales, que conducen a propiedades notables con pequeñas cantidades de grafeno dispersas en los nanofluidos. Por lo tanto, nuestro trabajo subraya el sólido potencial de estos sistemas para el almacenamiento de energía.